Statistical analysis of the X-ray morphology of galaxy clusters

Alexandra Weißmann

München 2013

Statistical analysis of the X-ray morphology of galaxy clusters

Alexandra Weißmann

Dissertation
an der Fakultät für Physik
der Ludwig–Maximilians–Universität
München

vorgelegt von
Alexandra Weißmann
aus Wien, Österreich

München, den 11.10.2013

Erstgutachter: Prof. Dr. Hans Böhringer
Zweitgutachter: Prof. Dr. Ortwin Gerhard
Tag der mündlichen Prüfung: 9.12.2013

Contents

List of Figures

List of Tables

Zusammenfassung

Die morphologische Analyse von Galaxienhaufen im Röntgenbereich ermöglicht eine zuverlässige Bestimmung ihres dynamischen Zustands. Substrukturen im (sub-)Mpc Bereich beeinflußen das Gravitationspotential eines Haufens und spiegeln sich in der Verteilung der Röntgenoberflächenhelligkeit als zusätzliche helle oder allgemein irreguläre Strukturen wider. Sie führen zu Abweichungen vom hydrostatischen Gleichgewicht und sphärischer Gestalt, zwei Annahmen, die in Studien von Galaxienhaufen oft gemacht werden, um globale astrophysikalische Eigenschaften zu bestimmen. Die Analyse der Röntgenmorphologie von Galaxienhaufen liefert daher wichtige Informationen, vorausgesetzt, die benutzten Substrukturmaße wurden eingehend getestet und kalibriert.

In dieser Arbeit wird die Röntgenmorphologie von Galaxienhaufen mithilfe von drei bekannten Substrukturparametern (Power ratios, Center shift Parameter und Asymmetrieparameter) quantifiziert, um den Anteil der gestörten Galaxienhaufen als Funktion der Rotverschiebung zu studieren. Um eine zuverlässige Anwendung der Substrukturparameter auf eine Vielzahl von Röntgenbildern zu ermöglichen, wird eine detaillierte Parameterstudie durchgeführt. Sie testet die Effizienz und Verlässlichkeit der Parameter bei unterschiedlicher Datenqualität und basiert auf der Auswertung von simulierten Röntgenbildern und Beobachtungsdaten. Gerade bei der Anwendung auf Röntgenbilder mit geringer Photonenanzahl, wie z.B. Beobachtungen von weit entfernten Galaxienhaufen oder Durchmusterungsdaten, ist die genaue Kenntnis der Parametercharakteristika erforderlich. Beim Vergleich der drei Substrukturparameter zeigt sich, dass der Center shift Parameter am Wenigsten von Poisson-Rauschen beeinflußt wird und eine zuverlässige Bestimmung des Haufenzustands auch bei Beobachtungen mit geringer Photonenanzahl erlaubt. Power ratios, besonders der Hexapol $P3/P0$, und der Asymmetrieparameter A andererseits, werden stark von Poisson-Rauschen beeinträchtigt, welches zu verfälscht hohen Substruktursignalen führt. Weiters präsentiert diese Arbeit Methoden, mit denen sich die Beeinträchtigung von Rauschen minimieren lässt.

Die Resultate der Parameterstudie tragen zur Verbesserung der morphologischen Analyse von weit entfernten Galaxienhaufen bei und werden in dieser Arbeit benutzt, um den Anteil der gestörten Galaxienhaufen als Funktion der Rotverschiebung zu quantifizieren. Hierfür wird die Röntgenmorphologie von 78 nahen ($z < 0.3$) und 51 weit entfernten ($0.3 < z < 1.08$) Objekten mit unterschiedlicher Datenqualität bestimmt. Die nahen Galaxienhaufen wurden mit dem *XMM-Newton* Observatorium beobachtet, haben eine hohe Photonenanzahl und sind Teil von mehreren, gut studierten und repräsentativen Stichproben von Galaxienhaufen. Für $z > 0.3$ werden die hoch-rotverschobenen Haufen des Katalogs der 400d^2 und SPT Durchmusterung benutzt. Diese Objekte wurden hauptsächlich mit dem *Chandra* Observatorium

beobachtet und haben eine geringe Photonenanzahl. Um einen fairen Vergleich zu gewährleisten, welcher unabhängig von der Datenqualität ist, wird die Photonenanzahl der nahen und entfernten Haufen vor der morphologischen Analyse angeglichen.

In Übereinstimmung mit dem hierarchischen Strukturbildungsmodell wird eine leicht positive Entwicklung mit der Rotverschiebung, d.h. ein größerer Anteil an Galaxienhaufen mit gestörter Röntgenmorphologie bei höherer Rotverschiebung, gefunden. Wegen der geringen Anzahl von Beobachtungen von weit entfernten Galaxienhaufen, die meist nur eine geringe Photonenanzahl haben, hat dieses Resultat eine geringe statistische Signifikanz. Für zwei der drei Substrukturparameter (Power ratios und Center shift Parameter) sind die Resultate innerhalb der Fehler auch konsistent mit keiner Entwicklung, aber eine negative Entwicklung des Anteils der gestörten Haufen kann für alle drei Substrukturparameter ausgeschlossen werden.

Summary

The morphological analysis of galaxy clusters in X-rays allows a reliable determination of their dynamical state. Substructures on (sub-)Mpc scale influence the gravitational potential of a cluster and manifest themselves in the X-ray surface brightness distribution as secondary peaks or overall irregular shape. They lead to deviations from the hydrostatic equilibrium and spherical shape, two assumptions which are widely used in galaxy cluster studies to derive global astrophysical properties. Analyzing the X-ray morphology of clusters thus yields valuable information, provided that the employed substructure measures are well-tested and well-calibrated.

In this work, the X-ray morphology of galaxy clusters is quantified using three common substructure parameters (power ratios, center shift and the asymmetry parameter), which are subsequently employed to study the disturbed cluster fraction as a function of redshift. To ensure a reliable application of these substructure parameters on a variety of X-ray images, a detailed parameter study is conducted. It focuses on the performance and reliability of the parameters for varying data quality using simulated and observed X-ray images. In particular, when applying them to X-ray images with low photon counts such as observations of distant clusters or survey data, it is important to know the characteristics of the parameters. Comparing the three substructure measures, the center shift parameter is most robust against Poisson noise and allows a reliable determination of the clusters' dynamical state even for low-count observations. Power ratios, especially the hexapole $P3/P0$, and the asymmetry parameter, on the other hand, are severely affected by noise, which results in spuriously high substructure signals. Furthermore, this work presents methods to minimize the noise bias.

The results of the parameter study provide a step forward in the morphological analysis of high-redshift clusters and are employed in the framework of this thesis to quantify the evolution of the disturbed cluster fraction. The sample used for this analysis comprises 78 low-z ($z < 0.3$) and 51 high-z ($0.3 < z < 1.08$) galaxy clusters with varying photon statistics. The low-redshift objects were observed with the *XMM-Newton* observatory, contain a high number of photon counts and are part of several well-known and representative samples. For $z > 0.3$, the high-redshift subsets of the 400d[2] and SPT survey catalog are used. These objects were mainly observed with the *Chandra* observatory and have low photon counts. To ensure a fair comparison, which is independent of the data quality, the photon statistics of the low- and high-redshift observations are aligned before performing the morphological analysis.

In agreement with the hierarchical structure formation model, a mild positive evolution with redshift, i.e. a larger fraction of clusters with disturbed X-ray morphologies at higher redshift, is found. Owing to the low photon counts and small number of high-redshift ob-

servations, the statistical significance of this result is low. For two of the three substructure parameters (power ratios and center shift) the findings are also consistent within the significance limits with no evolution, but a negative evolution of the disturbed cluster fraction can be excluded for all parameters.

Preamble

Galaxy clusters are extremely large and massive systems and are thus excellent laboratories to study numerous ongoing astrophysical processes in their deep gravitational potential wells. These properties also make them ideal tracers of the large-scale structure and testbeds for cosmological models. Global astrophysical properties of clusters are often derived assuming these objects to be roughly spherically symmetric and in hydrostatic equilibrium. This is especially true for cosmological studies, where clusters are seen as very simple objects governed essentially by one parameter – their mass. However, X-ray observations revealed the presence of substructures and other disturbances. This indicates that complex processes are taking place in galaxy clusters. Morphological studies present an interesting and important aspect of galaxy cluster research, because they characterize their general appearance and thus provide crucial information about the dynamical state of these systems.

This thesis aims at quantifying the dynamical state of galaxy clusters by analyzing their X-ray morphology. This enables studying the fraction of disturbed clusters as a function of redshift, which is predicted to be higher at earlier times by the current structure formation theory. Since X-ray observations suffer from photon noise, it is essential to use well-studied and calibrated morphology estimators to assess the dynamical state of these massive objects. A large fraction of this work is thus devoted to performance studies of different substructure parameters for varying data quality. In addition, methods to estimate and correct for the biases caused by Poisson noise and X-ray background are presented and tested thoroughly. This ensures a reliable quantification of the X-ray morphology of low- and high-quality data, which is indispensable when dealing with a large redshift range and thus varying photon statistics.

This thesis tries to resolve some of these issues by addressing the following questions:

- How reliable is the determination of the X-ray morphology and the dynamical state of galaxy clusters using common substructure measures such as power ratios, center shift or the asymmetry parameter, especially for varying data quality?
- Can the bias in the X-ray images due to shot noise be estimated and corrected sufficiently to ensure a fair comparison of low- and high-quality data?
- What is the best definition of a morphological boundary to divide a sample into relaxed and disturbed objects?
- Can the predicted increase of the fraction of disturbed galaxy clusters with redshift be confirmed by observations and quantified using the above mentioned substructure parameters?

To discuss the main concepts relevant for the analyses presented in this thesis, a general introduction to galaxy clusters, morphological studies and X-ray observations are given in the first chapters of this work. **Chapter 1** provides an introduction to galaxy clusters, focusing on the X-ray emission from the intracluster medium, mass estimates based on X-ray data and the use of clusters for cosmological studies. Substructures observed in galaxy clusters on different scales and the importance of the quantification of the cluster morphology with respect to cluster properties and especially mass estimates is discussed in **Chapter 2**. The X-ray images used for the morphological analysis were obtained from the current X-ray observatories, *XMM-Newton* and *Chandra*, which are described in **Chapter 3**. This chapter also provides the general aspects of reducing X-ray data of extended sources based on the example of *XMM-Newton* observations. A reduction pipeline for *Chandra* observations was compiled as part of this thesis and is given in **Appendix A**.

Original research performed in the framework of this thesis, which resulted in two publications in a refereed journal and a soon-to-be submitted paper draft, is provided in Chapters 4−6. **Chapter 4** presents a study of the noise and error properties of the morphology estimators power ratio $P3/P0$ and center shift w. For the first time their performance as a function of data quality is tested in great detail using X-ray images of simulated galaxy clusters. This enables a direct comparison between the real substructure measure and spuriously high signals due to shot noise in the X-ray image. In addition, a well-calibrated method to correct for the noise bias and morphological boundaries for $P3/P0$ and w to classify clusters as relaxed and disturbed objects are presented. The bias correction method is applied to a sample of 80 high-quality *XMM-Newton* observations of galaxy clusters to obtain morphological information and to test the classification using $P3/P0$ and w against a visual classification scheme. This chapter was published as Weißmann et al. (2013b) in A&A. **Chapter 5** provides a morphological analysis of a large number of X-ray observations with varying redshift and thus data quality. Using the well-calibrated substructure parameters from Chapter 4 and degrading high-quality low-redshift observations to the average data quality of low-quality high-redshift ones, a mild increase of the fraction of disturbed galaxy clusters is found with increasing redshift. However, within the uncertainty limits, the results are also consistent with no evolution. This chapter was published as Weißmann et al. (2013a) in A&A. A performance study of the asymmetry parameter A as substructure measure for galaxy clusters is presented in **Chapter 6**. This parameter is extremely sensitive to Poisson noise which is taken into account when classifying the morphology in X-ray images with varying photon statistics. In agreement with the study presented in Chapter 5, the asymmetry parameter shows a very mild positive, but in this case significant, redshift evolution of the disturbed cluster fraction.

The thesis closes with **Chapter 7**, where conclusions of this work are presented. It provides a summary of the research goals reached during the framework of this thesis and gives a future outlook.

Chapter 1

Galaxy clusters

Galaxy clusters are the largest gravitationally bound building blocks of the Universe. According to the current ΛCDM cosmological model, they are the last structures to form in a hierarchical fashion from primordial density fluctuations. They are tracers of cosmic structure formation and thus sensitive to the underlying cosmology. Their deep potential wells contain all components of the Universe and make galaxy clusters excellent astrophysical laboratories. The following sections provide an introduction to galaxy clusters, focusing on the points most relevant for X-ray analysis and the study of cluster morphology.

Clusters of galaxies were first observed in the optical band as spatial overdensities of galaxies in a particular sky region. Following the observations of Messier (1784) and Herschel (1785) of concentrations of galaxies (or "nebulae" back then) in the Virgo and Coma constellations, the number of known galaxy clusters increased significantly over the next two centuries (for a review see e.g. Biviano 2000). A milestone in the study of these objects was set by Abell with his cluster catalog (Abell 1958), containing most of the known nearby galaxy clusters. He was aware of the danger of projection effects and chose his cluster criteria very carefully by counting the number of galaxies above a certain magnitude limit inside a certain projected radius (Abell radius $\sim$ 2 Mpc). The optical cluster identification techniques used today are based on and an extension of Abell's work.

Probably the most important discovery after the first observations of galaxy clusters was made by Zwicky in the 1930s. He calculated the total cluster mass for a virialized and isolated system of galaxies. The result was astonishing. In order to be gravitationally bound, a cluster needed about 100 times the mass observed in galaxies. This missing mass was later ascribed to the hot intracluster medium and dark matter. In addition, Zwicky was the first to suggest the technique of gravitational lensing to obtain an independent measurement of the cluster mass. This method, however, could not be realized for the next few decades.

With the ascent of X-ray studies, another important aspect of galaxy clusters was revealed. Limber (1959) argued that galaxy formation from gas is inefficient and predicted the presence of hot intracluster gas which was lost during galaxy collisions. A few years later, Byram et al. (1966) published the discovery of X-ray emission associated with M87, the central galaxy of the Virgo Cluster. Early balloon- or rocket-borne detectors enabled more reports of X-ray detections in the direction of known clusters, suggesting that galaxy clusters are X-ray sources. Inspired by these results, Felten et al. (1966) described the X-ray emission as

thermal bremsstrahlung. These findings were confirmed with the launch of *Uhuru*, the first X-ray satellite, in 1970 which performed an extensive sky survey. In the following decades galaxy clusters were subject to detailed studies, which resulted in important discoveries such as the emission line of highly ionized iron ($\sim$ 7 keV) in the X-ray spectrum of the Perseus Cluster (Mitchell et al. 1976) or the complexity of cluster morphologies (e.g. Jones et al. 1979; Jones & Forman 1984).

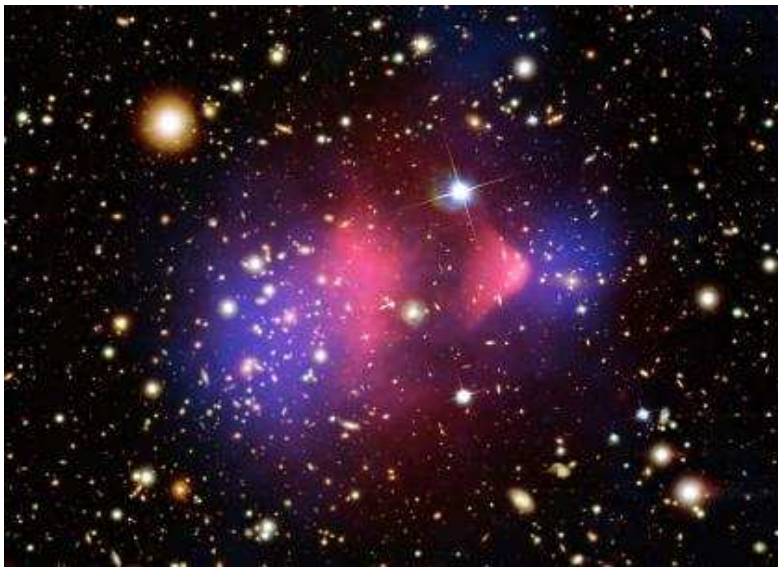

Figure 1.1: Composite image of the main constituents of a galaxy cluster using the example of the Bullet Cluster 1E 0657-56. The separation between the intracluster medium (red) and the non-collisional galaxies and dark matter (blue) is evident. Image credit: X-ray: NASA/CXC/CfA/M.Markevitch et al.; Lensing Map: NASA/STScI; ESO WFI; Magellan/U.Arizona/D.Clowe et al.; Optical: NASA/STScI; Magellan/U.Arizona/D.Clowe et al.

These studies slowly formed the current picture of galaxy clusters. The main constituent of these $\sim$ Mpc large gravitationally bound objects is dark matter, containing $\sim$ 84% of the total cluster mass. X-ray observations revealed the existence of hot gas, the intracluster medium, which accounts for $\sim$ 13% while optically visible components like galaxies, stars or dust comprise $\sim$ 3% of the total cluster mass. These three components are illustrated in a composite image of the Bullet Cluster 1E 0657-56 in Fig. 1.1 (Markevitch et al. 2002; Clowe et al. 2006). The merging system comprises a main cluster plus a smaller merging body ("bullet"). The optical image shows two well-separated galaxy concentrations after the core passage. Due to its collisional nature, the hot gas is lagging behind, forming a bullet-shaped shock front. The massive cluster acts as a gravitational lens and enables mass reconstruction of the otherwise invisible dark matter component using small distortions of lensed background galaxies. The reconstruction of the matter density distribution is shown in blue and coincides with the galaxy concentrations. Without dark matter, there would be no separation between the mass concentration and the X-ray gas. This system thus provides empirical evidence for the existence of dark matter.

All three components provide interesting insights into galaxy cluster physics. However,

Table 1.1: Characteristical properties of galaxy clusters.

Virial radius	$1 - 2$ Mpc
Virial mass	$10^{13} - 10^{15}\ M_\odot$
Temperature	$\sim 0.5 - 10$ keV ($10^7 - 10^8$ K)
ICM density	$10^{-5} - 10^{-1}$ cm^{-3}
Metallicity	$0.2 - 0.5\ Z_\odot$
X-ray luminosity	$10^{43} - 10^{45}$ erg/s

since this thesis is based on X-ray observations, only the intracluster medium will be discussed in more detail. Sect. 1.1 covers the main properties of the intracluster medium, which provide the base for the discussion of different methods to estimate the total cluster mass and how these estimates are affected by the cluster morphology (Sect. 1.2). Finally, cosmological applications of galaxy clusters, in particular the cluster mass function, are outlined in Sect. 1.3.

1.1 Intracluster medium

A part of the missing mass problem discussed by Zwicky was solved with the discovery of hot plasma, the so-called intracluster medium (ICM), inside the cluster potential. Since galaxy formation is ineffective and only $\sim$ 10% of the Universe's baryons formed stars, the majority is found in intergalactic space. During cluster formation, the infalling gas is shock-heated by the deep gravitational potential to temperatures in the keV regime and radiates in X-rays. This enables the otherwise very difficult study of the baryonic content of the Universe. X-ray studies revealed a contribution of $\sim$ 15% of the ICM to the total cluster mass, making it the most massive cluster component we can observe directly. According to cluster formation theory, the ICM thermalizes after its infall into the potential well and reaches a quasi-equilibrium state which can be described using the virial theorem. Assuming such a state, cluster properties such as the virial radius (typically $1 - 2$ Mpc) and the virial mass ($10^{13} - 10^{15}\ M_\odot$) can be inferred. A summary of these properties is given in Table 1.1. A more detailed discussion of mass estimates and how they are affected by the dynamical state of the cluster is provided in Sect. 1.2. The ICM is extremely hot with typical cluster temperatures of $0.5 - 10$ keV ($10^7 - 10^8$ K), while the density is very low with $10^{-5} - 10^{-1}$ particles per cm^3. This indicates that the ICM is an optically thin plasma. It contains mainly hydrogen with a typical abundance of heavy elements of $0.2 - 0.5\ Z_\odot$, where $Z_\odot$ denotes the solar abundance. These so-called metals are injected into the ICM through interactions with the galaxies and their stellar populations like stellar winds or supernova explosions (for details on metal enrichment of the ICM see e.g. Schindler & Diaferio 2008; Werner et al. 2008).

1.1.1 X-ray emission

The X-ray emission observed from galaxy clusters is mainly due to thermal bremsstrahlung emitted by the hot, highly-ionized ICM (Felten et al. 1966). It is a free-free emission process and is observed as continuum emission. Charged particles such as free ICM electrons are accelerated when being deflected by another charged particle (e.g. an atomic nucleus) and emit bremsstrahlung. The bremsstrahlung emissivity (luminosity per unit volume and frequency

interval) as a function of frequency is given for the collision of an electron with an ion as

$$\epsilon(\nu) \approx 6.8 \times 10^{-38}\ Z_{\rm i}^2\ n_{\rm e}\ n_{\rm i}\ g^{ff}(\nu, T)\ e^{-\frac{h\nu}{kT}}\ T^{-1/2}\ \mathrm{erg\ s^{-1}\ cm^{-3}\ Hz^{-1}}, \tag{1.1}$$

where $Z_{\rm i}$ is the ion charge, $n_{\rm e}$ and $n_{\rm i}$ the number densities of electrons and ions, $g^{ff}(\nu, T)$ the Gaunt factor, h the Planck constant, k the Boltzmann constant and T the temperature of the plasma. For an optically thin hydrogen plasma with $n_{\rm e} \approx n_{\rm i}$, integrating over the frequency range gives the total emissivity with $\epsilon \propto n_{\rm e}^2\ T^{1/2}$. The velocity distribution of the electrons follows a Maxwellian distribution, thus this radiation is named thermal bremsstrahlung.

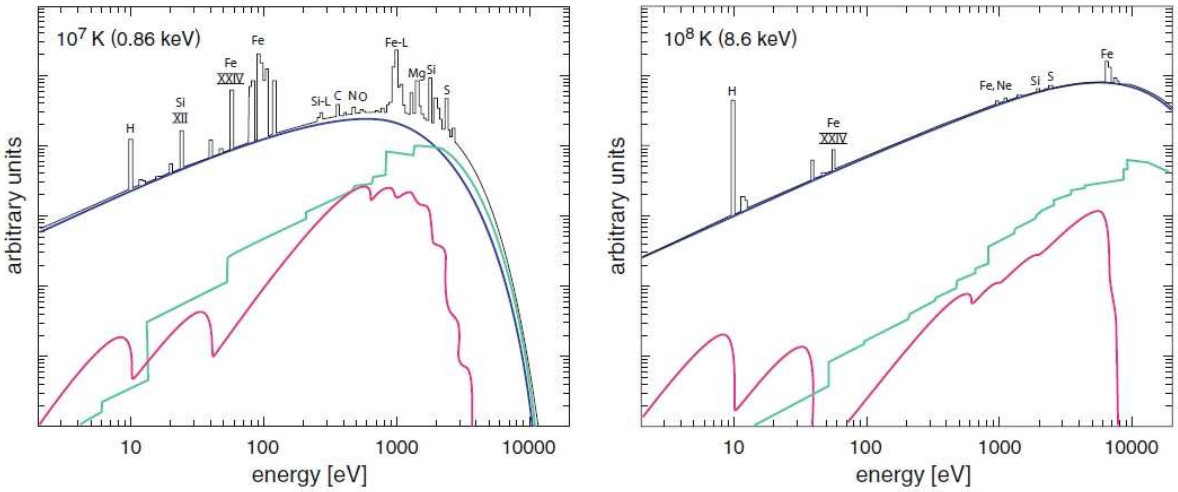

Figure 1.2: Comparison of X-ray spectra for solar abundance and different plasma temperatures. The continuum emission comprises bremsstrahlung (blue), which is dominant at these high temperatures, recombination radiation (green) and 2-photon radiation (red). In addition, the most important emission lines relevant for galaxy clusters are indicated. Figures taken from Böhringer & Werner (2010).

Fig. 1.2 shows X-ray spectra of two galaxy clusters with different ICM temperatures and the contributions of several radiation processes. The continuum emission determines the overall shape of the cluster spectrum and provides information about the cluster temperature. It is comprised mainly of bremsstrahlung with small contributions of recombination and 2-photon radiation. In addition, emission lines due to metals in the ICM are found superposed on the continuum emission. For higher ICM temperature, bremsstrahlung becomes more dominant and fewer emission lines contribute to the total radiation. Fig. 1.3 gives the cooling rate, the rate at which energy is radiated away, of a hot, optically thin plasma as a function of temperature. It illustrates the contribution of continuum and line emission and gives the individual cooling rates for a number of elements assuming solar abundance. For $kT \gtrsim 2$ keV (or $T \gtrsim 2 \times 10^7$ K), where the ICM is almost completely ionized, bremsstrahlung is the primary radiation process. However, at low temperatures line emission becomes dominant due to the abundance of heavy elements which are not fully ionized. More detailed information and references can be found in Böhringer & Werner (2010), a review of X-ray spectroscopy of galaxy clusters.

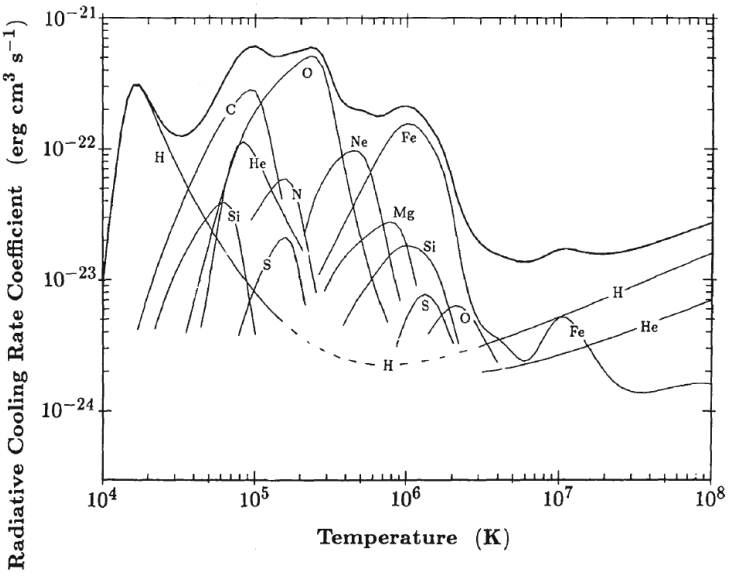

Figure 1.3: Cooling rate of an optically thin, hot plasma as a function of temperature, including the individual contributions to the total cooling rate of a number of elements assuming solar abundance. The high temperature end is dominated by bremsstrahlung while line emission becomes important for $T < 2 \times 10^6$ K. Figure taken from Böhringer & Hensler (1989).

The spatial distribution of the X-ray emission from galaxy clusters can be described by the so-called isothermal β model (Cavaliere & Fusco-Femiano 1976, 1978). Assuming hydrostatic equilibrium, spherically symmetric shape and isothermality, the density of the ICM can be approximated as

$$\rho_{\mathrm{g}} = \rho_{\mathrm{g},0} \left[1 + \left(\frac{r}{r_{\mathrm{c}}} \right)^2 \right]^{-3\beta/2} , \tag{1.2}$$

where $\rho_{\mathrm{g},0}$ is the central gas density and r_{c} the core radius. β is determined empirically scattered around $\sim 2/3$ (e.g. Jones & Forman 1984) and seems to decrease for poorer clusters (e.g. Finoguenov et al. 2001; Sanderson et al. 2003). Using this density distribution, isothermality and the fact that the X-ray emission is proportional to the square of the gas density, yields an X-ray surface brightness profile of the following form when integrating along the line of sight:

$$S \propto \left[1 + \left(\frac{r}{r_{\mathrm{c}}} \right)^2 \right]^{-3\beta+\frac{1}{2}} . \tag{1.3}$$

This simplified model allows the general description of the galaxy cluster X-ray surface brightness, but tends to underestimate the central surface brightness due to non-isothermality of the ICM for cool core clusters (e.g. Jones & Forman 1984, 1999) and overestimate it in the outskirts because the underlying King profile (King 1962) differs from the real cluster potential (e.g. Vikhlinin et al. 1999).

In addition, X-ray observations revealed a large number of clusters with disturbed morphologies and substructures, which do not agree with the assumptions made for the β model. Also

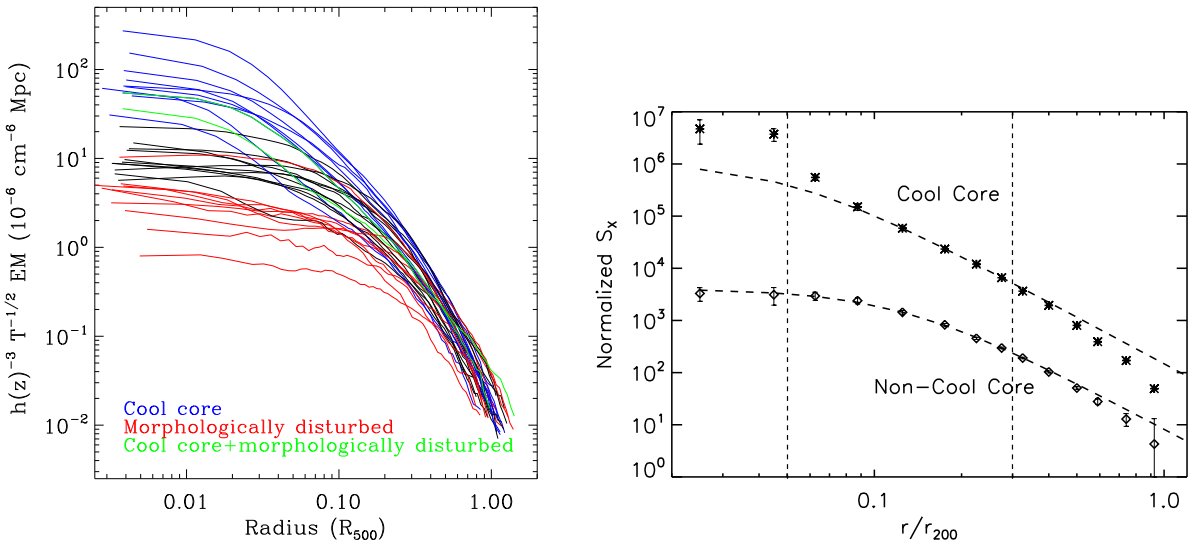

Figure 1.4: **Left:** Emission measure profiles of the REXCESS clusters. The peaked profiles in the central regions of cool core clusters (blue and green) in comparison to non-cool core clusters (red and black) are apparent. Figure taken from Pratt et al. (2009). **Right:** Average X-ray surface brightness profile for cool core and non-cool core clusters. The best-fit single β models are given as dashed curves and the disagreement for cool core clusters is clearly visible. For the purpose of clarity, the profile of the non-cool core clusters is shifted downwards by a factor of 10. Figure taken from Burns et al. (2008).

for clusters hosting a cool core, which is characterized by a steep central surface brightness peak (see Sect. 1.1.2), the simple β model solution does not resemble their surface brightness profiles (see Fig. 1.4). One way to resolve this issue was to use a combination of two β profiles, one for the cluster core and one for the outskirts (e.g. Ikebe et al. 1996; Ettori 2000a; Henning et al. 2009; Eckert et al. 2011).

Alternatively, Ettori (2000b) suggested the polytropic β model, where the gas density follows the β model, but assumes a polytropic relation between the gas density and temperature.

1.1.2 Cool core clusters

Cool core clusters are characterized by a very steep central peak in the surface brightness profile (see Fig. 1.4). Due to the $\rho_g(r)^2$ dependence of the X-ray emission, the cooling by radiation is particularly high in these dense cores and the cooling time can become shorter than the Hubble time (e.g. Lea et al. 1973; Silk 1976; Fabian & Nulsen 1977). This led to the idea of the *cooling flow model* with a cooling catastrophe in the cluster core (e.g. Fabian & Nulsen 1977). Because of the short cooling time and in absence of a heat source, a large fraction of cluster gas is expected to cool, flow into the cluster center and form stars with a typical mass deposition rate of $\sim 10^2 - 10^3\ M_\odot$/year (e.g. Fabian 1994). Observational evidence for gas cooling out of the X-ray band such as star-formation activity in the BCGs of suspected cooling flow clusters was found (e.g. McNamara & O'Connell 1989; Cavagnolo et al. 2008), but these signatures were far below the predictions of the cooling flow model. While the mean cluster temperature decreases towards the center of cool core clusters, giving rise to the very bright

core, there was no significant evidence that large amounts of the ICM cool below $1/2 - 1/3$ of the virial temperature (e.g. Peterson et al. 2001, 2003; Sanders et al. 2008). X-ray astronomers were thus in need of an energy source which generates just enough heat to stop most of the gas from cooling. The primary source of heating is now believed to be feedback from active galactic nuclei (AGN) of the brightest cluster galaxies. AGN are frequently observed in cool core clusters and are often radio sources (e.g. Burns 1990). AGN feedback provides enough energy output to stop the cooling catastrophe in the core (e.g. Birzan et al. 2004; Best et al. 2006; Dunn & Fabian 2006; Rafferty et al. 2006), although the exact feedback and transport mechanisms are still debated.

Cool cores are usually found in clusters with an overall regular X-ray morphology, which are assumed to be dynamically relaxed. However, they show small-scale substructures in the central region like X-ray cavities, ripples or jets, which can be explained through the interaction of the AGN and the surrounding gas (for more details and references see the reviews of e.g. Fabian 2012; Gitti et al. 2012; McNamara & Nulsen 2012, and Sect. 2.1). The presence of a cool and therefore very bright core has an effect on X-ray scaling relations (see Sect. 1.2.2), but does not influence the morphological classification on cluster-scale, since including and excluding the core region gives consistent results (see Sect. 5.6.2).

The most extreme cool core cluster known so far is the so-called Phoenix Cluster at $z \sim 0.6$ (McDonald et al. 2012). This system hosts an AGN and an extremely strong cooling flow is observed. In addition, its central galaxy seems to be experiencing a massive starburst, transforming vast amounts of gas into stars. This suggests that the AGN jets are not powerful enough to completely prevent the cluster gas from cooling and from flowing into the center. Since this is a high-redshift system and no clusters with such strong cooling flows are known at $z = 0$, this cluster may be the first observational indication that the mechanism which stops the cooling flow was less effective at earlier times. Future studies of high-redshift clusters are needed to see whether this theory holds or whether the Phoenix Cluster is a unique system.

The origin of cool cores is still debated, but observations support the picture that merging can disrupt an existing cool core, resulting in a non-cool core cluster. While a correlation between the lack of a cool core and recent or ongoing merging activity was found, a definite definition that all cool core clusters are relaxed and all non-cool core clusters disturbed systems does not hold (e.g. Sanderson et al. 2009; Hudson et al. 2010; Rossetti et al. 2011).

1.2 Mass estimates

After having discussed the properties of X-ray emission in Sect.1.1.1, this section will mainly focus on how to derive mass estimates from it. Determining the total cluster mass to a high precision is important for cluster physics but essential for testing cosmology (for reviews see e.g. Voit 2005; Borgani 2008). Observations in the optical or microwave range provide additional methods to estimate the cluster mass (Sect. 1.2.3). All methods, however, are based on certain assumptions (e.g. hydrostatic equilibrium), which are often not valid for all clusters. After describing the mass estimation methods, their limitations are discussed.

1.2.1 Hydrostatic mass estimates

X-ray observations provide information about the ICM, the gas component of the cluster, which is expected to be in approximate hydrostatic equilibrium (HE) for many objects. Assuming a spherically symmetric gas distribution, the hydrostatic equilibrium equation has the following form:

$$\frac{1}{\rho_\mathrm{g}}\frac{dP_\mathrm{g}}{dr} = -\frac{d\Phi}{dr} = -\frac{GM_\mathrm{tot}}{r^2}, \tag{1.4}$$

where P_g is the gas pressure, ρ_g the gas mass density, and G the gravitational constant. Solving this equation gives the total gravitating cluster mass within radius r as a function of the density and temperature profile:

$$M_\mathrm{tot}(<r) = -\frac{kTr}{\mu m_\mathrm{p} G}\left(\frac{d\ln\rho_\mathrm{g}}{d\ln r} + \frac{d\ln T}{d\ln r}\right). \tag{1.5}$$

The gas density profile $\rho_\mathrm{g}(r)$ can be derived from X-ray surface brightness measurements using e.g. the β model (see Sect. 1.1.1) or more realistic models (e.g. Croston et al. 2006; Vikhlinin et al. 2006). For the extraction of the temperature profile $T(r)$ from fitting models to the X-ray spectra, however, sufficiently good X-ray data (enough photons per radial bin) are required. The precision of this mass measurement thus depends on the amount of collected photons. Observations of high-redshift clusters or surveys often do not have a sufficient number of photons to derive a useful temperature profile; in such cases, scaling relations can be used (see Sect. 1.2.2).

This method strongly relies on the assumptions of hydrostatic equilibrium and spherical shape, giving rise to the so-called *hydrostatic mass bias* (HMB). When using a spherical model (e.g. β model), the second assumption is invalid for dynamically young clusters showing asymmetries in their ICM distribution or signs of merging (see Chapter 2) and will lead to inaccurate mass estimates for individual clusters. More important for the HMB is the question whether the equilibrium assumption holds (see Sect. 2.3 for a detailed discussion of the influence of merging on the HE assumption). The hydrostatic mass estimates are based on purely thermal ICM pressure support. In case of additional non-thermal pressure due to e.g. subsonic bulk or turbulent motions in the ICM, the mass estimates assuming HE will underestimate the total cluster mass. The HMB has been studied by many authors both with numerical simulations (e.g. Kay et al. 2004; Rasia et al. 2006; Nagai et al. 2007; Piffaretti & Valdarnini 2008; Lau et al. 2009; Meneghetti et al. 2010; Rasia et al. 2012) and observationally (e.g. Arnaud et al. 2007; Mahdavi et al. 2008; Zhang et al. 2010; Mahdavi et al. 2013). Mass estimates based on the HE assumption were typically found to give $\sim 5-20\%$ lower values than weak lensing measurements, which do not require this assumption (see Sect. 1.2.3). The comparison of weak lensing (M_WL) and hydrostatic mass estimates (M_X) for cool core and non-cool core clusters from Mahdavi et al. (2013) is shown in Fig. 1.5. Cool core clusters are usually relaxed systems on cluster scale and show on average no significant difference between the X-ray and lensing mass. For non-cool core clusters, which are typically disturbed or merging systems, the offset towards higher lensing masses is apparent. In general, the largest HMB is found for dynamically young objects showing signs of substructure, but also relaxed clusters suffer from it to some extent because of e.g. residual bulk motions due to past merging activities or the incomplete thermalization of the ICM.

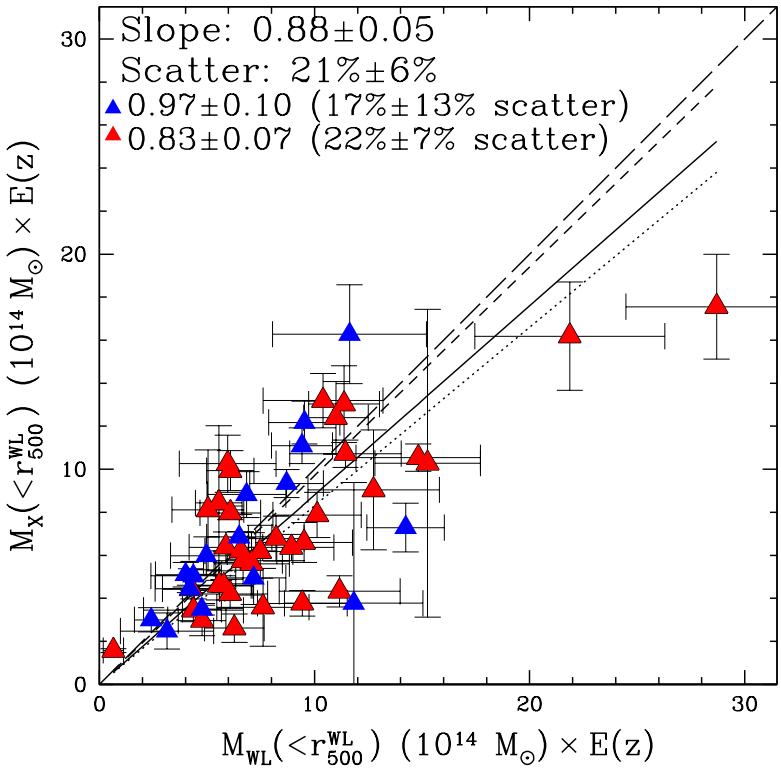

Figure 1.5: Comparison of weak lensing ($M_{\rm WL}$) and hydrostatic mass estimates ($M_{\rm X}$). Cool core clusters are shown as blue and non-cool core clusters as red triangles. As discussed in Sect. 1.1.2, cool cores are usually found in relaxed clusters while non-cool core clusters are often merging systems. The best fit to all clusters is shown by the solid line, while the short-dashed one indicates the relation for cool core and the dotted line for non-cool core clusters. For comparison, the long dashed line shows the 1-1 line. Figure taken from Mahdavi et al. (2013).

1.2.2 X-ray scaling relations

X-ray scaling relations relate X-ray cluster properties to each other and can be approximated by simple power laws. Compared to direct mass measurements such as hydrostatic mass estimates, where the temperature and density profile have to be extracted from the observations, scaling relations provide observationally cheap means to estimate the cluster mass for large data sets - if they are well-calibrated. This is often done by deriving hydrostatic mass estimates for a small sample of regular clusters due to the HE assumption and because they have a lower scatter in scaling relations which enables a more accurate definition of their shape (e.g. Rowley et al. 2004; Croston et al. 2008; Rasia et al. 2011). However, relations calibrated with relaxed clusters can then only be safely applied to such objects. While samples of relaxed clusters can be studied to answer specific astrophysical questions, all cluster types (relaxed and disturbed) are used for cosmological applications. It is therefore important to also calibrate scaling relations for all cluster types.

The scaling relations are predicted by a self-similar model under the assumption that

gravitation and shock heating are the dominant processes in cluster formation and evolution (Kaiser 1986). Small clusters are thus scaled down versions of bigger clusters which formed hierarchically through merging (for a discussion of the self-similarity of clusters see e.g. Böhringer et al. 2012).

X-ray mass measurements are often quoted as M_{Δ_c}, the mass within a spherical region of radius R_{Δ_c}, where the cluster has a mean overdensity Δ_c with respect to the critical density of the Universe at the redshift of the cluster. The total mass is thus

$$M_{\rm tot}(< R_{\Delta_c}) = \frac{4}{3}\pi\ \Delta_c\ \rho_c(z)\ R^3_{\Delta_c}, \tag{1.6}$$

where $\rho_c(z)$ is the critical density of the Universe at redshift z and is related to the current density through the scaling factor[1] $E(z)$. Eq. 1.6 also implies that $R \propto M^{1/3}E^{-2/3}$. Assuming hydrostatic equilibrium and spherical shape, the virial theorem equation can be simplified and eventually gives the $M - T$ relation between cluster mass and X-ray temperature

$$M_{\Delta_c} \propto T_{\rm g}^{3/2}\ E^{-1}(z). \tag{1.7}$$

Similarly, other relations such as X-ray luminosity-gas temperature ($L_{\rm X} - T_{\rm g}$), luminosity-total mass ($L_{\rm X} - M_{\rm tot}$) or $Y_{\rm X}$-mass ($Y_{\rm X} - M_{\rm tot}$) can be derived assuming further that i) the X-ray luminosity is only due to thermal bremsstrahlung, ii) the gas distribution is related to the dark matter distribution and iii) the gas mass fraction ($M_{\rm g}/M_{\rm tot}$) is constant. In this context, $L_{\rm X}$ is the bolometric X-ray luminosity and $T_{\rm g}$ the temperature of the ICM. $Y_{\rm X}$ was introduced by Kravtsov et al. (2006) as the X-ray equivalent of $Y_{\rm SZ}$, the integrated Compton parameter obtained from the Sunyaev-Zel'dovich (SZ) effect, and is defined as pseudo-pressure: $Y_{\rm X} = M_{\rm g} \times T_{\rm g}$. $Y_{\rm X}$ traces the total thermal energy of the ICM and seems to be a low-scatter mass proxy, which is not very sensitive to the clusters' dynamical state (e.g. Vikhlinin et al. 2009a; Arnaud et al. 2010; Andersson et al. 2011; Mahdavi et al. 2013).

The above mentioned assumptions lead to a set of self-similar scaling relations, where Δ_c is typically chosen to be 200 or 500 (radius at which X-ray data is still reliable):

$$\begin{aligned}
&\mathbf{M_{tot} - T_g} && M_{200} \propto T_{\rm g}^{3/2}\ E^{-1}(z)\\
&\mathbf{L_X - T_g} && L_{200} \propto T_{\rm g}^{2}\ E(z)\\
&\mathbf{L_X - M_{tot}} && L_{200} \propto M_{200}^{4/3}\ E^{7/3}(z)\\
&\mathbf{Y_X - M_{tot}} && Y_{\rm X,200} \propto M_{200}^{5/3}\ E^{2/3}(z).
\end{aligned}$$

Comparing these theoretical predictions to observations enables more detailed studies of cluster formation and evolution. These relations hold in the cluster center (in the absence of AGN activity) but not in the cluster outskirts (for a review of cluster outskirts see e.g. Reiprich et al. 2013) and for dynamically young objects (e.g. Poole et al. 2007). Scatter in these relations and most importantly deviations from the predictions thus bare witness of non-gravitational processes.

[1] For the critical density $\rho_c(z) = \rho_{c,0}\ E^2(z) = 3E^2(z)\ H_0^2/8\pi G$, where $E^2(z) = \Omega_{\rm M}(1+z)^3 + (1-\Omega_{\rm M}-\Omega_\Lambda)(1+z)^2 + \Omega_\Lambda$ and H_0 is the Hubble parameter, $\Omega_{\rm M}$ the matter density and Ω_Λ the dark energy density.

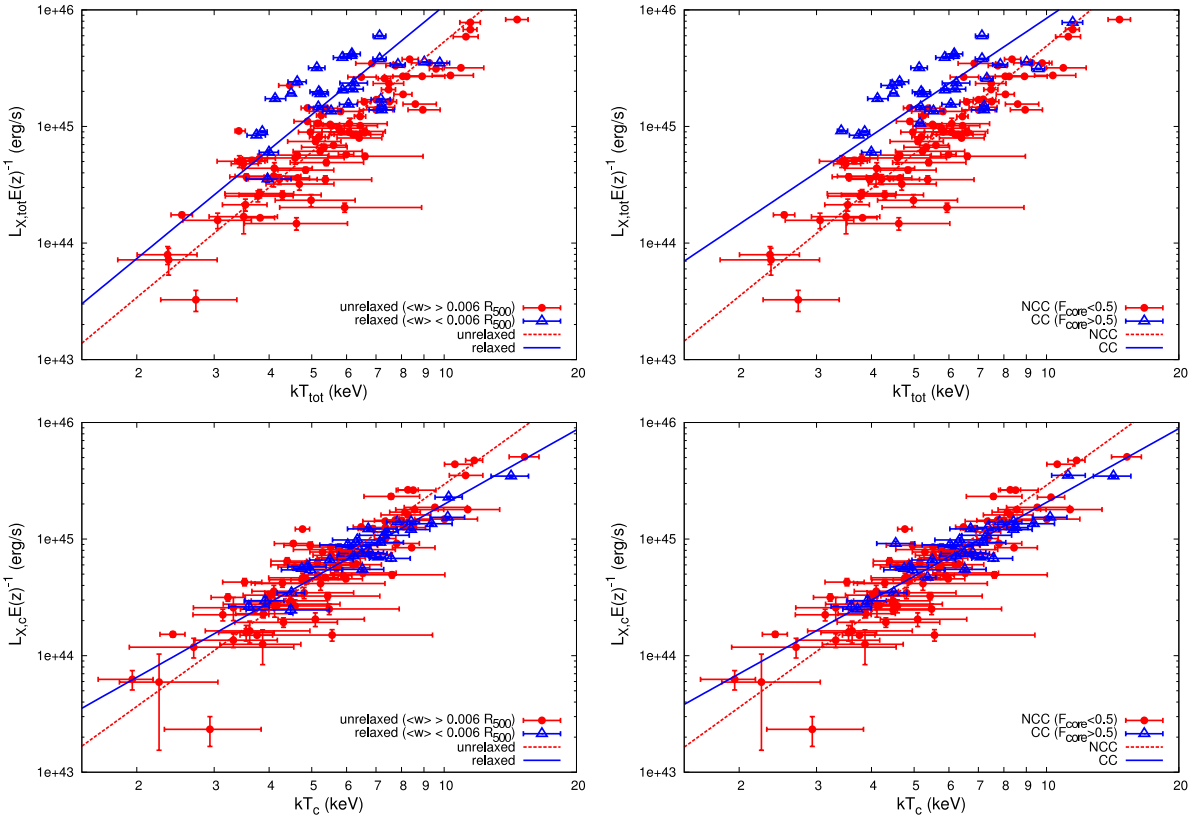

Figure 1.6: Comparison of the $L-T$ relation when including (top) and excluding (bottom) the central region. The left panels show the relation for relaxed (blue) and disturbed (red) clusters, classified using the center shift parameter (for details see Chapter 4). The right panels show the same data but divided into cool core (CC, blue) and non-cool core clusters (NCC, red). The correlation between morphology and presence of a cool core is apparent, but does not hold for all clusters. In addition, the reduction of the scatter when excluding the cluster core for the calculation of the luminosity and temperature is evident. Figures taken from Maughan et al. (2012).

The study of galaxy cluster scaling relations is an important topic under intensive development and a large number of datasets have been used to test the self-similar model and to quantify the scatter (for a review see e.g. Giodini et al. 2013, and references therein). A very important step in calibrating scaling relations was done by Fabian et al. (1994) who found that the scatter in the $L-T$ relation is mostly due to cool core clusters, and Markevitch (1998) who excluded the core region of all clusters before computing the scaling relation and reported an significantly reduced scatter. The effect of the cool core on the luminosity is now taken into consideration in scaling relation studies (e.g. Markevitch 1998; Pratt et al. 2009; Mittal et al. 2011; Maughan et al. 2012). Fig. 1.6 shows the $L-T$ relation for a sample of galaxy clusters, first classified by their dynamical state (relaxed/unrelaxed), then by the presence of a cool core (cool core and non-cool core clusters). Excluding the core region yields consistent results since most cool core clusters are relaxed and most non-cool core clusters disturbed systems. While the offset in the relation is driven by the presence of a cool core and

can be corrected by excluding the core region, an additional source of scatter is introduced by dynamically disturbed systems whose luminosity is affected by the merging process (for details see Sect. 2.3) and differs from the one predicted by scaling relations of relaxed objects (e.g. Maughan et al. 2012). Morphology also affects the scatter in the $M - T$ relation since the presence of substructure influences the mass estimates (e.g. Ventimiglia et al. 2008; Yang et al. 2009).

Recently, a comparative study of the redshift evolution of scaling relations up to $z \sim 1.5$ was performed by Reichert et al. (2011), who confirm previous findings that the evolution of the $M - T$ relation indeed follows the self-similar prediction, while the evolution of the $L - T$ and $L - M$ relation differs significantly from the self-similar model. Both relations are known to be significantly steeper than predicted (e.g. Mitchell et al. 1977, 1979; Markevitch 1998; Reiprich & Böhringer 2002; Zhang et al. 2008; Pratt et al. 2009; Vikhlinin et al. 2009a; Mittal et al. 2011; Böhringer et al. 2012; Maughan et al. 2012). In fact, the relations including luminosity differ most from the self-similar model indicating effects of non-gravitational processes such as radiative cooling, AGN feedback, star formation or galactic winds. Since the luminosity depends on the gas density squared, variations of the gas content directly affect the observed X-ray emission. Low mass systems have lower gas mass fractions (e.g. Vikhlinin et al. 2006; Pratt et al. 2009) and lower luminosities, thus steepening the slope of these relations. The gas fraction can be changed by an increase of entropy which stops the gas from reaching the cluster center. This entropy boost is still debated but can be explained by gas heating or the removal of low entropy gas. Although this topic is very interesting and essential to fully understand cluster physics, a detailed discussion of scaling relations is far beyond the scope of this introduction.

1.2.3 Other mass estimation methods

Hydrostatic mass estimates have limited precision due to the required assumptions. Complementary observations of the galaxy population of clusters in the optical give rise to mass estimation methods which do not require the same assumptions. Microwave observations probe the ICM through the Sunyaev-Zel'dovich (SZ) effect and yield additional information about the hot cluster gas due to e.g. the different density dependence. Mass estimates from the optical or microwave range can thus be used to calibrate X-ray mass measurements.

Velocity dispersion of cluster galaxies

Optical observations probe the galaxy population and enabled early mass estimates based on the dynamics of the member galaxies (e.g. Zwicky 1937). Using the virial theorem and the knowledge of the galaxy positions and redshifts, the mass can be derived as

$$M = \frac{\pi}{2}\frac{3\sigma_\mathrm{v}^2 R_\mathrm{V}}{G} \quad \text{with} \quad R_\mathrm{V} = N^2 \left(\sum_{i>j} r_{ij}^{-1} \right)^{-1} , \tag{1.8}$$

where σ_v is the line-of-sight velocity dispersion of the member galaxies, R_V the virialization radius, G the gravitational constant and $\pi/2$ a geometrical factor.

Apart from the question to which extent the virial theorem holds for clusters, the definition of a galaxy member is most crucial in this method. Galaxy clusters are no isolated systems and

it is often difficult to distinguish between galaxy members and the spurious inclusion of non-members lying in the line-of-sight. Including non-members would lead to an overestimation of the cluster mass, but different analysis techniques such as clipping in the velocity distribution minimize this bias (e.g. Beers et al. 1990; Biviano et al. 2006).

Regarding the validity of the virial theorem, many authors now solve the Jeans equation instead, which assumes that the cluster is in dynamical equilibrium and uses the radial dependence of the projected galaxy velocity dispersion (e.g. Carlberg et al. 1997; Biviano & Girardi 2003).

Weak lensing mass measurements

Gravitational lensing provides a mass estimation method, which is independent of the assumption of hydrostatic equilibrium and directly traces the depth and shape of the cluster potential (for a recent review of mass measurements from lensing see e.g. Hoekstra et al. 2013). Structures along the line-of-sight, in our case a galaxy cluster, deflect photons which are emitted from sources more distant than the cluster and act as gravitational lenses (for a review on gravitational lensing see e.g. Bartelmann 2010). The deflection angle depends on the gradient of the cluster potential, decreases with distance from the lens and produces distorted (sheared) and slightly magnified images of background sources, typically high-redshift galaxies. Measuring the distortions provides information about the gravitational tidal field, independent of the dynamical state of the cluster. In the case of large deflection angles in the context of the small angle approximation (i.e. $\lesssim 30''$), multiple images of the background source and arcs are observed. Such cases are called *strong gravitational lensing* and provide good mass estimates for the region of the lens which is enclosed by the distorted images. The most accurate estimates can be derived when the underlying potential is modeled to reproduce the observed signatures such as multiple images and arcs (e.g. Kneib et al. 1996; Broadhurst et al. 2005; Meneghetti et al. 2010). For smaller deflection angles and thus less obvious distortions, so-called *weak lensing* techniques are applied. The small shear distortion of a large number of background sources is measured and enables the reconstruction of the projected surface mass density.

This method is not based on the assumptions of hydrostatic equilibrium and spherical shape, but it requires a model for the underlying mass distribution and is thus also not an unbiased mass estimator. However, owing to the different assumptions made, weak lensing estimates can be used to calibrate X-ray mass estimates, which are observationally cheaper than weak lensing analyses (see Sect. 1.2.1 and Fig. 1.5).

The integrated Compton parameter Y_{SZ}

Information about the ICM can also be obtained from microwave observations through the thermal Sunyaev-Zel'dovich (SZ) effect (Sunyaev & Zeldovich 1970, 1972). Cosmic microwave background (CMB) photons are Compton-scattered by free ICM electrons and shifted to slightly higher energies, which results in distortions of the black body CMB spectrum. The shape of the distorted spectrum is characterized by the Compton parameter y, which is proportional to the probability that a photon, which passes through the ICM, will be Compton scattered and the typical energy gain of the scattered photon. Since y gives the integrated thermal pressure of the ICM along the line-of-sight, it is a good proxy for the gas mass M_{g}

and consequentially the total cluster mass. For cosmological purposes, y is integrated over the solid angle A, which yields the integrated Compton parameter Y

$$Y = \int y \, dA \propto \int n_\mathrm{e} \, T_\mathrm{e} \, dV \propto M_\mathrm{g} \, T_\mathrm{e}, \tag{1.9}$$

where A is the projected surface area, n_e the electron density of the ICM, V the cluster volume and T_e the electron temperature.

Y_SZ is a low-scatter mass proxy which is quite insensitive to the dynamical state of the cluster (e.g. da Silva et al. 2004; Motl et al. 2005; Andersson et al. 2011; Planck Collaboration et al. 2013b), and hence is an ideal tool for precision cosmology. Contrary to X-rays, the SZ signal is redshift-independent and not subject to surface-brightness-dimming since the dimming is exactly compensated by the increase of the CMB intensity. This makes SZ observations ideal for the detection of high-redshift clusters. On the other hand, this leads to the problem of projection effects due to overlapping SZ signals from structures at different redshifts (e.g. White et al. 2002).

Mass estimates derived from several wavelengths and methods have complementary advantages and disadvantages. For example, X-ray data requires the assumption of hydrostatic equilibrium and spherical shape, which is not valid for dynamically young clusters. Projection effects are problematic for the measurement of velocity dispersions, SZ signals or weak-lensing shear, but not for X-ray data. In addition, most SZ and weak lensing analyses are currently limited to larger scales because of their limited spatial resolution. Combining different measurements therefore yields the best way towards robust, morphology-independent and precise mass estimates.

1.3 Clusters as cosmological probes

Accurate mass measurements and thus morphological information are essential when using galaxy clusters for cosmology. According to the current ΛCDM cosmological model[2], galaxy clusters are the most recent objects to collapse under their own gravity and to virialize, making them excellent tracers of the process of structure formation in the Universe through e.g. the evolution of the cluster mass function. Their deep potential wells preserve the gas against energetic processes like supernovae or AGNs and should provide a fair example of the matter content of the Universe. Recent reviews of galaxy clusters as cosmological probes are provided by e.g. Voit (2005) and Borgani (2008).

1.3.1 Structure formation theory

The understanding of cluster formation in a ΛCDM Universe is based on the spherical (top-hat) collapse model and the hierarchical bottom-up structure formation theory (for a review of large-scale structure formation see e.g. Peacock 2003; Kravtsov & Borgani 2012). The current cosmological model predicts a phase of inflation in the very early Universe, which sets

[2]The ΛCDM cosmological model can be described by a number of parameters. The most relevant ones for cluster cosmology are: the dark energy density parameter Ω_Λ, the matter density parameter Ω_M, the Hubble parameter H_0 and the variance of the density fluctuation field on a $8h^{-1}$ Mpc scale σ_8.

the initial conditions for the evolution of all structures. Small quantum fluctuations during this phase give rise to the initial (Gaussian) fluctuations in the matter density field. If $\rho(x)$ describes the density field at position x and $\bar{\rho}$ the mean density of the Universe, an overdensity or relative density contrast can be defined as

$$\delta(x) = \frac{\rho(x) - \bar{\rho}}{\bar{\rho}}. \tag{1.10}$$

Perturbations with $\delta > 0$ are overdense regions and grow by accreting matter from their surroundings, while $\delta < 0$ characterizes underdense regions.

The Fourier transform of $\xi(r)$, the two-point correlation function of the density contrast, gives the power spectrum of the perturbations:

$$P(k) = \langle \left|\tilde{\delta}(\mathbf{k})\right|^2 \rangle = \frac{1}{2\pi^2} \int r^2 \, \xi(r) \, \frac{sin\ kr}{kr} \, dr, \tag{1.11}$$

where r is the separation vector and $\mathbf{k}$ the wavevector.

In order to study structures with mass M, which are formed from density fluctuations of size R ($R \propto (M/\bar{\rho})^{1/3}$), the density fluctuation field, which is assumed to be a Gaussian random field, is convolved with a window function W (e.g. top-hat) to filter out all fluctuations smaller than R. The variance of the smoothed field at mass scale M is then defined as:

$$\sigma_M^2(z) = \frac{1}{2\pi^2} \int_0^\infty k^2 \, P(k) \, \tilde{W}(k)^2 \, dk. \tag{1.12}$$

Numerical simulations provide precise means to study structure formation (for a review see e.g. Springel 2010), but this process can be nicely illustrated using the following toy model. The *spherical top-hat collapse model* presents a simple analytic approach for the formation of gravitationally bound objects. It assumes a spherical low-amplitude density perturbation, which can be described by a top-hat model with a constant overdensity inside and $\delta = 0$ outside the sphere. In addition, the overdensity evolves independent of its surroundings (Birkhoff theorem). Perturbations with $\delta > 0$ initially expand along with the Hubble flow. The expansion gets slowed down by the gravitational pull of the region until the overdensity exceeds the critical overdensity δ_c at the turn-around point, detaches from the background expansion and starts to collapse due to gravity. In this simple model without internal pressure, the spherical region would collapse to infinite density. For a realistic density perturbation which is not spherical and has no constant overdensity, the collapse will be stopped and the result is a virialized object which formed through violent relaxation.

As long as perturbations are small ($|\delta| \ll 1$), their evolution can be studied using linear perturbation theory. However, this approximation eventually breaks down when the perturbations become stronger. Extrapolating linear growth in the non-linear regime significantly underestimates the overdensity at the point of turn-around and virialization. The non-linear treatment gives $1 + \delta^{vir} \sim 178$ for an Einstein-de-Sitter Universe. For the ΛCDM cosmology ($\Omega_M = 0.27$ and $\Omega_\Lambda = 0.73$, Komatsu et al. 2011), the density contrast of collapsed objects at $z = 0$ is $1 + \delta^{vir} \sim 358$ (Kravtsov & Borgani 2012).

According to the hierarchical bottom-up scenario, small-scale perturbations are the first to decouple from the background expansion and collapse. They grow through merging, forming

progressively larger structures such as galaxies. Galaxy clusters originate from large-scale perturbations and are thus the most recent and most massive objects to be formed by dropping out of the Hubble flow, collapsing and reaching virial equilibrium.

1.3.2 Cluster mass function

The mass function $n(M,z)$ gives the number density of halos with masses between M and $M + dM$ at redshift z. Using the formalism of Press & Schechter (1974), which includes the above outlined scenario of structure formation from initial density perturbations, the mass function can be expressed as (for a detailed derivation see e.g. Borgani 2008; Weinberg 2008):

$$\frac{dn(M,z)}{dM} = \sqrt{\frac{2}{\pi}}\frac{\bar{\rho}}{M^2}\frac{\delta_c}{\sigma_M(z)}\left|\frac{d\log\sigma_M(z)}{d\log M}\right| exp\left(-\frac{\delta_c^2}{2\sigma_M^2(z)}\right), \tag{1.13}$$

where M is the halo mass, $\bar{\rho}$ the mean matter density, δ_c the critical overdensity (independent of z for Einstein-de-Sitter Universe) and $\sigma_M^2(z)$ the variance of the density fluctuation field at mass scale M. The Press-Schechter formalism is a widely-used semi-analytic approach and is well-suited to explain the importance of the cluster mass function for cosmology. However, it was found to deviate from numerical simulations by overpredicting the number of low-mass and underpredicting the number of high-mass objects (e.g. Gross et al. 1998; Governato et al. 1999; Springel et al. 2005) and therefore alternative and more accurate expressions were provided by several authors who include e.g. non-spherical collapse and calibrate it with numerical simulations (e.g. Sheth & Tormen 1999; Jenkins et al. 2001; Tinker et al. 2008).

The mass function (in particular σ_M^2) and its evolution are sensitive to the cosmological parameters. In the high-mass i.e. cluster regime, Eq. 1.13 is dominated by the exponential tail, making it exponentially sensitive to the underlying cosmology. Fig. 1.7 illustrates that comparing the observed cluster mass function or cluster abundance[3] $n(z)$ and its evolution with model predictions, makes it possible to distinguish between different cosmological models (e.g. Schuecker et al. 2003; Vikhlinin et al. 2009b; Mantz et al. 2010).

The variance $\sigma_M^2(z)$ depends on the power spectrum $P(k,z)$, whose shape is sensitive to the matter density Ω_M, the Hubble parameter H_0 and to lesser extent the baryon density Ω_b (e.g. Sugiyama 1995; Eisenstein & Hu 1999). Since the cluster mass function extends only over about two decades in mass (see Table 1.1), the power spectrum cannot be probed over a large enough range to put strong constraints on its shape. Galaxy clusters, however, are well-suited to measure the normalization of the power spectrum. It can be defined in different ways but is commonly referred to as σ_8 parameter[4], which measures the amplitude of the (linear) power spectrum on the $8h^{-1}$ Mpc, i.e. cluster scale, and can be well constrained by the local cluster mass function ($z < 0.1$). To be more precise, constraints can be put on the relation between σ_8 and Ω_M, since the scale on which the amplitude is measured depends not only on the mass but also on Ω_M ($R^3 \propto M/\Omega_M\rho_c$).

[3]The cluster number counts $n(z)$ give the total number of clusters at redshift z. Predictions for surveys take into account the cluster mass function, the survey volume and the selection function.

[4]$\sigma_8 = \sigma(M_8, z = 0)$ is the variance of the density fluctuation field at mass scale M_8, which is the mass contained in a top-hat sphere with $8h^{-1}$ Mpc radius: $M_8 \sim 6\times10^{14}\ \Omega_M\ h^{-1}\ M_\odot$, the typical mass of a moderately rich cluster.

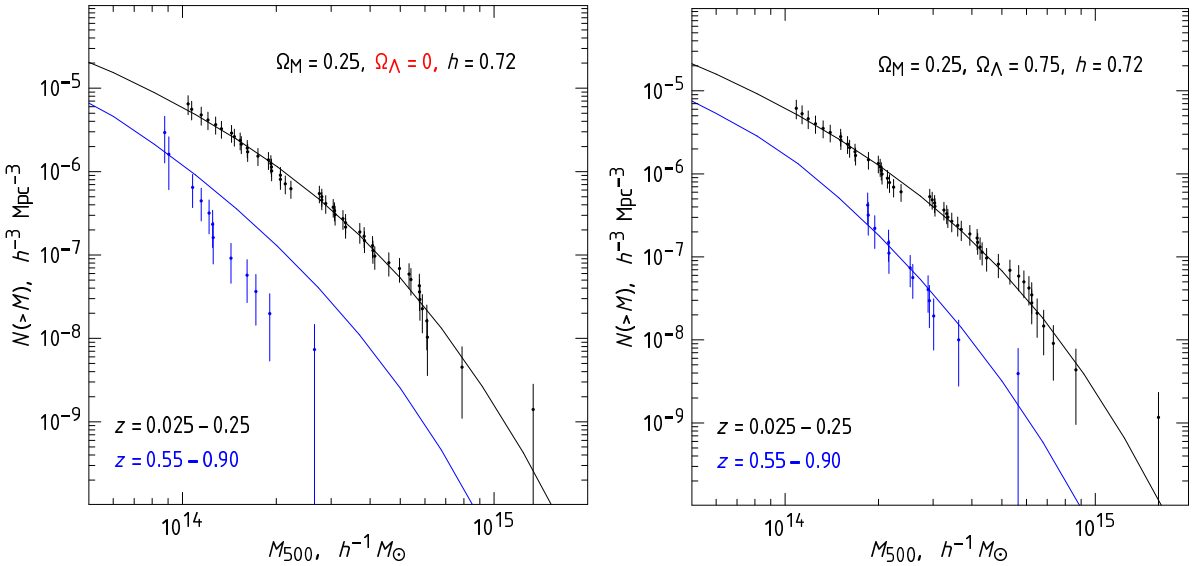

Figure 1.7: Example for the comparison of the observed cluster mass function with predictions from cosmological models. The data and the model are computed for $\Omega_\Lambda = 0$ in the left panel and for $\Omega_\Lambda = 0.75$ in the right one. The overall normalization is adjusted to $z = 0$. Figures taken from Vikhlinin et al. (2009b).

The evolution of the mass function reflects the growth rate of the density fluctuations and thus provides very strong constraints on Ω_M and σ_8 (see Fig. 1.8) and, in combination with other probes such as the cosmic microwave background, helps to better constrain e.g. Ω_Λ or w, the dark energy equation of state parameter (e.g. Vikhlinin et al. 2009b; Planck Collaboration et al. 2013a,b).

The exponential tail of the mass function in the high-mass regime makes galaxy clusters, especially the massive ones, excellent laboratories to test the cosmological model, however, also requires very accurate mass measurements.

1.3.3 Other cosmological tests

Apart from the cluster mass function or the cluster abundance in general, other properties of galaxy clusters can be used to put constraints on the cosmological parameters. Among these are the clustering of galaxy clusters, which traces the large-scale structure of the Universe and thus the cosmological density parameters through the growth of fluctuations, or the study of the gas mass fraction. In galaxy clusters, the baryonic mass content is dominated by the ICM. Due to the deep cluster potential well, the baryonic or gas mass fraction $f_g = M_b/M_{tot}$ is not expected to change with time and should be a fair representation of the cosmological ratio Ω_b/Ω_M (e.g. White et al. 1993; Eke et al. 1998). The gas mass fraction of nearby (relaxed) clusters can thus be used to constrain Ω_M once Ω_b, the baryonic matter density parameter, and H_0 are known from other measurements such as the CMB (e.g. White et al. 1993; Allen et al. 2008).

Although f_g should be fairly constant, measurements of the *apparent* evolution provide means to probe the geometry and thus the dark energy density and acceleration of the Uni-

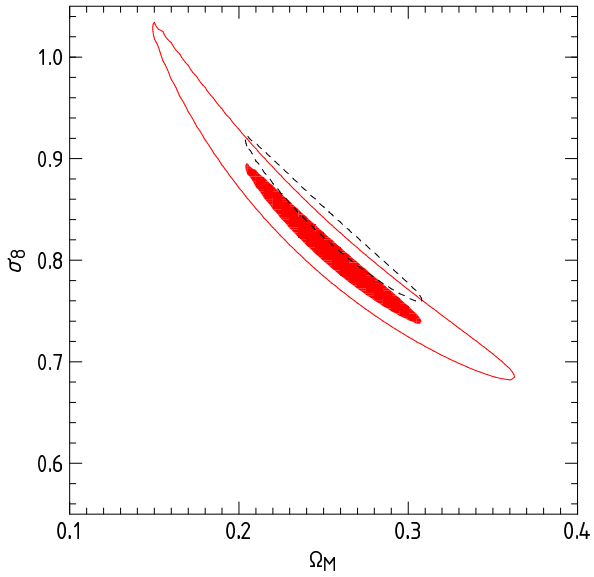

Figure 1.8: Constraints on Ω_M and σ_8 in a flat ΛCDM cosmology. The red regions give the 68% (solid) and 95% confidence level intervals. The dashed region indicates the 68% constraints when the normalization of the absolute cluster mass vs. observable relations and thus the mass calibration is changed by +9%. This value is the estimated size of the systematic errors in σ_8 due to uncertainties in the mass measurements. Figure taken from Vikhlinin et al. (2009b).

verse (e.g. Sasaki 1996; Pen 1997; Allen et al. 2004, 2008). The derived value of f_g depends on the angular diameter distance to the cluster, which in turn depends on the values of the cosmological parameters used for the derivation. The correct cosmological parameters thus yield a constant gas mass fraction as predicted by theory. The assumption of a constant f_g holds best for massive, relaxed clusters and thus limits the sample selection. However, this approach has the advantage that it does not require the knowledge of the total mass profile but only of the gas mass and temperature profile, which can be determined precisely from X-ray data.

Recent cosmological constraints using X-ray observations of galaxy clusters are reported by e.g. Vikhlinin et al. (2009b) and Mantz et al. (2010). Large collaborations such as Planck (e.g. Planck Collaboration et al. 2013b), SPT (e.g. Benson et al. 2013) or ACT (e.g. Hasselfield et al. 2013) derive cosmological parameters by detecting clusters and determining their mass to calculate the mass function through the SZ effect. All these studies agree on the current values of $\Omega_M \sim 0.3$ and $\sigma_8 \sim 0.8$. Combining constraints from galaxy clusters with other measurements such as the cosmic microwave background, baryonic acoustic oscillations (BAO) and Type Ia supernovae, yields the best constraints on the cosmological parameters.

Chapter 2

Cluster substructure and morphology

The analysis of galaxy cluster structure provides valuable information about the dynamical state of these massive systems. According to the current structure formation scenario, clusters form from fluctuations in the initial density field and grow through merging (see Sect. 1.3.1). Since the Universe was denser at earlier times, the merger rate is expected to drop with decreasing redshift and clusters should be on average relaxed systems now. The presence of substructures is therefore a demonstration of the fact that cluster formation has not finished yet.

Galaxy clusters containing substructure have an overall irregular shape and often show secondary peaks in the galaxy distribution (optical range), the X-ray emission (substructure in the ICM) or the underlying dark matter distribution. They can exhibit substructures from scales smaller than the size of a galaxy (e.g. few kpc) up to (sub-)Mpc scales. In cluster studies, however, only cluster structures and sub-halos larger than galaxies are of interest. In this thesis cluster morphology denotes the large-scale appearance of a galaxy cluster. Clusters which show large-scale substructures are called disturbed systems, while an overall regular appearance indicates that the object is relaxed on this scale.

The radial profile of the X-ray emission of galaxy clusters can be – to first order – described by the isothermal β model (see Sect. 1.1.1), assuming among others spherical shape and hydrostatic equilibrium. However, it was early recognized that many clusters show a certain degree of substructure, indicating a deviation from these assumptions. Optical studies in the 1980s gave controversial results about the statistical significance of substructures in galaxy clusters (e.g. Geller & Beers 1982; West et al. 1988). Projection effects when analyzing the projected galaxy distribution lead to an overestimate of the amount of sub-clustering. Redshift information about possible substructures and the deviation from a Gaussian distribution of the galaxy radial velocities improved the distinction between projected and true substructures (e.g. Bothun et al. 1983; West & Bothun 1990). X-ray observations are less prone to projection effects since the emission from the hot ICM is much brighter than that of fore- and background galaxies. The advent of X-ray imaging observatories thus enabled a leap forward in the study of galaxy cluster morphology (see Sect. 2.2 and Chapters 4–6).

Detecting and characterizing substructure in galaxy clusters is essential to study their astrophysical properties. It provides the base for morphological analyses, which aim to quantify the dynamical state of the cluster, but also enables investigations of the clusters' hydro- and

thermodynamics (temperature, density, entropy profiles) and other astrophysical processes acting in the cluster potential. Detailed analyses of substructures in a single cluster yield information about e.g. the geometry and dynamics of the merging process (e.g. Finoguenov et al. 2005), how much turbulence is introduced by the merging system (e.g. Hallman & Jeltema 2011) or the role of merging activity in the formation of radio halos (e.g. Buote 2001; Cassano et al. 2010).

The following sections will provide an overview on galaxy cluster morphologies and substructures, focusing on X-ray observations. A few examples of the variety of substructure on small and large scales and their impact on cluster physics are discussed in Sect. 2.1. For morphological studies of large cluster samples (see e.g. Chapters 4–6), the overall cluster shape, which reflects the dynamical state of the cluster, is of interest. Sect. 2.2 thus outlines different methods to characterize the cluster morphology. Sect. 2.3 finally discusses the impact of merging on the assumption of hydrostatic equilibrium and cluster properties.

2.1 Substructure on different scales

Galaxy clusters show a variety of substructures on different scales, ranging from small, several kpc wide, X-ray cavities to large ones with $\sim$ 100 kpc diameter and to merging subsystems on a sub-Mpc scale. A detailed discussion of all different kinds of substructures is beyond the scope of this thesis, but a few illustrative examples will be given.

Small-scale substructures and cluster cores

Small-scale fluctuations in the ICM distribution do not influence the overall gravitational potential and thus the morphology of the cluster. They are, however, extremely interesting to study gas dynamics and non-gravitational processes, especially the mechanism of AGN feedback. High-resolution images obtained from *XMM-Newton* and *Chandra* revealed highly irregular structures in the central region of many clusters hosting a cool core (see Sect. 1.1.2). These systems show a smooth distribution and a relaxed morphology on cluster scale, but interesting features in the core regions. In addition, cool core clusters commonly host a central radio source called active galactic nuclei (AGN), which is thought to heat the ICM and stop the cooling flow (e.g. Burns 1990; Mittal et al. 2009).

X-ray observations show different kinds of features, including cavities, shocks, ripples or sharp density discontinuities in the ICM distribution. Additional radio data indicated that these structures are due to the interaction of the AGN and the central cluster gas (for a review on AGN feedback see e.g. Gitti et al. 2012; Fabian 2012; McNamara & Nulsen 2012). Fig. 2.1 shows examples of small-scale substructures in the cores of the intensively studied Perseus Cluster (e.g. Böhringer et al. 1993; Fabian et al. 2000, 2003; Churazov et al. 2003; Fabian et al. 2011) and RBS 797. *Chandra* observations revealed a number of cavities in the X-ray distribution, which spatially coincide with radio emission from the AGN, in the core of the Perseus Cluster but also in a large number of other cool core clusters such as RBS 797 or the famous Virgo Cluster with the central galaxy M87 (e.g. Böhringer et al. 1995; Churazov et al. 2001; Forman et al. 2007; Million et al. 2010). The central black hole (AGN) is feeding from the inflowing gas and generates powerful jets, highly collimated and fast outflows of relativistic particles which emerge in opposite directions from the AGN. These outflows inflate

bubbles or lobes of relativistic plasma, which rise buoyantly, push aside the X-ray gas, creating the observed X-ray cavities. Cavities thus provide direct evidence for the interaction of jets and the ICM. The Perseus Cluster core, however, shows additional proof for the AGN-ICM interaction, namely concentric ripples, which are most likely sound waves generated during the release of the relativistic jets. Using deeper observations and examining a larger area, Fabian et al. (2011) found evidence for previously unknown bubbles and also indications of merged bubbles at larger radii.

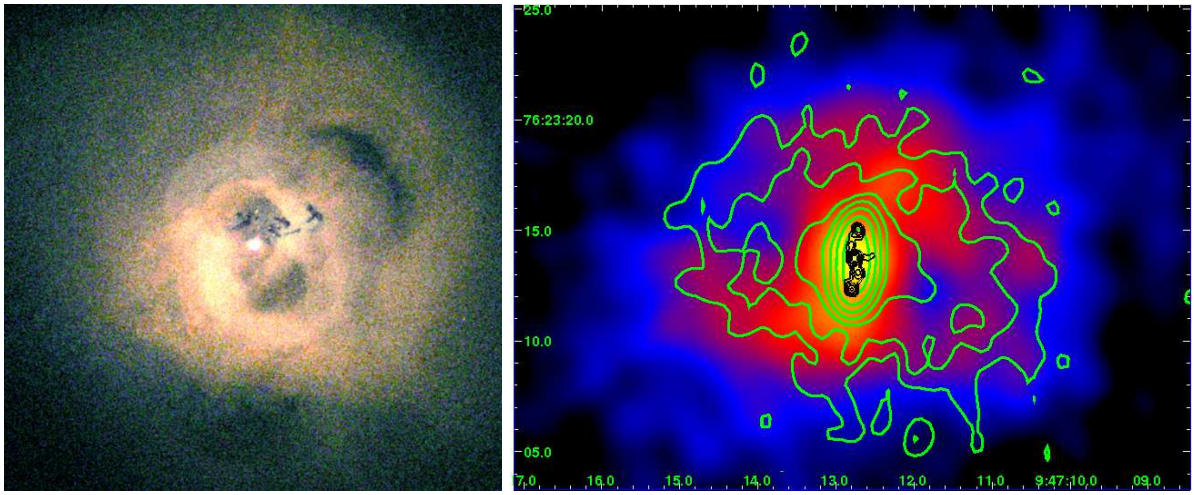

Figure 2.1: Examples of substructures in cluster cores. **Left:** *Chandra* 3-color image of the central region of the Perseus Cluster at $z = 0.02$. Cavities in the X-ray distribution due to relativistic jets are apparent, as are concentric ripples, which are most probably weak shocks or sound waves generated by the jet outbursts from the central AGN (bright spot). Image credit: NASA/CXC/IoA/A.Fabian et al. **Right:** Central region of the galaxy cluster RBS 797 at $z = 0.35$. Smoothed *Chandra* image with radio contours overlaid (black 4.8 GHz, green 1.4 GHz). This cluster shows X-ray cavities similar to the Perseus Cluster and also radio emission on different scales. On a $\sim$ 10 kpc scale the emission from the jets extending in the north-south direction is shown as black contours. It is remarkable that they are oriented perpendicular to the X-ray cavities, which are spatially coinciding with emission on $\sim$ 100 kpc scale (green contours). Not shown in this image is the possible mini-halo which extends in the north-south direction on even larger scales. Figure taken from Gitti et al. (2006).

Radio emission is not only found spatially correlated with X-ray cavities but also as extended, diffuse emission. The central region of the cluster RBS 797 shows radio emission on different scales and with different orientations (e.g. Schindler et al. 2001; Gitti et al. 2006; Cavagnolo et al. 2011; Doria et al. 2012). On smallest scales ($\sim$ 10 kpc), the bright emission from the jets is observed in the north-south direction. These are almost perpendicular to the X-ray cavities and the extended emission on $\sim$ 100 kpc scale, which are oriented in the northeast-southwest direction. These two radio features and the X-ray cavities are shown in Fig. 2.1. However, on even larger scales, emission with an amorphous morphology elongated in the north-south direction was found. This emission is roughly the same size as the cooling region and is most likely a mini-halo. Mini-halos are still poorly understood, but they are

expected to be as large as 200 – 500 kpc and to be located around the central radio galaxy in cool core clusters. Although this cluster may be a peculiar case, it provides strong evidence for complex interaction of the AGN and the ICM beyond the inflation of radio bubbles.

Another very interesting case is MS 0735.6+7421. This cluster shows huge cavities with a diameter of ∼ 200 kpc, which are filled with radio emission, and a large-scale cocoon shock (e.g. McNamara et al. 2005, 2009). MS 0735 experienced the most powerful outburst known so far and is an example that shows that the effects of AGN outbursts are not limited to the central region, but could also affect global cluster properties. This system and also Hydra A, where similarly large cavities were found (e.g. Nulsen et al. 2005; Gitti et al. 2011), are significantly more luminous than predicted by scaling relations, indicating that it might bias the selection of flux-limited samples in the sense that systems with energetic outbursts are favoured because they are brighter.

The impact of AGN on the intracluster gas has received much attention in recent years, but details about this feedback process are still debated. Studies of a large number of X-ray cavities and other small-scale features such as rims, shocks and cold fronts in the core regions thus help to resolve this question. Large-scale cavities, which are only found in three objects so far (MS 0735, Hydra A, Hercules A), provide additional laboratories to test models which predict strongly variable AGN activity and occasional powerful outbursts for all systems. A more detailed discussion of the current knowledge of all the processes acting in the cluster core due to AGN activity and their impact on the understanding of cluster physics is not possible in the framework of this thesis, but the above mentioned examples should give some insight into currently investigated phenomena.

Large-scale substructures and the cluster morphology

The most dominant and apparent substructure on cluster scale is a merging subsystem. Galaxy clusters grow through the infall of matter and merging events. In this context, the term merging denotes the infall of a galaxy groups and other clusters, producing large-scale substructure and fluctuations in the gravitational potential, leading to a variety of morphologies (see Sect. 2.2 and Chapter 4 and as an example also the Bullet Cluster in Fig. 1.1). Systems showing such signatures are called disturbed, while relaxed galaxy clusters are characterized by an overall smooth ICM distribution. The extremely energetic merging events lead to a deviation from spherical shape and the assumption of hydrostatic equilibrium and can influence the global cluster properties, mass estimates (see Sect. 1.2) and X-ray scaling relations (see Sect. 2.3). The merging process creates shocks, hydrodynamic instabilities and turbulences in the ICM (for review on shock fronts in galaxy clusters see e.g. Markevitch & Vikhlinin 2007; Markevitch 2010), which have an impact on the magnetic fields and lead to diffuse, cluster-wide, synchrotron emission seen as radio halos (for a review on diffuse radio emission in galaxy clusters see e.g. Feretti et al. 2012).

The X-ray emission of the Bullet Cluster is shown in Fig. 2.2 as an example of a disturbed X-ray morphology due to merging and an induced shock front. The overlaid radio contours show the ∼ Mpc wide radio halo. This system was already discussed in Chapter 1 because it provided the first (indirect) evidence for the existence of dark matter through the reconstruction of the potential well via gravitational lensing (Fig. 1.1). This cluster, however, harbors much more information. The X-ray image shows two surface brightness edges with

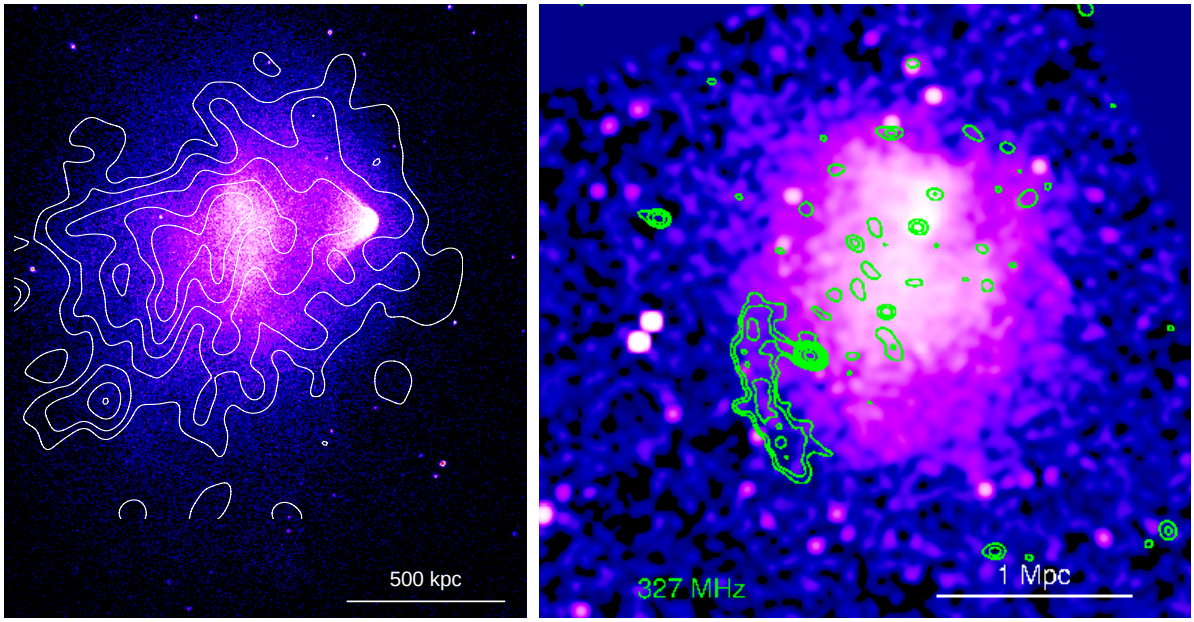

Figure 2.2: Substructures on large scales. **Left:** X-ray image of the Bullet Cluster with radio contours overlaid. The *Chandra* image shows clear signs of merging activity and a shock front in the ICM, which spatially coincides with the edge of the radio halo, in front of the bullet (boundary blue-black). Figure taken from Markevitch & Vikhlinin (2007), X-ray: Markevitch (2006), Radio: Liang et al. (2000). **Right:** Example of a radio relic in the cluster outskirts of A521. This image shows the disturbed ICM distribution with radio contours overlaid. Figure taken from Markevitch (2010), X-ray and Radio: Giacintucci et al. (2008).

similar density jumps, but different pressure profiles. The so-called cold front is a contact discontinuity and observed as a very bright surface brightness edge on the boundary between the infalling subsystem ("bullet") and the shock-heated gas from the main cluster (boundary white-blue). The shock front, on the other hand, shows a large pressure jump and propagates ahead of the cold front. In the left panel of Fig. 2.2 it is located at the blue-black boundary and spatially coincides with the edge of the radio halo.

Cold fronts are now observed in most merging systems and, interestingly, also in a large fraction of cool core clusters, as will be discussed below (e.g. Ghizzardi et al. 2010). Shock fronts, on the other hand, are harder to detect since they quickly travel outwards from the central region into the faint outskirts. In addition, the geometry of the merging event has to be in favor of the observer to detect a merger induced shock. Radio observations provide another way of detecting shock fronts. Peripheral radio relics caused by accelerated electrons are expected to occur at shock fronts due to merging in the outskirts of clusters. Such radio relics are found in a number of merging clusters such as A521 shown in Fig. 2.2 (e.g. Giacintucci et al. 2008). However, since the X-ray surface brightness is very low in these regions it is often challenging to confirm the shock front through temperature and pressure profiles (e.g. Finoguenov et al. 2010; Markevitch 2010; Russell et al. 2010; Mazzotta et al. 2011; Russell et al. 2012).

As a final example, gas sloshing in the central region of cool core clusters will be ad-

dressed. This is a small-scale effect but it is most probably a remnant from a past merging event and thus mentioned in this section. Cold fronts are observed in the central region of many cool core clusters, which do not show recent merging activity (e.g. Markevitch et al. 2001; Mazzotta et al. 2001; Sanders et al. 2005; Ettori et al. 2013). These cold fronts are small, typically $\leq$ 100 kpc, but definitely indicate motion of the gas in the cluster core, not from an infalling subsystem. Detailed investigations of the core of e.g. the cool core cluster A1795 indicated that the gas outside the cold front is in approximate hydrostatic equilibrium but the gas inside is not (e.g. Markevitch et al. 2001). The radial profiles show a jump in the surface brightness, the temperature and the total mass, but as expected from a cold front, the pressure profile looks smooth. Similar results were found for other clusters such as RXJ 1720.1+2638 (Mazzotta et al. 2001), A2029 (Clarke et al. 2004) or A2204 (Sanders et al. 2005). The explanation proposed by Markevitch et al. (2001) was that low-entropy gas is sloshing in the gravitational potential of the cluster core, which could be induced by a past merging event or alternatively by the central AGN. Numerical simulations indicate that off-center minor mergers (small subclusters falling into the potential well) can induce sloshing which persists for gigayears and can produce the observed signatures of concentric cold fronts (e.g. Ascasibar & Markevitch 2006). In recent years, there has been increasing evidence from simulations and observations that a sloshing core is indeed due to a past merging event and that it can cause enough turbulence to create a radio mini-halo (e.g. Mazzotta & Giacintucci 2008; ZuHone et al. 2010; Roediger et al. 2011, 2012, 2013; ZuHone et al. 2013). In addition, large-scale features due to sloshing extending over several hundred kpc were reported, showing that this effect is not limited to the cluster core (e.g. Simionescu et al. 2012; Nulsen et al. 2013; Paterno-Mahler et al. 2013; Rossetti et al. 2013).

All these observational signatures indicate that galaxy clusters (and their core regions) are not in complete hydrostatic equilibrium and that several of these complex physical processes can be acting together in the cluster potential. Disentangling the origin of the different substructures and their interplay requires a detailed analysis of these systems and enables a deeper understanding of cluster physics. This issue is very complex and currently under intense investigation with multi-wavelength studies and numerical simulations. Substructure detection and quantification through X-ray observations is the aim of this thesis and is discussed in more detail in the next section.

2.2 Morphological analysis

X-ray observations provide ideal tools to study the dynamical state of a cluster by probing the morphology of the ICM. X-ray images from the *Einstein* and *ROSAT* satellite revealed a variety of morphologies and raised the question of how many clusters are dynamically young (e.g. Jones & Forman 1984, 1999; Schuecker et al. 2001). The first systematic study was performed by Jones & Forman, who visually classified *Einstein* images according to different morphological types (Jones & Forman 1991, 1992). These morphologies were based on the X-ray surface brightness distribution and were called e.g. single symmetric peak, elliptical, complex multiple structures or double with equal components. As an example, four morphological types are shown in Fig. 2.3. This classification scheme set the base for the following

studies of X-ray morphology. To illustrate the variety of galaxy clusters, a large gallery of X-ray images from *XMM-Newton* with different morphologies is provided in Sect. 4.11.2. Morphological analysis and classification can also be applied to other wavelengths, e.g. the galaxy population of the cluster observed in the optical band, but this section will concentrate on the X-ray surface brightness.

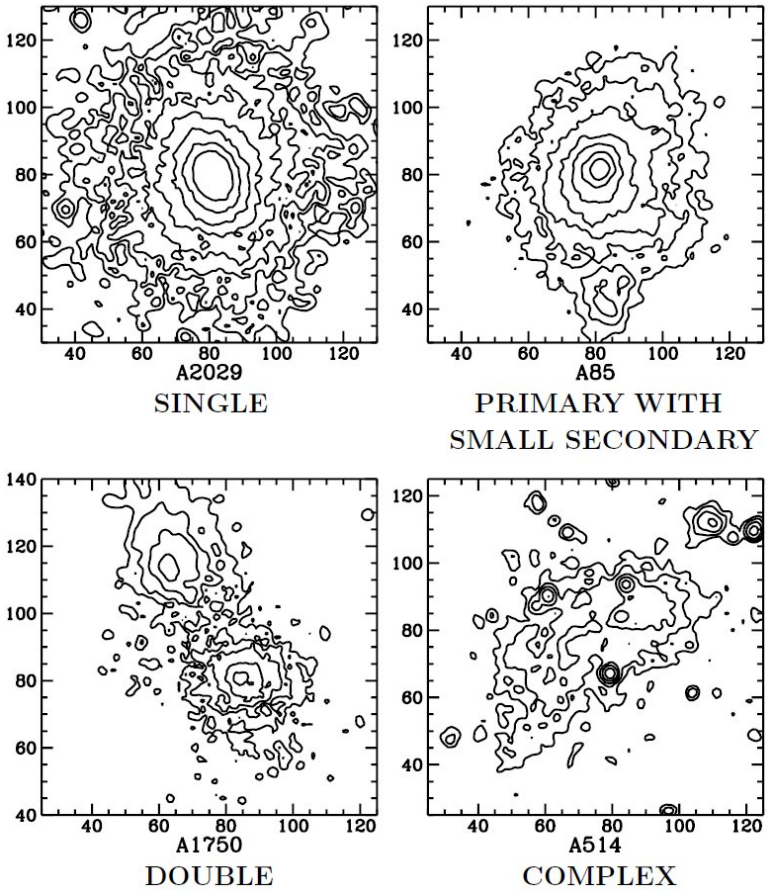

Figure 2.3: X-ray contours from the *ROSAT* satellite for four morphological types defined by Jones & Forman (1992). Figure taken from Buote (2002). Original data published in Buote & Tsai (1995).

The increasing number of available X-ray images called for quantiative methods to characterize the cluster morphology. A number of different methods have been proposed (for reviews see e.g. Buote 2002; Rasia et al. 2013), but they can be roughly separated into two groups. The first one aims at detecting and characterizing individual and sometimes very subtle substructures in the cluster to study their astrophysical properties and their impact on hydro- and thermodynamics (temperature, density, entropy profiles) in the cluster. A common method for detecting substructures is the subtraction of a smooth β model, which is fitted to the surface brightness profile of the cluster and represents a relaxed object, from the X-ray image and to examine the residuals (e.g. Neumann & Böhringer 1997; Andrade-Santos et al. 2012; Pandge et al. 2013). The method of wavelet decomposition allows the analysis of the clusters' X-ray

surface brightness or, galaxy distribution in the optical, on several scales. On largest scales the overall cluster morphology is quantified, but on progressively smaller scales individual substructures are detected and can be analyzed separately (e.g. Escalera & Mazure 1992; Slezak et al. 1994; Flin & Krywult 2006).

The other approach does not provide detailed information about the individual substructures, but aims to quantify the morphology and thus the global dynamical state of the cluster. Starting from the visual classification of Jones & Forman, several quantitative algorithms were presented to analyze the X-ray morphology of clusters. An early approach was measuring the clusters' ellipticity (e.g. McMillan et al. 1989; Melott et al. 2001; Hashimoto et al. 2007a). However, both disturbed and relaxed objects can appear elliptical, which does not qualify it as a good indicator for the dynamical state. Also other simple statistical measures such as the degree of concentration or asymmetry of the surface brightness profile, the offset between the X-ray peak and the centroid or the ratio between the minor and major axis provide information about the morphology and tend to be robust regarding image quality and cluster redshift (e.g. Mohr et al. 1995; Hashimoto et al. 2007a; Ventimiglia et al. 2008).

The most commonly used substructure parameters or morphology estimators are the center shift parameter, power ratios and the asymmetry parameter. These estimators, and especially their sensitivity to Poisson noise and the data quality in general, were tested in detail in the course of this thesis. A profound knowledge of their behavior is especially important when dealing with observations of objects at different redshift because of the variation in the photon statistics of the images. A detailed discussion of these parameters and a morphological analysis employing them is presented in Chapters 4–6 and their definitions are only outlined here.

Power ratios

In contrary to most other morphology estimators presented before, Buote & Tsai (1995) wanted to asses the projected morphology of galaxy clusters and to quantify their dynamical state by analyzing the gravitational potential. In this context, only large substructures comparable to the cluster scale are of interest since smaller components such as galaxies have no effect on the global gravitational potential and thus the dynamical state of the cluster.

The derivation and a detailed discussion of this method are given in Buote & Tsai (1995) and in Chapter 4. The power ratio method is based on the multipole expansion of the two-dimensional gravitational potential due to material inside of $R_{\rm ap}$, the radius within which the dynamical state is measured. The individual powers yield the contribution of the mth multipole moment to the total gravitational potential within $R_{\rm ap}$, which is typically chosen to be 0.5 Mpc, 1 Mpc or r_{500}. In addition, the powers are most sensitive to structures on the scale of $R_{\rm ap}$. The choice of $R_{\rm ap}$ therefore defines on which scale the dynamical state of the cluster is quantified and motivated the definition of a modified parameter, the peak of the power ratio profile computed in several apertures (for details see Sect. 4.8.1).

For the computation of the powers from X-ray images, the projected mass density is replaced by the X-ray surface brightness, which traces the gravitational potential. $P0$, the monopole, gives the total flux within the aperture, $P1$ the dipole, $P2$ the quadrupole, $P3$ the hexapole and $P4$ the octopole moment. Higher moments are not considered since they probe structures on smaller scales which are dynamically not significant on cluster scale. The final power ratios are obtained by normalizing the powers by $P0$, which ensures a fair comparison of clusters

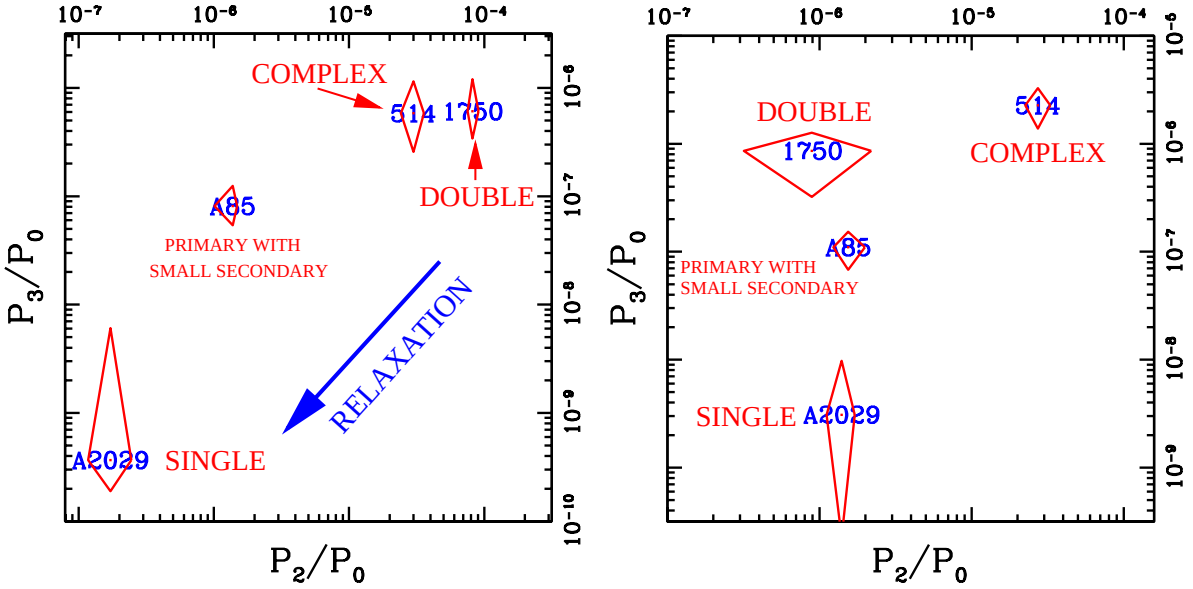

Figure 2.4: Power ratios (from Buote & Tsai 1996) computed within a circular aperture of 1 Mpc (left) and 0.5 Mpc (right) radius located at the centroid of the X-ray emission. Figures taken from Buote (2002).

with different X-ray brightness. The center of the aperture radius is typically chosen to be the center of the projected mass because in this case $P1$ vanishes. This leaves the classification of the cluster morphology to the three remaining power ratios $P2/P0$, $P3/P0$ and $P4/P0$. Even moments are sensitive to both bimodality and ellipticity, which is not a clear indicator of the dynamical state. A regular elliptical cluster contributes only to even moments and gives a low to moderate $P2/P0$ and $P4/P0$ signal. Larger signals are found for merging systems, making $P2/P0$ and $P4/P0$ good measures of the cluster morphology. A more clear indicator, however, is $P3/P0$. Odd moments reflect asymmetry and unequal-sized bimodality and vanish for relaxed, single-component objects. $P3/P0$ is thus chosen to quantify the dynamical state of galaxy clusters and to classify them as relaxed or disturbed objects (e.g. Buote & Tsai 1996; Jeltema et al. 2005; Poole et al. 2006; Böhringer et al. 2010, and Chapter 4 and 5 of this work).

Since individual morphologies contribute by a different extent to the powers, a combination of odd and even moments can give viable information about the cluster morphology. Looking at the location of several clusters in the $P2/P0$ – $P3/P0$ plane, Buote & Tsai (1996) reported the detection of a *morphological evolutionary track*, which is shown in Fig. 2.4. For a cluster scale aperture size of 1 Mpc, dynamically young objects have high odd and even moments since their X-ray images show a double-component object or a generally disturbed and thus complex morphology. With time they relax and arrive at the bottom left, where all signs of substructure are gone and a single, relaxed cluster remains. Evaluating this information for a smaller aperture such as 0.5 Mpc shows a very similar trend, but with the exception that the double-component cluster has now a much lower $P2/P0$ since the smaller aperture encloses only one of the two components. $P3/P0$ on the other hand still gives a very high signal, showing again that it is the best indicator for the dynamical state.

However, the calculation of power ratios suffers from shot noise, which is present in every X-ray image. This was acknowledged already by Buote & Tsai (1996) and further investigated by Jeltema et al. (2005) and Böhringer et al. (2010). While both studies offer a method to correct for the noise contribution, they lack a detailed evaluation of the performance of $P3/P0$ for different observational depths, i.e. net and background photon counts. One aim of this thesis is thus to provide such a performance study, which sets the stage for a well-calibrated bias correction method and enables a precise definition of $P3/P0$ boundary values for high- and low-quality observations to classify clusters as relaxed and disturbed objects. Details of this analysis and the bias correction method are given in Chapter 4, which was published as Weißmann et al. (2013b).

Center shift

The center or centroid shift method was introduced by Mohr et al. (1993) and characterizes the displacement of the centroid calculated in several apertures of different size. Several variations of the definition of the center shift parameter w exist, depending on the number, size and shape of the apertures. The general motivation behind this parameter is, however, the same for all definitions. While the position of the centroid is expected to remain roughly the same for relaxed objects, clusters containing substructure will yield a different position of the centroid for different aperture radii (e.g. Mohr et al. 1995; Suwa et al. 2003; O'Hara et al. 2006; Ventimiglia et al. 2008; Böhringer et al. 2010). This method is sensitive to asymmetries and thus regular and irregular morphologies. However, it cannot distinguish between all classes defined in the classification scheme of Jones & Forman.

As in the case of power ratios, this method is discussed and tested in detail in Chapter 4. Owing to the definition of this parameter, it is more robust against Poisson noise than power ratios, making it a reliable tool for the morphological study of high-redshift objects. Such a study is presented in Chapter 5 (original publication Weißmann et al. 2013a), where a mild evolution of $P3/P0$ and w with redshift is found.

Asymmetry parameter

The asymmetry parameter A is a measure of the normalized absolute residual flux after subtracting a rotated image from the original image. It was originally used to study the morphology of galaxies (Conselice 1997; Conselice et al. 2000), but was recently also discovered for galaxy clusters (Okabe et al. 2010; Rasia et al. 2013). As in the case of the center shift parameter, A is a phenomenological parameter motivated by the fact that larger substructures or complex morphologies yield higher residual flux after subtracting the rotated image.

A detailed description is given in Chapter 6, where it was found that A is highly sensitive to Poisson noise because of its definition as a per-pixel statistic. The performance study presented in this chapter shows that it is essential to take the data quality into account before applying it to X-ray images of galaxy clusters.

The substructure parameters discussed in this section provide statistical means to quantify the morphology of large cluster samples. They all allow a rough separation into relaxed and disturbed objects, but are most sensitive to certain morphologies. Combining different parameters thus increases the detection likelihood of moderately disturbed objects, which would

not be detected by all methods in the same way.

2.3 Impact of merging on the dynamics and morphology of galaxy clusters

The previous sections gave some insights into substructures and their quantification, focusing on large-scale disturbances which alter the X-ray morphology and the gravitational potential. As was discussed in Sect. 1.2.1, typical cluster observations (especially in surveys) do not have enough photon statistics to obtain precise hydrostatic mass estimates and instead scaling relations are employed. These are sensitive to deviations from the hydrostatic equilibrium (HE) and can be affected by substructure as was demonstrated on the example of cool cores in Sect. 1.2.2 and Fig. 1.6. Since most (morphologically) disturbed clusters are results of merging activity, the mechanism by which merging influences the assumption of HE and the observed mass proxies are reviewed in this section based on simulations published in a paper series of Poole et al. (Poole et al. 2006, 2007, 2008). In particular, the following question will be addressed: i) How valid is the assumption of hydrostatic equilibrium during and after a merging event? ii) How does a deviation from this state influence the mass estimates? and iii) What is the impact on scaling relations?

Also other authors, recently e.g. Nelson et al. (2012), studied the impact of a merging event on the accuracy of hydrostatic mass estimates using simulations, but the work of Poole et al. offers an illustrative discussion of the influence of an infalling substructure on the HE, the time-evolution of the location of the merging cluster in scaling relations and the effect on the cool core (which is not discussed in this thesis) using the same set of simulations.

The first of the three papers, Poole et al. (2006), describes the numerical simulations, the dynamical evolution and transient structures which appear in the course of a merging event. Poole et al. (2007) studied the influence on X-ray properties and scaling relations and finally, Poole et al. (2008) investigated the effect on cool cores.

The presented simulations include several merging scenarios of relaxed, cool core clusters with different mass ratios (1:1, 3:1 and 10:1) and impact parameters (head-on and off-axis). The impact parameter is characterized by v_t/V_c, the ratio between the relative tangential velocity of the merging system when its core reaches the virial radius of the primary system and the circular velocity of the primary system at its virial radius. $v_t/V_c = 0$ depicts the head-on case, while $v_t/V_c = 0.15$ and 0.40 represent off-axis merger. The primary cluster always has an initial mass of $M_{vir} = 10^{15} M_\odot$ and a circular velocity at r_{200} of $V_{200} = 1340$ km/s.

The process of merging comprises of several phases and starts at t_0. The two systems approach each other and reach the minimal distance at $t_{closest}$. During this phase the gas clouds of the two clusters interact, compressing and heating the material between them, creating shock fronts which drive towards the cores, subsequently increasing the luminosity and temperature. After this first core passage and the point of maximum separation (t_{apoge}), the two gas clouds approach each other again and reach the second minimal distance at $t_{accrete}$. Dispersed material from the core of the merging body is accreted on the core of the primary system. The secondary core – or parts of it – can survive, leading to more encounters with the primary core. In case of no further encounters the system starts to relax after $t_{accrete}$ and shows a regular morphology at t_{relax}.

In the following, this scenario is used to study the impact of merging on the hydrostatic equilibrium hypothesis, mass estimates and X-ray scaling relations. Especially interesting is the phase between $t_{\rm closest}$ and $t_{\rm relax}$, when the system shows a disturbed morphology and after $t_{\rm relax}$ when it has a regular appearance.

Impact on the hydrostatic equilibrium hypothesis and mass estimates
It is commonly assumed that galaxy clusters with a regular X-ray morphology are relaxed systems for which the HE assumption holds. Merging, on the other hand, introduces disturbances in the gravitational potential and the cluster deviates from HE. Since all galaxy clusters grow through merging, it is interesting to study how valid the HE assumption is during and especially after a merging event when the cluster already appears relaxed.

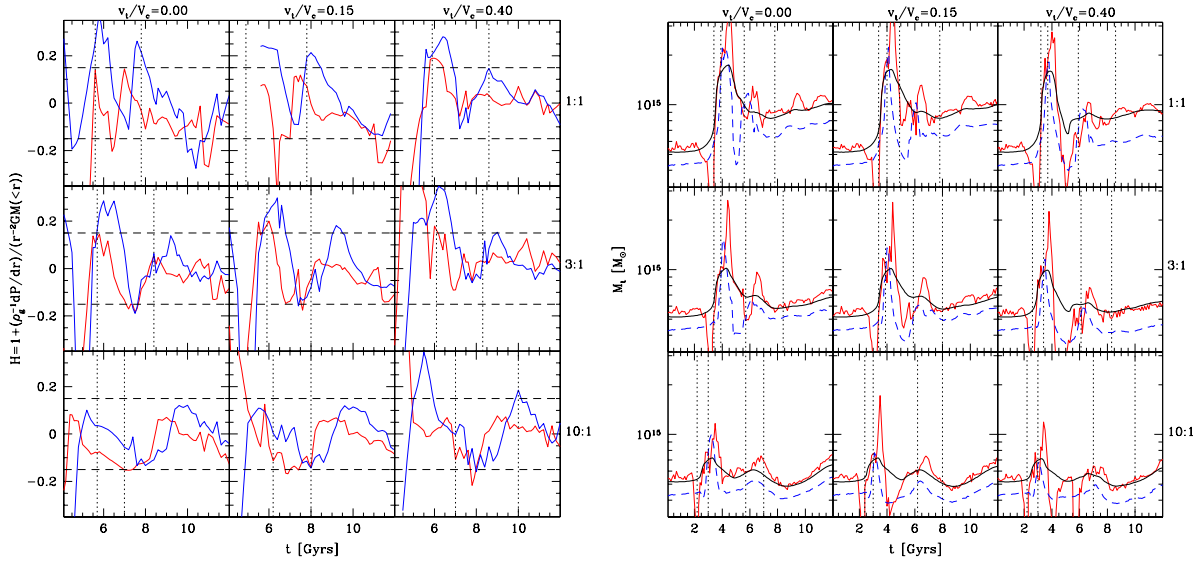

Figure 2.5: Results from the merging process for three mass ratios (1:1, 3:1 and 10:1) and different impact parameters $v_{\rm t}/V_{\rm c}$. **Left:** Evolution of the hydrostatic disequilibrium H at r_{500} (red) and r_{200} (blue). The horizontal lines show the 15% range where the hydrostatic equilibrium assumption roughly holds. The vertical lines indicate the second core-core interaction ($t_{\rm accrete}$, left) and $t_{\rm relax}$ (right), where the cluster shows a regular X-ray morphology again. Figure taken from Poole et al. (2006). **Right:** Evolution of the actual total mass (black solid line) and mass estimates based on the hydrostatic equilibrium assumption (red line) and the isothermal β model (blue line). Vertical lines indicate the merging phases (left to right): t_0, $t_{\rm closest}$ (first core-core interaction), $t_{\rm accrete}$ and $t_{\rm relax}$. Figure taken from Poole et al. (2007).

The left panel of Fig. 2.5 shows the time-evolution of the deviation from the HE assumption, which is given by H in the aperture of r_{200} and r_{500}. Poole et al. (2006) find a sharp increase of the disequilibrium shortly before the second core passage at $t_{\rm accrete}$, followed by a damped, oscillating pattern. At $t_{\rm relax}$ the clusters show a relaxed X-ray morphology according to power ratios and the center shift parameter and are generally virialized around this time. In some cases, adiabatically oscillating merger remnants are found after $t_{\rm relax}$, which results in a deviation from HE around 10 – 20%.

The impact of the disequilibrium on the mass determination is shown in the right panel of Fig. 2.5, where the actual total mass is compared to mass estimates using the HE assumption and the isothermal β model. The hydrostatic mass estimates (HME) are in general higher than the actual total cluster mass, but their overall evolution is similar. During the most disturbed phases (first and second core-core interactions), the HME largely overestimates the total cluster mass. Interestingly, deviations from the HE assumption are found also after $t_{\rm relax}$, but the mass estimates are accurate to within $\sim 5-10\%$. These results agree well with combined X-ray and weak-lensing studies (see Sect. 1.2.1), which find $\sim 5-20\%$ lower values for HME than for estimates from weak lensing measurements which do not require the assumption of hydrostatic equilibrium and spherical shape. While the largest deviations are reported for clusters with a disturbed X-ray morphology, also relaxed objects can show a small hydrostatic mass bias.

Mass estimates from the isothermal β model, which assumes hydrostatic equilibrium, isothermality of the ICM and that the density profile can be described by the β model (see Sect. 1.1.1), systematically underestimate the actual cluster mass by $25-40\%$. Using such a mass estimate strongly affects cosmological studies based on the cluster mass function and changes the normalization of mass scaling relations, but should not influence their general trend.

Impact on X-ray scaling relations

After establishing to which extent the HE assumption holds and how it influences mass estimates based on the HE assumption and the β model, the influence of merging on X-ray properties and thus X-ray scaling relations (for a discussion on scaling relations see Sect. 1.2.2) is shown. Detailed studies of deviations from the self-similar relations and the implications for cluster physics are manifold and interesting, but beyond the scope of this thesis. The aim of this section is to illustrate merely how cluster properties change during different merging phases and to which extent merging of two cool core clusters can reproduce the scatter in the observed relations. A detailed discussion is provided in Poole et al. (2007) and is omitted here.

Fig. 2.6 shows the evolution of the merging system in the $L-T$ and $M-T$ relation. The temperature is obtained from spectral fitting, the luminosity is the bolometric luminosity and the mass is estimated using the β model. All parameters are obtained including the central region to explore the effect of merging on cool cores (for a detailed discussion see Poole et al. 2008). The position of the primary system at t_0 and $t_{\rm relax}$ is indicated, as is the evolution between $t_{\rm closest}$ to $t_{\rm relax}$, where the cluster shows a disturbed X-ray morphology. For comparison, observed clusters from Horner (2001), whose properties were derived analogously to the ones of the simulated clusters, and theoretical scaling laws from different entropy injection models are added. The model which reproduces the observed scaling relation best is depicted by a thick dashed line. Since the mass estimates from the β model systematically underestimate the actual cluster mass, the entropy models are adjusted accordingly for the mass-observable relations.

The merging of two massive systems is a very energetic event and affects the X-ray properties. Since they are derived based on temperature and density profiles, their time-evolution is expected to be similar. In agreement with previous studies, Poole et al. (2007) find two

peaks in the luminosity and temperature evolution due to shocks and compression around the time of the first and second core-core interaction. As the system relaxes, luminosity and temperature increase smoothly due to the presence of a cool core. Until the end of the simulation, the temperature roughly reaches the value predicted from scaling relations, but the luminosity remains below the predictions. The offset depends on the geometry of the merger and can be partly corrected by excluding the core region. The similar double-peaked pattern is found in the evolution of the cluster mass due to accretion processes around and after the core interactions.

The combined evolution of bolometric luminosity, spectral temperature and the cluster mass obtained from the β model is shown in Fig. 2.6. The low scatter in the $M - T$ relation in comparison to the $L - T$ (and $M - L$ which is not shown) plane is apparent, however, not surprising since the cluster mass traces the depth of the gravitation potential which in turn influences the gas temperature. In addition, owing to the definition of the β model, an increase in temperature leads to the same effect in mass.

Since the primary cluster is a relaxed system which hosts a cool core and the core region was not excised, it is located at higher luminosity and mass for a given temperature than predicted by the $L - T$ and $M - T$ relation at the start of the simulation. During the approach of the two systems, compression and shocks lead to an increase in luminosity and temperature which peak at t_{closest} and t_{accrete}. The same is seen in the evolution of the cluster mass due to accretion processes. Between the first and second approach the properties fall back to almost their initial values when the two cluster cores break apart again. After t_{accrete} the observed substructure fades as the system relaxes and it evolves parallel to the model again after t_{relax}. The luminosity increases due to cooling and an increasingly denser core, while loose remnant material from the merging process is accreted onto the primary system, which results in a deeper potential well and thus a higher temperature and mass. Comparing the position of the system in the $L - T$ and $M - T$ plane at the end of the simulation with the one predicted by the observed scaling laws (green cross in the figure) shows that merging of two cool core systems leads to a less luminous and massive system than predicted by the observed scaling relations.

Although the system moves around in the $L - T$ and $M - T$ plane between t_{closest} and t_{relaxed}, thus when the cluster shows a disturbed X-ray morphology, it does not move through the full range of observed scatter in the different merging phases. The $M - T$ relation shows only low scatter, but in some cases the system is found outside of the observational scatter for a short time. These phases correspond to the largest deviation of the β model mass estimates from the actual total cluster mass (see Fig. 2.5). In addition, after the second core passage, some systems show a very high-temperature, an effect which is not visible in the $L - T$ plane and which is due to the use of the β model.

The presence of a cool core has a large impact on the position of the cluster in X-ray scaling relations. While the core is excluded for cosmological purposes, including it offers means to study the effect of processes acting in the core such as AGN activity or merging on X-ray scaling relations. Combining the results from the $L - T$, $M - T$ and $M - L$ relation, Poole et al. (2007) conclude that a single merging event of two relaxed, cool core clusters introduces some dispersion in these relations, but it cannot fully account for the observed scatter. Several such mergers or off-axis collisions of equal mass systems, which are only rarely observed, however, could explain the dispersion, even though it is unlikely.

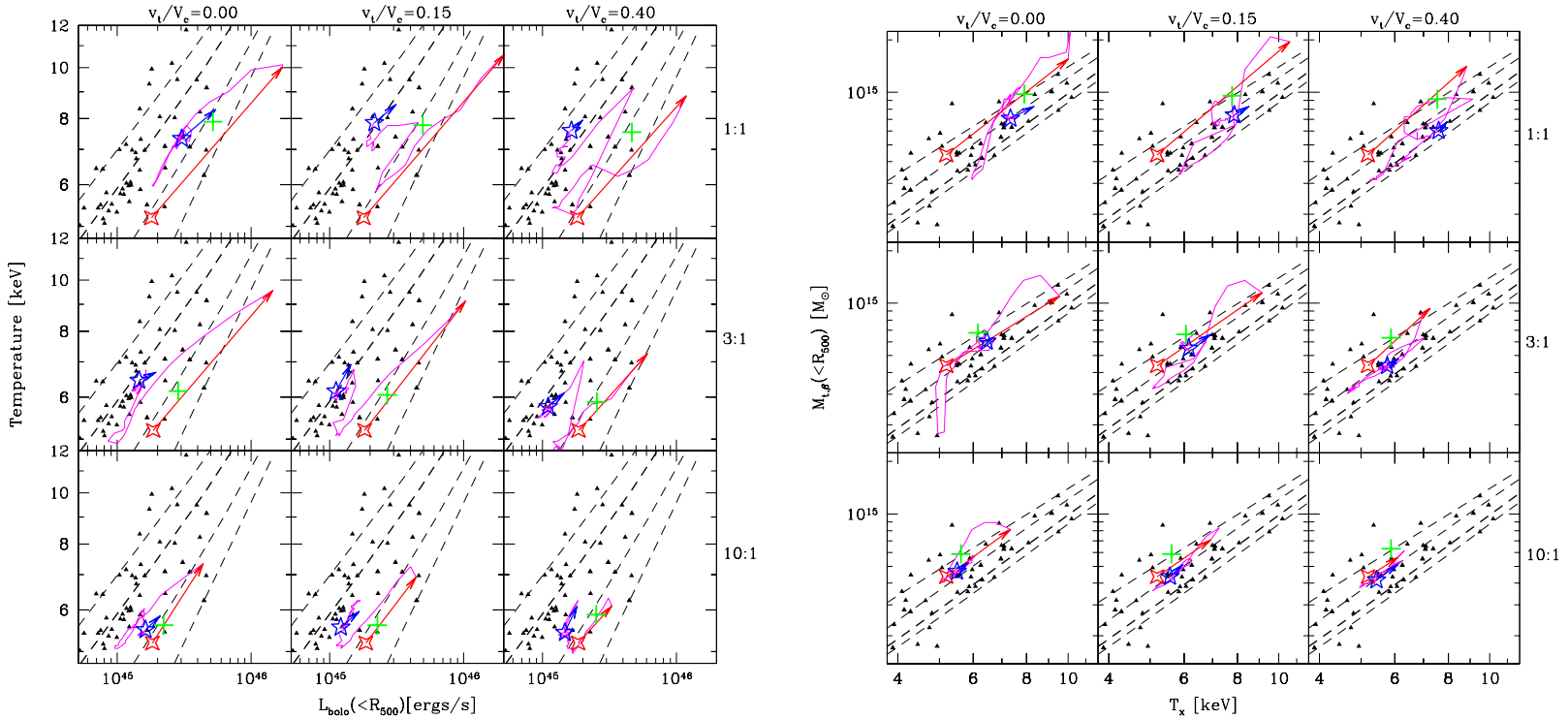

Figure 2.6: Evolution of the merging system in X-ray scaling relations. The position of the merging system at t_0 and $t_{\rm relax}$ is depicted by a red four-point and blue five-point star, while the evolution between the phases is shown as follows: red arrow from t_0 to $t_{\rm closest}$, magenta line from $t_{\rm closest}$ to $t_{\rm relax}$ and blue arrow after $t_{\rm relax}$. The green cross gives the position of the system after the merging event predicted by the observed scaling relation. The black points show galaxy clusters observed by Horner (2001), while the dashed lines indicate theoretical predictions for scaling relations using different entropy injection models. The thick dashed line depicts the model which fits the median scaling relation best. All parameters are computed including the central region to explore the influence of merging. **Left:** Luminosity-temperature relation. For this relation, the temperatures from spectral fitting and the bolometric luminosities are used. **Right:** Mass-temperature relation. As in the previous case, the temperature is obtained from spectral fitting, while the mass is computed using the isothermal β model. Figures taken from Poole et al. (2007).

This shows that although merging of two relaxed systems cannot fully explain the scatter in the X-ray scaling relations, morphological information can help to significantly decrease the dispersion. Additional simulations of non-cool core systems or several merging processes are necessary to obtain a more detailed understanding of the impact of the dynamical state of the cluster on X-ray scaling relations.

While simulations illustrate the effect of merging and allow a detailed analysis, only a comparison to observations can ensure their reliability. Testing the numerical predictions with X-ray observations calls for well-studied and well-calibrated morphology estimators when analyzing the dynamical state of galaxy clusters. Such estimators were tested thoroughly in the course of this thesis and are presented in Chapter 4 for clusters at low-redshift and Chapter 5 and 6 for clusters up to redshift ~ 1. Especially interesting for the future is their application to large samples of high-redshift clusters to study the evolution of X-ray scaling relations, which is currently still limited by the rather low number of objects observed at high redshift.

Chapter 3

X-ray observatories and data analysis

The scientific results of this work are based on the analysis of observations obtained with the X-ray observatories *XMM-Newton* and *Chandra*. Both enable imaging and spectroscopy of incoming X-rays and are discussed in more detail in the following sections. A discussion of the spectrometers on-board the X-ray observatories is omitted since spectra are not analyzed in this work. *XMM-Newton* and *Chandra* are both equipped with X-ray telescopes, but there are differences due to their set-up and instruments. An overview of the most relevant properties regarding imaging is provided in Table 3.1. One of the main differences is the number of telescopes and detectors in the focal plane. *XMM-Newton* consists of three telescopes which allows simultaneous observations with three imaging instruments, the two MOS and the pn CCD camera. For two telescopes the focal plane is shared between a MOS detector and a spectrometer (RGS). *Chandra* hosts only one X-ray telescope which results in the need to alternate between the operation of the Imaging Spectrometer (ACIS) and the High Resolution Camera (HRC). This single telescope has the same FOV as each of the *XMM* telescopes and therefore receives a significantly lower number of collected photons. In terms of spatial resolution, the ACIS-I camera is superior to MOS or pn. Depending on the scientific goal, one chooses to observe a target with *XMM-Newton* (more photon collecting power) or *Chandra* (better spatial resolution). For this work, *XMM-Newton* observations of low-redshift galaxy clusters, which provide very good photon statistics, were used. High-redshift clusters were observed with *Chandra* in order to resolve their structure.

Technical details of the two X-ray satellites quoted in this work were taken from the *Chandra* Proposers' Observatory Guide[1] Cycle 15 provided by the CXC and the *XMM-Newton* Users Handbook[2] v2.10.

3.1 *XMM-Newton*

The *XMM-Newton* observatory is a 4 t and 10 m long spacecraft and thus the largest scientific satellite ever launched by the European Space Agency. Since its launch on December 10th 1999 from Kourou, French Guiana, it has provided a vast number of high-quality X-ray observations and allowed for a tremendous amount of high-impact scientific publications. The pay-

[1] `http://cxc.cfa.harvard.edu/proposer/POG/html/index.html`
[2] `http://xmm.esac.esa.int/external/xmm_user_support/documentation/uhb/XMM_UHB.html`

Table 3.1: Characteristics of the *Chandra* ACIS-I and *XMM-Newton* MOS and pn detectors relevant for imaging. The full width at half maximum (FWHM) and half energy width (HEW) of the PSF are on ground measurements at 1.5 keV and almost identical to the on-axis in orbit measurements which are given in the text.

Characteristic	***Chandra* ACIS-I**	***XMM-Newton* MOS**	***XMM-Newton* pn**
Number of instruments	1	2	1
Energy range in keV	0.3 – 10	0.15 – 12	0.15 – 12
FOV in diameter	16.9′	30′	30′
PSF (FWHM/HEW)	0.2″/0.5″	5″/14″	6″/15″
Pixel size	0.5″	1.1″	4.1″

load comprises three identical co-aligned X-ray telescopes, which each consist of 58 Wolter type 1 grazing-incidence mirrors nested in a coaxial and co-focal configuration. They allow to cover a spectral range of 0.15 – 12 keV but were optimized for high quantum efficiency in the 0.1 – 10 keV range with a maximum efficiency at 1.5 keV. Each telescope has a 30 arcmin field of view (FOV), a focal length of 7.5 m, a collecting area of 1550 cm^2 at 1.5 keV and is equipped with baffles for visible and X-ray stray-light suppression and an electron deflector to divert soft electrons. An illustration is given in Fig. 3.1. The *XMM-Newton* observatory hosts several instruments: the European Photon Imaging Camera (EPIC) consisting of three X-ray CCD cameras, two Reflection Grating Spectrometers (RGS) and the optical mirror (OM).

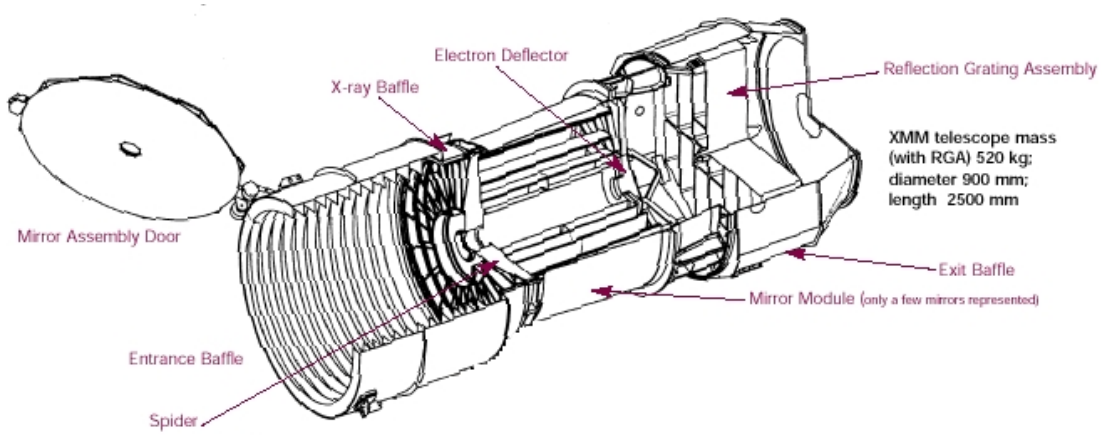

Figure 3.1: *XMM-Newton* telescope configuration. Image credit: ESA/ESAC.

Two of the X-ray telescopes carry an EPIC MOS (Metal Oxide Semi-conductor) CCD array in the primary and an RGS in the secondary focus. The set-up is illustrated in Fig. 3.2 on the left, with the nested X-ray mirrors, the grating assemblies to diffract part of the incoming flux onto the secondary focus and the two back-end instruments. The incoming flux is split almost equally between the MOS detector and the RGS. As is shown in Fig. 3.3 on the left, a MOS camera is made of seven front-illuminated CCDs in the focal plane, of which one is located at the focal point and six positioned around it. They each consist of 600×600 pixel.

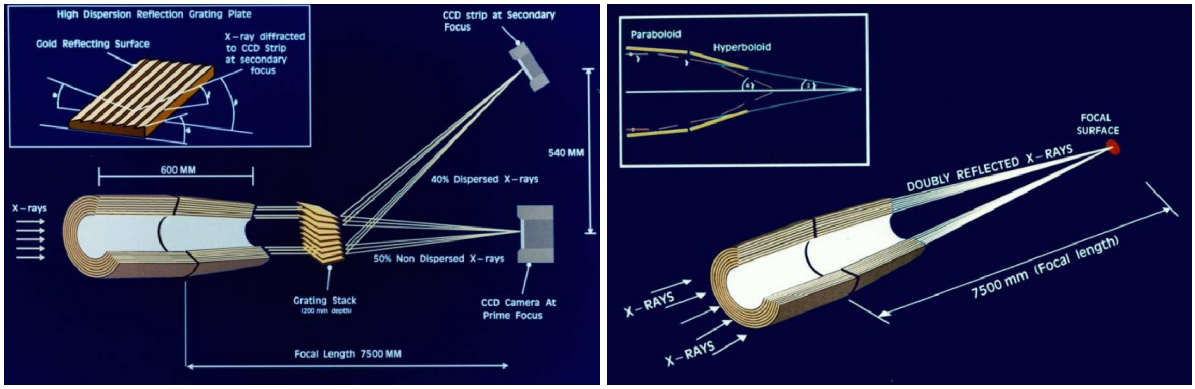

Figure 3.2: Light path in the *XMM-Newton* telescopes for the EPIC MOS (left) and EPIC pn (right) cameras. Figures taken from ESA: XMM-Newton SOC (2012).

With a pixel size of 40 μm (1.1 arcsec) square, the imaging area of each CCD array is about 2.5×2.5 cm. All seven detectors cover the focal plane 28.4 arcmin in diameter and thus almost the full FOV of 30 arcmin. At 1.5 keV the full width at half maximum (FWHM) of the on-axis in orbit PSF is 4.3 (4.4) arcsec for MOS1 (MOS2) and the half energy width (HEW) 16.8 (17) arcsec. The quantum efficiency (QE) of the MOS detectors is high in the $0.2-10$ keV range, but drops below 20% above 10 keV, limiting the MOS detectors to energies $\leq$ 10 keV. The two EPIC MOS arrays are arranged orthogonal to each other to cover gaps between the outer CCDs of the other detector. In March 2005 and December 2012, the two peripheral CCDs of MOS1 (CCD 6 and 3) suffered significant damage and had to be switched off.

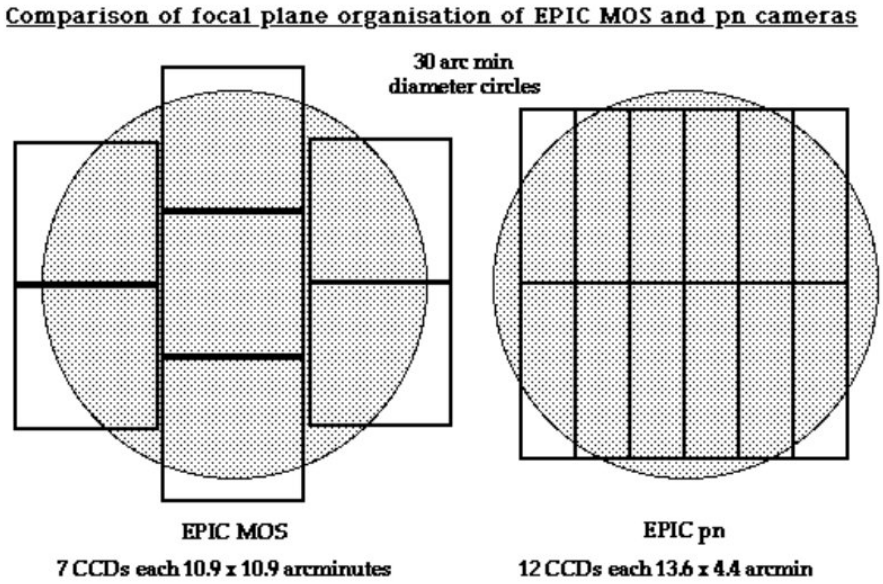

Figure 3.3: Comparison of the CCD arrays of EPIC MOS (left) and EPIC pn (right). The shaded circle has a diameter of 30 arcmin and depicts the FOV. Figure taken from ESA: XMM-Newton SOC (2012).

The third EPIC camera, pn, is more sensitive than the MOS chips. In order to fully exploit its abilities, it is the only detector in the focus of the third X-ray telescope and receives an unobstructed beam (Fig. 3.2). The EPIC pn consists of twelve 3×1 cm back-illuminated CCDs on a single wafer as is shown in Fig. 3.3 on the right. The array is subdivided into four quadrants with 3 CCDs each. Each CCD comprises 200×64 pixels with a pixel size of 150 μm (4.1 arcsec) square. This yields a total imaging area of 6×6 cm, covering about 97% of the FOV. Due to the large pixel size of the pn detector, the core of this mirror module cannot be resolved in orbit. This leads to the upper limit of 12.5 arcsec for the on-axis in orbit measured PSF at FWHM at 1.5 keV, which is consistent with the 6.6 arcsec measured on the ground. For the same energy, the HEW of the PSF is 16.6 arcsec in orbit and 15.1 arcsec previously measured on ground. The QE of the pn camera is a lot higher than that of the MOS detectors, with a QE(pn) > 90% over a very large energy range. Due to this high QE, the pn camera can operate well up to 12 keV. Each pixel column in the pn camera has its own read-out node, which reduces the read-out time compared to MOS. The pn camera does not have frame store buffers which results in so-called *out-of-time events* (OoT). Incoming X-ray photons are registered during the readout phase and especially for bright sources this produces a smeared event streak along the pixel column of the event. Such OoT events are corrected statistically during the data reduction process.

3.2 *Chandra*

The *Chandra* X-ray observatory was launched on July 23rd 1999 from Cape Canaveral as NASA's flagship mission for X-ray astronomy. The spacecraft hosts one X-ray telescope made of four pairs of nested Wolter type 1 grazing-incidence mirrors. This High Resolution Mirror Assembly (HRMA) was designed for high-resolution imaging and spectroscopy of X-rays. The telescope has a FOV of 30 arcmin, a focal length of 10 m and an unobscured clear aperture of 1145 cm^2 with less than 10% obscuration by supporting struts. Like *XMM-Newton*, *Chandra* has mechanisms for the suppression of stray-light and soft protons. An illustration of the *Chandra* spacecraft is given in Fig. 3.4.

The observatory carries four science instruments for imaging and spectroscopy in the 0.1 – 10 keV range. The two focal plane instruments are the Advanced CCD Imaging Spectrometer (ACIS) and the High Resolution Camera (HRC). For spectroscopy two transmission grating spectrometers are installed which can be moved into the light path just behind the mirrors: the High Energy Transmission Grating (HETG) and the Low Energy Transmission Grating (LETG). The two focal plane instruments are installed on the Science Instrument Module (SIM) and cannot be operated simultaneously. The HRC consists of two micro-channel plate imaging detectors (HRC-I and HRC-S) and offers the highest spatial (~0.4 arcsec) and temporal (16 μsec) resolution.

Observations discussed in this work were obtained with the ACIS instrument which consists of ten 1024×1024 pixel CCDs. The pixels are 24 μm (~ 0.5 arcsec) square which results in an array size of 16.9×16.9 arcmin for the 2×2 (I0 through I3) ACIS-I array optimized for imaging wide fields. The 1×6 CCD array (S0 through S5) ACIS-S has a size of 8.3×50.6 arcmin and can be used for imaging or as a grating readout. A schematic view of the ACIS CCD arrays is given in Fig. 3.5. S1 and S3 from the ACIS-S array are back-illuminated (BI)

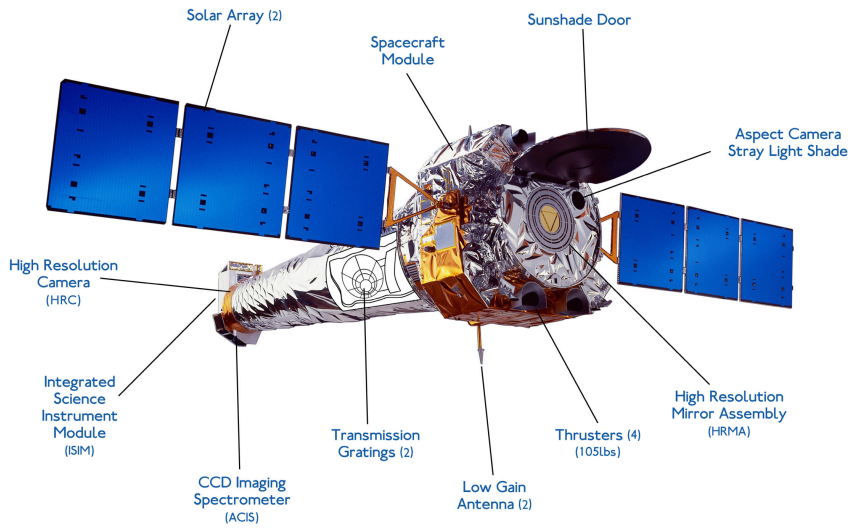

Figure 3.4: Illustration of the *Chandra* X-ray observatory including the science instruments and the support structure. Figure taken from the *Chandra* website: `http://chandra.harvard.edu/about/spacecraft.html`.

CCDs while the eight others are front-illuminated (FI). Owing to their technical details, FI and BI chips differ in their QE. BI chips have QE > 80% for 0.8 – 5.5 keV and QE > 30% for 0.4 – 10 keV. FI CCDs reach QE > 80% only for the narrow 3.0 – 6.5 keV range and QE > 30% for 0.7 – 11 keV. BI chips therefore have a wider range with QE > 80%, have good QE down to lower energies and a better chip-average energy resolution than FI CCDs.

3.3 X-ray data reduction

X-ray observatories provide raw event files in which the position and energy of each incoming photon is registered. To obtain a scientific image, a number of calibration and correction steps need to be taken. The analysis software and guidelines for the analysis are provided by the Science Operation Centers of *XMM-Newton* and *Chandra*. The Science Analysis Software (SAS[3]) is tailored for the analysis of *XMM-Newton* observations, while the *Chandra* Interactive Analysis of Observations (CIAO[4]) was optimized to deal with *Chandra* data.

This section provides a general overview of the main steps in the process of deriving scientific images, exposure maps and background images from raw X-ray data using the example of *XMM-Newton* observations. I reduced the *XMM-Newton* data discussed in Chapters 4–6 following these steps, which are based on the Users Guide to the *XMM-Newton* Science Analysis System[5], Issue 9.0 and the recipe for the treatment of X-ray data and production of images provided in Böhringer et al. (2007, 2010). For *Chandra* data I compiled a reduction pipeline using the standard CIAO tools as described in the CIAO Analysis Guides[6]. Details on this pipeline and the *Chandra*-specific data reduction are discussed in Appendix A.

[3] `http://xmm.esa.int/sas`
[4] `http://cxc.cfa.harvard.edu/ciao`
[5] `http://xmm.esac.esa.int/external/xmm_user_support/documentation/sas_usg/USG`
[6] `http://cxc.cfa.harvard.edu/ciao/guides`

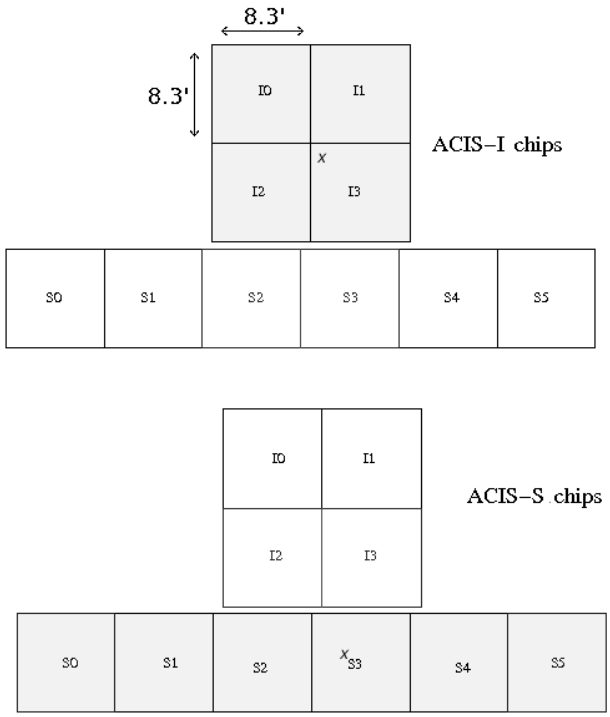

Figure 3.5: Schematic view of the ACIS CCD arrays. The nominal aimpoints are marked with crosses on I3 when using the ACIS-I (top) and S3 when using the ACIS-S array (bottom). Figure taken from CXC – The *Chandra* Proposers' Observatory Guide.

Data preparation and processing

Raw data contains the uncalibrated observations of the instruments, attitude files of the satellite and other data necessary for calibration. In the case of *XMM-Newton* these files are called Observation Data File (ODF). ODFs need to be transformed into a format suitable for further processing. Several tasks generate calibrated photon event lists and auxilliary files like attitude files, bad pixel lists or background light curves. Calibrated photon event files contain information on each incoming event including arrival time, energy and sky position. The attitude file contains the attitude information of the entire observation such as the time interval of the observation or the coordinates and the position angle of the pointing and the reference star as a function of time. This file is used to correct for the slew motion of the spacecraft in order to obtain accurate sky coordinates for each incoming event and to filter out periods where the true pointing is too far off from the desired position.

Flare cleaning and X-ray background

Apart from source photons, event lists contain several background components[7] due to photons (Cosmic X-ray Background), particles (soft proton flares and interaction with the detector) and electronic detector noise. Electronic detector noise is already corrected on-board the X-ray satellite and does not appear in the science data. The Cosmic X-ray background and particle

[7]For a comprehensive list see `http://www.star.le.ac.uk/~amr30/BG/BGTable.html`

interactions with the detector can be considered constant, but soft proton flares are highly variable and need to be removed individually for each observation. Due to the removal of flared periods, the effective exposure time decreases. The remaining intervals are called *good time intervals* (GTI) and can be further processed to obtain science products. Flare-cleaned science data still contains the X-ray background, which can be estimated by extracting a local background from a region close to the source or by using so-called blank sky images. The latter method is used in this work, where blank sky files for each detector are provided by the *XMM-Newton* Science Team. They consist of a superposition of long exposures of a sky region and were subject to a detailed source removal and flare-cleaning process. In order to match the observations, the blank sky file of each detector is recast onto the sky position of the observation and an image in the $0.5 - 2$ keV range is extracted. A two-component model which takes into account the particle induced background and instrumental noise and the vignetted X-ray background is fitted to the blank sky image. The normalization of the background model is obtained from a comparison to the surface brightness in the outer cluster and point source free region of the observation. This is done for each detector separately to obtain a detector-specific background map.

Creation of science products

Calibrated and cleaned photon event lists allow the creation of X-ray images and of exposure maps, which in addition require the attitude information of the observation to determine the exact pointing direction as a function of time. For the studies presented in Chapters 4–6, the standard $0.5 - 2$ keV range is used which yields the highest signal-to-noise ratio for clusters. Unless stated otherwise, the term image implies count image, hence the total detected counts per pixel. Images with a pixel size of 4 arcsec are created for each of the three detectors. Exposure maps contain the effective exposure time (i.e. the total on-source time folded with the effective area which is normalized to the on-axis value) for each pixel and correct for the varying sensitivity across the detectors and e.g. hot pixels. They can be used to convert a count image into a sensitivity-corrected image in flux units.

For pn observations, out-of-time (OoT) event corrections need to be applied. Incoming events are also registered during the readout phase, which leads to a fraction of 2.3% OoT events for the Extended Full Frame and 6.3% for the Full Frame imaging mode. OoTs are included in the event list because they cannot be distinguished from events during the regular observation time. They can cause smeared stripes on the image and if the observed source is located in such a stripe, a major contamination is caused. These effects are corrected statistically by simulating an OoT event list from which an image can be extracted. This image is scaled by a factor of 0.023 or 0.063, depending on the imaging mode to match the raw pn image from which it is subtracted, to create the final OoT cleaned pn image.

The final science products of all three detectors are combined to increase the photon statistics. Images and MOS exposure maps can be added directly. Due to the different sensitivity of the MOS and the pn detector, a weighting factor (~ 3.3) calculated from the surface brightness profiles of the MOS and pn data is applied to the combined MOS exposure map before adding the pn exposure map. The results are a combined (count) image and a combined exposure map with preserved photon statistics.

Point source removal
The last and for this work very important step in the data reduction is the detection and exclusion of sources (also called point sources) not associated with the cluster. Standard-source detection algorithms are applied to the final images to detect and exclude these objects. The source detection task is run on the combined (i.e. the pn and both MOS cameras) *XMM-Newton* image to increase the sensitivity of the source detection. In contrary to Böhringer et al. (2007, 2010), the sources are removed from the individual detector images. After refilling the gaps using the CIAO task *dmfilth* and subtracting the background, the individual images are combined to create a background-subtracted point-source corrected image.

The source removal needs to be done with the outermost care to avoid incorrect classification of substructures and point sources. Whenever the distinction between substructure and point sources is unclear, additional information including *Chandra* observations, NED information and previous published discussions of the cluster are used.

These final point-source corrected images, background and exposure maps are then used to obtain substructure parameters. For details on the calculation see Chapter 4 and 6.

Chapter 4

Studying the properties of galaxy cluster morphology estimators

A. Weißmann, H. Böhringer, R. Šuhada, A. Ameglio

A&A, **549** (2013), A19

Abstract
X-ray observations of galaxy clusters reveal a large range of morphologies with various degrees of disturbance, showing that the assumptions of hydrostatic equilibrium and spherical shape, which are used to determine the cluster mass from X-ray data are not always satisfied. It is therefore important for the understanding of cluster properties as well as for cosmological applications to detect and quantify substructure in X-ray images of galaxy clusters. Two promising methods to do so are power ratios and center shifts. Since these estimators can be heavily affected by Poisson noise and X-ray background, we performed an extensive analysis of their statistical properties using a large sample of simulated X-ray observations of clusters from hydrodynamical simulations. We quantify the measurement bias and error in detail and give ranges where morphological analysis is feasible. A new, computationally fast method to correct for the Poisson bias and the X-ray background contribution in power ratio and center shift measurements is presented and tested for typical *XMM-Newton* observational data sets. We studied the morphology of 121 simulated cluster images and established structure boundaries to divide samples into relaxed, mildly disturbed and disturbed clusters. In addition, we present a new morphology estimator – the peak of the $0.3 - 1\ r_{500}$ $P3/P0$ profile to better identify merging clusters. The analysis methods were applied to a sample of 80 galaxy clusters observed with *XMM-Newton*. We give structure parameters ($P3/P0$ in r_{500}, w and $P3/P0_{\mathrm{max}}$) for all 80 observed clusters. Using our definition of the $P3/P0$ (w) substructure boundary, we find 41% (47%) of our observed clusters to be disturbed.

4.1 Introduction

Clusters of galaxies form from positive density fluctuations and grow hierarchically through the extremely energetic process of merging and mass accretion. With due time they are thought to reach dynamical equilibrium and form the largest virialized structures in the Universe. This makes them very interesting tools to study cosmology and the evolution of large scale structure in which they appear as nodes at the intersection of filaments. In the soft X-ray band the hot intracluster medium (ICM) which resides in the intergalactic space and makes up about 15% of the total cluster mass is observed. Already early X-ray observations of galaxy clusters revealed that the ICM distribution is not smooth and azimuthally symmetric for all objects. In the beginning of the 1990s it became more clear from *ROSAT* observations that galaxy clusters are not relaxed objects but that they contain substructure (e.g. Briel et al. 1991, 1992). Since then, a lot of effort was put into the identification and characterization of substructure in the ICM to determine the dynamical state of the cluster. Jones & Forman (1991) showed that around 30% of their ~200 clusters observed with the *Einstein* satellite contain substructure. This was an important step in the understanding of structure formation, because it showed that cluster formation and evolution has not finished yet. In previous studies different parameter boundaries for the distinction of substructured and regular clusters have been used. The fraction of clusters with substructure was estimated to be about $40 - 70\%$ for X-ray observations (Mohr et al. 1995; Jones & Forman 1999; Schuecker et al. 2001; Kolokotronis et al. 2001). This indicates that the merging and accretion activity, which is reflected by the presence of multiple surface brightness peaks or disturbed morphologies, has not yet ceased in clusters. Substructure as a tracer of merging activity indicates a deviation from the relaxed and virialized state and can make a precise cluster mass determination very difficult. Since hydrostatic equilibrium is one of the main assumptions for cluster mass estimates, large errors can occur, which influence the constraints of cosmological parameters which are derived using cluster masses. Recent studies of simulations (e.g. Nagai et al. 2007; Piffaretti & Valdarnini 2008; Jeltema et al. 2008; Lau et al. 2009; Meneghetti et al. 2010; Rasia et al. 2012) and observations (e.g. Zhang et al. 2008; Okabe et al. 2010) show that the hydrostatic X-ray mass can be biased low between 10% and 30%. The largest deviations are expected to occur for galaxy clusters with substructure and it is therefore very important to accurately characterize substructure and the dynamical state of a cluster.

Over the years many methods to characterize and quantify substructure in galaxy clusters were proposed (see Buote 2002 for a review). A simple and descriptive method to reveal substructure in a galaxy cluster is to subtract a smooth elliptical β model from the X-ray cluster image and to examine the residuals (e.g. Davis 1993; Neumann & Böhringer 1997). Wavelet analysis and decomposition have been applied to many clusters in X-rays (e.g. Slezak et al. 1994; Arnaud et al. 2000; Maurogordato et al. 2011). This technique enables substructure analysis on different scales and the separation of different components. Another approach is the classification of cluster morphologies by visual inspection for X-ray images (e.g. Jones & Forman 1991). Several other methods classify the morphology of galaxy clusters. Measuring e.g. a clusters ellipticity is very common (e.g. McMillan et al. 1989; Pinkney et al. 1996; Schuecker et al. 2001; Plionis 2002), but this property is not a good indicator for a clusters' dynamical state because both relaxed and disturbed clusters can have significant ellipticities.

Better indicators of the dynamical state of a cluster are power ratios (Buote & Tsai 1995, 1996) and center shifts (Mohr et al. 1993), which will be both addressed in this paper.

Most substructure studies were performed on low-redshift clusters (e.g. Mohr et al. 1995; Buote & Tsai 1996; Jones & Forman 1999). With the recent increase in the detection of high-redshift clusters, also the number of substructure studies of fairly large high-z samples using power ratios and other substructure parameters became important (e.g. Bauer et al. 2005; Jeltema et al. 2005; Hashimoto et al. 2007b). However, studies of the uncertainties and bias using these methods especially for low-quality (low net counts and/or high background) observations are sparse (e.g. Buote & Tsai 1996; Jeltema et al. 2005; Böhringer et al. 2010).

This is the main issue we want to address in this paper. We use a large sample of simulated X-ray cluster images to study the influence of shot noise on the power ratio and center shift calculation and present a method based on Böhringer et al. (2010, B10 hereafter) to correct for it. We give parameter ranges in which a cluster can be expected to be relaxed or significantly disturbed. In addition, we give updated substructure parameters for a sample of 80 galaxy clusters based on *XMM*-observations which are part of several well-known samples. We discuss power ratios, center shifts and a new parameter in detail and present possible applications.

The paper is structured as follows. In Sect. 4.2 we introduce structure parameters used in this study. We briefly present the set of simulated X-ray cluster images in Sect. 4.3 which were used to calibrate and test our method. The investigation of the influence of Poisson noise and net counts on the reliability of power ratios and center shifts is given in Sect. 4.4. We also introduce our method to correct for the noise and background contribution and test its accuracy. In Sect. 4.5 we define different morphological boundaries for power ratios and center shifts. We apply our analysis to a sample of 80 galaxy clusters observed with *XMM-Newton*, which is characterized in Sect. 4.6. A short overview of the data reduction is given in Sect. 4.7. In Sect. 4.8 we show results of the morphological analysis of the observed cluster sample and introduce an improved morphological estimator. We discuss the results in Sect. 4.9 and conclude with Sect. 4.10. Throughout the paper, the standard ΛCDM cosmology was assumed: H_0=70 km s^{-1} Mpc^{-1}, Ω_Λ=0.7, Ω_M=0.3.

4.2 Substructure parameters

Power ratios

The power ratio method was introduced by Buote & Tsai (1995) with the aim to parametrize the amount of substructure in the ICM and to relate it to the dynamical state of a cluster. Only the distribution of structure on cluster scales which dominates the global dynamical state is of interest. Power ratios are based on a 2D multipole expansion of the clusters' gravitational potential using the surface mass density distribution. Power ratios are thus giving an account of the azimuthal structure where moments of increasing order describe finer and finer structures. The powers are calculated within a certain aperture radius (e.g. r_{500}) with the aperture centered on the mass centroid.

The 2D multipole expansion of the two-dimensional gravitational potential $\psi(R,\phi)$ can be

written as

$$\psi(R,\phi) = -2G\left[a_0 \ln\frac{1}{R} + \sum_{m=1}^{\infty}\frac{1}{mR^m}\left(a_m \cos(m\phi) + b_m \sin(m\phi)\right)\right] \tag{4.1}$$

where a_m and b_m are

$$a_m(R) = \int_{R'\leq R} \Sigma(\mathbf{x}')(R')^m \cos(m\phi')\, \mathrm{d}^2x' \tag{4.2}$$

$$b_m(R) = \int_{R'\leq R} \Sigma(\mathbf{x}')(R')^m \sin(m\phi')\, \mathrm{d}^2x' \tag{4.3}$$

where $\mathbf{x}' = (R', \phi')$ are the coordinates, G is the gravitational constant and Σ represents the surface mass density (Buote & Tsai 1995). The powers are defined by the integral of the magnitude of ψ_m, the mth term in the multipole expansion of the potential, and evaluated in a circular aperture with radius R

$$P_m(R) = \frac{1}{2\pi}\int_0^{2\pi} \psi_m(R,\phi)\, \psi_m(R,\phi)\, \mathrm{d}\phi. \tag{4.4}$$

Ignoring factors of 2G, this relates to the following relations which are used to calculate the powers, where a_m and b_m are taken from Eqs. 4.2 and 4.3

$$P_0 = [a_0 \ln(R)]^2 \tag{4.5}$$

and

$$P_m = \frac{1}{2m^2R^{2m}}\,(a_m^2 + b_m^2). \tag{4.6}$$

In X-rays the surface brightness is used instead of the projected surface mass density, assuming that the X-ray surface brightness distribution traces the gravitational potential (Buote & Tsai 1995). In order to obtain powers which are independent of the X-ray luminosity, they are normalized by the zeroth-order moment and thus called power ratios. This allows a direct comparison of clusters with different X-ray brightness. $P0$, the monopole, gives the flux. $P1$ and $P2$ represent dipole and quadrupole, $P3$ and $P4$ can be associated with hexapole and octopole moments. Higher order moments become more sensitive to disturbances on smaller scales which do not significantly contribute to the characterization of the global dynamical state of a cluster. The power ratios $P2/P0$ and $P4/P0$ are strongly correlated, however $P4$ is more sensitive to smaller scales than $P2$. While relaxed but elliptical clusters rather yield low $P2/P0$ and merging systems show higher $P2/P0$, this power ratio is not a clear indicator of the dynamical state because it is sensitive to both ellipticity or bimodality. Odd moments are sensitive to unequal-sized bimodal structures and asymmetries, while they vanish for relaxed, single-component clusters. $P3/P0$ is thus the smallest moment which unambiguously indicates substructure in the ICM and provides a clear measure for the dynamical state of a cluster (e.g. Buote & Tsai 1995; Jeltema et al. 2005, B10). It is therefore the primary substructure measure in our analysis.

Center shifts

The center shift parameter w measures the centroid variations in different aperture sizes. The centroid is defined as the "center of mass" of the X-ray surface brightness and obtained for each aperture size separately. The X-ray peak is determined from an image smoothed with a Gaussian with σ of 8 arcsec. We calculate the offset of the X-ray peak from the centroid for 10 aperture sizes ($0.1 - 1\ r_{500}$) and obtain the final parameter w as the standard deviation of the different center shifts in units of r_{500} (e.g. Mohr et al. 1993; O'Hara et al. 2006, B10):

$$w = \left[\frac{1}{N-1}\sum_i (\Delta_i - \langle\Delta\rangle)^2\right]^{1/2} \times \frac{1}{r_{500}}, \tag{4.7}$$

where Δ_i is the offset between the centroid and the X-ray peak in aperture i.

4.3 Sample of simulated clusters

We use a set of 121 simulated cluster X-ray images to test the power ratio and center shift method, their bias due to shot noise and their uncertainties. This set includes 117 simulations from Borgani et al. (2004) and 4 from Dolag et al. (2009) to populate the desired mass range. All clusters were simulated using the TreePM/SPH code GADGET-2 (Springel 2005). The clusters were extracted from the simulation at $z = 0$ and the X-ray images were created by Ameglio et al. (2007, 2009). The simulated cluster images do not include any observational artifacts (noise, bad pixels etc.) or background and were already used by B10. Due to the so-called overcooling problem in galaxy cluster simulations (e.g. Borgani & Kravtsov 2011), the images may contain clumps of cold gas, which appear as point-like sources. Ameglio et al. (2007) detected and removed these gas clumps. All remaining structures are therefore infalling groups or clusters. Keeping cold gas clumps in the simulated X-ray images may lead to a larger fraction of disturbed clusters and a different distribution of substructure parameters than is observed (Nagai et al. 2007; Piffaretti & Valdarnini 2008, B10 – Sect. 5.2.). The distribution of the parameters, however, is only critical for a direct comparison of simulations and observations, which is not the scope of this paper.

Although the clusters are drawn from two sets of simulations they cover the full range of morphologies of clusters in the Universe and include a wide mass range ($0.8 \times 10^{14} - 2.2 \times 10^{15} h^{-1}\ M_\odot$). This sample is used exclusively to test the bias correction method and to calibrate the structure boundaries, thus to relate the visual impression of the image to a $P3/P0$ and w range. For these purposes it is not crucial to use a representative sample of the full mass range, especially since the simulated cluster morphology distribution is only weakly mass dependent. We only required the sample to cover the full range of morphological parameters and do not take into account any global cluster properties.

A comparison between the substructure parameters w and $P3/P0$ of the sample of 80 observed clusters and the simulations without noise is given in Fig. 4.1. This figure also gives a first impression of the parameter range clusters occupy in this diagram – namely $10^{-10} < P3/P0 < 10^{-4}$ and $10^{-4} < w < 1$. Clusters sometimes yield negative $P3/P0$ values after the bias correction ($P3/P0_c$, see Sect. 4.4.3) with an uncertainty indicating that the result is consistent with zero. Such clusters are not displayed in the figures.

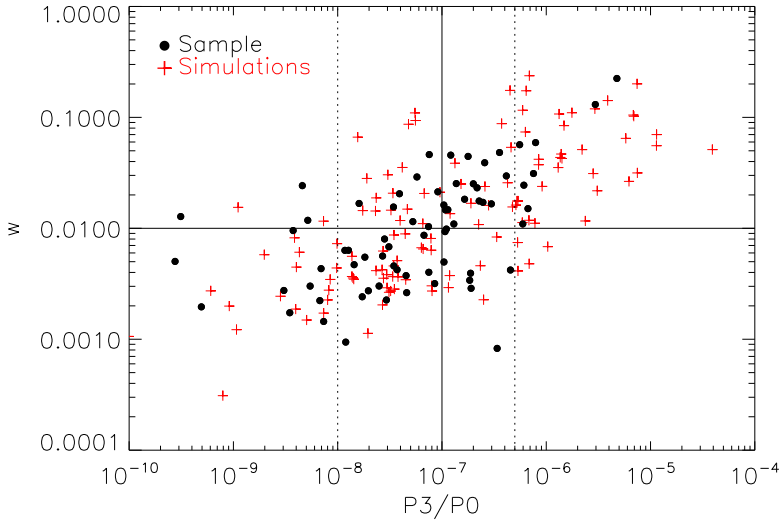

Figure 4.1: Comparison of the sample of 80 clusters observed with *XMM-Newton* (black circles) and 121 simulated X-ray cluster images (red crosses) in the $P3/P0 - w$ plane. The solid and dotted lines show the different morphological ranges as discussed below in Sect. 4.5.

4.4 Study of the systematics of substructure measures

Observations, in particular those with low photon statistics, suffer from shot noise which will produce artificial structure and lead to inaccurate results in the substructure analysis. It is therefore important to characterize this bias (difference between real and spuriously detected amount of structure). Power ratios are applied to clusters since 1995 and several studies regarding the influence of photon noise on the measured power ratios and center shifts were performed (e.g. Jeltema et al. 2005; Hart 2008, B10). In this paper we extend the work of B10 who introduced two methods (azimuthal redistribution and repoissonization) to estimate the bias and the uncertainties. However it was left open which approach yields better results in which signal-to-noise range. Using the repoissonization algorithm of B10, we make a comprehensive investigation of the performance of the bias and uncertainty estimates for a wide range of observational parameters and derive recipes on how to best correct the bias.

4.4.1 Study of shot noise bias and uncertainties

Let's consider an idealized, radially symmetric cluster. Such an object should yield substructure parameters (power ratios and w) equal to zero. Once noise is added, the parameters of the same cluster increase significantly. We therefore denote the difference between the power ratio signal of the ideal image of a cluster ($P_{\rm ideal}$) and the signal of the same cluster with noise as true bias. For the simulations and if not stated otherwise, we give the bias as the true bias in % of the ideal value:

$$\frac{P - P_{\rm ideal}}{P_{\rm ideal}} \times 100 = B_{\rm P}. \tag{4.8}$$

For center shifts, the bias (B_w) is defined analogously. In this and all following sections, we focus our analysis on the power ratio $P3/P0$, which is more sensitive to shot noise than the center shift parameter w.

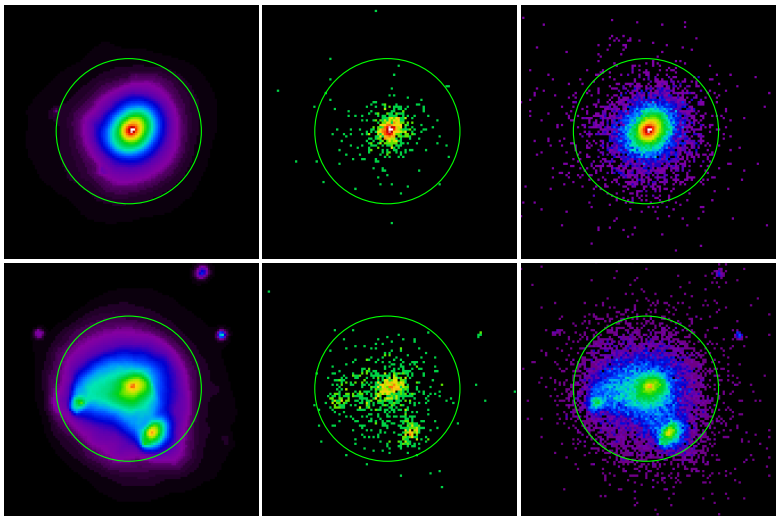

Figure 4.2: Example of a relaxed (upper panels) and a disturbed (lower panels) simulated cluster X-ray image including no noise (left) and poissonized images with 1 000 (middle) and 30 000 counts (right) within r_{500} (indicated by circle).

Shot noise makes very symmetric clusters appear more structured (positive bias). On the other hand, it can smooth out structure and a very structured cluster may actually seem more relaxed (negative bias). How the amount of shot noise and thus the reliability of the identification of substructure depend on the photon statistics of an observation and the measured substructure value is investigated using our set of 121 simulated clusters with different morphologies. To perform a realistic study, we create four images with different total count numbers (1 000, 2 000, 30 000 and 170 000 counts within r_{500}) for each simulated cluster. These four different count levels were chosen to sample a range of *XMM-Newton* cluster observations, e.g. 1 000 – 2 000 counts are typical for high-redshift systems, while the values for the REXCESS sample for example range between 30 000 and 170 000 counts.

First, we take the simulated cluster image and normalize the surface brightness in such a way that the counts equal the chosen total count number. At this point, the pixel content is still a real number. In a second step, we poissonize the ideal cluster image (introducing shot noise) using the *zhtools*[1] task *poisson*. We call such images poissonized images or realizations, with integers as pixel content.

As is apparent from the visual inspection of two simulated clusters in Fig. 4.2, the effect of photon noise is severe at low counts (middle), but also high-count images (right) are affected. It is therefore important to estimate and correct the bias as accurately as possible. The influence of shot noise and the uncertainties can be explained using Fig. 4.3, which provides a summary of our study. In the 4 subpanels we show the behavior of $P3/P0$ for different total count numbers (top left: 1 000, top right: 2 000, bottom left: 30 000 and bottom right: 170 000 counts) and several dynamical states (5 simulated cluster observations). The solid line indicates $P3/P0_{\mathrm{ideal}}$, the power ratio of the ideal image without shot noise. The mean $P3/P0$ of 1 000 poissonizations of the ideal cluster image is shown by the dotted line. In addition this

[1] hea-www.harvard.edu/RD/zhtools

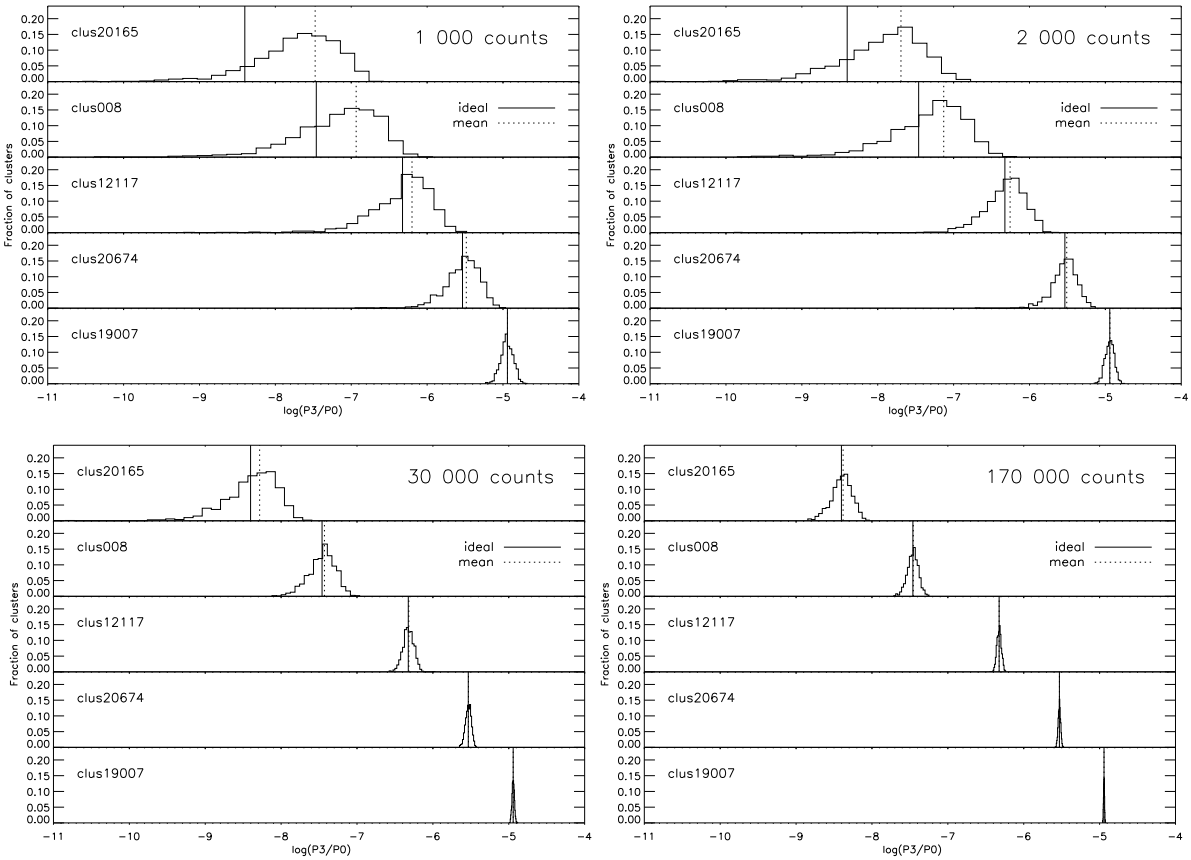

Figure 4.3: $P3/P0$ distribution (reflecting the bias) for different structured clusters and counts. The solid line marks the ideal $P3/P0$ value, the dotted line indicates the mean of 1 000 realizations with noise. Details are given in Table 4.1. A comparison between this figure and Table 4.1 shows that 100 realizations are sufficient to estimate the bias.

figure shows the uncertainty (σ) of the mean $P3/P0$ as the width of the $P3/P0$ distribution.

We find that the bias introduced to the $P3/P0$ results behaves differently for different morphologies (subpanels in all 4 figure panels). The upper panel shows the case of clus20165 – a cluster with little intrinsic structure. Photon noise boosts the power ratio signal and the whole $P3/P0$ distribution is shifted to higher substructure values. This is reflected by the obtained mean signal (dotted line), which is significantly larger than the real signal (solid line). This effect is strong, especially below 30 000 counts. In addition, the uncertainty (width of the distribution) is large. Going step by step to more disturbed clusters (from top to bottom panel) shows the dependence of the bias on the degree of disturbance and the total count number. While clus008 still shows a large bias up to 2 000 counts, it is already very small for 30 000 counts. More disturbed clusters therefore are not as affected by photon noise as relaxed objects. This is apparent when looking at the $P3/P0$ distribution in the bottom panels (clus20674 and clus19007). Even at 1 000 counts the bias is very small and the $P3/P0$ distribution narrow, which reflects a mean $P3/P0$ signal with a relatively small bias and uncertainty. The statistical summary of these results is given in Table 4.1, where we list the ideal and mean

Table 4.1: Statistical results on $P3/P0$ and w for poissonized simulated cluster images. **Notes.** We give the ideal substructure values and the mean for 100 realizations including their 1-σ uncertainties in real (top) and log space (bottom). The bias (B_{P3} and B_w) is listed in % of the ideal value, as defined in Eq. 4.8. The results are given for 4 different total count numbers. This table corresponds to Fig. 4.3, but with less realizations.

$P3/P0$	$P3/P0_{\rm ideal}$	1 000 cts mean $P3/P0$	B_{P3}	2 000 cts mean $P3/P0$	B_{P3}	30 000 cts mean $P3/P0$	B_{P3}	170 000 cts mean $P3/P0$	B_{P3}
clus20165	4.0×10^{-9}	$3.7\times10^{-8}\pm3.5\times10^{-8}$	839	$1.9\times10^{-8}\pm2.0\times10^{-8}$	376	$4.9\times10^{-9}\pm3.1\times10^{-9}$	24	$4.1\times10^{-9}\pm1.4\times10^{-9}$	3
clus008	3.5×10^{-8}	$8.7\times10^{-8}\pm8.4\times10^{-8}$	152	$7.2\times10^{-8}\pm6.7\times10^{-8}$	109	$3.6\times10^{-8}\pm1.3\times10^{-8}$	5	$3.4\times10^{-8}\pm5.7\times10^{-9}$	-1
clus12117	4.7×10^{-7}	$6.1\times10^{-7}\pm5.0\times10^{-7}$	28	$5.4\times10^{-7}\pm2.7\times10^{-7}$	14	$4.8\times10^{-7}\pm7.9\times10^{-8}$	2	$4.7\times10^{-7}\pm3.1\times10^{-8}$	-0.3
clus20674	3.0×10^{-6}	$3.2\times10^{-6}\pm1.4\times10^{-6}$	8	$3.2\times10^{-6}\pm1.1\times10^{-6}$	9	$2.9\times10^{-6}\pm2.6\times10^{-7}$	-0.4	$3.0\times10^{-6}\pm1.0\times10^{-7}$	-0.1
clus19007	1.1×10^{-5}	$1.1\times10^{-5}\pm1.9\times10^{-6}$	-4	$1.1\times10^{-5}\pm1.5\times10^{-6}$	0.1	$1.1\times10^{-5}\pm3.9\times10^{-7}$	0.4	$1.1\times10^{-5}\pm1.6\times10^{-7}$	0.05
w	$w_{\rm ideal}$	1 000 cts mean w	B_w	2 000 cts mean w	B_w	30 000 cts mean w	B_w	170 000 cts mean w	B_w
clus20165	0.0019	0.0029 ± 0.0012	55	0.0025 ± 0.0010	35	0.0020 ± 0.0003	6.2	0.0019 ± 0.0001	-0.13
clus008	0.0087	0.0090 ± 0.0030	4	0.0094 ± 0.0024	8	0.0088 ± 0.0007	1.4	0.0087 ± 0.0003	0.3
clus12117	0.0156	0.0163 ± 0.0036	5	0.0153 ± 0.0025	-2	0.0157 ± 0.0008	0.6	0.0156 ± 0.0003	0.3
clus19007	0.0700	0.0662 ± 0.0061	-5	0.0679 ± 0.0046	-3	0.0662 ± 0.0061	0.1	0.0700 ± 0.0004	-0.01
clus20674	0.1193	0.1194 ± 0.0099	0.03	0.1193 ± 0.0076	-0.05	0.1193 ± 0.0018	-0.07	0.1193 ± 0.0008	0.005
$P3/P0$	$\log(P3/P0_{\rm ideal})$	1 000 cts log(mean $P3/P0$)	B_{P3}	2 000 cts log(mean $P3/P0$)	B_{P3}	30 000 cts log(mean $P3/P0$)	B_{P3}	170 000 cts log(mean $P3/P0$)	B_{P3}
clus20165	-8.40	-7.66 ± 6.9	839	-7.99 ± 8.5	376	-8.42 ± 5.3	24	-8.41 ± 2.8	3
clus008	-7.46	-7.26 ± 6.8	152	-7.32 ± 6.6	109	-7.47 ± 2.7	5	-7.47 ± 1.2	-1
clus12117	-6.32	-6.38 ± 5.2	28	-6.34 ± 3.1	14	-6.32 ± 1.0	2	-6.33 ± 0.4	-0.3
clus20674	-5.53	-5.54 ± 2.5	8	-5.52 ± 1.9	9	-5.54 ± 0.5	-0.4	-5.53 ± 0.2	-0.1
clus19007	-4.94	-4.97 ± 0.9	-4	-4.95 ± 0.6	0.	-4.94 ± 0.17	0.4	-4.94 ± 0.1	0.05
w	$\log(w_{\rm ideal})$	1 000 cts log(mean w)	B_w	2 000 cts log(mean w)	B_w	30 000 cts log(mean w)	B_w	170 000 cts log(mean w)	B_w
clus20165	-2.721	-2.539 ± 1.012	55	-2.598 ± 1.081	35	-2.702 ± 0.463	6.2	-2.729 ± 0.211	-0.13
clus008	-2.061	-2.045 ± 0.681	4	-2.028 ± 0.520	8	-2.054 ± 0.162	1.4	-2.059 ± 0.067	0.3
clus12117	-1.807	-1.787 ± 0.391	5	-1.815 ± 0.297	-2	-1.805 ± 0.090	0.6	-1.806 ± 0.038	0.3
clus19007	-1.155	-1.179 ± 0.108	-5	-1.168 ± 0.079	-3	-1.179 ± 0.108	0.1	-1.155 ± 0.006	-0.01
clus20674	-0.923	-0.923 ± 0.076	0.03	-0.923 ± 0.059	-0.05	-0.924 ± 0.014	-0.07	-0.923 ± 0.006	0.005

structure parameter of poissonized images along with the bias in percent and the uncertainties in real (top) and log space (bottom). For all values in the table we have repeated the poissonization process using just 100 instead of 1 000 realizations and found this lower number to be sufficient to obtain accurate statistical results. We thus work in the following studies with 100 poissonizations per case. In addition, we studied the influence of Poisson noise on the individual powers – $P0$ and $P3$. The flux $P0$ is only marginally sensitive to Poisson noise and does not contribute to the bias of $P3/P0$. The bias of $P3/P0$ thus reflects the influence of Poisson noise on $P3$.

The dependence on the counts is due to the increasing effect of photon noise when dealing with low photon statistics. For relaxed clusters this leads to a very large bias and uncertainties, especially for low counts. In the case of very structured clusters with e.g. two components, the bias is negligible and the uncertainties small. For clusters with only a moderate amount of structure, we find a clear dependence on the counts. Therefore, one should be careful when applying this method to low-count observations (significantly less than 30 000 counts).

For the center shift parameter w the behavior is similar, but less pronounced. B_w is more robust and in general significantly smaller than B_{P3}. In addition, the distributions are narrower, which shows that w is less sensitive to photon noise than $P3/P0$. This allows an accurate calculation of the center shift parameter down to ∼200 counts. An overview of the absolute value of the bias as a function of counts (different colored lines) and the ideal value is given in Fig. 4.4, left. We combined the bias of the substructure parameters (B_{P3} thick black solid and red dotted line, B_w different thin lines) as a function of $P3/P0_{\rm ideal}$ (lower $x-$axis) and $w_{\rm ideal}$ (upper $x-$axis) for a direct comparison. However, while the simulated clusters occupy the full $P3/P0$ range, they only have w parameters between 3.1×10^{-4} and 2.4×10^{-1}. This and all other fits which will be displayed later are obtained using the orthogonal BCES linear regression method (Akritas & Bershady 1996).

The dependence of the bias on photon statistics and the substructure measurement encourages a bias correction as a function of these parameters. However, the bias depends also on the morphology of the cluster itself. We thus performed the following test: if we consider two clusters with the same $P3/P0$ or center shift value, they have nominally the same amount of structure. If this cluster pair also has the same amount of counts, only the intrinsic shape of the cluster remains variable. We chose six pairs of clusters with the same $w_{\rm ideal}$ and $P3/P0_{\rm ideal}$ value and four different counts: 1 000, 2 000, 30 000 and 170 000 counts. For a dependence of the bias on the amount of structure and counts only, one would expect very similar distributions and mean values. However, this is not the case. Especially for the unstructured cluster pair and low counts the offset and the behavior of B_{P3} is significant. For high counts or structured clusters, this offset decreases. We thus cannot give a general correction factor as a function of counts and $P3/P0$ or w but have to treat the estimate of the bias correction for each cluster individually.

4.4.2 Significance threshold

As we have shown, shot noise can introduce spurious structure. While our bias correction alleviates this to some extent it is useful to relate the measured (and corrected) signal to its error. To do so, we define a significance S as

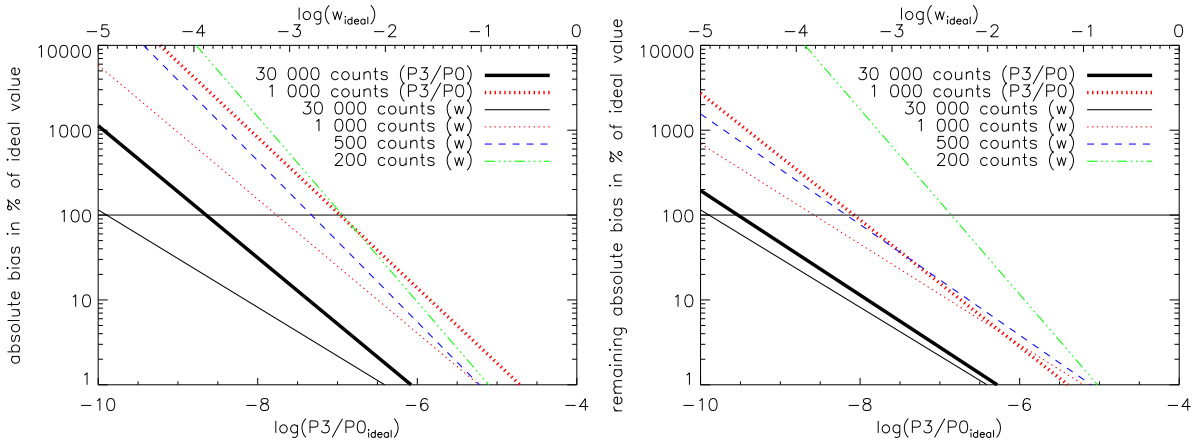

Figure 4.4: Dependence of the bias as a function of $P3/P0_{\rm ideal}$ (lower axis) and $w_{\rm ideal}$ (upper axis). **Left:** Absolute value of the bias before correcting. **Right:** Absolute value of the remaining bias after applying the bias correction $B^*_{\rm P3}$ and B^*_w. The different counts are color-coded: 30 000 black, 1 000 red, 500 blue, 200 green. $B_{\rm P3}$ is shown using thick lines, B_w is represented by different thin lines. The dependencies are fits to all 121 simulated cluster images using the BCES linear regression method (Akritas & Bershady 1996).

$$S = \frac{\textit{bias corrected signal}}{\textit{error}}, \tag{4.9}$$

and call values with $S \geq 3$ significant signals. This value however strongly depends on the photon statistics.

We studied the significance S as a function of the bias corrected substructure parameters for different total count numbers and show some results in Fig. 4.5. The bias correction was done using the method described in Sect. 4.4.3. Different total count numbers are color-coded and displayed using different linestyles (left: 1 000 red dotted and 30 000 black solid line; right: 200 green dot-dashed and 500 blue dashed line) for $P3/P0$ (left) and w (right). The lines represent a BCES fit to all 121 simulated clusters. The significance thresholds ($S = 3$) for both structure parameters and several total count numbers are given in Table 4.2 and displayed as horizontal lines in Fig. 4.5.

We will take a closer look at $P3/P0$ first. For a typical observation of 30 000 counts we are able to detect intrinsic structures corresponding to $P3/P0 = 6 \times 10^{-8}$ at $S = 3$ confidence level ($P3/P0 \ll 10^{-8}$ at $S = 1$ level). This shows that the errors are small enough to ensure significant results even for clusters with little intrinsic structure. In the case of a low-count observation with only 1 000 counts, the $S = 3$ confidence level is located around 3.4×10^{-6}, which means that we can only obtain significant results for very structured clusters. In such cases, we use a less conservative and lower value like $S = 1$. However, when dealing with such low-count observations special care has to be taken. The well-defined behavior of the center shift parameter is confirmed by the significance of the measurements. We find the $S = 3$ values to be in the lower center shift range and can thus obtain significant results even for relaxed clusters. This result holds well below 1 000 counts. For 200 and 500 counts we find $S = 3$ to coincide with the median of the sample. A discussion of the implications of

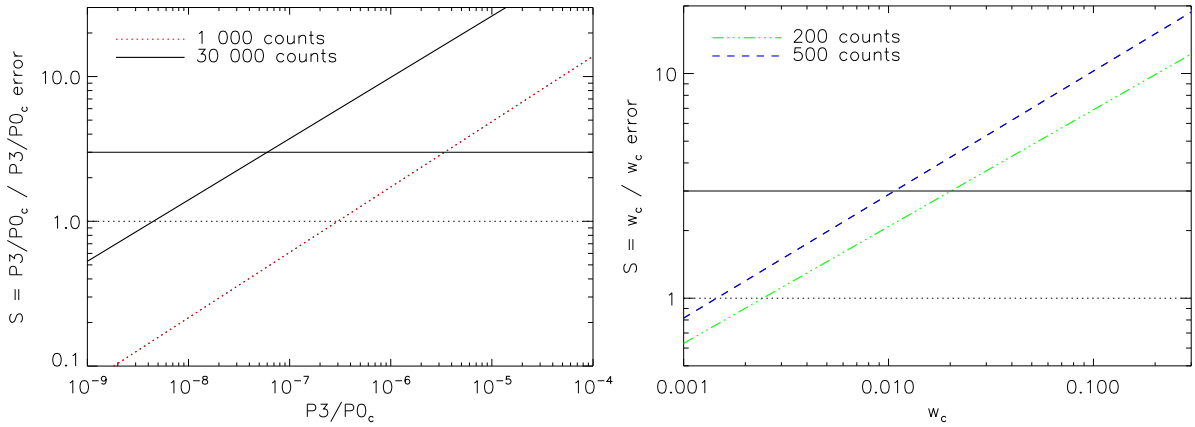

Figure 4.5: Significance S of the $P3/P0$ (left) and w (right) measurements for different counts. **Left:** 1 000 red dotted line and 30 000 black solid line. **Right:** 200 green dot-dashed, 500 blue dashed line. The different thresholds are marked ($S = 3$: solid line, $S = 1$ dotted line).

these results for a morphological analysis will be provided in a later section.

4.4.3 Bias correction method

After characterizing the bias and its dependence on the photon statistics, we propose a statistical method to estimate and correct for the true bias $B_{\rm P3}$ and B_w (for $P3/P0$ and w). In Sect. 4.4.1 we defined the true bias as the difference between the true signal $P3/P0_{\rm ideal}$ or $w_{\rm ideal}$ and $P3/P0_{\rm raw}$ or $w_{\rm raw}$, the signal obtained after the first poissonization or the signal of the observation. Simulated images do not contain noise and give the true structure parameters. Observations however are poissonized, where this first poissonization is due to photon shot noise. They allow us to measure only $P3/P0_{\rm raw}$ or $w_{\rm raw}$ but not the true signal $P3/P0_{\rm ideal}$ and $w_{\rm ideal}$. We therefore cannot obtain the true bias directly but need to estimate it.

We assume that a second poissonization step returns roughly the same bias and error as the first poissonization. Analogously to the true bias we therefore define the "estimated bias" as the difference between the signal after the first ($P3/P0_{\rm raw}$ or $w_{\rm raw}$) and second poissonization ($P3/P0_{\rm realization}$ or $w_{\rm realization}$). For simulated images, we mimicked the effect of the first poissonization by adding artificial Poisson noise creating observation-like images. The second poissonization is performed on the observation/observation-like image to create a repoissonized image (realization of the observation). Using the mean $P3/P0$ or w value of 100 realizations of the observation in combination with $P3/P0_{\rm raw}$ or $w_{\rm raw}$ to calculate the estimated bias $B^*_{\rm P3}$ or B^*_w yields a good approximation for the true bias. Subtracting $B^*_{\rm P3}$ or B^*_w from the substructure parameters of the cluster image returns the corrected substructure parameters $P3/P0_{\rm c}$ and $w_{\rm c}$. The remaining bias after this correction approaches zero for high-quality observations and is defined as $B_{\rm P3,c}$ and $B_{w,\rm c}$, respectively.

Considering this, we present a refined version of the B10 method including the following steps:

1. Calculate the substructure parameters ($P3/P0$ and w) of the cluster image: $P3/P0_{\rm raw}$ and $w_{\rm raw}$.

Table 4.2: Dependence of the significance of the signal (S = signal/error) on total number counts (net counts within r_{500}) for $P3/P0_c$ and w_c. **Notes.** We call values with $S > 3$ significant signals, however for low-count observations a less conservative value like $S = 1$ has to be used.

$P3/P0_c$	Total count number	$S = 1$	$S = 3$
	1 000	3.0×10^{-7}	3.4×10^{-6}
	2 000	1.4×10^{-7}	1.6×10^{-6}
	30 000	4.5×10^{-9}	6.0×10^{-8}
w_c	Total count number	$S = 1$	$S = 3$
	200	2.4×10^{-3}	2.0×10^{-2}
	500	1.4×10^{-3}	1.0×10^{-2}
	1 000	9.0×10^{-4}	6.0×10^{-4}
	30 000	1.6×10^{-4}	8.0×10^{-4}

2. Create 100 poissonized realizations of the cluster image.
3. Calculate the substructure parameters ($P3/P0$ and w) of all 100 realizations and their mean: $\langle P3/P0_{\text{realizations}} \rangle$ and $\langle w_{\text{realizations}} \rangle$.
4. Obtain the estimated bias B^*_{P3} and B^*_w as the difference of the mean parameters of these 100 realizations and $P3/P0_{\text{raw}}$ and w_{raw}:
   $B^*_{\text{P3}} = \langle P3/P0_{\text{realizations}} \rangle - P3/P0_{\text{raw}}$ and
   $B^*_w = \langle w_{\text{realizations}} \rangle - w_{\text{raw}}$
5. Subtracting the estimated bias from the substructure parameters of the cluster image yields the corrected parameters:
   $P3/P0_c = P3/P0_{\text{raw}} - B^*_{\text{P3}}$ and
   $w_c = w_{\text{raw}} - B^*_w$
6. Obtain the uncertainty as the standard deviation σ of the structure parameters of the 100 realizations of the cluster image.

In case of a real observation, also the background needs to be considered (see Sect. 4.4.5). After testing several methods, the generally best performing method for power ratios is to subtract the moments a_m and b_m (where $m = 1, 2, 3, 4$; see Eqs. 2 and 3) of the background image from the measured moments of the cluster image and its realizations before calculating the powers (Jeltema et al. 2005). Since w is not additive as a_m and b_m, we have taken a different approach in the case of the center shift method and subtract the background prior to the calculation of w_{raw} and $w_{\text{realizations}}$. This rather simple method works very well in a statistical way, as is shown below.

In some cases, we do not gain any information about the cluster because the estimated bias is larger than the true bias. We then obtain a negative $P3/P0_c$ with a large uncertainty which indicates that the signal is consistent with zero. For a few % of realizations we found that the repoissonization leads to a change of the brightest pixel and thus the zero-point of the center

shift calculation. This can change the values significantly, however does not influence the mean w value of all 100 realizations. Also the centroid, which is calculated using the surface brightness distribution, can change for different realizations, especially when dealing with low photon statistics. This shift is included in the error estimation when recalculating the centroid for each realization. In our analysis however we found that the remaining bias of the corrected $P3/P0$ values ($B_{\mathrm{P3,c}}$) vary only slightly. The mean change in the absolute $P3/P0$ value for 1 000 counts is a factor of 2, however in 19 cases the increase is larger (max. 17). All clusters with such a considerable change in the centroid are very obvious merging systems with two distinct surface brightness peaks. The error increases especially for large $P3/P0$ values, but still remains small compared to the $P3/P0$ value itself.

4.4.4 Testing of the method

We tested and refined this method using simulated images as described in Sect. 4.3. As with the characterization of the bias, we used different counts to simulate different depths of observations. We poissonized each simulated image 100 times and treated each of those 100 images as an "observation" which are subject to a second poissonization step. After the bias correction of all 100 "observations" using the estimated bias from the second poissonization, we obtain a mean value of the corrected parameter to show the statistical strength of this method.

The results of the bias correction method are shown in Fig. 4.4 for $P3/P0$ and w. The figure on the left shows the absolute value of the bias before noise correction (discussed in Sect. 4.4.1), while the right side displays the remaining bias after applying the correction method. In both panels, we simultaneously show the absolute value of the bias as defined in Sect. 4.4.1 for $P3/P0$ (thick lines and lower $x-$axis) and w (thin lines and upper $x-$axis) for different counts. The decrease of $B_{\mathrm{P3,c}}$ is apparent for cases with 1 000 counts, where the correction method is successful down to the detection limit ($S = 1$ at 3×10^{-7}). In the insignificant range ($S < 3$) $B_{\mathrm{P3,c}}$ lies below 10% after noise-correction. The solid black line shows the case for high-count observations, where a drop below 10% can be seen around the $S = 3$ cut at 6×10^{-8}.

The center shift parameter is more robust, even at 200 counts, where $B_{w,\mathrm{c}} \sim 10\%$ for $S = 3$. Center shifts are less sensitive to shot noise and their bias is smaller. This is especially interesting when looking at relaxed clusters ($w < 0.01$), where $B_{w,\mathrm{c}}$ is significantly smaller than $B_{\mathrm{P3,c}}$. Motivated by these results at low counts, we decided to test even lower photon statistics – 500 and 200 counts. With such observations the power ratios are not reliable anymore, but the center shifts show remarkably good results.

In some of the 100 realizations of the poissonized images we find that a negative bias correction is needed, where the structure in the poissonized images has a too small value. However, the mean of the bias correction of all poissonizations is always positive, except for a few cases with very high structure parameters. For these clusters the bias correction is only around 1% as is shown in Fig. 4.6, where we plot the applied bias correction B^{*}_{P3} (mean of 100 realizations) as a function of $P3/P0_{\mathrm{c}}$.

4.4.5 Effect of the X-ray background

The quality of X-ray observations suffers from several components – including photon noise which was discussed in Sect. 4.4.3 and the X-ray background, which was not taken into ac-

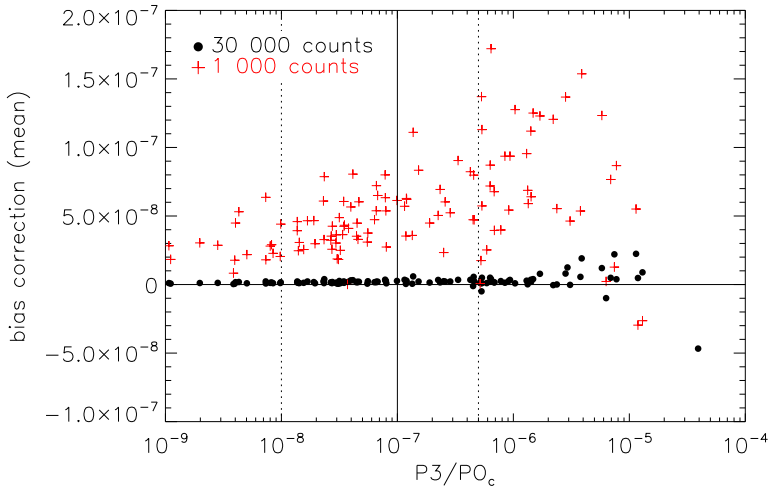

Figure 4.6: Illustration of the probability of a negative bias. We show the applied bias correction B^*_{P3} (mean of 100 realizations) as a function of $P3/P0_{\mathrm{c}}$. The colors indicate the different counts within r_{500}: 1 000 (red crosses) and 30 000 (black circles). A negative bias correction is only needed for very structured clusters and even then it is only of the order of 1%. The solid and dotted lines show the different morphological ranges as discussed below in Sect. 4.5.

count yet. We thus investigated how the background and different cluster-to-background count (S/B) ratios influence the measurements. Motivated by the work of Jeltema et al. (2005), in which the authors use an analytic approach to assess and correct for the background contribution for power ratios by subtracting moments due to noise, we inspected the behavior of power ratios and moments when adding or subtracting them. Power ratios are not additive, moments (a_0 to b_4) however are and thus can be used for background noise subtraction.

When correcting for the background two issues have to be addressed: the increase of total counts (normalization) and the noise component of the background image. Depending on S/B, the noise in the background image can influence the power ratio and center shift calculation. In order to account for the noise in both the cluster signal and in the background, we add a poissonized cluster and a poissonized flat background image to obtain an "observation". As during the bias study, we create 100 "observations" per simulated cluster image and show mean values. The correction of the bias is done using a two-step process. In step one, the background is treated by subtracting the moments (a_0 to b_4) of the background image from the moments of the observation before calculating the power ratios (in Sect. 4.4.3, Step 1). For a flat background image without noise, only a_0 should be non-zero. However, vignetting and other instrumental artifacts cause also higher moments to be non-zero. The background-subtracted moments should thus (statistically) only contain the cluster emission and the signal noise component. The background moments have to be subtracted also from the 100 realizations of the observation. As a second step, the power ratios and the bias are calculated using the background-subtracted moments. We therefore recommend the following power ratio treatment of the observation:

1. Calculate moments of the observation (incl. background) and of the background model/ image.
2. Create 100 poissonizations of the observation and obtain their moments.
3. Subtract the background moments from the moments of the observation and the 100 poissonizations.
4. Calculate power ratios of the observation and the 100 poissonizations
5. Correct the bias and obtain the σ as described in Sect. 4.4.3, Step 4-6.

In the next step, we studied the influence of the background noise component as a function of net/background counts using typical *XMM-Newton* values. We first discuss the power ratios and show the results for 30 000 net counts and a S/B (net/background counts within r_{500}) of 2:1 and 1:1. We chose these values to test the method simulating an observation with a large number of net counts but poor S/B ratios. Figure 4.7 (left) compares the background and bias corrected power ratio $P3/P0_{\rm c}$ with $P3/P0_{\rm ideal}$ for these cases and shows that we can very accurately determine $P3/P0$ well below 10^{-8} for an observation with 30 000 net counts and a $\mathrm{S/B} = 2$ (black circles). For a higher background (red crosses) the method still works well, however below 10^{-7} the scatter increases. Our sample of 80 observed low-z clusters includes only 6 clusters with a $\mathrm{S/B} < 2$ of which RXCJ0225.1-2928 shows the lowest with $\mathrm{S/B} = 1.2$. For observations with more than 30 000 net counts, we find a mean S/B of 6.7 and a median S/B of 5.6. In such cases, the background noise component is not significant.

This situation changes when analyzing high-z observations which typically have low-photon statistics ($< 1\,000$ net counts) and where the S/B can become < 1. We therefore show on the right side of Fig. 4.7 the results of the background and bias correction for 1 000 net counts and a S/B of 0.5 (blue asterisks), 1 (red crosses) and 2 (black circles). Although the relation shows more scatter than for the high-count case, the method works well down to 10^{-7} for $\mathrm{S/B} = 1$. For observations with higher background the scatter increases, however even under such conditions we can distinguish well between high power ratios values ($S > 1$) and values below 10^{-7}, with typically $S < 1$.

In the case of center shifts, the background noise influences mainly the position of the centroid. This effect is more pronounced for smaller center shifts and higher backgrounds. Analogous to the power ratios, we correct the bias using poissonizations of the observation (incl. background). However, we subtract the background counts for each pixel (instead of the moments) from the observation and its 100 poissonizations before calculating the X-ray peak and the centroid. The bias is then obtained as described in Sect. 4.4.3. We again tested the method for the above mentioned cases and found that the correction works very well down to 10^{-3} for the 30 000 net counts case, even for $\mathrm{S/B} = 1$. This behavior is due to the lower sensitivity to noise and shown in Fig. 4.8 on the left. In addition, it enables us to probe even lower photon statistics, going down to 200 net counts. Even in such an extreme case, the method works well down to about $w = 10^{-2}$. A plateau forms which characterizes the remaining noise level (Fig. 4.8, right). As expected, the plateau level moves to lower values for larger S/B, representing the decreasing influence of the background with larger S/B.

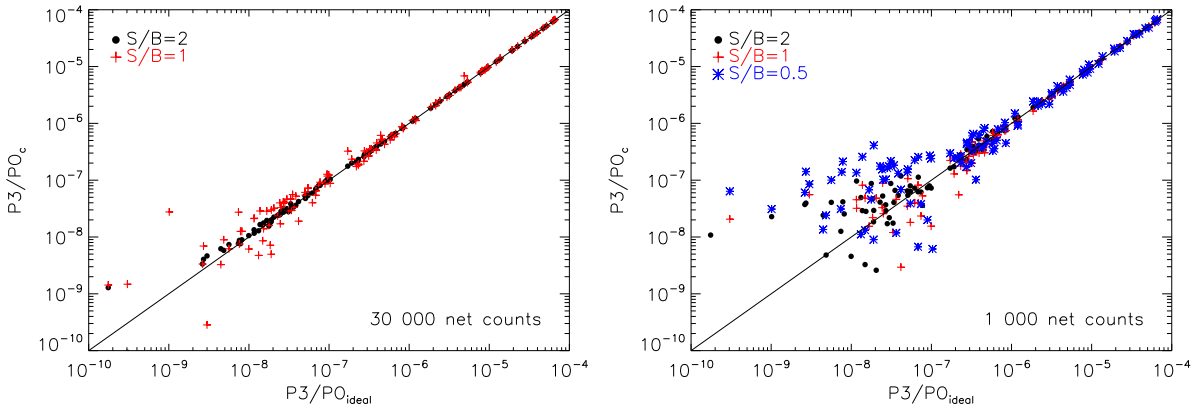

Figure 4.7: Background and bias corrected $P3/P0$ as a function of $P3/P0_{\rm ideal}$. **Left:** Testing the bias correcting method simulating an observation with 30 000 net counts but poor S/B ratios (S/B = 2 black circles, S/B = 1 red crosses). **Right:** Simulating a high-z observation with 1 000 net counts and S/B = 2 (black circles), 1 (red crosses), 0.5 (blue asterisks). The increasing influence of the background for decreasing net counts and S/B is shown.

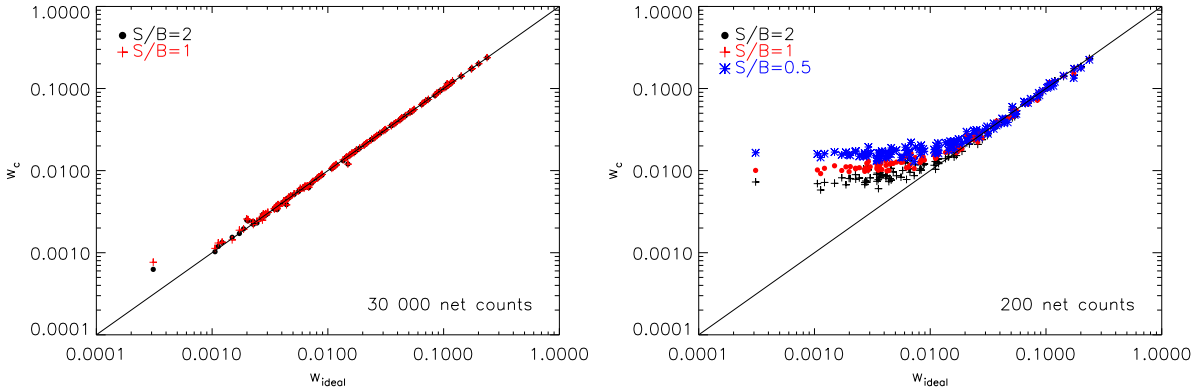

Figure 4.8: Background and noise corrected center shifts as a function of $w_{\rm ideal}$ for good photon statistics (left, same S/B ratio as in Fig. 4.7 on the left side) and low-count observations (right).

4.5 Morphology

After establishing in which parameter range we can obtain significant results, we want to discuss the strength of power ratios and center shifts in distinguishing different cluster morphologies. One aim of this analysis is to find a substructure value below which a cluster can be considered essentially relaxed. An overview of the results is given in Table 4.3.

We first consider $P3/P0$. As a result of the visual screening of the ideal simulated cluster images (no noise or background contribution), we classified all clusters as essentially relaxed (relaxed hereafter) or disturbed, depending on whether they show some signs of substructure (asymmetries, second component of comparable size, general disturbed appearance) within r_{500} or not. A few examples are given in Fig. 4.9, which also illustrates that this division is not always unambiguous, however the overall visual appearance within r_{500} (green circle) was more important than small-scale disturbances.

Table 4.3: Overview of the boundaries for $P3/P0$ and w including statistics when applying them to the simulated cluster sample.

	Boundary	Relaxed	Disturbed	
$P3/P0_{\mathrm{ideal}}$	simple	$< 10^{-7}$	$> 10^{-7}$	
1 000 counts		$< 3 \times 10^{-7}$	$> 3 \times 10^{-7}$	
Number of clusters		58 (48%)	63 (52%)	
Classified differently		10%	20%	
w_{ideal}	w	$< 10^{-2}$	$> 10^{-2}$	
Number of clusters		55 (45%)	66 (55%)	
Classified differently		7%	5%	
	Boundary	Relaxed	Mildly disturbed	Disturbed
$P3/P0_{\mathrm{ideal}}$	morphological	$< 10^{-8}$	$10^{-8} - 5 \times 10^{-7}$	$> 5 \times 10^{-7}$
Number of clusters		20 (17%)	62 (51%)	39 (32%)

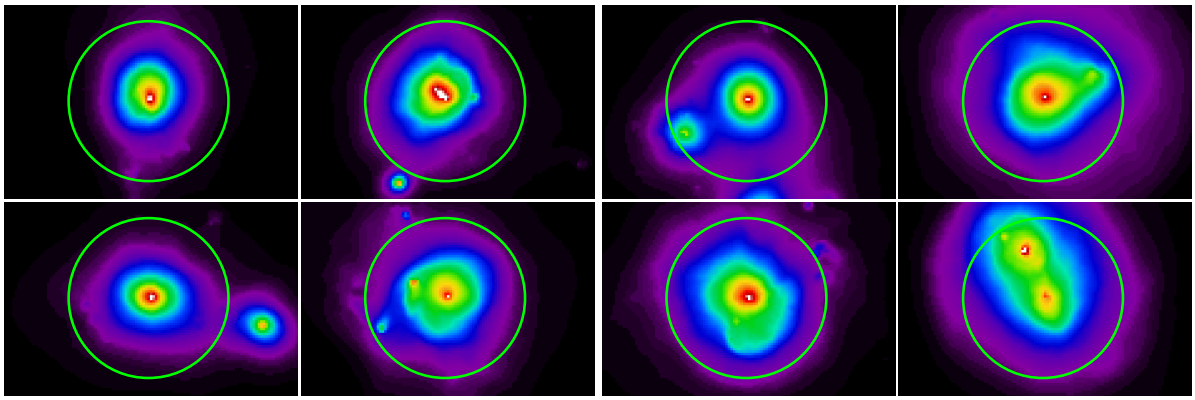

Figure 4.9: Example gallery of clusters visually classified as essentially relaxed (left four panels) and disturbed (right four panels). The classification is not unambiguous in all cases, however the overall visual appearance within r_{500} (green circle) was more important than small-scale disturbances.

Taking all this into account, we found $P3/P0$ ranges for relaxed and disturbed morphologies with a boundary value of about 10^{-7}, which we call *simple* $P3/P0$ *boundary*. The motivation for this condition is shown in Fig. 4.10, where we give the substructure parameters for all 121 simulated ideal cluster images including their visual classification as relaxed or disturbed. The horizontal line at $P3/P0 = 10^{-7}$ divides the sample into the two populations. Out of 121 we find 6/58 (~10%) relaxed and 13/63 (~20%) disturbed clusters to be differently classified. For two of these 6 relaxed clusters however a merging subcluster is just entering r_{500} and thus boosting the $P3/P0$ signal while the main cluster still seems relaxed. The remaining 4 show a slight elongation but no clear sign of structure or disturbance. For the 13 disturbed clusters we found that they have structure mostly in the inner region of the aperture

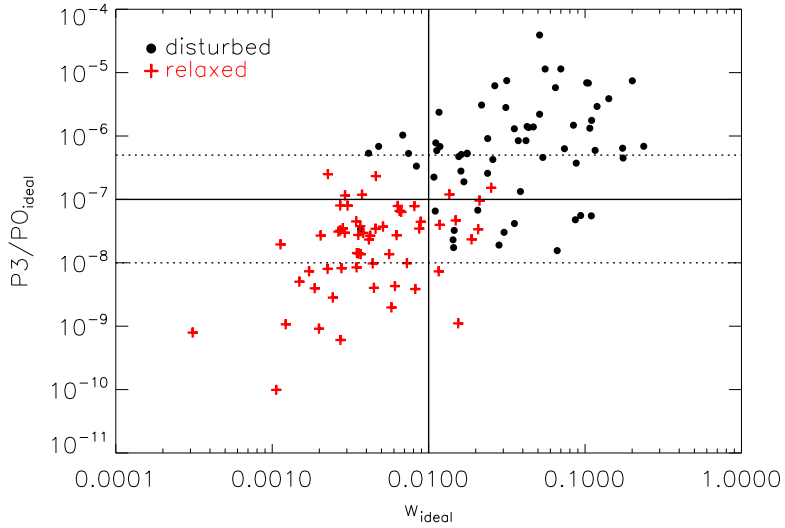

Figure 4.10: Motivation for the *simple* and *morphological boundaries* for $P3/P0$ and w. We show the $P3/P0 - w$ plane for ideal simulated cluster images. The classification into relaxed (red crosses) and disturbed (black circles) was done visually. The boundaries are displayed by horizontal and vertical lines and fit the data well.

radius which is not picked up by the power ratio method.

For high-quality observations a more detailed morphological analysis is possible because power ratios can be obtained more precisely. Taking a closer look again at Fig. 4.10, three distinct regions present themselves: $P3/P0 < 10^{-8}$, $10^{-8} < P3/P0 < 5 \times 10^{-7}$ and $P3/P0 > 5 \times 10^{-7}$. These three regions are occupied by only relaxed, a mix of relaxed and disturbed and only disturbed clusters and are indicated by the dotted lines in the figure. The borders between these regions at $P3/P0 = 10^{-8}$ and $P3/P0 = 5 \times 10^{-7}$ are named *morphological boundaries*. At the lower boundary of 10^{-8} we reach $S = 2$ for 30 000 counts images. With lower photon statistics such a classification is not possible. Making use of the *morphological boundaries*, we find 32% of our simulated clusters to be significantly disturbed, while only 17% show no signs of structure (see Table 4.3). The majority however (51%) is found somewhere in the middle and called mildly disturbed objects.

For the center shift parameter we define a boundary at $w = 0.01$. This value also agrees with our visual classification and analysis (see Fig. 4.12). Figure 4.11 shows $w_{\rm ideal}$ histograms for relaxed (filled black histogram) and disturbed (filled red histogram) clusters, including the distribution of all clusters (thick black line). This *w boundary* at $\log(w_{\rm ideal}) = -2$ is apparent and the misclassification lies below 10%. The *w boundary* is significant with $S > 2$ down to lowest counts (e.g. 200).

4.6 Cluster sample

Our sample comprises 80 galaxy clusters which are part of different larger samples observed with *XMM-Newton*. An overview of the samples from which the clusters were taken and their redshift are given in Table 4.6. For this study we use 31 targets from the Representative X-ray Cluster Substructure Survey (REXCESS, Böhringer et al. 2007), which was created as

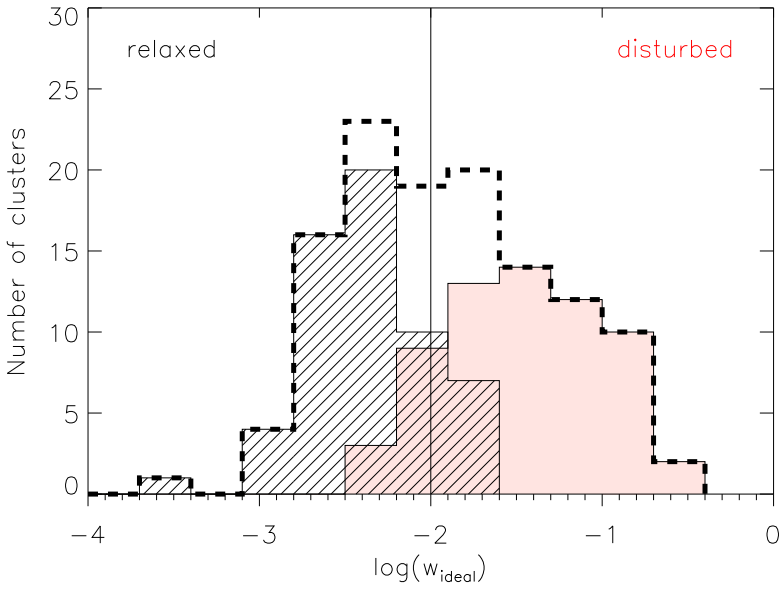

Figure 4.11: Center shift histogram of all simulated clusters (thick black dashed line) defining the *w boundary*. Relaxed clusters are represented by the filled black (left) and disturbed ones by the red filled histogram (right). The vertical line marks the *w boundary* at $\log(w_{\mathrm{ideal}})$=-2.

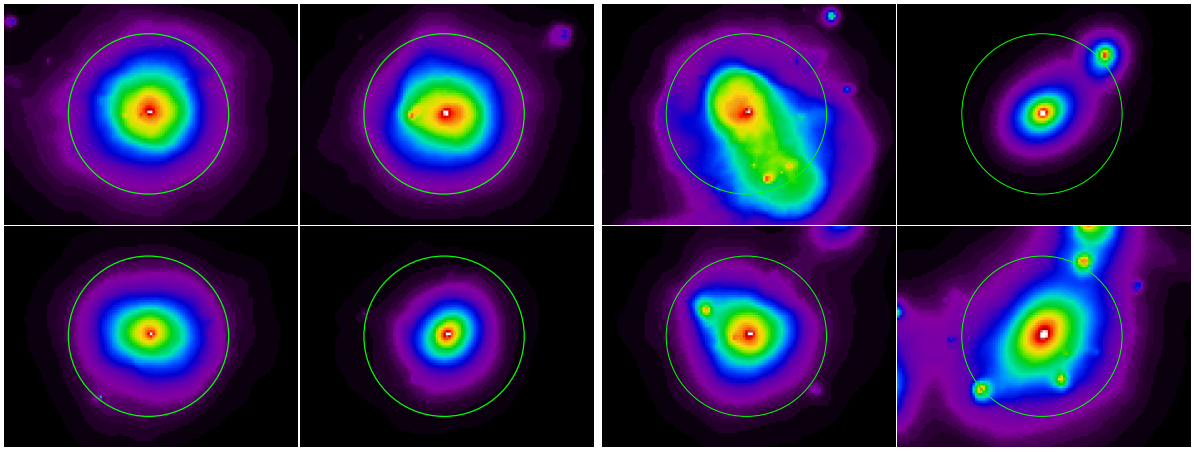

Figure 4.12: Example of cluster images classified using the *w boundary*. Left 4 panels: $w < 0.01$, right 4 panels: $w > 0.01$.

a morphologically and dynamically unbiased sample, selected mainly by X-ray luminosity and restricted to redshifts $z < 0.2$. Except for RXC J2157.4-0747 (OBSID: 0404910701) and RXC J2234.5-3744 (OBSID: 0404910801), where we were able to obtain longer exposures, we used the observation IDs as described in Böhringer et al. (2007, Table 5).

From the Local Cluster Substructure Survey (LoCuSS, Smith et al.), we use a small subsample of 30 clusters, which was published by Zhang et al. (2008). Except for A2204 (OBSID: 0306490401), we use the same observations as stated in Zhang et al. (2008, Table A.1.).

34 targets were taken from the Snowden Catalog (Snowden et al. 2008), while 10 clusters are part of the REFLEX-DXL sample (Zhang et al. 2006). In addition, we use 9 clusters discussed in Buote & Tsai (1996), from which only A1651 (properties taken from Arnaud et al. 2005) is not part of the Snowden sample. In total, 28 clusters are found in at least two samples. In such cases, the cluster properties are taken from the larger sample – as indicated in Table 4.6. The clusters were chosen to be well-studied, nearby ($0.05 < z < 0.45$) and publicly available (in 2009) in the *XMM*-Archive[2]. In addition, we required r_{500} to fit on the detector. Our full sample populates the whole observed substructure range, as is shown in Fig. 4.1. In addition, except for 13 cases, all clusters are high-quality observations with $> 30\,000$ net counts. Of those 13 observations, only RXCJ2308.3-0211 has less than 9 000 net counts (~ 2130 net counts with a S/B ~ 4.6). This merged sample has no unique selection function, but a wide spread in luminosity, temperature and mass. A large fraction of the clusters comes from representative samples like REXCESS and LoCuSS and we therefore expect the sample to have a very roughly representative character. In addition, the aim to test the presented structure estimators does not necessarily need a representative sample but a large number of clusters with different morphologies which is fulfilled with this sample.

4.7 Data analysis

4.7.1 *XMM-Newton* data reduction

The *XMM-Newton* observations were analyzed with the *XMM-Newton* SAS[3] v. 9.0.0. The data reduction is described in detail in B10 and Böhringer et al. (2007). We followed their recipe except for the point source removal and background subtraction. Our method of detecting point sources is consistent with B10 and Böhringer et al. (2007), where the SAS task *ewavelet* is run on the combined image from all 3 detectors in order to increase the sensitivity of the point source detection. However, we removed the point sources from each detector image in the 0.5 – 2 keV band individually and refilled the gaps using the CIAO[4] task *dmfilth*. In the next step we subtracted the background from the point source corrected images and combined them. This method yields point source corrected images without visible artifacts of the cutting regions.

4.7.2 Structure parameters

Power ratios and center shifts were calculated according to the repoissonization method described in Sect. 4.4.3, subtracting the background moments from the full (background in-

[2] `http://xmm.esac.esa.int/xsa/`

[3] Science Analysis Software: `http://xmm.esa.int/sas/`

[4] *Chandra* Interactive Analysis of Observations software package: `http://cxc.harvard.edu/ciao/`

Table 4.4: Sample statistics. **Notes.** Clusters defined as relaxed, disturbed and mildly disturbed objects using different boundary conditions and three different substructure estimators $P3/P0_{\rm c}$, $P3/P0_{\rm max}$ and $w_{\rm c}$.

Boundary	Relaxed	Disturbed	Mildly disturbed
Simple $P3/P0$	59%	41%	
w	53%	47%	
Morphological $P3/P0$	25%	10%	65%
Simple $P3/P0_{\rm max}$	33%	67%	
Morphological $P3/P0_{\rm max}$	5%	24%	71%

cluded) image to obtain power ratios and correcting the bias due to shot noise.

For center shifts we subtract the background pixel values before calculating the positions of the X-ray peak and centroid. Errors were taken as the σ of 100 poissonized realizations. Unless stated otherwise, all displayed $P3/P0$ and w values are background and bias corrected and calculated in the full r_{500} aperture.

4.8 Morphological analysis of 80 observed clusters

In this section, we will apply the substructure estimation method to our sample of 80 observed clusters and show that power ratios can give more than just a global picture of the cluster. We will briefly recapitulate the dependence of the power ratio signal on the aperture size and discuss improved morphology estimators based on these findings. To do so, we visually classify and divide the sample into 4 categories: a) DOUBLE − clusters with two distinct maxima, b) COMPLEX − clusters without two distinct maxima but global complex structure, c) INTERMEDIATE − overall regular clusters which show some kind of locally restricted structure or slight asymmetry, d) REGULAR − regular clusters without structure. The classification was done visually using two smoothed images (smoothed with a Gaussian with $\sigma = 4$ and 8 arcsec). This classification can then be compared to the boundaries defined in the morphological analysis of simulated cluster images. All 80 clusters are sorted according to their morphology and displayed in Figs. 4.17−4.20. We give the three different structure parameters ($P3/P0_{\rm c}$, $w_{\rm c}$ and $P3/P0_{\rm max}$) and the morphology for each cluster in Table 4.7, while an overview of the dynamical state of the sample using these three morphology estimators is detailed in Table 4.4.

4.8.1 Improved structure estimator

A simple application of $P3/P0$ and w using the repoissonization method to estimate the bias yields good results. As expected, we find very structured and in particular double clusters at high $P3/P0$ and w, while regular clusters are found to have low power ratios, but have a large spread in the w range. This was already shown by Buote & Tsai (1996) for power ratios and several authors afterwards for both substructure measures. The center shift parameter was already discussed in detail (e.g. Mohr et al. 1995; O'Hara et al. 2006; Poole et al. 2006, B10) and shows a wide spread for disturbed and regular clusters. We therefore focus on the $P3/P0$

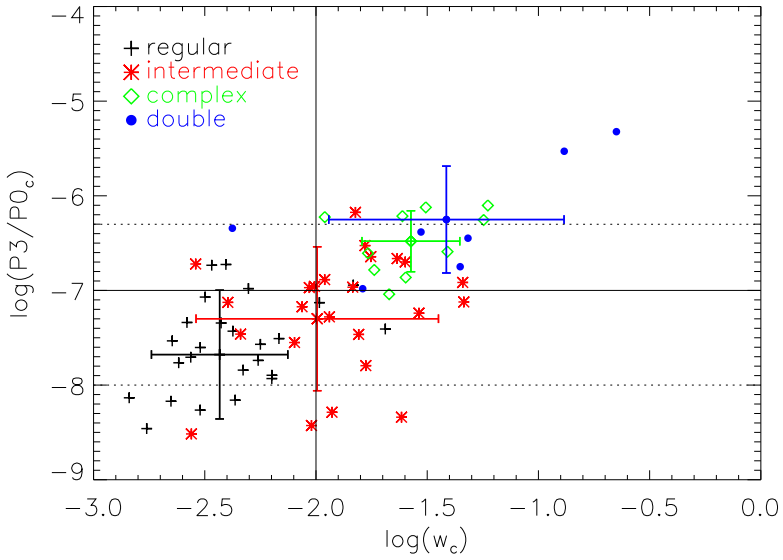

Figure 4.13: $P3/P0 - w$ plane for all 80 observed clusters including the *w boundary* at 10^{-2} and both the *simple* (10^{-7}, black solid line) and the *morphological* $P3/P0$ *boundaries* (10^{-8}, 5×10^{-7}, dotted lines) in an r_{500} aperture. The substructure parameters are background and bias-corrected. The outlier at $w < 10^{-4}$ can be considered as $w = 0$ and is excluded from the analysis. The different morphological types show a rough segregation with double (blue circles) and complex (green diamonds) with high structure parameters, while intermediate (red asterisks) and regular (black crosses) clusters are found to have very low structure values. In addition, we show the mean of the 4 populations and their spread (standard deviation).

parameter and discuss it in more detail.

For a sizeable cluster sample with the $P3/P0$ parameter calculated in the r_{500} aperture we are able to distinguish between very structured clusters ($P3/P0 > 5 \times 10^{-7}$ – double in our classification), clusters which show some kind of structure ($5 \times 10^{-7} < P3/P0 < 10^{-8}$ – complex and intermediate) and regular clusters ($P3/P0 < 10^{-8}$ – regular). However, as is shown in Fig. 4.13, there is an overlap of all three classifications in the $P3/P0 = 5 \times 10^{-7} - 10^{-8}$ range. This is due to the definition of the powers (see Sect. 4.2) and the stronger weighting of structures closer to the aperture radius. In a large aperture like r_{500} structures in the cluster center are less important than e.g. a merging subcluster at r_{500}. To illustrate this and motivate the next step, we show a $P3/P0$-profile ($P3/P0$ calculated in different aperture sizes) in Fig. 4.14 for three different clusters. In addition to the profiles we show the *simple* (solid line) and *morphological* $P3/P0$ *boundaries* (dotted lines). The different behavior of the three clusters is clearly visible. While both the Bullet Cluster (green circles, RXCJ0658.5-5556 in Fig. 4.20) and A115 (red asterisks) show prominent substructure in the visual inspection, only A115 is classified as such in the r_{500} aperture. This is due to the fact that the "bullet" in the Bullet Cluster lies at 0.3 r_{500} and is less prominent in the full r_{500} aperture. However, in the smaller aperture it would be detected as prominent substructure. As a reference cluster, we use the regular object A2204 (black crosses), which shows low substructure values in all apertures.

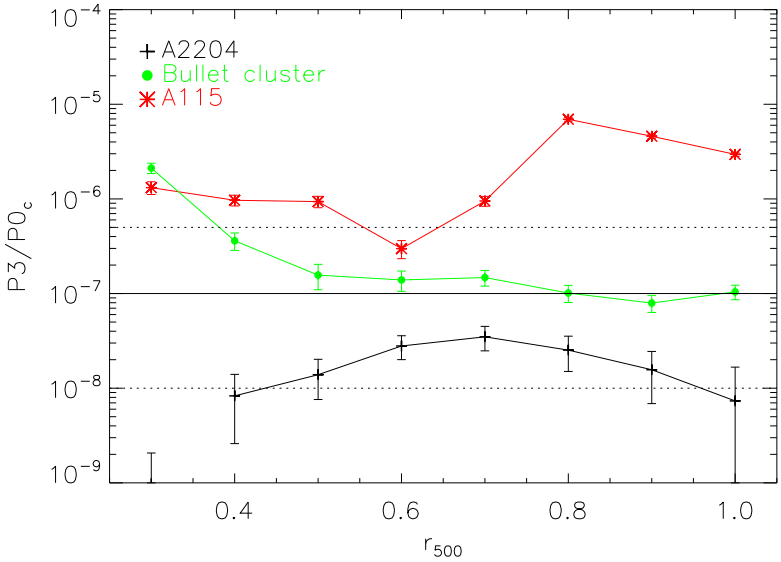

Figure 4.14: $P3/P0$ profile. $P3/P0$ calculated in 8 apertures ($0.3-1\ r_{500}$) is shown for 3 different clusters. The horizontal lines show the *simple* (solid line) and the *morphological* $P3/P0$ *boundaries* (dotted lines). A115 (red asterisks) shows a clear second component, which is located around $0.8\ r_{500}$. In the r_{500} aperture it is thus classified as highly disturbed. The Bullet Cluster (green circles) also clearly shows a second component, however this component lies at $0.3\ r_{500}$ and thus $P3/P0$ becomes less important for larger apertures. A2204 (black crosses) on the other hand is a regular cluster, which does not reach a large $P3/P0$ value in any aperture.

We use this characteristic to introduce an improved substructure estimator, which will be detailed in the next section: the peak of the $P3/P0$ profile ($0.3-1\ r_{500}$, in $0.1\ r_{500}$ steps), thereafter called $P3/P0_{\rm max}$. If the peak is not significant ($S < 1$ or $P3/P0 < 0$), we take the next highest significant value. $P3/P0_{\rm max}$ correlates well with $P3/P0$ in all apertures (Spearman ρ between 0.5 and 0.75, prob $< 10^{-7}$). The relation between $P3/P0_{\rm max}$ and w is stronger than that of $P3/P0$ and w, no matter in which aperture. Figure 4.15 shows the relation between $P3/P0_{\rm max}$ and w, details are given in Table 4.5. In addition, one can see the separation of double (blue), complex and intermediate (green and red) and regular (black) much clearer than in the $P3/P0 - w$ plane in Fig. 4.13.

4.9 Discussion

4.9.1 Substructure estimation and bias correction

The reliability of these substructure estimators suffers from shot noise, especially when dealing with observations with low photon statistics. We therefore performed a detailed analysis of power ratios and center shifts using 121 simulated cluster images to study the influence of shot noise for different observational set-ups (net counts and background).

We find that the center shift parameter is only affected by shot noise at very low photon statistics. This is due to the definition of this parameter, which uses the distance between the X-ray peak and the centroid in several apertures. The position of the X-ray peak is determined

Table 4.5: Correlations between structure estimators. For correlations with $P3/P0$ we only show the strongest and most interesting apertures. **Notes.** $^{(a)}$ Peak of the $0.3 - 1\ r_{500}$ $P3/P0$ profile.

Relation	$P3/P0$ radius	Spearman ρ	prob.	Kendall τ	prob.
$P3/P0 - w$	r_{500}	0.55	6.4×10^{-7}	0.40	7.7×10^{-7}
$P3/P0 - w$	$0.9\ r_{500}$	0.62	2.1×10^{-8}	0.46	6.0×10^{-8}
$P3/P0 - w$	$0.3\ r_{500}$	0.47	3.0×10^{-5}	0.34	2.7×10^{-5}
$P3/P0^{a}_{\rm max} - w$		0.58	1.8×10^{-8}	0.42	6.0×10^{-8}
$P3/P0_{\rm max} - P3/P0$	r_{500}	0.66	4.3×10^{-10}	0.51	0.0
$P3/P0_{\rm max} - P3/P0$	$0.3\ r_{500}$	0.75	8.4×10^{-15}	0.62	0.0

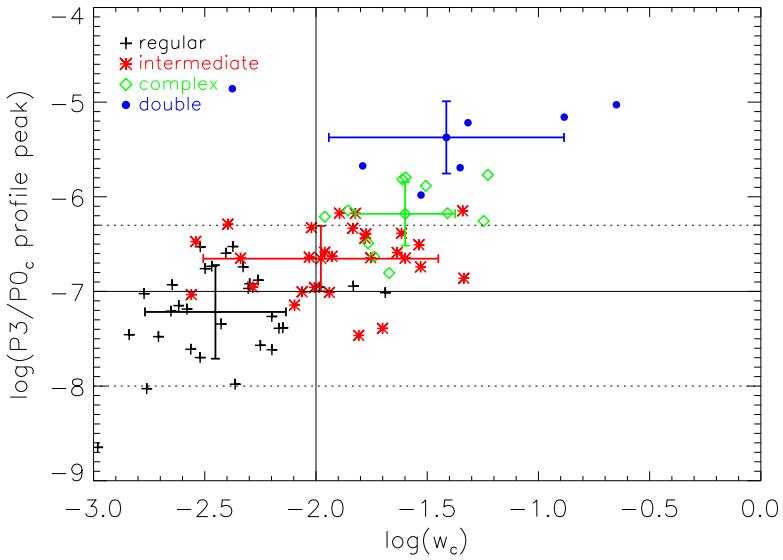

Figure 4.15: Relation between the significant peak ($S > 0$) of the $P3/P0$ profile and the center shift parameter for different morphologies. A tighter correlation than in the $P3/P0 - w$ plane (Fig. 4.13) can be seen. In addition, a clearer separation between the different morphological categories is apparent. The horizontal lines mark the $P3/P0$ boundaries (solid: *simple* at 10^{-7}, dotted: *morphological* at 5×10^{-7} and 10^{-8}), the vertical line displays the *w boundary* at 10^{-2}. The colors are as described in Fig. 4.13.

from a smoothed image and robust to noise (shift of the position of the brightest pixel in < 5% of the realizations of 5% of the most disturbed cluster cores). The centroid is slightly more influenced by low photon statistics than the X-ray peak. However, in units of r_{500}, this shift of the centroid due to shot noise is rather small. This assures a reliable center shift measurement down to low net counts (~200).

The possible effect of noise on power ratios can be severe, because they are calculated in an aperture, where each pixel can be influenced by shot noise. We find a clear dependence of the bias (spuriously detected structure due to noise) on the photon statistics and the amount

of intrinsic structure. Very structured clusters can be identified even in shallow observations (e.g. 1 000 net counts in r_{500}). Clusters without prominent substructure (e.g. without a visible second component) might be misclassified in some cases. We therefore present an improved method to estimate the shot noise and correct for background contributions which suffer from additional noise. We use 100 poissonized realizations of the X-ray image (background included) and calculate moments (a_0 to b_4) for the image, each realization and the background image. We subtract the background moments from the image moments and those of the 100 realizations before calculating power ratios. The mean power ratio of the poissonized versions of the image gives the bias, which is subtracted from the signal of the original image.

This method was influenced by several previous studies. Hart (2008) estimates the bias in a similar way using a smoothed (Gaussian with 1-pixel width) image and 20 poissonized realizations of the cluster. Jeltema et al. (2005) use an analytic approach to correct the noise in the cluster but also in the background image.

B10 introduced two methods to estimate the bias. The approach of poissionizing observed cluster images is the basis of our refined method presented above (see Sect. 4.4.3). The second method they proposed estimates the bias by azimuthally redistributing the counts in all pixels at a certain radial distance with random angles. Thus only the radial information is stored, but all azimuthal structure is now randomly distributed. The final bias is the mean of 100 such randomizations. Ideally, this mean gives the power ratio of a regular cluster with the same amount of shot noise as the real observation. We performed a direct comparison with this method (thereafter called azimuthal redistribution) using all 121 simulated cluster images and found that both methods yield very similar results for 1 000 counts. Our method yields slightly better results at high counts (e.g. 30 000) because it determines the bias more accurately than the azimuthal redistribution. In addition, our method gives better results at low $P3/P0$ values, partly already above the lower *morphological boundary* of 10^{-8}. However, for the high-quality observations like our sample of *XMM-Newton* observations, the differences are small.

Our method to correct the bias for the center shift parameter is analogous to the one for power ratios, however with the subtraction of background pixel values instead of moments before the calculation. Mohr et al. (1995) already investigated the influence of photon noise on w, however they define their center shift parameter in a different way and thus a direct comparison is not possible.

Having established a method to correct the bias in the power ratio and center shift calculation to obtain meaningful results, we defined parameter ranges for different morphologies. Due to the variety and complexity of the morphologies of the simulated (and observed) cluster sample, a direct link between a certain substructure value and a distinct morphology could not be found. However, we showed that different types of morphologies occupy on average different regions of the substructure parameter space. Our aim to characterize a large sample can be reached using two types of boundaries for $P3/P0$ (*simple boundary* at 10^{-7} or *morphological boundaries* at 5×10^{-7} and 10^{-8}) and a center shift value of 10^{-2} to divide the sample into relaxed, mildly disturbed and disturbed objects. In previous studies, similar values for significant substructure were found. B10 used 1.5×10^{-7} and $2 - 4 \times 10^{-8}$ for significant and insignificant structure, while Jeltema et al. (2008) define all clusters with $P3/P0 > 4.5 \times 10^{-7}$ as disturbed and $< 10^{-8}$ as relaxed. This agrees well with our findings.

The definition of the boundaries shows the large range of cluster morphologies. Merging

clusters with two clear components or very irregular structure can be identified under almost all conditions because of their strong signal. Clusters which appear relaxed (spherical or elongated) yield very low substructure values, however noise might increase their signal and some relaxed clusters might have $P3/P0 > 10^{-8}$. Applying the *morphological boundaries* to our sample of simulated clusters, we identify 32% as significantly disturbed. On the other hand, only 17% of our simulated sample show no signs of structure. This leaves the majority of clusters (51%) to be mildly disturbed objects. They show a slightly disturbed surface brightness distribution but no clear sign of a second component, the beginning of a merger, where the merging body lies outside of the aperture radius but already influences the ICM or a post-merger. This agrees well with observed values in X-rays which range between 40 – 70% of disturbed clusters (e.g. Mohr et al. 1995; Jones & Forman 1999; Kolokotronis et al. 2001; Schuecker et al. 2001). Using the same visual analysis as for the power ratios, a useful boundary for the center shift parameter was found to be $w = 0.01$. This value agrees well with the values of B10 and Cassano et al. (2010) who also give $w = 0.01$, and of Maughan et al. (2008) and O'Hara et al. (2006) with $w = 0.02$.

In general, using this method, we can significantly lower the influence of noise, especially for power ratios. For a shallow observation (1 000 counts), we find significant results ($S > 1$) for $P3/P0_c > 3 \times 10^{-7}$ and are able to reduce the mean bias for this subsample of disturbed clusters from 13% to 5%. At 30 000 counts, even relaxed clusters yield significant results ($S = 1$ at $P3/P0 = 4.5 \times 10^{-9}$) and reach a mean bias of 7% of the ideal value after applying the correction. Using the *morphological boundaries* at 5×10^{-7} and 10^{-8} to divide the sample into relaxed, mildly disturbed and disturbed objects, we see that the high bias is mainly due to truly relaxed objects with $P3/P0 < 10^{-8}$.

4.9.2 Morphological analysis of cluster sample

We investigated the morphologies of a sample of 80 galaxy clusters observed with *XMM-Newton* in detail to give a profound and detailed illustration of these two structure estimators. In addition, we want to demonstrate the statistical strength of power ratios and center shifts and test the above defined boundaries.

While power ratios are mainly used in a large aperture of r_{500} and are more sensitive to structures close to the aperture (e.g. merging component just inside r_{500}), center shifts are sensitive to the change of the centroid in different apertures and should thus be more sensitive to central gas properties. The center shift parameter indeed shows a tighter correlation with e.g. the central cooling time than $P3/P0$ (aperture of r_{500}), but also the power ratios are not insensitive to central gas properties (e.g. Croston et al. 2008). In agreement with B10, we find the best correlation between w and power ratios for a large aperture of $0.9\ r_{500}$ of $P3/P0$ (B10: $0.7\ r_{500}$). This indicates that while power ratios are most sensitive to substructures close to the aperture radius, they are also sensitive to large central disturbances and strong cool core activity. Merging clusters like the "Bullet Cluster" however are not identified as very disturbed in large apertures when the second component is well within the aperture. Although we can see clear signs of merging, the disturbance in the outer region of r_{500} is not severe enough to be identified as such. Simulations show that a powerful event like a merger influences the global cluster properties and boosts the luminosity and temperature of the cluster for a few hundred Myrs (Poole et al. 2006). In such a case, a misclassification might lead to a false

interpretation.

The dependence of the power ratios on the aperture size was already discussed in detail by e.g. Buote & Tsai (1996); Buote (2001); Jeltema et al. (2005). Looking at $P3/P0$ profiles, peaks due to substructure are visible in dynamically unrelaxed clusters. Not taking only one aperture size but the whole profile into account increases the probability of finding clusters with prominent structure – also in the central parts of the cluster. We thus introduced a new substructure estimator: $P3/P0_{\rm max}$, the peak of the $P3/P0$ profile. Comparing the detection of a merging cluster ($P3/P0 > 5\times10^{-7}$; morphological type double – as defined in Sect. 4.8) using $P3/P0$ in r_{500} and $P3/P0_{\rm max}$, we see that the probability of detecting substructure increases from 33% to 100% (compare Figs. 4.13 and 4.15). Also complex clusters are more likely to be identified as disturbed using the $P3/P0$ profile (45% for $P3/P0$ and 73% for $P3/P0_{\rm max}$). This is due to a shift towards larger power ratio values when using the maximum of the profile. In the lower power ratio range this increase leads to a jump of all relaxed clusters (regular and some intermediate) to power ratio values higher than 10^{-8}. This shows that for this new parameter, the upper *morphological boundary* at 5×10^{-7} yields best results in dividing the sample into relaxed and disturbed clusters. A few intermediate clusters cross this value, however the statistical strength remains. To demonstrate this again, we show the mean of each subsample and the width of the distribution in Figs. 4.13 and 4.15. It is visible that disturbed clusters (double (circles) and complex (diamonds)) are in a more defined region and better separated from the relaxed clusters (crosses).

In addition to the improved classification when using $P3/P0_{\rm max}$, it is interesting to see in which aperture this peak resides. A histogram of the position of the $P3/P0$ peak is shown in Fig. 4.16 for regular and intermediate (left) and complex and double (right) clusters. For complex and double clusters the distribution is as expected with no favored position. While regular clusters show a very homogeneous distribution, intermediate clusters mostly peak in small apertures. This is partly due to noise, which is larger in smaller apertures. However, these values are significant ($S > 1$). This suggests that the distribution reflects the visual classification. While double and complex clusters are characterized as having two maxima in the surface brightness distribution or a complex global appearance, intermediate clusters show no global structure but slight inhomogeneities or asymmetry in the central region.

Comparing our morphological classification to other works with clusters used for our analysis, we find a good agreement. Okabe et al. (2010) use asymmetry (A) and fluctuations of the X-ray surface brightness distribution in the 0.2 – 7 keV band (F) to divide their sample of 12 LoCuSS clusters into relaxed (low A and F) and disturbed (high A or F or both) clusters. For 9 overlapping clusters, we both find A115 to be very disturbed and agree on 2 relaxed clusters. The remaining 6 clusters are found in the $P3/P0$ range of mildly disturbed clusters and with not too high w values. They show a low A but a spread in the F range, which fits to our definition of intermediate, showing only slight asymmetries and/or some kind of locally restricted structure. We find a large overlap of 59 clusters with Andersson et al. (2009) who used power ratios to study the evolution of structure with redshift. However, they use a fixed aperture of 500 kpc for all redshifts (0.069 to 0.89), which relates to very different apertures sizes in our analysis. Bauer et al. (2005) also use a radius of 500 kpc to obtain power ratios, however their sample is more restricted in redshift (0.15 – 0.37). In addition they give a visual classification and divide their sample into relaxed, disturbed and double clusters. We have 11

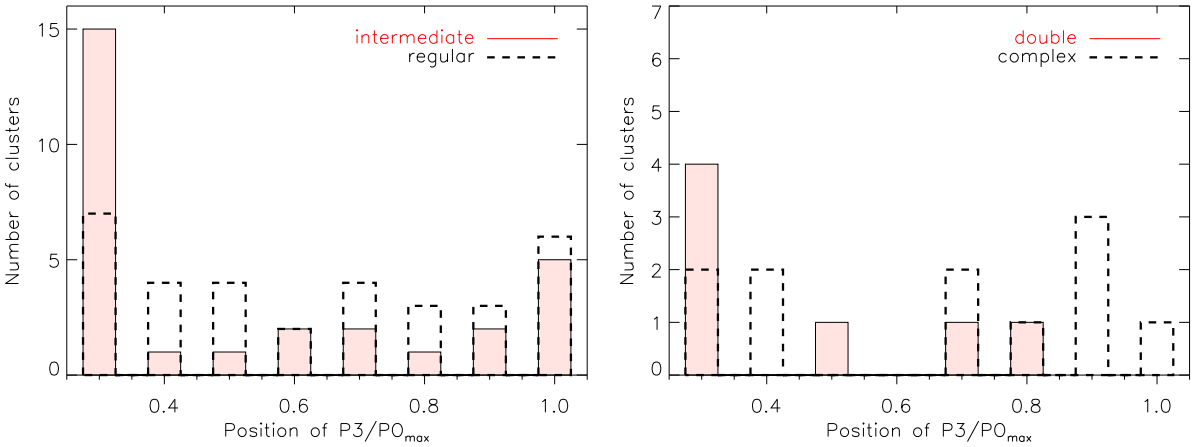

Figure 4.16: Histogram for all four morphological types showing the position of $P3/P0_{\rm max}$. **Left:** Regular (black dashed line) and intermediate (red filled histogram) clusters are shown. There is a clear excess in the 0.3 r_{500} aperture. **Right:** Complex (black dashed line) and double (red filled histogram) clusters are displayed. The distribution is homogeneous since the position of the peak depends on the location of the second component or structure.

common clusters and our morphology classification agrees well. Other studies having an overlapping sample but using a different aperture radius are e.g. Jeltema et al. (2005) or Cassano et al. (2010).

For their comparison of X-ray and lensing scaling relations, Zhang et al. (2008) visually classified a subsample of the LoCuSS clusters according to Jones & Forman (1991) as single, primary with small secondary, elliptical, off-center and complex. The last 4 classes characterize disturbed clusters. Comparing the overlapping 30 clusters to our visual classification, we find all 14 "single" clusters to be either regular or intermediate, which agrees well with our definition. Three "primary with a small secondary" are found to be complex (A1763, A13) or intermediate (RXCJ2234.5-3744). For the elliptical class, we find 4 intermediate, 1 complex and 3 regular clusters, showing that the definition of "elliptical" seems not very precise to asses the dynamical state of a cluster. The same holds for the definition of "off-center" for which we find 1 complex, 1 double and 2 intermediate clusters. The last morphological type, "complex", does not agree with our definition of complex. The only cluster defined as such, A115, is a clear double cluster. Placing these 30 clusters in the $P3/P0 - w$ and $P3/P0_{\rm max} - w$ plane, we find the "single" clusters at low $P3/P0$ and w value, agreeing with our definition of regular and intermediate. For 4 cases, we find either $P3/P0$ slightly $> 10^{-7}$ (RXCJ2308.3-0211 and RXCJ0547.6-3152) or w slightly > 0.01 (A209, A2218 and RXCJ0547.6-3152).

The result of a direct comparison between power ratios and the "primary" class depends on the position and size of the second component. The same holds for center shifts. A small second component close to the center will lead to a much smaller shift than one further outside. Clusters of this class can thus be found almost in the whole $P3/P0$ range and spread around the $w = 0.01$ boundary. The same is expected for "elliptical" clusters. They will not reach a center shift value as high as for merging clusters due to the lack of a strong second component. On the other hand one would not expect extremely high or low power ratio values. The lower limit

is set by the fact that the cluster is elliptical and not completely symmetric and will thus show $P3/P0 > 10^{-8}$. Due to an asymmetric elliptical structure however the centroid on which the aperture is centered shifts when going to larger radii, therefore setting an upper limit of a few times 10^{-7} to the expected value. The "off-center" class showing no clear sign of substructure has similar characteristics as the elliptical one and is thus found in the same $P3/P0$ and w range. Therefore only the morphological type "complex" remains to be discussed, which characterizes clusters with complex, multiple structures. This fits to our definition of double clusters with two distinct maxima in the surface brightness distribution. Overall one can conclude that clearly relaxed clusters and apparent mergers are very well described using both morphology schemes. The intermediate range, however, is defined ambiguously. We discussed these two classification schemes in detail because we have a large overlap of clusters and therefore can derive statistics from it.

It is important to point out again that morphological classifications are very often done using visual impressions and are dependent on the observer. Power ratios and center shifts on the other hand give numbers, which – using the results of our analysis – can be related to different, simple morphologies. Recalling the *morphological boundaries* defined for $P3/P0$ at 10^{-8} and 5×10^{-7}, we find a clear overlap between our mildly disturbed class and the three intermediate classes of Jones & Forman (1991), "primary with small secondary", "elliptical" and "off-center". Using $P3/P0_{\rm max}$ would help to better filter out clusters of the "primary" class, due to the sensitivity in all aperture sizes.

It is clearly shown that each of the three discussed parameters ($P3/P0$ in one aperture, $P3/P0$ profile and w) is sensitive on different scales. We therefore propose to use all three substructure estimators to characterize the dynamical state of large cluster samples. This can be done without a large computational effort for a large number of objects and help in identifying the potentially most interesting clusters for further analysis.

4.10 Conclusions

In this paper we provide a well tested method to obtain bias and background corrected substructure measures (power ratio $P3/P0$ and center shift w). We studied the influence of shot noise in detail and are able to correct for it sufficiently. We demonstrate that a simple parametrized bias correction is not possible and thus we propose a non-parametric bias correction method applicable to each cluster individually. We tested the method for different observational set-ups (net counts and background) using typical *XMM-Newton* values. We conclude that for low-count observations the influence of the background and bias can be severe. In general, the center shift parameter w is less sensitive to noise and more reliable than power ratios, especially for low photon statistics. However, one should be reminded that this method is statistically strong but might not be completely accurate for each individual cluster. We thus looked in more detail into the power ratio method and how certain parameter ranges can be related to different morphologies.

- Using a sample of 121 simulated X-ray cluster images, we visually inspected each cluster and established two kinds of substructure boundaries for $P3/P0$ (simple and morphological) and similarly one boundary for the center shift parameter.
- The *simple* $P3/P0$ *boundary* at $P3/P0 = 10^{-7}$ or the *w boundary* at $w = 0.01$ divide

a large sample into relaxed and disturbed clusters. For a more detailed morphological analysis, we introduce the *morphological* $P3/P0$ *boundaries* at 10^{-8} and 5×10^{-7}, which divide the sample into relaxed, mildly disturbed and disturbed objects. The two classification schemes can be used for low (*simple* $P3/P0$ *boundary*) and high photon statistics (*simple* and *morphological* $P3/P0$ *boundaries*).

- We applied the bias correction method and the defined boundaries to a sample of 80 galaxy clusters observed with *XMM-Newton*. We give structure parameters ($P3/P0$ in r_{500}, w and $P3/P0_{\rm max}$) for all clusters which are mostly part of well-known samples like LoCuSS or REXCESS.
- Applying the simple $P3/P0$ (w) substructure boundary, we find 41% (47%) of our observed clusters to be disturbed. The *morphological boundaries* yield 10% disturbed, 65% mildly disturbed and 25% relaxed objects. This large difference in the number of disturbed objects using the different conditions shows that most objects are not significantly but only mildly disturbed and do not show a clear second component.
- We visually classified all clusters into 4 groups (regular, intermediate, complex, double) to further test the strength of the structure estimators and find 8.75% double, 13.75% complex, 36.25% intermediate and 41.25% regular objects.
- We introduce the use of the $P3/P0$ profile, which picks up structures at all distances from the cluster center and in all aperture sizes.
- At last, we propose to use the maximum of the $P3/P0$ profile because it is not sensitive to the aperture size but finds clusters with structure on all scales. This parameter is more correlated with w than $P3/P0$ at any fixed aperture.

Using the proposed methods is especially interesting when dealing with a large sample, where visual classification of each individual cluster is not required but the global dynamical state of the whole sample is of interest. Applying the modified structure estimators like $P3/P0_{\rm max}$ gives additional constraints and helps to single out very structured or very relaxed clusters. Finding cluster mergers to study structure evolution or strong cool core clusters (very relaxed clusters) requires only a small computational effort, but gives a first indication about the dynamical state and properties of the cluster and whether a detailed analysis is desired.

Acknowledgements
We would like to thank the anonymous referee for constructive comments and suggestions. AW wants to thank Heike Modest for helpful discussions. This work is based on observations obtained with *XMM-Newton*, an ESA science mission with instruments and contributions directly funded by ESA Member States and NASA. The *XMM-Newton* project is supported by the Bundesministerium für Wirtschaft und Technologie/Deutsches Zentrum für Luft- und Raumfahrt (BMWI/DLR, FKZ 50 OX 0001), the Max-Planck Society and the Heidenhain-Stiftung. AW acknowledges the support from and participation in the International Max-Planck Research School on Astrophysics at the Ludwig-Maximilians University. An early part of this work was financed by the Bundesministerium für Wissenschaft und Forschung, Austria, through a "Förderungsstipendium nach dem Studienförderungsgesetz" granted by the University of Vienna.

4.11 Appendix

4.11.1 Tables

Table 4.6: Details about the cluster sample. **References.** (1) LoCuSS: Zhang et al. (2008); (2) REFLEX-DXL: Zhang et al. (2006); (3) Snowden et al. (2008); (4) Arnaud et al. (2005); (5) Buote & Tsai (1996); (6) REXCESS: Böhringer et al. (2010).

Cluster	z	Source	Cluster	z	Source
RXCJ0307.0-2840	0.2580	1,2	A2597	0.0804	3,4
RXCJ0516.7-5430	0.2940	1,2	A1775	0.0754	3
RXCJ0528.9-3927	0.2840	1,2	A1837	0.0663	3,5
RXCJ0532.9-3701	0.2750	1,2	RXCJ0014.3-3022	0.3066	2
RXCJ0658.5-5556	0.2960	1,2,3,5	RXCJ1131.9-1955	0.3075	2
RXCJ0945.4-0839	0.1530	1	A1651	0.0845	5
RXCJ2129.6+0005	0.2350	1	A133	0.0575	3
RXCJ2308.3-0211	0.2970	1,2	A2626	0.0549	3
RXCJ2337.6+0016	0.2750	1,2	A2065	0.0728	3
A68	0.2550	1,3	RXCJ0003.8+0203	0.0924	6
A115	0.1970	1	RXCJ0006.0-3443	0.1147	6
A209	0.2090	1,3	RXCJ0020.7-2542	0.1410	6
A267	0.2300	1	RXCJ0049.4-2931	0.1084	6
A383	0.1870	1,3	RXCJ0145.0-5300	0.1168	6
A773	0.2170	1,3	RXCJ0211.4-4017	0.1008	6
A963	0.2060	1	RXCJ0225.1-2928	0.0604	6
A1413	0.1430	1,3,4,5	RXCJ0345.7-4112	0.0603	6
A1763	0.2280	1	RXCJ0547.6-3152	0.1483	1,6
A1914	0.1710	1,3,5	RXCJ0605.8-3518	0.1392	6
A2390	0.2330	1	RXCJ0616.8-4748	0.1164	6
A2667	0.2300	1,3	RXCJ0645.4-5413	0.1644	1,6
A2204	0.1520	1,3,4,5	RXCJ0821.8+0112	0.0822	6
A2218	0.1760	1,3,5	RXCJ0958.3-1103	0.1669	1,6
RXCJ0232.2-4420	0.2840	1,2	RXCJ1044.5-0704	0.1342	6
A13	0.1035	3	RXCJ1141.4-1216	0.1195	6
A520	0.1946	3	RXCJ1236.7-3354	0.0796	6
A665	0.1788	3,5	RXCJ1302.8-0230	0.0847	6
A1068	0.1471	3,4,5	RXCJ1311.4-0120	0.1832	1,3,6
A1589	0.0722	3	RXCJ1516.3+0005	0.1181	6
A2163	0.2021	3	RXCJ1516.5-0056	0.1198	6
A2717	0.0510	3,4,5	RXCJ2014.8-2430	0.1538	6
A3112	0.0723	3	RXCJ2023.0-2056	0.0564	6
A3827	0.0959	3	RXCJ2048.1-1750	0.1475	6
A3911	0.0958	3	RXCJ2129.8-5048	0.0796	6
A3921	0.0919	3	RXCJ2149.1-3041	0.1184	6
1E1455.0+2232	0.2583	3	RXCJ2217.7-3543	0.1486	6
PKS0745-19	0.0986	3,4	RXCJ2218.6-3853	0.1411	1,6
RXJ1347.5-1145	0.4477	3	RXCJ2234.5-3744	0.1510	1,6
Sersic159-3	0.0563	3	RXCJ2319.6-7313	0.0984	6
ZwCl3146	0.2817	3	RXCJ2157.4-0747	0.0579	6

Table 4.7: Structure parameters of the cluster sample. **Notes.** We show the bias and background corrected parameters $P3/P0_c$ in r_{500}, w_c and the new morphology estimator $P3/P0_{max}$, the peak of the 0.3-1 r_{500} $P3/P0$ profile. Details can be found in Sect. 4.4.3 for $P3/P0_c$ and w_c and Sect. 4.8.1 for $P3/P0_{max}$. In addition, the morphology as defined in Sect. 4.8 is given. $^{(*)}$ No significant peak in any aperture, not shown in figures.

Cluster	$P3/P0_c$	w_c	$P3/P0_{max}$	Morphology
RXCJ0307.0-2840	$-3.3\times10^{-9}\pm1.4\times10^{-8}$	$1.7\times10^{-3}\pm4.5\times10^{-4}$	$9.5\times10^{-8}\pm4.3\times10^{-8}$	regular
RXCJ0516.7-5430	$7.9\times10^{-7}\pm3.3\times10^{-7}$	$6.0\times10^{-2}\pm4.3\times10^{-3}$	$1.7\times10^{-6}\pm6.0\times10^{-7}$	complex
RXCJ0528.9-3927	$9.1\times10^{-8}\pm6.3\times10^{-8}$	$2.1\times10^{-2}\pm1.3\times10^{-3}$	$1.6\times10^{-7}\pm8.6\times10^{-8}$	complex
RXCJ0532.9-3701	$7.5\times10^{-8}\pm5.7\times10^{-8}$	$4.0\times10^{-3}\pm6.6\times10^{-4}$	$5.1\times10^{-7}\pm2.6\times10^{-7}$	intermediate
RXCJ0658.5-5556	$1.0\times10^{-7}\pm1.8\times10^{-8}$	$1.6\times10^{-2}\pm5.6\times10^{-4}$	$2.1\times10^{-6}\pm2.6\times10^{-7}$	double
RXCJ0945.4-0839	$2.3\times10^{-7}\pm1.4\times10^{-7}$	$1.8\times10^{-2}\pm1.7\times10^{-3}$	$2.3\times10^{-7}\pm1.4\times10^{-7}$	intermediate
RXCJ2129.6+0005	$1.3\times10^{-8}\pm6.9\times10^{-9}$	$6.3\times10^{-3}\pm3.5\times10^{-4}$	$2.4\times10^{-8}\pm1.9\times10^{-8}$	regular
RXCJ2308.3-0211*	$1.9\times10^{-7}\pm4.0\times10^{-7}$	$2.9\times10^{-3}\pm1.7\times10^{-3}$	$3.4\times10^{-7}\pm4.5\times10^{-7}$	intermediate
RXCJ2337.6+0016	$-1.4\times10^{-8}\pm3.1\times10^{-8}$	$3.0\times10^{-2}\pm3.4\times10^{-3}$	$1.8\times10^{-7}\pm9.6\times10^{-8}$	intermediate
A68	$1.3\times10^{-7}\pm4.1\times10^{-8}$	$1.1\times10^{-2}\pm6.3\times10^{-4}$	$2.6\times10^{-7}\pm1.5\times10^{-7}$	intermediate
A115	$3.0\times10^{-6}\pm1.5\times10^{-7}$	$1.3\times10^{-1}\pm6.9\times10^{-4}$	$6.9\times10^{-6}\pm3.1\times10^{-7}$	double
A209	$5.3\times10^{-8}\pm3.5\times10^{-8}$	$1.1\times10^{-2}\pm9.8\times10^{-4}$	$9.8\times10^{-8}\pm4.1\times10^{-8}$	intermediate
A267	$1.1\times10^{-7}\pm4.8\times10^{-8}$	$9.8\times10^{-3}\pm1.1\times10^{-3}$	$1.1\times10^{-7}\pm4.8\times10^{-8}$	intermediate
A383	$1.7\times10^{-8}\pm1.0\times10^{-8}$	$2.4\times10^{-3}\pm3.0\times10^{-4}$	$7.1\times10^{-8}\pm2.5\times10^{-8}$	regular
A773	$-2.0\times10^{-8}\pm2.2\times10^{-8}$	$5.2\times10^{-3}\pm6.8\times10^{-4}$	$1.1\times10^{-7}\pm7.7\times10^{-8}$	intermediate
A963	$1.4\times10^{-8}\pm1.3\times10^{-8}$	$4.7\times10^{-3}\pm4.0\times10^{-4}$	$1.8\times10^{-7}\pm7.1\times10^{-8}$	regular
A1413	$1.9\times10^{-7}\pm2.9\times10^{-7}$	$3.9\times10^{-3}\pm1.5\times10^{-3}$	$2.5\times10^{-7}\pm2.1\times10^{-7}$	regular
A1763	$6.0\times10^{-7}\pm1.1\times10^{-7}$	$1.1\times10^{-2}\pm1.1\times10^{-3}$	$6.2\times10^{-7}\pm1.1\times10^{-7}$	complex
A1914	$3.5\times10^{-8}\pm8.8\times10^{-9}$	$4.6\times10^{-3}\pm1.9\times10^{-4}$	$2.2\times10^{-7}\pm2.9\times10^{-8}$	intermediate
A2390	$6.7\times10^{-8}\pm2.0\times10^{-8}$	$8.7\times10^{-3}\pm5.4\times10^{-4}$	$9.9\times10^{-8}\pm6.4\times10^{-8}$	intermediate
A2667	$5.2\times10^{-9}\pm7.0\times10^{-9}$	$1.2\times10^{-2}\pm3.4\times10^{-4}$	$2.4\times10^{-7}\pm5.7\times10^{-8}$	intermediate
A2204	$7.3\times10^{-9}\pm9.4\times10^{-9}$	$1.4\times10^{-3}\pm1.4\times10^{-4}$	$3.5\times10^{-8}\pm1.0\times10^{-8}$	regular
A2218	$1.6\times10^{-8}\pm1.4\times10^{-8}$	$1.7\times10^{-2}\pm1.2\times10^{-3}$	$4.1\times10^{-7}\pm1.8\times10^{-7}$	intermediate
RXCJ0232.2-4420	$1.6\times10^{-7}\pm6.3\times10^{-8}$	$1.8\times10^{-2}\pm5.6\times10^{-4}$	$2.3\times10^{-7}\pm1.1\times10^{-7}$	complex
A13	$3.0\times10^{-7}\pm6.3\times10^{-8}$	$1.7\times10^{-2}\pm6.2\times10^{-4}$	$3.6\times10^{-7}\pm1.1\times10^{-7}$	intermediate
A520	$1.4\times10^{-7}\pm3.4\times10^{-8}$	$2.5\times10^{-2}\pm3.0\times10^{-3}$	$1.6\times10^{-6}\pm2.4\times10^{-7}$	complex
A665	$1.2\times10^{-7}\pm6.1\times10^{-8}$	$4.6\times10^{-2}\pm8.0\times10^{-4}$	$7.1\times10^{-7}\pm1.4\times10^{-7}$	intermediate
A1068	$-4.1\times10^{-9}\pm7.4\times10^{-9}$	$7.1\times10^{-3}\pm3.3\times10^{-4}$	$4.1\times10^{-8}\pm1.4\times10^{-8}$	regular
A1589	$1.1\times10^{-7}\pm4.2\times10^{-8}$	$1.5\times10^{-2}\pm1.2\times10^{-3}$	$4.6\times10^{-7}\pm9.7\times10^{-8}$	intermediate
A2163	$4.1\times10^{-7}\pm5.7\times10^{-8}$	$3.0\times10^{-2}\pm6.6\times10^{-4}$	$1.0\times10^{-6}\pm1.7\times10^{-7}$	double
A2717	$4.6\times10^{-8}\pm2.1\times10^{-8}$	$2.6\times10^{-3}\pm5.3\times10^{-4}$	$6.5\times10^{-8}\pm2.3\times10^{-8}$	regular
A3112	$1.8\times10^{-7}\pm1.7\times10^{-8}$	$3.4\times10^{-3}\pm1.5\times10^{-4}$	$1.8\times10^{-7}\pm1.7\times10^{-8}$	regular
A3827	$7.4\times10^{-8}\pm1.8\times10^{-8}$	$1.0\times10^{-2}\pm3.2\times10^{-4}$	$1.1\times10^{-7}\pm1.7\times10^{-8}$	regular
A3911	$4.7\times10^{-9}\pm8.6\times10^{-9}$	$2.4\times10^{-2}\pm1.1\times10^{-3}$	$4.1\times10^{-7}\pm9.4\times10^{-8}$	intermediate
A3921	$7.5\times10^{-7}\pm1.1\times10^{-7}$	$3.1\times10^{-2}\pm8.7\times10^{-4}$	$1.3\times10^{-6}\pm1.2\times10^{-7}$	complex
1E1455.0+2232	$4.5\times10^{-8}\pm1.2\times10^{-8}$	$3.7\times10^{-3}\pm1.7\times10^{-4}$	$4.5\times10^{-8}\pm1.2\times10^{-8}$	regular
PKS0745-19	$-1.1\times10^{-8}\pm7.6\times10^{-9}$	$1.0\times10^{-3}\pm2.4\times10^{-4}$	$2.3\times10^{-9}\pm1.2\times10^{-9}$	regular
RXJ1347.5-1145	$1.8\times10^{-8}\pm6.1\times10^{-9}$	$5.5\times10^{-3}\pm2.7\times10^{-4}$	$1.3\times10^{-7}\pm4.3\times10^{-8}$	regular
Sersic159-3	$3.5\times10^{-9}\pm5.6\times10^{-10}$	$1.7\times10^{-3}\pm5.2\times10^{-5}$	$9.4\times10^{-9}\pm2.0\times10^{-9}$	regular
ZwCl3146	$6.7\times10^{-9}\pm2.0\times10^{-9}$	$2.2\times10^{-3}\pm1.4\times10^{-4}$	$6.2\times10^{-8}\pm1.3\times10^{-8}$	regular
A2597	$1.2\times10^{-8}\pm1.1\times10^{-8}$	$9.4\times10^{-4}\pm1.6\times10^{-4}$	$1.2\times10^{-8}\pm1.1\times10^{-8}$	regular
A1775	$2.5\times10^{-7}\pm5.0\times10^{-8}$	$1.7\times10^{-2}\pm3.0\times10^{-4}$	$3.2\times10^{-7}\pm5.2\times10^{-8}$	complex
A1837	$1.1\times10^{-7}\pm3.0\times10^{-8}$	$9.3\times10^{-3}\pm3.1\times10^{-4}$	$2.3\times10^{-7}\pm3.4\times10^{-8}$	intermediate
RXCJ0014.3-3022	$3.6\times10^{-7}\pm7.3\times10^{-8}$	$4.8\times10^{-2}\pm1.7\times10^{-3}$	$6.1\times10^{-6}\pm5.7\times10^{-7}$	double
RXCJ1131.9-1955	$2.6\times10^{-7}\pm1.0\times10^{-7}$	$3.9\times10^{-2}\pm1.5\times10^{-3}$	$6.8\times10^{-7}\pm2.0\times10^{-7}$	complex
A1651	$5.0\times10^{-10}\pm8.3\times10^{-9}$	$2.0\times10^{-3}\pm6.6\times10^{-4}$	$3.3\times10^{-8}\pm1.1\times10^{-8}$	regular
A133	$3.1\times10^{-8}\pm1.8\times10^{-8}$	$6.8\times10^{-3}\pm4.0\times10^{-4}$	$4.1\times10^{-8}\pm1.7\times10^{-8}$	regular
A2626	$6.9\times10^{-9}\pm4.1\times10^{-9}$	$4.3\times10^{-3}\pm2.9\times10^{-4}$	$1.0\times10^{-8}\pm4.5\times10^{-9}$	regular
A2065	$3.4\times10^{-8}\pm2.3\times10^{-8}$	$1.6\times10^{-2}\pm3.3\times10^{-4}$	$3.4\times10^{-8}\pm2.3\times10^{-8}$	intermediate
RXCJ0003.8+0203	$-3.3\times10^{-9}\pm1.3\times10^{-8}$	$-1.8\times10^{-4}\pm8.9\times10^{-4}$	$2.7\times10^{-7}\pm6.7\times10^{-8}$	regular
RXCJ0006.0-3443	$2.2\times10^{-7}\pm1.0\times10^{-7}$	$2.3\times10^{-2}\pm1.5\times10^{-3}$	$2.6\times10^{-7}\pm9.5\times10^{-8}$	intermediate
RXCJ0020.7-2542	$-7.9\times10^{-9}\pm1.3\times10^{-8}$	$1.4\times10^{-2}\pm9.3\times10^{-4}$	$7.2\times10^{-7}\pm1.8\times10^{-7}$	complex
RXCJ0049.4-2931	$2.9\times10^{-8}\pm5.7\times10^{-8}$	$2.3\times10^{-3}\pm1.2\times10^{-3}$	$1.2\times10^{-7}\pm8.1\times10^{-8}$	regular
RXCJ0145.0-5300	$7.6\times10^{-8}\pm6.0\times10^{-8}$	$4.6\times10^{-2}\pm1.5\times10^{-3}$	$1.4\times10^{-7}\pm8.5\times10^{-8}$	intermediate
RXCJ0211.4-4017	$3.7\times10^{-8}\pm5.0\times10^{-8}$	$4.2\times10^{-3}\pm7.1\times10^{-4}$	$3.0\times10^{-7}\pm1.0\times10^{-7}$	regular

Table 4.7: continued.

Cluster	$P3/P0_c$	w_c	$P3/P0_{max}$	Morphology
RXCJ0225.1-2928	$4.3 \times 10^{-7} \pm 2.0 \times 10^{-7}$	$5.8 \times 10^{-5} \pm 1.5 \times 10^{-3}$	$4.3 \times 10^{-7} \pm 2.0 \times 10^{-7}$	intermediate
RXCJ0345.7-4112	$3.4 \times 10^{-7} \pm 8.7 \times 10^{-8}$	$8.3 \times 10^{-4} \pm 1.1 \times 10^{-3}$	$3.4 \times 10^{-7} \pm 8.7 \times 10^{-8}$	regular
RXCJ0547.6-3152	$1.1 \times 10^{-7} \pm 4.3 \times 10^{-8}$	$1.5 \times 10^{-2} \pm 6.5 \times 10^{-4}$	$1.1 \times 10^{-7} \pm 4.3 \times 10^{-8}$	regular
RXCJ0605.8-3518	$1.2 \times 10^{-8} \pm 4.1 \times 10^{-9}$	$6.3 \times 10^{-3} \pm 2.6 \times 10^{-4}$	$5.4 \times 10^{-8} \pm 2.7 \times 10^{-8}$	regular
RXCJ0616.8-4748	$6.7 \times 10^{-7} \pm 1.6 \times 10^{-7}$	$1.5 \times 10^{-2} \pm 1.2 \times 10^{-3}$	$6.7 \times 10^{-7} \pm 1.6 \times 10^{-7}$	intermediate
RXCJ0645.4-5413	$3.1 \times 10^{-10} \pm 2.1 \times 10^{-8}$	$1.3 \times 10^{-2} \pm 4.9 \times 10^{-4}$	$6.7 \times 10^{-7} \pm 1.5 \times 10^{-7}$	intermediate
RXCJ0821.8+0112	$4.5 \times 10^{-7} \pm 2.4 \times 10^{-7}$	$4.2 \times 10^{-3} \pm 1.2 \times 10^{-3}$	$1.4 \times 10^{-5} \pm 2.7 \times 10^{-6}$	double
RXCJ0958.3-1103	$2.5 \times 10^{-8} \pm 2.4 \times 10^{-8}$	$3.0 \times 10^{-3} \pm 6.7 \times 10^{-4}$	$3.0 \times 10^{-7} \pm 1.4 \times 10^{-7}$	regular
RXCJ1044.5-0704	$2.8 \times 10^{-10} \pm 2.0 \times 10^{-9}$	$5.0 \times 10^{-3} \pm 2.2 \times 10^{-4}$	$1.2 \times 10^{-7} \pm 3.4 \times 10^{-8}$	regular
RXCJ1141.4-1216	$2.0 \times 10^{-8} \pm 1.4 \times 10^{-8}$	$2.7 \times 10^{-3} \pm 3.8 \times 10^{-4}$	$2.5 \times 10^{-8} \pm 1.7 \times 10^{-8}$	regular
RXCJ1236.7-3354	$3.0 \times 10^{-9} \pm 3.7 \times 10^{-8}$	$2.8 \times 10^{-3} \pm 5.3 \times 10^{-4}$	$9.3 \times 10^{-8} \pm 8.3 \times 10^{-8}$	intermediate
RXCJ1302.8-0230	$2.0 \times 10^{-7} \pm 5.6 \times 10^{-8}$	$2.5 \times 10^{-2} \pm 6.3 \times 10^{-4}$	$2.2 \times 10^{-7} \pm 6.5 \times 10^{-8}$	intermediate
RXCJ1311.4-0120	$5.4 \times 10^{-9} \pm 2.2 \times 10^{-9}$	$3.0 \times 10^{-3} \pm 2.1 \times 10^{-4}$	$2.0 \times 10^{-8} \pm 6.7 \times 10^{-9}$	regular
RXCJ1516.3+0005	$2.8 \times 10^{-8} \pm 1.8 \times 10^{-8}$	$8.0 \times 10^{-3} \pm 5.3 \times 10^{-4}$	$7.2 \times 10^{-8} \pm 4.2 \times 10^{-8}$	intermediate
RXCJ1516.5-0056	$6.1 \times 10^{-7} \pm 1.6 \times 10^{-7}$	$2.4 \times 10^{-2} \pm 1.3 \times 10^{-3}$	$1.5 \times 10^{-6} \pm 2.7 \times 10^{-7}$	complex
RXCJ2014.8-2430	$2.7 \times 10^{-8} \pm 7.1 \times 10^{-9}$	$5.6 \times 10^{-3} \pm 1.9 \times 10^{-4}$	$2.7 \times 10^{-8} \pm 7.1 \times 10^{-9}$	regular
RXCJ2023.0-2056	$5.8 \times 10^{-8} \pm 5.1 \times 10^{-8}$	$2.9 \times 10^{-2} \pm 1.1 \times 10^{-3}$	$3.1 \times 10^{-7} \pm 1.3 \times 10^{-7}$	intermediate
RXCJ2048.1-1750	$5.6 \times 10^{-7} \pm 1.2 \times 10^{-7}$	$5.7 \times 10^{-2} \pm 6.1 \times 10^{-3}$	$5.6 \times 10^{-7} \pm 1.1 \times 10^{-7}$	complex
RXCJ2129.8-5048	$1.8 \times 10^{-7} \pm 9.8 \times 10^{-8}$	$4.4 \times 10^{-2} \pm 1.5 \times 10^{-3}$	$2.0 \times 10^{-6} \pm 4.1 \times 10^{-7}$	double
RXCJ2149.1-3041	$1.0 \times 10^{-7} \pm 3.3 \times 10^{-8}$	$5.0 \times 10^{-3} \pm 4.9 \times 10^{-4}$	$1.1 \times 10^{-7} \pm 2.9 \times 10^{-8}$	regular
RXCJ2217.7-3543	$8.5 \times 10^{-8} \pm 2.8 \times 10^{-8}$	$3.2 \times 10^{-3} \pm 5.6 \times 10^{-4}$	$1.7 \times 10^{-7} \pm 5.4 \times 10^{-8}$	regular
RXCJ2218.6-3853	$3.9 \times 10^{-8} \pm 1.7 \times 10^{-8}$	$2.0 \times 10^{-2} \pm 7.4 \times 10^{-4}$	$9.7 \times 10^{-8} \pm 4.6 \times 10^{-8}$	regular
RXCJ2234.5-3744	$3.7 \times 10^{-9} \pm 3.2 \times 10^{-9}$	$9.5 \times 10^{-3} \pm 4.1 \times 10^{-4}$	$4.7 \times 10^{-7} \pm 8.0 \times 10^{-8}$	intermediate
RXCJ2319.6-7313*	$-3.2 \times 10^{-9} \pm 1.8 \times 10^{-8}$	$2.0 \times 10^{-2} \pm 1.1 \times 10^{-3}$	$4.1 \times 10^{-8} \pm 6.8 \times 10^{-8}$	intermediate
RXCJ2157.4-0747	$4.8 \times 10^{-6} \pm 1.2 \times 10^{-6}$	$2.2 \times 10^{-1} \pm 9.5 \times 10^{-2}$	$9.4 \times 10^{-6} \pm 2.5 \times 10^{-6}$	double

4.11.2 Gallery

Below we show images of our cluster sample. The clusters are sorted by morphological type and ordered as in Table 4.6. All images are background subtracted, smoothed and normalized to the surface brightness at 0.3 r_{500}.

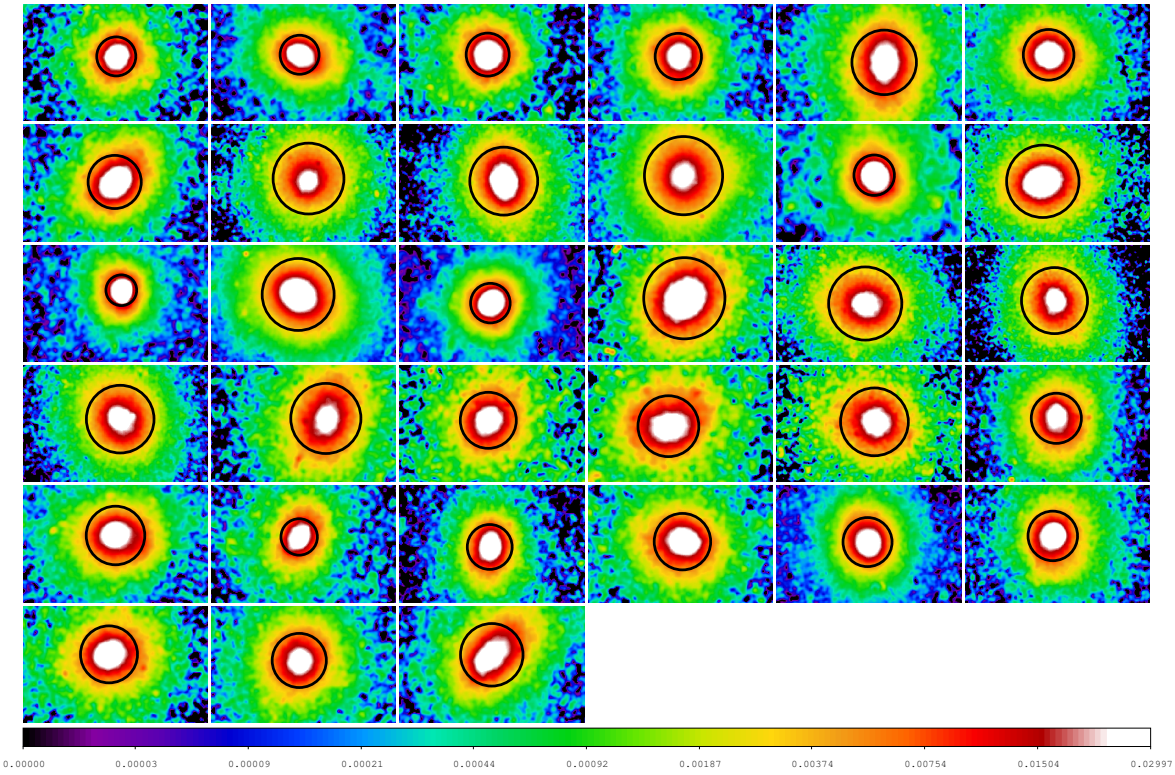

Figure 4.17: Clusters classified as regular – regular clusters without structure. From top left to bottom right: RXCJ0307.0-2840, RXCJ2129.6+0005, A383, A963, A1413, A2204, A1068, A2717, A3112, A3827, 1E1455.0+2232, PKS0745-19, RXJ1347.5-1145, Sersic159-3, ZwCl3146, A2597, A1651, A133, A2626, RXCJ0003.8+0203, RXCJ0049.4-2931, RXCJ0211.4-4017, RXCJ0345.7-4112, RXCJ0547.6-3152, RXCJ0605.8-3518, RXCJ0958.3-1103, RXCJ1044.5-0704, RXCJ1141.4-1216, RXCJ1311.4-0120, RXCJ2014.8-2430, RXCJ2149.1-3041, RXCJ2217.7-3543, RXCJ2218.6-3853.

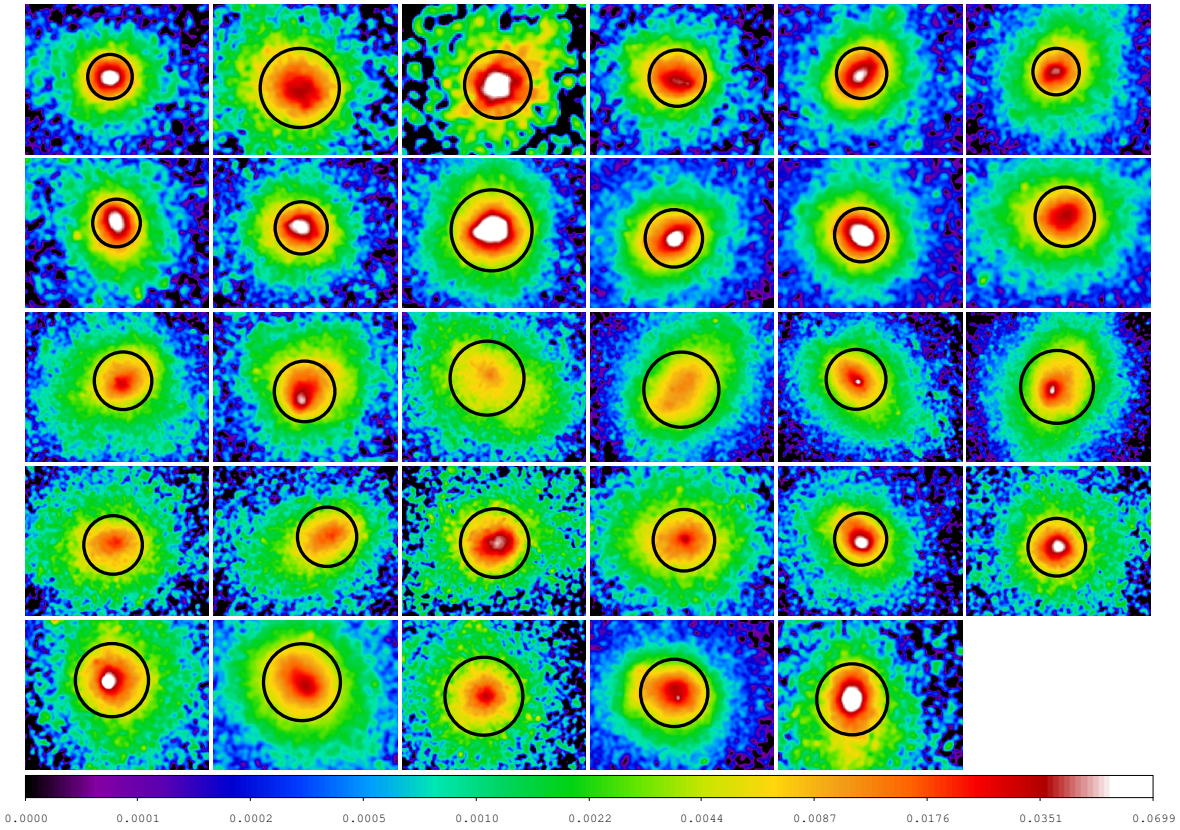

Figure 4.18: Clusters classified as intermediate – overall regular clusters which show some kind of locally restricted structure or slight asymmetry. From top left to bottom right: RXCJ0532.9-3701, RXCJ0945.4-0839, RXCJ2308.3-0211, RXCJ2337.6+0016, A68, A209, A267, A773, A1914, A2390, A2667, A2218, A13, A665, A1589, A3911, A1837, A2065, RXCJ0006.0-3443, RXCJ0145.0-5300, RXCJ0225.1-2928, RXCJ0616.8-4748, RXCJ0645.4-5413, RXCJ1236.7-3354, RXCJ1302.8-0230, RXCJ1516.3+0005, RXCJ2023.0-2056, RXCJ2234.5-3744, RXCJ2319.6-7313.

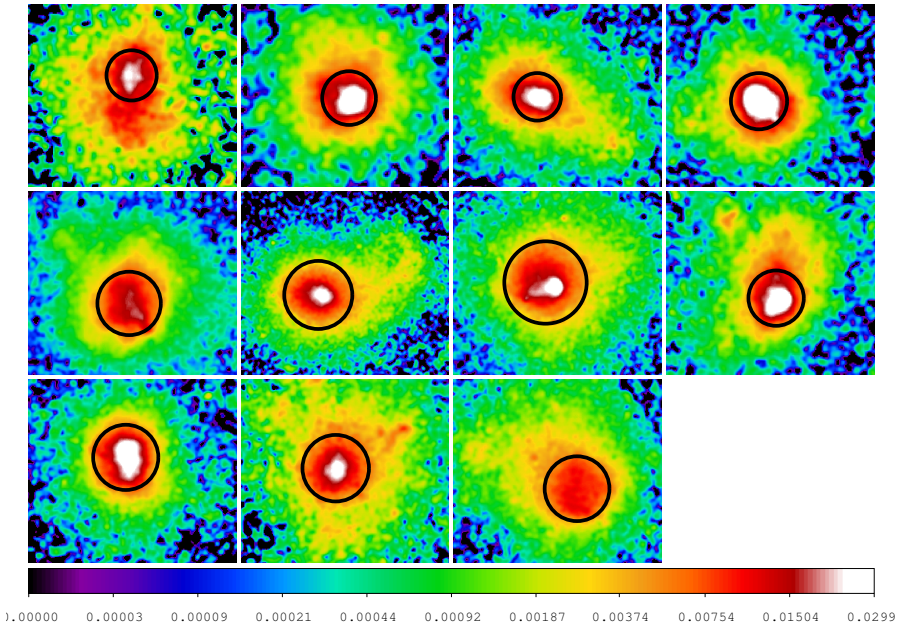

Figure 4.19: Clusters classified as complex – clusters without two distinct maxima but global complex structure. From top left to bottom right: RXCJ0516.7-5430, RXCJ0528.9-3927, A1763, RXCJ0232.2-4420, A520, A3921, A1775, RXCJ1131.9-1955, RXCJ0020.7-2542, RXCJ1516.5-0056, RXCJ2048.1-1750.

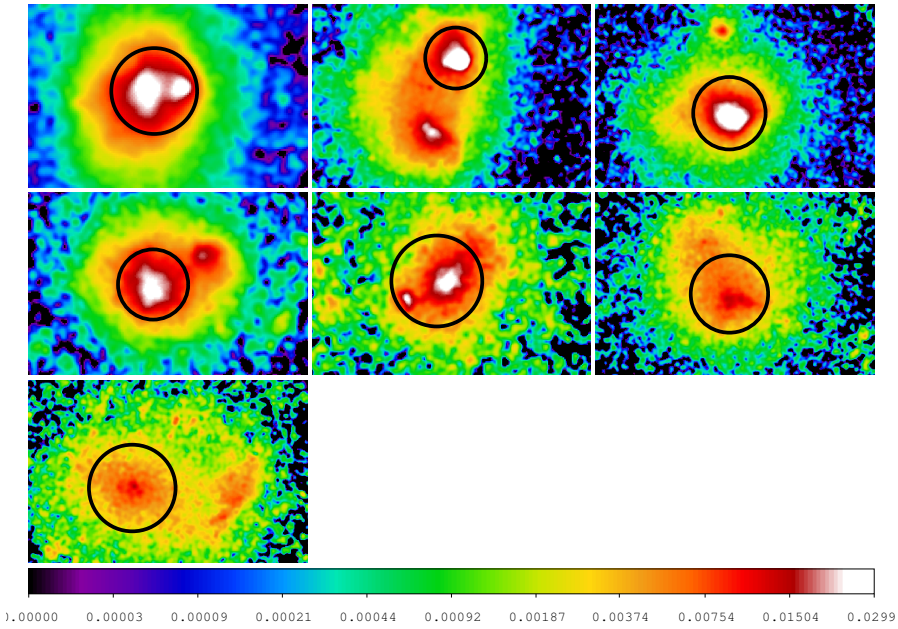

Figure 4.20: Clusters classified as double – clusters two distinct maxima. From top left to bottom right: RXCJ0658.5-5556, A115, A2163, RXCJ0014.3-3022, RXCJ0821.8+0211, RXCJ2129.8-5048, RXCJ2157.4-0747.

Chapter 5

Probing the evolution of the substructure frequency in galaxy clusters up to $z \sim 1$

A. Weißmann, H. Böhringer, G. Chon

A&A, **555** (2013), A147

Abstract

Context. Galaxy clusters are the last and largest objects to form in the standard hierarchical structure formation scenario through merging of smaller systems. The substructure frequency in the past and present epoch provides excellent means for studying the underlying cosmological model.

Aims. Using X-ray observations, we study the substructure frequency as a function of redshift by quantifying and comparing the fraction of dynamically young clusters at different redshifts up to $z = 1.08$. We are especially interested in possible biases due to the inconsistent data quality of the low-z and high-z samples.

Methods. Two well-studied morphology estimators, power ratio $P3/P0$ and center shift w, were used to quantify the dynamical state of 129 galaxy clusters, taking into account the different observational depth and noise levels of the observations.

Results. Owing to the sensitivity of $P3/P0$ to Poisson noise, it is essential to use datasets with similar photon statistics when studying the $P3/P0 - z$ relation. We degraded the high-quality data of the low-redshift sample to the low data quality of the high-z observations and found a shallow positive slope that is, however, not significant, indicating a slightly larger fraction of dynamically young objects at higher redshift. The $w - z$ relation shows no significant dependence on the data quality and gives a similar result.

Conclusions. We find a similar trend for $P3/P0$ and w, namely a very mild increase of the disturbed cluster fraction with increasing redshifts. Within the significance limits, our findings are also consistent with no evolution.

5.1 Introduction

The standard theory of structure formation predicts hierarchical growth from positive fluctuations in the primordial density field. Subgalactic scale objects decouple first, then collapse and virialize due to the greater amplitudes of the density fluctuations on small scales. They grow through merging, finally forming galaxy clusters, which are considered the largest virialized objects in the Universe. Galaxy cluster growth probes the evolution of density perturbations and directly traces the process of structure formation in the Universe. Galaxy clusters are thus important laboratories for studying and testing the underlying cosmological model (e.g. Voit 2005; Borgani 2008). Especially important in this context is the study of the cluster mass function, whose evolution provides constraints on the linear growth rate of density perturbations. Using X-rays and analyzing the hot intracluster medium (ICM) that resides in the deep potential well of galaxy clusters, mass determination is based on the assumptions of hydrostatic equilibrium and spherical shape. These assumptions may be unsatisfactory for dynamically young objects showing multiple surface brightness peaks in the distribution of the ICM, however (e.g. Zhang et al. 2008; Nelson et al. 2012; Rasia et al. 2012). In addition, the influence of dynamical activity such as merging on $L_{\rm X}$, $T_{\rm X}$ etc. needs to be known in detail to explain possible deviations from scaling relations for disturbed clusters (e.g. Rowley et al. 2004; Pratt et al. 2009; Chon et al. 2012) with the aim to reduce the errors in cosmological studies.

Observations of substructure and disturbed morphologies in the optical (see e.g. West & Bothun 1990; Girardi & Biviano 2002, and references therein) and X-ray band (for a review see e.g. Buote 2002) indicate that a large fraction of clusters is dynamically young and has not reached a relaxed state yet. It is therefore essential to quantify the fraction of disturbed clusters that reflects the formation rate and to probe higher redshifts to constrain cosmological parameters.

X-ray observations provide excellent probes for studying the dynamical state of clusters because the ICM traces their deep potential well. Over the years, X-ray studies became very efficient in quantifying cluster structure, and a variety of X-ray morphology estimators was introduced (for a review see Rasia et al. 2013). However, only recently, larger samples of high-z observations of galaxy clusters became available and allowed statistical studies of the evolution of the substructure frequency up to $z \sim 1$. Since then, several observational X-ray studies have shown a larger fraction of dynamically relaxed clusters at lower redshift than at $z > 0.5$ (e.g. Melott et al. 2001; Plionis 2002; Jeltema et al. 2005; Bauer et al. 2005; Hashimoto et al. 2007a; Maughan et al. 2008; Andersson et al. 2009; Mann & Ebeling 2012). A less clear evolution was found in hydrodynamical simulations, but higher merger rates at high redshift support the observational results (e.g. Cohn & White 2005; Rahman et al. 2006; Kay et al. 2007; Burns et al. 2008; Jeltema et al. 2008).

Opening the window toward higher-redshift clusters is accompanied by the problem of the insufficient data quality of X-ray images in terms of net photon counts and background contribution. Exploring a broad redshift range directly translates into probing data with quite substantial quality differences. It is therefore not only essential to use well-studied morphology estimators but also to understand possible biases caused by uneven data quality.

In this work, we used two common X-ray substructure estimators, power ratio $P3/P0$

(Buote & Tsai 1995) and center shift w (Mohr et al. 1993), to study the relation between cluster structure and redshift up to $z = 1.08$. To do so, we took advantage of the detailed study of the influence of net photon counts and background on the computation of $P3/P0$ and w in our recently published work (Weißmann et al. 2013b). Jeltema et al. (2005) presented the first analysis of the $P3/P0 - z$ relation using 40 X-ray selected luminous clusters in the redshift range $0.1 < z < 0.89$. Using different statistical measures, they reported on average higher $P3/P0$ for clusters with $z > 0.5$ than for low-z objects. While they accounted for the bias caused by photon noise and background, they did not fully consider the strong decrease of data quality at higher redshifts and overestimated the $P3/P0 - z$ relation. In addition to using a larger sample, we explored possible biases caused by different observational depths in the low-z and high-z samples and determined how to account for them when analyzing the $P3/P0 - z$ and $w - z$ relation.

The paper is organized as follows. We characterize the sample and briefly discuss the data reduction process in Sect. 5.2. In Sect. 5.3 we introduce the morphology estimators $P3/P0$ and w used in this work. Sect. 5.4 summarizes how we degraded the high-quality data of the low-z sample to match the high-z observations. We give results in Sect. 5.5, including a detailed study of the influence of the different data quality in samples. Previous studies and the effect of cool cores are discussed in Sect. 5.6. We finally conclude with Sect. 5.7. Throughout the paper, the standard ΛCDM cosmology was assumed: H_0=70 km s^{-1} Mpc^{-1}, Ω_Λ=0.7, Ω_M=0.3.

5.2 Observations and data reduction

In this section we discuss the three samples used for our study: the low-z sample and the high-z subsamples of the 400SD and SPT surveys. An overview of the redshift distribution is shown in Fig. 5.1. Table 5.1 summarizes the sample statistics including the number of clusters, the redshift range, the mean net photon counts within r_{500}, and the mean net-(signal-)to-background photon counts ratio S/B. This table is discussed in more detail in Sect. 5.4, where we concentrate on the problem of the data quality. Details of the galaxy clusters and observational properties are given in Table 5.5. r_{500} was calculated for all clusters using the formula given by Arnaud et al. (2005). The temperature and redshift values were taken from previous works as indicated in Table 5.5. For a full gallery of the X-ray images of the galaxy clusters used in this study we refer to Weißmann et al. (2013b) for the low-z sample, the website of the 400d[2] cluster survey[1] for the high-z 400SD objects, and to Andersson et al. (2011) for the high-z SPT clusters. To give an impression of the substructure values and the data quality, we provide a few examples of background-included, point-source-corrected smoothed X-ray images in Fig. 5.2 (left panels) for the low-z sample and in Fig. 5.3 for the high-z samples.

5.2.1 Low-z cluster sample

The low-redshift sample (short: low-z) was previously used and discussed in detail in Weißmann et al. (2013b, W13 hereafter). For our current work, we excluded two clusters that were part of the W13 sample: RX J1347-1145 and RXC J0516-5430. RX J1347-1145 was omitted because of its high redshift of $z = 0.45$ and because we did not want to add this cluster to the high-z samples with defined origin. RXC J0516-5430 or SPT-CLJ0516-5430 ($z = 0.29$) was

[1] http://hea.iki.rssi.ru/400d/catalog/

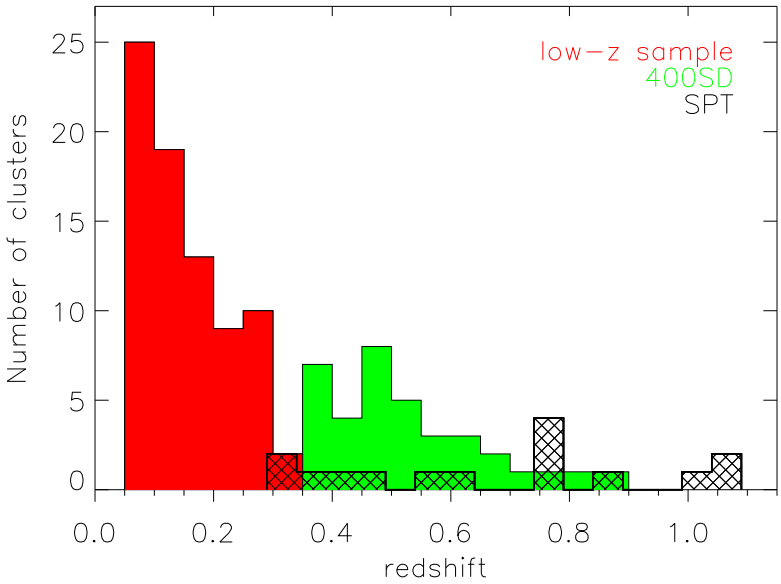

Figure 5.1: Redshift distribution of the low-z (red filled histogram), high-z 400SD (green filled histogram), and high-z SPT sample (black dashed histogram) .

already part of the high-z SPT sample. We thus excluded it from the low-z sample because of its high redshift.

The low-z sample now comprises 78 archival *XMM-Newton* observations of galaxy clusters covering redshifts between 0.05 and 0.31, with $\langle z \rangle = 0.15$. The clusters were drawn from several well-known samples observed with *XMM-Newton* (for details see Table 5.5): REXCESS (Böhringer et al. 2007), LoCuSS (Smith et al., Zhang et al. 2008), the Snowden Catalog (Snowden et al. 2008), the REFLEX-DXL sample (Zhang et al. 2006), and Buote & Tsai (1996). The clusters were chosen to be well-studied, nearby ($0.05 < z < 0.31$), and publicly available (in 2009) in the *XMM-Newton* science archive[2]. In addition, we required r_{500} to fit on the detector. The calculation of r_{500} using the formula of Arnaud et al. (2005) led to slightly different r_{500} and hence $P3/P0$ and w values to those quoted in W13. The differences are small, however. This merged low-z sample has no unique selection function, but a wide spread in luminosity, temperature, and mass. A large part of the clusters comes from representative samples such as REXCESS and LoCuSS and we therefore expect the sample to have a very roughly representative character. To check in more detail that no bias effect is introduced by the merged sample, we also performed all tests with the 31 REXCESS clusters only. The results are consistent with the full low-z sample and we therefore do not quote them in detail.

5.2.2 High-z cluster samples

In the high-redshift range, we used two samples to account for possible selection effects and performed our analysis on each sample individually: the X-ray-selected high-z subsample from the 400SD survey (Burenin et al. 2007; Vikhlinin et al. 2009a) and the SZ-selected

[2] http://xmm.esac.esa.int/xsa/

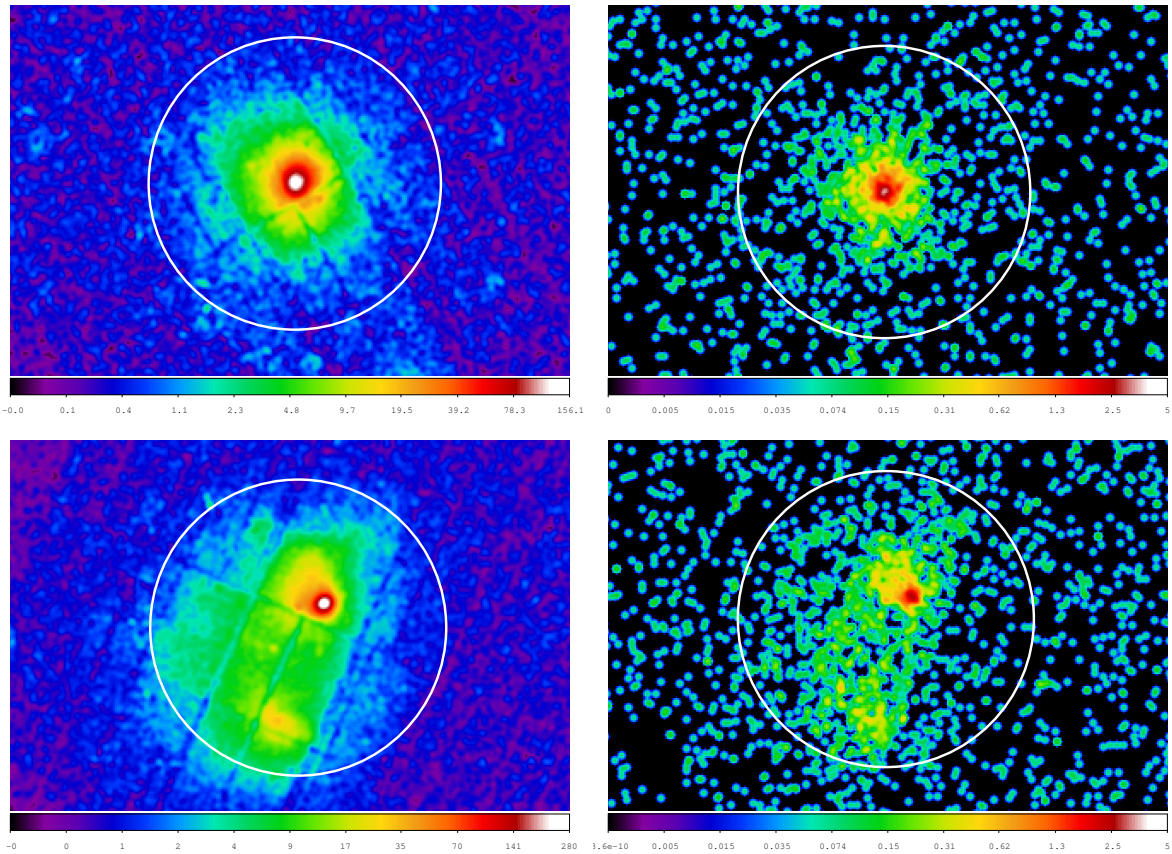

Figure 5.2: Examples of the background-included, point-source-corrected smoothed X-ray images of the low-z sample. **Left:** high-quality (undegraded) images. **Right:** degraded images (for details see Sect. 5.4.1). **Top panels:** A963 – relaxed galaxy cluster at $z = 0.21$ with $P3/P0 = (1.77 \pm 1.42) \times 10^{-8}$ and $w = (4.40 \pm 0.30) \times 10^{-3}$, non-significant detection after degrading. **Bottom panels:** A115 – merging cluster at $z = 0.20$ with $P3/P0 = (5.33 \pm 0.19) \times 10^{-6}$ and $w = (8.54 \pm 0.05) \times 10^{-2}$, significant detection after degrading. The circle indicates r_{500}.

subsample from SPT discussed in Andersson et al. (2011).

The high-z 400SD sample (short: 400SD) forms a complete subsample of the $z > 0.35$ clusters from the 400SD survey. It is composed of 36 objects in the $0.35 < z < 0.89$ range and was selected as a quasi-mass-limited sample at $z > 0.5$. This was done by requiring a luminosity above a threshold of $L_{\mathrm{X,min}} = 4.8{\times}10^{43}(1{+}z)^{1.8}$ erg s^{-1}. All 36 400SD clusters were observed with *Chandra* and are publicly available in the *Chandra* archive[3]. Several authors (e.g. Santos et al. 2010) have raised the question whether there might be a possible bias in the 400SD sample due to the detection algorithm. This may result in a lack of concentrated clusters compared with other high-redshift samples such as the *ROSAT* Deep Cluster Survey (RDCS, Rosati et al. 1998) or the Wide Angle *ROSAT* Pointed Survey (WARPS, Jones et al. 1998). We accounted for these effects by using the high-z SPT sample for comparison.

[3] `http://cxc.cfa.harvard.edu/cda/`

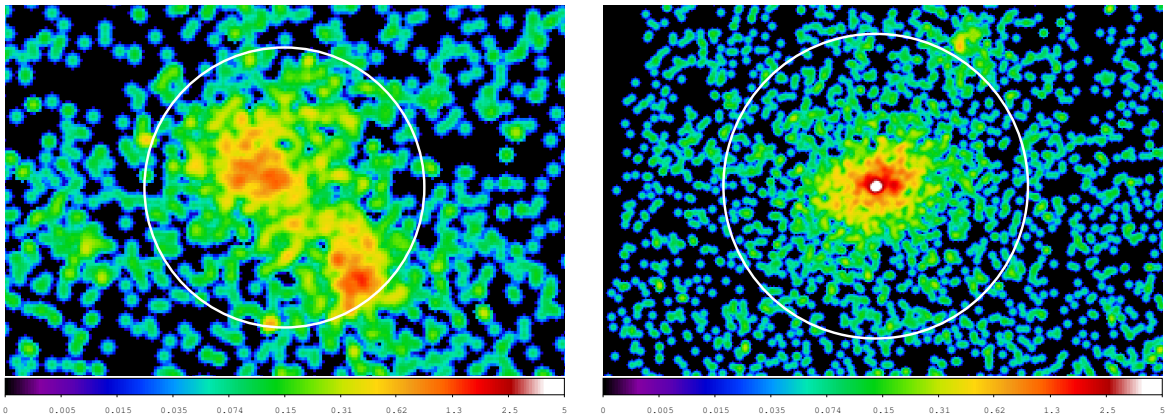

Figure 5.3: Examples of the background-included, point-source-corrected smoothed X-ray images of the high-z samples. **Left:** 0152-1358 – very structured cluster at $z = 0.83$ with $P3/P0 = (5.76 \pm 0.95) \times 10^{-5}$ and $w = (6.64 \pm 0.57) \times 10^{-2}$. This 400SD cluster has the highest $P3/P0$ value and is marked by a circle in Figs. 5.5-5.7. **Right:** SPT-CLJ0509-5342 – rather relaxed SPT cluster at $z = 0.46$ with a non-significant detection in $P3/P0$ and $w = (3.13 \pm 1.33) \times 10^{-3}$. The circle indicates r_{500}.

The high-z SPT sample (short: SPT) is a subsample of the first SZ-selected cluster catalog, obtained from observations of 178 deg^2 of sky surveyed by the South Pole Telescope (SPT). Vanderlinde et al. (2010) presented a significance-limited catalog of 21 SZ-detected galaxy clusters of which 15 objects with SZ-detection-significance above 5.4 were selected for an X-ray follow-up program. This subsample covers the redshift range $0.29 < z < 1.08$. The majority of the clusters was observed with *Chandra*, but for three objects we used *XMM-Newton* data because no *Chandra* data are available (SPT-CLJ2332-5358 and SPT-CLJ0559-5249) or because of the better photon statistics of the *XMM-Newton* observation (SPT-CLJ0516-5430). This results in 12 *Chandra* and 3 *XMM-Newton* observations (for details see Table 5.5, Column 9).

5.2.3 Data reduction

The 78 low-z and additional 3 high-z SPT *XMM-Newton* observations (SPT-CLJ2332-5358, SPT-CLJ0559-5249 and SPT-CLJ0516-5430) were taken from the public *XMM-Newton* Science archive and were analyzed with the *XMM-Newton* SAS[4] in the well-established standard 0.5 – 2 keV band, which covers most of the cluster signal. The low-z clusters and SPT-CLJ0516-5430 were reduced prior to this study using SAS v. 9.0.0, while we used v. 12.0.1 for the other two SPT objects. In both cases we followed the data reduction recipe described in detail in Böhringer et al. (2010, 2007), except for the point source removal. Point sources were detected with the SAS task *ewavelet* in the combined image from all three detectors to increase the sensitivity of the point source detection. However, we removed the point sources from each detector image in the 0.5 – 2 keV band individually and refilled the

[4]Science Analysis Software: `http://xmm.esa.int/sas/`

Table 5.1: Overview of the data quality of the samples. **Notes.** Mean net photon counts and mean S/B calculated within r_{500} of the reduced and point source corrected X-ray image. S/B gives the ratio of net photon counts (signal) to background photon counts. $P3/P0$ and w are computed in the r_{500} aperture. $P3/P0 > 0$ and $w > 0$ include all clusters with positive corrected substructure values, including positive non-significant detections. For clusters with non-significant results, we quote upper limits, which are taken as the sum of the non-significant result (or zero for a neg. corrected $P3/P0$ or w) and the 1-σ error (for details see Sect. 5.3). The significance S is computed as the ratio of $P3/P0$ or w with respect to its error. This table is discussed in more detail in Sect. 5.4.

	Low-z	400SD	SPT
Number of clusters	78	36	15
Redshift range	0.05 – 0.31	0.35 – 0.89	0.29 – 1.08
Mean net photon counts	96997	1203	1735
Mean S/B	6.6	3.7	3.2
$P3/P0 > 0$	68	22	11
Upper limits	14	21	8
$S_{P3} > 1$	55	6	3
$S_{P3} > 3$	28	2	0
Mean S_{P3}	2.6	0.5	0.4
Median S_{P3}	2.0	0.2	0.1
$w > 0$	78	35	15
Upper limits	1	3	1
$S_w > 1$	77	28	13
$S_w > 3$	74	19	5
Mean S_w	23.0	3.8	3.4
Median S_w	17.0	3.8	2.6

gaps using the CIAO[5] task *dmfilth*. In the next step we subtracted the background, which was obtained from a vignetting model fit to a source-excised, hard-band-scaled blank sky field from the point-source-corrected images and combined them. This method yields point-source-corrected images without visible artifacts of the cutting regions.

The high-z *Chandra* observations of the 400SD and SPT sample were treated as follows. A standard data reduction in the $0.5-2$ keV band was performed using the CIAO software package v4.4 and CALDB v4.4.7. This band was chosen to match the *XMM-Newton* data. For each observation, the level = 1 event file was reprocessed using *chandra_repro*, including amongst others the detection of afterglows, the generation of a new bad pixel file and corrections for differing gains across the CCDs, time-dependent gain, and charge transfer inefficiencies (CTIs). For observations taken in the VFAINT mode, we applied the additional background cleaning using the task *acis_process_events* while setting *check_vf_pha=yes*. This procedure uses the outer 5×5 pixel (instead of 3×3 for FAINT) event island to search for potential cosmic-ray

[5] *Chandra* Interactive Analysis of Observations software package: `http://cxc.harvard.edu/ciao/`

background events. Flared periods were excluded from the level = 2 event file using *lc_clean*. We created images in the 0.5 – 2 keV range and used *fluximage* to generate monochromatic 1 keV exposure maps. Point sources were detected and removed using *dmfilth*, which also refills the excised regions. For the background, blank-sky event files were reprojected, scaled to the exposure time of the flare-cleaned observation, restricted to the 0.5 – 2 keV range and binned with a factor of 4 to match the observations. When there were several pointings per cluster, we reduced the observations individually, but detected point sources on the merged 0.5 – 2 keV image. Images and exposure maps were merged using *reproject_image*.

5.3 Morphological analysis

We used power ratios and center shifts as morphology estimators for our analysis. The power ratio method was introduced by Buote & Tsai (1995) to quantify the amount of substructure in a cluster and its dynamical state. The powers are based on a 2D multipole expansion of the cluster's gravitational potential and are evaluated within a certain aperture radius (e.g. r_{500}). It is already well established that the normalized hexapole of the X-ray surface brightness, $P3/P0$, is sensitive to asymmetries on scales of the aperture radius and provides a useful measure of the dynamical state of a cluster (e.g. Buote & Tsai 1995; Jeltema et al. 2005; Böhringer et al. 2010; Chon et al. 2012, W13). Moreover, the center shift parameter w (e.g. Mohr et al. 1993; O'Hara et al. 2006; Böhringer et al. 2010; Chon et al. 2012, W13) characterizes the morphology of the cluster X-ray surface brightness. It measures the shift of the centroid, defined as the center of mass of the X-ray surface brightness, with respect to the X-ray peak in different apertures. The X-ray peak was determined from an image smoothed with a Gaussian with σ of 8 arcsec. The offset of the X-ray peak from the centroid was then calculated for ten aperture sizes ($0.1-1\ r_{500}$) and the final parameter w obtained as the standard deviation of the different center shifts in units of r_{500}. Unless stated otherwise, all presented $P3/P0$ and w values were calculated within an aperture of r_{500} and including the central region. However, we exclude the central $0.1\ r_{500}$ region when we calculated the X-ray centroid for the discussion in Sect. 5.6.2 to study possible effects of cool cores.

Both morphology estimators were discussed in our previous paper W13, where we studied the influence of background and shot noise on $P3/P0$ and w as a function of photon counts and presented a method to correct for these effects. In short, we first subtract the moments of the background image from those of the full (background-included) image to obtain a background-corrected power ratio. In a second step, we correct the bias caused by shot noise using repoissonized realizations of the cluster image. For w we subtract the background pixel values before calculating the position of the X-ray peak and centroid and estimate the shot noise bias analogous to the power ratios. For very regular clusters or observations highly influenced by noise, we sometimes overestimate the bias and obtain negative corrected $P3/P0$ and w values with errors exceeding the negative value. We call such results non-significant detections. Substructure values that are positive after the bias correction, but have a 1-σ error $\sigma(P3/P0)$ that exceeds the $P3/P0$ or w value by more than a factor of 3 are also considered as non-significant detections. For a more conservative factor of 1, hence taking values with $\sigma(P3/P0) > P3/P0$ or $\sigma(w) > w$ as non-significant detections, we find consistent results within the errors. For non-significant detections, we use upper limits (UL) in the analysis,

where $UL = \sigma(P3/P0) + P3/P0_{\mathrm{non-significant}}$ for positive and $UL = \sigma(P3/P0)$ for negative corrected $P3/P0$ values. The definition is analogous for w. All presented $P3/P0$ and w values are background and bias corrected.

During our discussion we will refer to different thresholds for $P3/P0$ and w to divide the sample according to the dynamical state of the clusters. These dividing boundaries are taken from our previous work W13, where we also defined the significance S of a $P3/P0$ or w value as the ratio of the bias-corrected signal with respect to the obtained error. For high-quality data ($S > 3$) we established two *morphological* $P3/P0$ *boundaries* to divide the sample into relaxed ($P3/P0 < 10^{-8}$), mildly disturbed ($10^{-8} < P3/P0 < 5 \times 10^{-7}$), and disturbed objects ($P3/P0 > 5 \times 10^{-7}$). High S values down to 10^{-8} allow for this detailed classification. When dealing with low-count observations, we reach $S = 1$ around 10^{-7} and use this value as *simple* $P3/P0$ *boundary* to separate disturbed and relaxed clusters. Owing to the data quality of the high-z samples (see Table 5.1), we only used the $P3/P0$ boundary at 10^{-7} for our analysis.

For the center shift parameter, we used $w = 0.01$ to split the sample. Since w is only severely affected by Poisson noise for considerably less than 1 000 net photon counts within r_{500} for a reasonably low background, this threshold can be used for high- and low-quality data.

5.4 Data quality

The strongest potential disadvantage when dealing with a combination of low- and high-z observations is the difference in the photon statistics of the observations, as can be seen by comparing Figs. 5.2 (left) and 5.3. Details of the sample statistics are given in Table 5.1, which shows that the low-z sample is not only larger in numbers but also in terms of higher photon statistics and a higher ratio of net (signal) to background photon counts (S/B). This results in a significant difference between the two samples in the extent and importance of photon shot noise. As we have shown in our previous work W13, photon shot noise can have a severe effect on the determination of the cluster morphology. We studied and quantified these effects and the influence of the background as a function of photon counts and S/B ratio for $P3/P0$ and w. We found that the center shift parameter can be determined with a small error even below the $w = 0.01$ threshold for low photon statistics ($< 1\,000$ net photon counts) and a reasonable S/B of e.g. ~ 2. We can therefore obtain reasonable results for all morphologies, partly with relative large errors for very relaxed objects. The power ratio method needs sufficient photon counts to overcome the influence of Poisson noise, however. We showed that this problem is not important for disturbed objects, which do not suffer severely from shot noise and thus enable an accurate estimation even for low-quality data. For decreasing photon counts, however, mildly disturbed and relaxed objects undergo a boost of their signal due to an underestimation of the bias contribution that yields substructure parameters that are too high. In the case of excessive noise, we obtain a non-significant result. High-quality data therefore enable a more reliable determination of $P3/P0$ (w) and better statistics, including a higher number of clusters with $P3/P0 > 0$ ($w > 0$) and a higher mean significance $\langle S \rangle$. A direct comparison between low- and high-quality data may thus not be conclusive.

Fig. 5.4 shows that the low-z data have more than sufficient photon counts with a mean of $\sim 97\,000$ net photon counts within r_{500} to give $P3/P0$ and w values with very good error

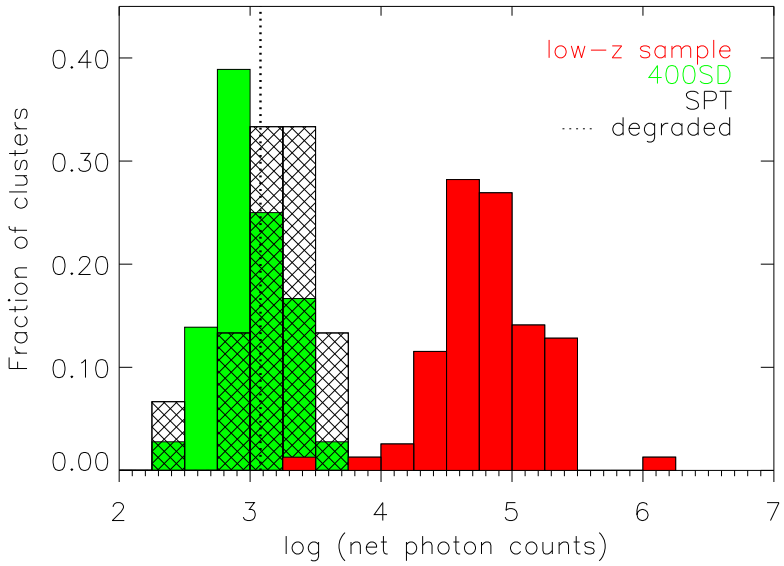

Figure 5.4: Overview of the net photon counts distribution within r_{500} of the low-z (red filled histogram), high-z 400SD (green filled histogram) and high-z SPT sample (black dashed histogram). The dotted line indicates the net photon counts of the degraded data.

properties and large S. The high-z objects, however, peak just above 1 000 net photon counts with a mean of $\sim$ 1 200 for 400SD and $\sim$ 1700 for SPT. According to simulations presented in W13, these high-z observations meet the criteria to roughly separate the sample into disturbed clusters with high and accurately determined substructure parameters and relaxed ones with parameters below the $P3/P0$ (w) threshold with large errors or non-significant detections. High-z observations contain a higher contribution from the background with a mean S/B of $\sim$ 3.5. This causes additional uncertainties due to the extra noise from the background and results in the low number of objects with $S > 1$. To obtain conclusive results we need to establish the influence of noise and the possible boost of the $P3/P0$ (w) signal due to the lower data quality in the high-z sample.

5.4.1 Degrading of high-quality low-z observations

To test how robust our results are to the difference in the data quality of the samples, we first performed our analysis using the high-quality or so-called undegraded low-z data. In addition, we created a degraded low-z sample by aligning the data quality of the low-z observations to that of the high-z objects. This was done by degrading the high-quality low-z observations to the photon statistics (1 200 net photon counts and S/B = 3.7 within r_{500}) of the 400SD high-z sample (see Table 5.1). The degrading was done in several steps, taking care of the different net and background photon counts and the increased Poisson noise. Two examples of degraded cluster images are given in Fig. 5.2 (right panels), compared with the undegraded images (left panels). The undegraded cluster image (IM_0) is not background subtracted. In the following recipe we denote images with capital letters and photon counts with lowercase letters. The recipe to obtain a low-z cluster and background image with the same photon statistics as the average high-z cluster is outlined in steps 1 – 4. However, observations with

low photon statistics do not only lack the sufficient number of photon counts, but also suffer from a considerable amount of Poisson noise. This is included by adding additional Poisson noise to the degraded image using the *zhtools*[6] task *poisson*. In steps 5 – 7 we summarize the statistical analysis using the poissonized realizations of these images.

1. Extract total photon counts (im_0) and background photon counts (bkg_0) within r_{500} from the undegraded cluster (IM_0) and background image (BKG_0). Obtain net photon counts of the cluster as $cl_0 = im_0 - bkg_0$ and the S/B as cl_0/bkg_0.

2. Calculate the additional background photon counts needed to obtain an S/B=3.7: $bkg_{\rm add} = (cl_0/3.7) - bkg_0$. Rescale the undegraded background image by $bkg_{\rm add}$: $BKG_{\rm add} = BKG_0 \cdot bkg_{\rm add}/bkg_0$

3. Add the additional background image to the undegraded cluster image: $IM_1 = IM_0 + BKG_{\rm add}$. This image has the desired S/B of 3.7.

4. Rescale IM_1 to 1 530 total photon counts within r_{500}: $IM_{\rm deg} = IM_1 \cdot (1530/im_1)$. Due to its S/B of 3.7, this degraded cluster image $IM_{\rm deg}$ comprises 330 background and 1 200 net photon counts. Rescale BKG_0 to 330 photon counts within r_{500}: $BKG_{\rm deg} = BKG_0 \cdot (330/bkg_0)$ to obtain the degraded background image.

5. Create 100 poissonized realizations of the degraded cluster image $IM_{\rm deg}$. Calculate background- and bias-corrected power ratios and center shifts including their errors for all 100 realizations of the cluster as described in W13.

6. Randomly select one realization per cluster to create a new sample of 78 degraded low-z observations and obtain statistical measures like BCES fits or mean values.

7. Repeat the previous step 100 times for statistical purposes and obtain the mean values. These are quoted when discussing our results including the mean errors.

5.5 Results

We studied the evolution of the substructure frequency up to $z = 1.08$ using different statistical measures on the morphology estimators $P3/P0$ and w: i) fitting the data in the $P3/P0 - z$ and $w - z$ plane with the linear relation $log(Y) = A \times log(z/0.25) + B$ for Y=$P3/P0$ and w respectively, ii) calculating mean values for the different redshift intervals and iii) analyzing the fraction of relaxed and disturbed objects using $P3/P0$ and w boundaries. For non-significant detections, we used upper limits as discussed in Sect. 5.3. These are not included in the BCES fits given in Table 5.2 and Figs. 5.5-5.7. All analyses were performed on the log-distribution of $P3/P0$ and w to take into account very low $P3/P0$ and w values. Fitting parameters were calculated using the BCES (Y|X) fitting method (Akritas & Bershady 1996), which minimizes the residuals in Y.

To study the $P3/P0-z$ and $w-z$ relation we formed two samples to study possible selection effects of the high-z samples: i) sample I – low-z sample and high-z subsample of 400SD

[6]hea-www.harvard.edu/RD/zhtools

sample, ii) sample II – low-z sample and high-z subsample of SPT sample. We argue that using the degraded low-z data might be essential to obtain reliable and conclusive results. We therefore performed the identical analysis on sample I/II and the degraded sample I/II, where we used the degraded low-z data. We point out that only the high-quality low-z observations are degraded and thus are different in sample I/II and degraded sample I/II. The high-z data remains unchanged. In the following we focus on the heavily noise-affected $P3/P0$ parameter and then consider the more robust w parameter.

During our analysis, we tried to include the information given by the upper limits in the $P3/P0 - z$ and $w - z$ fits and tested the ASURV (Feigelson & Nelson 1985; Isobe et al. 1986) and the LINMIX_ERR (Kelly 2007) routine. For upper limits, both methods use estimated data points for fitting that are computed from the input upper limit and the distribution of the detected data points. Several tests using simulated images showed that the estimated data points are strongly coupled to the fit obtained from the detected data points and do not reflect the true $P3/P0$ values. Since the censorship in our data is due to low counts and dependent on $P3/P0$ itself, we conclude that our data do not fulfill the requirements for these routines to work properly.

Table 5.2: Overview of the BCES (Y|z) fits in the log-log plane using the linear relation $log(Y) = A \times log(z/0.25) + B$ for Y=$P3/P0$ and w, respectively. **Notes.** Upper limits are omitted for these fits.

$P3/P0$	A	B	Fig.
Sample I	1.01 ± 0.31	-6.74 ± 0.10	5.5, left
Sample II	0.59 ± 0.36	-6.90 ± 0.12	5.5, left
Degraded sample I	0.24 ± 0.28	-6.03 ± 0.08	5.6, left
Degraded sample II	0.17 ± 0.24	-6.07 ± 0.08	5.6, left
w	A	B	Fig.
Sample I	0.18 ± 0.14	-2.01 ± 0.04	5.7, left
Sample II	0.02 ± 0.13	-2.05 ± 0.04	5.7, left
Degraded sample I	0.23 ± 0.12	-2.00 ± 0.04	
Degraded sample II	0.07 ± 0.11	-2.04 ± 0.04	

5.5.1 $P3/P0 - z$ relation

We first discuss the structure parameter $P3/P0$ as a function of redshift for sample I and II using Fig. 5.5. On the left side we show only the significant data points, while we include non-significant results as upper limits (arrows) on the right. For illustration, we show the $P3/P0$ boundary at 10^{-7} to separate relaxed and disturbed objects. When looking at this figure, one immediately notices the lack of significant detections of high-z clusters with $P3/P0 < 10^{-7}$. In addition, essentially all upper limits are found above this $P3/P0$ boundary. We quantified the $P3/P0 - z$ relation using the undegraded low-z data and different statistical measures. On the left of Fig. 5.5 we show the linear BCES fit. For sample I we obtained a more than 3σ significant slope with $A = 1.01 \pm 0.31$, for sample II we found a somewhat shallower

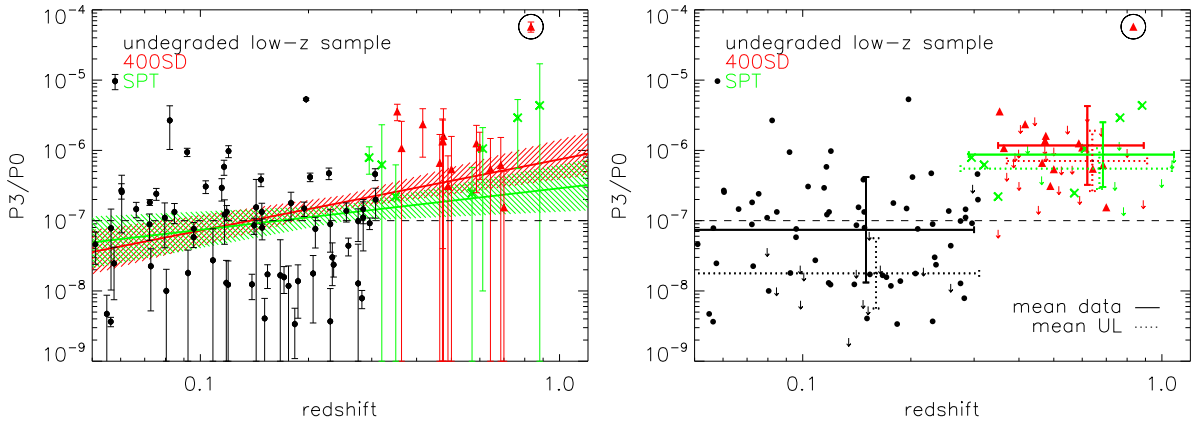

Figure 5.5: Undegraded $P3/P0 - z$ relation. Low-z (black circles), 400SD (red triangles), and SPT (green crosses) sample. **Left:** The BCES fit to sample I is shown as a red line while the green line indicates the fit to sample II. The dashed areas show the 1-σ error of best-fitting values. Fitting parameters are given in Table 5.2. The very structured 400SD cluster 0152-1358 at $z \sim 0.8$ with $P3/P0 > 10^{-5}$ is marked by a black circle. Excluding this cluster from sample I gives consistent results. In addition we show the $P3/P0$ boundary at 10^{-7} (dashed line). **Right:** Same data points as on the left, but including upper limits as downward arrows. For all three samples the solid lines give the mean of the log distribution of the significant data points including the 1-σ errors, while the dotted lines show the mean of the upper limits.

slope of $A = 0.59 \pm 0.36$. We then tested the influence of the very structured 400SD cluster 0152-1358 ($z \sim 0.8$) with $P3/P0 > 10^{-5}$ on the fit, finding a shallower, but consistent slope when excluding it from the fit.

Another way of quantifying the observed relation is computing the fraction of relaxed and disturbed objects in comparison to upper limits, which are shown in Table 5.3. Because of the high data quality of the undegraded low-z observations, the fraction of upper limits is small. All these objects can be considered as relaxed clusters because $P3/P0$ can detect significant signals well below 10^{-7} for such good data quality. Their non-significant signals or upper limits are consistent with $P3/P0 \ll 10^{-7}$. In addition, we find 45% of the low-z objects to be relaxed. The majority of clusters in this sample is found below the $P3/P0$ threshold of 10^{-7} with a mean of the log $P3/P0$ distribution of -7.1 ± 0.8. The high-z samples yield a higher mean of -5.9 ± 0.6 (-6.1 ± 0.5) for 400SD (SPT). The mean values are given in Table 5.4 and are denoted as *mean data* for the significant data points and *mean UL* for the upper limits. We plot the mean data values in Fig. 5.5 on the right side to illustrate this offset. In addition, we add the mean UL values to emphasize again the difference in the location of upper limits for the high- and low-quality data.

All statistical measures used on this dataset so far give a clear trend of a larger fraction of disturbed clusters at higher redshift. This conclusion should not be drawn without caution, however, since we are comparing very different datasets. We already argued that $P3/P0$ is heavily influenced by noise for observations with low net photon counts and/or high background. The computation of substructure parameters for the high-z objects therefore suffers

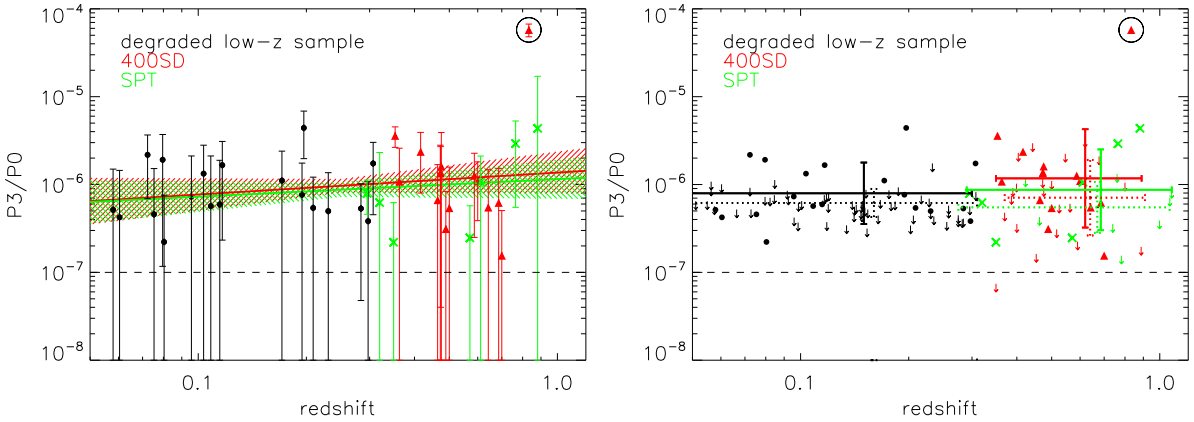

Figure 5.6: Degraded $P3/P0 - z$ relation. Details are the same as in Fig. 5.5.

severely from noise. According to results presented in W13, we can obtain significant $P3/P0$ values for the majority of the disturbed clusters even with fewer than 1 000 net photon counts within r_{500}. Mildly disturbed and relaxed objects will mostly either yield non-significant detections or undergo a boost of the $P3/P0$ signal. Except for some mildly disturbed objects whose $P3/P0$ values are just below the 10^{-7} boundary in the undegraded case, this boost will not result in $P3/P0 > 10^{-7}$. We should thus be able to very roughly separate the sample into disturbed ($P3/P0 > 10^{-7}$) and relaxed ($P3/P0 < 10^{-7}$ and upper limits) objects.

We repeated the analysis using the degraded low-z data and show the results in Fig. 5.6. We found significantly shallower slopes of $A = 0.24 \pm 0.28$ ($A = 0.17 \pm 0.24$) and higher intercepts B for the degraded sample I (II). This is due to the apparent loss of data points with $P3/P0 < 10^{-7}$ and large errors on the detected $P3/P0$ signals after degrading. We find a significant increase of the upper limit fraction to 72% while the fraction of relaxed clusters decreases from 45% to on average 0% (Table 5.3). The fraction of disturbed objects stays roughly the same, showing that we can detect a signal for the majority of structured objects while only a small number gives upper limits. With these low-quality data, we cannot measure a significant $P3/P0$ value for mildly disturbed or relaxed clusters anymore, but only detect disturbed objects.

For the high-z samples, we found no objects with $P3/P0 < 10^{-7}$ but a large number of upper limits (Table 5.3) and a disturbed cluster fraction of 42% for 400SD and 47% for SPT. Assuming that the majority of the disturbed objects yield significant detections, we found a slightly higher fraction of disturbed objects in the high-z samples than in the degraded low-z sample.

We performed more tests by varying the degree of degradation of the low-z data. We found that the larger the disagreement between the net photon counts and S/B of the samples, the more biased the obtained slope or mean value. It is therefore of extreme importance to take this issue into account when analyzing the $P3/P0 - z$ relation.

5.5.2 $w - z$ relation

Analogously to $P3/P0$, we used the same statistical measures on the w parameter to probe its behavior as a function of redshift. Fig. 5.7 shows the w distribution for sample I and

Table 5.3: Fraction of relaxed and disturbed objects using $P3/P0$ and w boundaries taken from W13 (see Sect. 5.3). Upper limits (UL) are given for non-significant detections. **Notes.** [(a)] Mean values of 100 randomly selected samples.

$P3/P0$	$P3/P0 < 10^{-7}$	$P3/P0 > 10^{-7}$	UL
Undeg. low-z data	45%	37%	18%
Deg. low-z data[a]	0%	31%	72%
400SD	0%	42%	58%
SPT	0%	47%	53%
w	$w < 0.01$	$w > 0.01$	UL
Undeg. low-z data	58%	41%	1%
Deg. low-z data[a]	52%	43%	6%
400SD	39%	53%	8%
SPT	60%	33%	7%

II, including upper limits on the right and the $w = 0.01$ boundary to separate relaxed and disturbed objects. We performed a linear BCES fit and give the fitting parameters in Table 5.2. The fits are illustrated on the left side of Fig. 5.7, with slope $A = 0.18 \pm 0.14$ ($A = 0.02 \pm 0.13$) for sample I (II). These slopes are both positive, but not significant and consistent with zero within 1-σ. In contrast to $P3/P0$, low- and high-z clusters populate the full w range. This is reflected in the very similar mean values of the samples and their upper limits. We show these values in Table 5.4 and Fig. 5.7 on the right side.

Because the w parameter is not very sensitive to noise when dealing with $> 1\,000$ net photon counts and a background that is not too high – as is the case with the high-z observations -, degrading the low-z observations to match the data quality of the 400SD clusters shows little effect. All statistical measures show very similar results when using the degraded low-z sample (Tables 5.2-5.4). The slopes stay well within the errors, and the mean data value does not change either. Only the mean upper limit value increases slightly, because the undegraded low-z data contains only one upper limit, but the degraded sample contains a few more. This is reflected in the slight increase of the upper limit fraction from 1% to 6%, which is very similar to those of the 400SD (8%) and SPT (7%) sample. The fraction of relaxed objects decreases slightly for the degraded data from 58% to 52%, while it increases for disturbed objects from 41% to 43%. These changes are within the errors and again show the robustness of w against noise. Comparing the low-z fractions with those of the high-z samples, we see a very similar behavior of the SPT clusters, but the 400SD sample shows a larger fraction of objects with $w > 0.01$.

5.6 Discussion

Assessing the dynamical state of a galaxy cluster calls for a well-studied method for detecting and quantifying substructure in the ICM. Well-understood error properties are of great importance, especially when dealing with high-z observations and thus low photon statistics. The two applied methods, power ratios and center shifts, fulfill these requirements. A strong

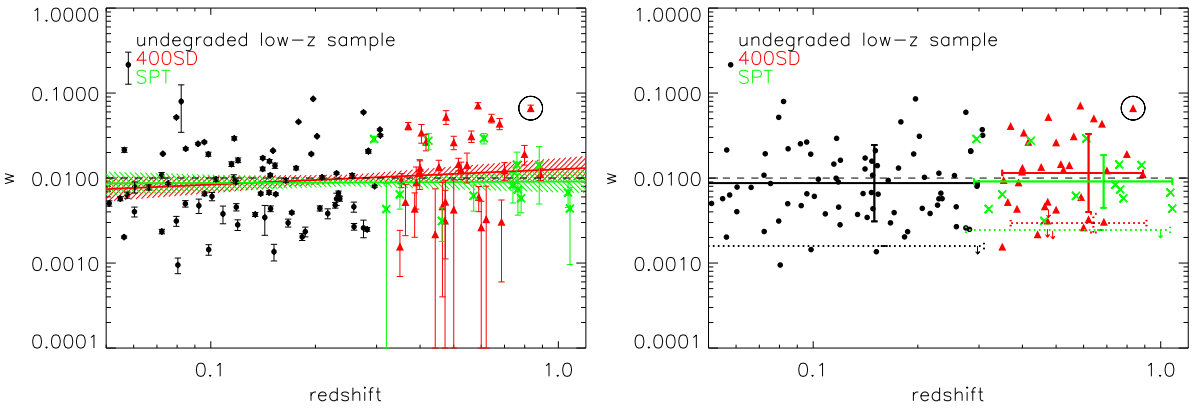

Figure 5.7: Undegraded $w - z$ relation. Details are the same as in Fig. 5.5, except for the w boundary at 10^{-2} (dashed line).

Table 5.4: Mean log($P3/P0$) and log(w) values for the low- and high-redshift samples. **Notes.** We give the mean of the significant data points (mean data) and the upper limits (mean UL) including their 1-σ errors.

	Low-z data		400SD	SPT
log($P3/P0$)	undegraded	degraded	undegraded	
Mean data	-7.1 ± 0.8	-6.1 ± 0.4	-5.9 ± 0.6	-6.1 ± 0.5
Mean UL	-7.8 ± 0.5	-6.2 ± 0.2	-6.2 ± 0.4	-6.3 ± 0.3
log(w)	undegraded	degraded	undegraded	
Mean data	-2.1 ± 0.5	-2.1 ± 0.4	-1.9 ± 0.5	-2.0 ± 0.3
Mean UL	-2.8	-2.6 ± 0.1	-2.5 ± 0.1	-2.6

correlation with a large scatter between $P3/P0$ and w is known from previous studies (e.g. Böhringer et al. 2010) and therefore a similar trend in both relations is expected. Comparing the results obtained from applying $P3/P0$ and w on sample I/II shows a very large discrepancy. While $P3/P0$ shows a significant increase with redshift in all statistical measures used, w shows a positive but non-significant slope and no trend in the mean values either. We claim that the discrepancy between these results is caused by the inconsistent data quality of the full sample, which affects $P3/P0$ more than w. Taking into account the slopes, mean values, and fractions, one can conclude that w is not sensitive to different data quality since the results hardly change.

For of $P3/P0$, degrading the high-quality low-z observations to the net photon counts and background of the high-z objects yields very different results. The slope flattens significantly, yielding a similar result to w – a positive but non-significant slope. The fraction of upper limits increases dramatically, because all relaxed objects yield non-significant detections. The fraction of low-z disturbed object is therefore only slightly smaller than those of the 400SD and SPT sample. Moreover, the mean data and mean UL values match those of the high-z samples when using equal data quality.

The results using $P3/P0$ and w on this particular dataset show a similar trend. We found a very mild positive evolution, which is also consistent with no change with redshift within the significance limits. We excluded a strong increase of the disturbed cluster fraction with redshift and set an upper limit with the shallow slopes of the BCES fits. For the lower limit, we found no indication of a negative evolution because all statistical measures show an increase of $P3/P0$ and w with redshift, but with low significance.

5.6.1 Comparison with previous studies

In the light of our finding that the different data quality between the low-z and high-z sample can severely bias the results, we compared our work with previous studies that did not take this problem into account. Jeltema et al. (2005) presented the first analysis of the $P3/P0 - z$ relation using 40 X-ray-selected luminous clusters in the $0.1 < z < 0.89$ range and a fixed physical aperture of 0.5 Mpc. They found the slope of the linear $P3/P0 - z$ relation to be 4.1×10^{-7}, but did not provide an intercept. We argue that a linear fit is not sensitive enough when working with a $P3/P0$ range of $10^{-9} - 10^{-5}$. High $P3/P0$ values like that of the 400SD cluster 0152-1358 ($P3/P0 > 10^{-5}$ at $z \sim 0.8$) dominate a linear fit, while low $P3/P0$ values are not adequately taken into account. We therefore did not include this result in Fig. 5.8, which compares our findings with previous studies. Jeltema et al. (2005) also provided mean $P3/P0$ values for $z < 0.5$ and $z > 0.5$ objects. For a fair comparison, we calculated $P3/P0$ in the same 0.5 Mpc aperture, since r_{500} is typically larger than 1 Mpc for the low-z sample and on average 0.8 Mpc for high-z objects. A fixed aperture of 0.5 Mpc probes the cluster structure on a different scale than r_{500}. For the 0.5 Mpc aperture, the slopes of the fits are steeper and the intercepts higher with $A = 1.52 \pm 0.30$ ($A = 1.08 \pm 0.39$) and $B = -6.61 \pm 0.07$ ($B = -6.75 \pm 0.10$) for sample I (II). After degrading, the $P3/P0 - z$ fits flatten significantly to $A = 0.42 \pm 0.18$ ($A = 0.08 \pm 0.31$) with $B = -5.96 \pm 0.06$ ($B = -6.09 \pm 0.10$) for the degraded sample I (II) and agree well with the degraded results when using r_{500} as aperture. The general impression of a very mild increase of the disturbed cluster fraction with redshift thus holds also for the 0.5 Mpc aperture. We show the fits for sample I and the degraded sample I using the 0.5 Mpc aperture in Fig. 5.8. The discrepancy between our fit of the degraded sample I and the mean values of Jeltema et al. (2005) is apparent. While Jeltema et al. (2005) took general noise properties into account, they did not address the problem of the data quality difference, which results in an overestimation of the slope and a large offset between the mean low-z and high-z sample.

Another study was performed by Andersson et al. (2009), who also calculated $P3/P0$ in an 0.5 Mpc aperture for 101 galaxy clusters in the range $0.07 < z < 0.89$. They reported an increase in $P3/P0$ and provided average $P3/P0$ values given for three redshift bins ($0.069 < z < 0.1$, $0.1 < z < 0.3$ and $z > 0.3$). We see an offset to our degraded fits here as well.

Several studies using both simulations (e.g. Ho et al. 2006) and observations (e.g. Melott et al. 2001; Plionis 2002; Maughan et al. 2008) explored the evolution of ellipticity with redshift. The asymmetry in the X-ray surface brightness distribution was studied by Hashimoto et al. (2007a), reporting no significant difference regarding ellipticity and off-center between the low- and high-z sample, but a hint of a weak evolution for the concentration and asymmetry parameter. Recently, Mann & Ebeling (2012) presented a study of the evolution of the cluster

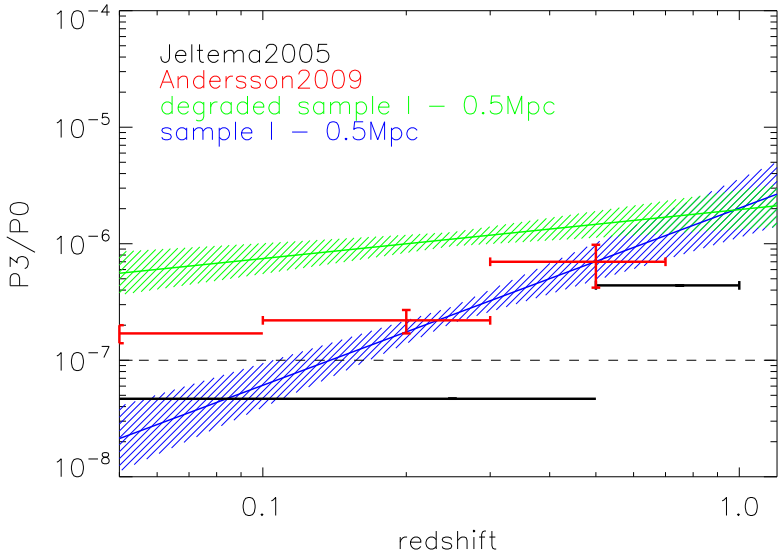

Figure 5.8: Comparison with previous studies. From Jeltema et al. (2005) we show the mean $P3/P0$ values for $z < 0.5$ and $z > 0.5$ objects (black). Errors on these values are not provided. In addition, we plot the mean $P3/P0$ of Andersson et al. (2009) for three redshift bins ($0.069 < z < 0.1$, $0.1 < z < 0.3$ and $z > 0.3$) in red. We provide our slope of the $P3/P0 - z$ plane calculated using an aperture of 0.5 Mpc for sample I (blue line) and the degraded sample I (green line) including the 1-σ errors as dashed area. The dashed line indicates the $P3/P0$ boundary at 10^{-7}.

merger fraction using 108 of the most X-ray-luminous galaxy clusters at $0.15 < z < 0.7$. They used optical and X-ray data and classified mergers according to their morphological class, X-ray centroid – BCG separation and X-ray peak – BCG separation. They reported an increase of the fraction of disturbed clusters with redshift, starting around $z = 0.4$.

In addition to observational studies, we compared our findings with those of Jeltema et al. (2008), who studied the evolution of cluster structure with $P3/P0$ and w in hydrodynamical simulations performed with Enzo, a hybrid Eulerian adaptive mesh refinement/N-body code. Their simulations did not include the effect of noise or instrumental response, therefore only a broad comparison to low-z observed data with high signal-to-noise is possible. They reported a dependence of the evolution of $P3/P0$ with redshift on the selection criterium and on the radius chosen. While for w they found a significant increase with redshift for a mass as well as a luminosity cut, $P3/P0$ showed an evolution only for a luminosity-limited sample. In agreement with our results, they stated that the evolution of cluster structure is mild compared with the variety of cluster morphologies seen at all redshifts.

5.6.2 Effect of cool cores

Several studies showed that cool cores are preferentially found in relaxed systems. Santos et al. (2010) and Andersson et al. (2009) found a negative evolution of the fraction of cool-core clusters, reporting that the number of cooling core clusters appears to decrease with redshift. This suggests a higher fraction of relaxed clusters at low than at high redshift. They

also argued that the evolution is significantly less pronounced than previously claimed. Bauer et al. (2005) used the high-z end of the BCS sample and concluded that the fraction of cool-cores does not significantly evolve up to $z \sim 0.4$.

It is therefore an interesting exercise to study whether the $P3/P0 - z$ and $w - z$ relation is driven by the presence of a cool core or by the overall dynamical state of the cluster. To do this, we excluded the 0.1 r_{500} region when calculating the centroid, but kept it to determine the X-ray peak. For an aperture of r_{500} we found very similar slopes for both relations. For w the slope becomes somewhat shallower but remains well within the 1-σ error with $A = 0.10 \pm 0.14$ ($A = -0.07 \pm 0.13$) and $B = -1.97 \pm 0.04$ ($B = -2.02 \pm 0.04$). As expected, degrading has no real effect on the center-excised $w - z$ relation, and the mean values also stay well within the errors. Contrary to our findings, Maughan et al. (2008) reported a significant absence of relaxed clusters at high redshift using a sample of 115 galaxy clusters in the $0.1 < z < 1.3$ range and center shifts with the central 30 kpc excised as morphology estimator.

$P3/P0$, on the other hand, yields slightly higher values on average when excluding the center, which results in a very similar slope of $A = 0.97 \pm 0.29$ ($A = 0.58 \pm 0.32$), but in a higher intercept of $B = -6.53 \pm 0.09$ ($B = -6.68 \pm 0.10$) and higher mean values for sample I (II). The same effects are seen when using the degraded low-z sample. The analysis was repeated using the fixed 0.5 Mpc aperture. We found a larger difference between the core-included and excised $P3/P0 - z$ relation for this aperture, because it is more sensitive to substructure in the inner region of the cluster. The obtained results are comparable with the r_{500} case, however. We conclude that based on the method to obtain $P3/P0$ and w, the $P3/P0 - z$ and $w - z$ relations seem to be mainly driven by the dynamical state of the cluster on the scale of the aperture radius.

5.7 Conclusions

We studied the evolution of the substructure frequency by comparing a merged sample of 78 low-z observations of galaxy clusters with the high-z subsample of the 400SD and SPT sample. The analysis was performed on two samples individually to exclude possible selection effects of the high-z samples: i) sample I: 78 low-z and 36 400SD, ii) sample II: 78 low-z and 15 SPT clusters. Power ratios $P3/P0$ and the center shift parameter w were used to quantify the amount of substructure in the cluster X-ray images.

We found that directly comparing high-quality low-z and low-quality high-z observations using $P3/P0$

- yields a very steep $P3/P0 - z$ relation with slopes of 1.01 ± 0.31 (0.59 ± 0.36) for sample I (II),
- gives a significant difference in the mean $P3/P0$ values of the low-z and high-z samples, and
- returns a very large fraction of relaxed objects at low-z (45%), but none at high-z.

However, as was shown in our previous work (Weißmann et al. 2013b), $P3/P0$ is very sensitive to noise and thus to the depth and quality of the observation. We corrected for the noise bias, but uncertainties in the results of low-quality data remained. Since there is a significant

difference in the data quality of the samples, this problem needed to be considered during the analysis. We therefore degraded the high-quality low-z observations to the photon statistics of the high-z 400SD observations. This enabled a comparison of data with similar quality and thus more reliable results. Using equal data quality and $P3/P0$, we found

- a weak, but not very significant evolution in the $P3/P0 - z$ relation with slopes of 0.24 ± 0.28 (0.17 ± 0.24) for the degraded sample I (II),
- no difference in the mean $P3/P0$ value of the low-z and high-z samples,
- that all relaxed ($P3/P0 < 10^{-7}$) low-z clusters yield non-significant detections after degradation, and
- a slightly larger fraction of disturbed clusters in the high-z samples (42% for 400SD, 47% for SPT) than in the degraded low-z sample (31%).

We performed the same analysis using the center shift parameter w as morphology estimator. w is more robust against Poisson noise and not very sensitive to the data quality difference of the samples. We therefore found very similar results using the undegraded and degraded low-z data, namely

- a very shallow slope of the $w - z$ relation: 0.18 ± 0.14 (0.02 ± 0.13) for sample I (II), 0.23 ± 0.12 (0.07 ± 0.11) for the degraded sample I (II),
- no difference in the mean w value of the low-z and high-z samples, and
- no significant difference in the fraction of relaxed and disturbed objects.

Considering that the 400SD high-z sample may contain an unrepresentatively large number of disturbed clusters, the slopes obtained using this dataset should be taken as upper limits. They are consistent with the results when using the SPT clusters as high-z sample, however. In summary, we agree with previous findings, which indicate an evolution of the substructure frequency with redshift.

We conclude that the results using $P3/P0$ and w on this particular dataset show a similar and very mild positive evolution of the substructure frequency with redshift. However, within the significance limits, our findings are also consistent with no evolution. A strong increase of the disturbed cluster fraction is excluded and the BCES fits are taken as upper limits. For the lower limit, we found no indication of a negative evolution. All statistical measures show a slight increase of $P3/P0$ and w with redshift, but with low significance. Larger samples of deep observations of $z > 0.3$ galaxy clusters would provide a better way to quantify these relations and allow unambiguous conclusions.

Acknowledgements
We would like to thank the anonymous referee for constructive comments and suggestions. This work is based on observations obtained with *XMM-Newton* and *Chandra*. *XMM-Newton* is an ESA science mission with instruments and contributions directly funded by ESA Member States and NASA. The *XMM-Newton* project is supported by the Bundesministerium für Wirtschaft und Technologie/Deutsches Zentrum für Luft- und Raumfahrt (BMWI/DLR, FKZ 50 OX 0001), the Max-Planck Society and the Heidenhain-Stiftung. A part of the scientific

results reported in this article is based on data obtained from the *Chandra* Data Archive. AW acknowledges the support from and participation in the International Max-Planck Research School on Astrophysics at the Ludwig-Maximilians University. GC acknowledges the support from Deutsches Zentrum für Luft- und Raumfahrt (DLR) with the program ID 50 R 1004. HB and GC acknowledge support from the DfG Transregio Program TR33 and the Munich Excellence Cluster "Structure and Evolution of the Universe".

Table 5.5: Details of the individual galaxy clusters including structure parameters. **Notes.** Column 2: cluster redshift; Column 3: r_{500} in Mpc estimated from the formula given by Arnaud et al. (2005); Column 4/6: bias- and background-corrected $P3/P0$ and w values calculated in an aperture of r_{500} including the central region. Errors are 1-σ uncertainties; Column 5/7: flags for upper limits where 0 indicates a significant detection and 1 an upper limit. For flag 1 $P3/P0/w$ and its error are the same. The upper limit is calculated as described in Sect. 5.3; Column 8: Reference. In case of multiple references, * indicates the temperature source for the r_{500} calculation; Column 9: Flag indicating whether an *XMM-Newton* (X) or *Chandra* (C) image was used in the analysis. **References.** (1) LoCuSS: Zhang et al. (2008); (2) REFLEX-DXL: Zhang et al. (2006); (3) Snowden et al. (2008); (4) Arnaud et al. (2005); (5) Buote & Tsai (1996); (6) REXCESS: Böhringer et al. (2010); (7) high-z 400SD sample: Vikhlinin et al. (2009a); (8) high-z SPT sample: Andersson et al. (2011).

Cluster	Redshift	r_{500}	$P3/P0$	UL	w	UL	Reference	Image
Low-z sample								
RXCJ0307.0-2840	0.26	1.18	1.26×10^{-8}	1	$(4.59 \pm 0.52) \times 10^{-3}$	0	1,2	X
RXCJ0528.9-3927	0.28	1.12	$(1.11 \pm 0.74) \times 10^{-7}$	0	$(2.06 \pm 0.11) \times 10^{-2}$	0	1,2	X
RXCJ0532.9-3701	0.28	1.23	$(9.88 \pm 4.84) \times 10^{-8}$	0	$(2.59 \pm 0.61) \times 10^{-3}$	0	1,2	X
RXCJ0658.5-5556	0.30	1.46	$(9.19 \pm 1.72) \times 10^{-8}$	0	$(8.01 \pm 0.23) \times 10^{-3}$	0	1*,2,3,5	X
RXCJ0945.4-0839	0.15	1.06	6.92×10^{-8}	1	$(1.40 \pm 0.10) \times 10^{-2}$	0	1	X
RXCJ2129.6+0005	0.24	1.12	$(2.36 \pm 0.79) \times 10^{-8}$	0	$(5.72 \pm 0.37) \times 10^{-3}$	0	1	X
RXCJ2308.3-0211	0.30	1.20	3.24×10^{-7}	1	1.58×10^{-3}	1	1*,2	X
RXCJ2337.6+0016	0.28	1.21	$(1.28 \pm 3.35) \times 10^{-8}$	0	$(5.94 \pm 0.10) \times 10^{-2}$	0	1*,2	X
A68	0.26	1.20	$(1.37 \pm 0.42) \times 10^{-7}$	0	$(1.07 \pm 0.06) \times 10^{-2}$	0	1*,3	X
A115	0.20	1.13	$(5.33 \pm 0.19) \times 10^{-6}$	0	$(8.54 \pm 0.05) \times 10^{-2}$	0	1	X
A209	0.21	1.22	$(7.63 \pm 3.55) \times 10^{-8}$	0	$(1.02 \pm 0.04) \times 10^{-2}$	0	1*,3	X
A267	0.23	1.11	$(8.93 \pm 5.37) \times 10^{-8}$	0	$(5.70 \pm 0.94) \times 10^{-3}$	0	1	X
A383	0.19	0.97	$(1.38 \pm 0.97) \times 10^{-8}$	0	$(2.34 \pm 0.31) \times 10^{-3}$	0	1*,3	X
A773	0.22	1.32	2.14×10^{-8}	1	$(3.83 \pm 0.52) \times 10^{-3}$	0	1*,3	X
A963	0.21	1.16	$(1.77 \pm 1.42) \times 10^{-8}$	0	$(4.40 \pm 0.30) \times 10^{-3}$	0	1	X
A1413	0.14	1.21	$(1.55 \pm 2.31) \times 10^{-7}$	0	$(3.44 \pm 1.32) \times 10^{-3}$	0	1*,3,4,5	X
A1763	0.23	1.07	$(4.72 \pm 0.89) \times 10^{-7}$	0	$(4.80 \pm 0.37) \times 10^{-3}$	0	1	X
A1914	0.17	1.40	$(1.57 \pm 0.65) \times 10^{-8}$	0	$(3.92 \pm 0.13) \times 10^{-3}$	0	1*,3,5	X
A2390	0.23	1.59	$(3.01 \pm 1.82) \times 10^{-8}$	0	$(6.63 \pm 0.40) \times 10^{-3}$	0	1	X
A2667	0.23	1.19	$(3.69 \pm 7.12) \times 10^{-9}$	0	$(1.14 \pm 0.03) \times 10^{-2}$	0	1*,3	X
A2204	0.15	1.37	6.03×10^{-9}	1	$(1.36 \pm 0.30) \times 10^{-3}$	0	1*,3,4,5	X
A2218	0.18	1.19	$(1.18 \pm 1.09) \times 10^{-8}$	0	$(1.31 \pm 0.06) \times 10^{-2}$	0	1*,3,5	X
RXCJ0232.2-4420	0.28	1.12	$(1.45 \pm 0.55) \times 10^{-7}$	0	$(2.09 \pm 0.06) \times 10^{-2}$	0	1*,2	X
A13	0.10	0.95	$(3.06 \pm 0.63) \times 10^{-7}$	0	$(9.68 \pm 0.51) \times 10^{-3}$	0	3	X
A520	0.19	1.31	$(1.49 \pm 0.35) \times 10^{-7}$	0	$(1.92 \pm 0.04) \times 10^{-2}$	0	3	X
A665	0.18	1.32	$(1.78 \pm 0.76) \times 10^{-7}$	0	$(4.58 \pm 0.07) \times 10^{-2}$	0	3*,5	X
A1068	0.15	0.99	7.41×10^{-9}	1	$(6.76 \pm 0.35) \times 10^{-3}$	0	3,4*,5	X
A1589	0.07	0.88	$(8.85 \pm 3.60) \times 10^{-8}$	0	$(1.08 \pm 0.08) \times 10^{-2}$	0	3	X
A2163	0.20	1.85	$(4.17 \pm 0.58) \times 10^{-7}$	0	$(3.10 \pm 0.05) \times 10^{-2}$	0	3	X
A2717	0.05	0.74	$(4.62 \pm 2.23) \times 10^{-8}$	0	$(5.03 \pm 0.36) \times 10^{-3}$	0	3,4*,5	X
A3112	0.07	0.98	$(1.82 \pm 0.17) \times 10^{-7}$	0	$(2.35 \pm 0.14) \times 10^{-3}$	0	3	X
A3827	0.10	1.21	$(7.62 \pm 1.78) \times 10^{-8}$	0	$(6.53 \pm 0.34) \times 10^{-3}$	0	3	X
A3911	0.10	1.15	$(5.81 \pm 1.67) \times 10^{-8}$	0	$(2.65 \pm 0.06) \times 10^{-2}$	0	3	X
A3921	0.09	1.08	$(9.44 \pm 1.27) \times 10^{-7}$	0	$(2.53 \pm 0.07) \times 10^{-2}$	0	3	X
E1455+2232	0.26	0.97	$(4.40 \pm 1.25) \times 10^{-8}$	0	$(2.68 \pm 0.24) \times 10^{-3}$	0	3	X
PKS0745-19	0.10	1.37	7.24×10^{-9}	1	$(1.44 \pm 0.51) \times 10^{-3}$	0	3,4*	X
Sersic159-3	0.06	0.68	$(3.65 \pm 0.56) \times 10^{-9}$	0	$(2.02 \pm 0.01) \times 10^{-3}$	0	3	X
ZW3146	0.28	1.21	$(7.87 \pm 2.28) \times 10^{-9}$	0	$(2.49 \pm 0.13) \times 10^{-3}$	0	3	X
A2597	0.08	0.89	$(1.00 \pm 1.03) \times 10^{-8}$	0	$(9.48 \pm 1.98) \times 10^{-4}$	0	3,4*	X
A1775	0.08	0.91	$(2.41 \pm 0.46) \times 10^{-7}$	0	$(8.63 \pm 0.18) \times 10^{-3}$	0	3	X
A1837	0.07	0.79	$(1.46 \pm 0.36) \times 10^{-7}$	0	$(7.76 \pm 0.53) \times 10^{-3}$	0	3*,5	X
RXCJ0014.3-3022	0.31	1.41	$(4.60 \pm 0.88) \times 10^{-7}$	0	$(3.71 \pm 0.08) \times 10^{-2}$	0	2	X
RXCJ1131.9-1955	0.31	1.33	$(1.99 \pm 0.90) \times 10^{-7}$	0	$(3.18 \pm 0.08) \times 10^{-2}$	0	2	X

Table 5.5: continued.

Cluster	Redshift	r_{500}	$P3/P0$	UL	w	UL	Reference	Image
A1651	0.08	1.21	1.22×10^{-8}	1	$(4.99 \pm 0.43) \times 10^{-3}$	0	5	X
A133	0.06	0.92	$(2.47 \pm 1.72) \times 10^{-8}$	0	$(6.32 \pm 0.53) \times 10^{-3}$	0	3	X
A2626	0.05	0.75	$(4.71 \pm 3.98) \times 10^{-9}$	0	$(5.72 \pm 0.32) \times 10^{-3}$	0	3	X
A2065	0.07	1.05	$(2.25 \pm 1.73) \times 10^{-8}$	0	$(1.93 \pm 0.03) \times 10^{-2}$	0	3	X
RXCJ0003.8+0203	0.09	0.91	$(1.80 \pm 2.01) \times 10^{-8}$	0	$(4.74 \pm 0.91) \times 10^{-3}$	0	6	X
RXCJ0006.0-3443	0.11	1.05	$(2.93 \pm 1.03) \times 10^{-7}$	0	$(1.46 \pm 0.09) \times 10^{-2}$	0	6	X
RXCJ0020.7-2542	0.14	1.11	2.00×10^{-8}	1	$(1.28 \pm 0.06) \times 10^{-2}$	0	6	X
RXCJ0049.4-2931	0.11	0.80	$(2.73 \pm 4.93) \times 10^{-8}$	0	$(3.79 \pm 0.89) \times 10^{-3}$	0	6	X
RXCJ0145.0-5300	0.12	1.11	$(1.22 \pm 0.76) \times 10^{-7}$	0	$(2.93 \pm 0.13) \times 10^{-2}$	0	6	X
RXCJ0211.4-4017	0.10	0.64	1.82×10^{-8}	1	$(6.09 \pm 0.69) \times 10^{-3}$	0	6	X
RXCJ0225.1-2928	0.06	0.72	$(2.55 \pm 1.88) \times 10^{-7}$	0	$(7.83 \pm 1.17) \times 10^{-3}$	0	6	X
RXCJ0345.7-4112	0.06	0.67	$(2.69 \pm 0.67) \times 10^{-7}$	0	$(4.02 \pm 0.54) \times 10^{-3}$	0	6	X
RXCJ0547.6-3152	0.15	1.14	$(1.33 \pm 0.44) \times 10^{-7}$	0	$(1.08 \pm 0.04) \times 10^{-2}$	0	1,6*	X
RXCJ0605.8-3518	0.14	0.98	$(1.24 \pm 0.49) \times 10^{-8}$	0	$(6.57 \pm 0.24) \times 10^{-3}$	0	6	X
RXCJ0616.8-4748	0.12	0.95	$(5.83 \pm 1.41) \times 10^{-7}$	0	$(9.95 \pm 0.99) \times 10^{-3}$	0	6	X
RXCJ0645.4-5413	0.16	1.23	2.29×10^{-8}	1	$(9.38 \pm 0.48) \times 10^{-3}$	0	1,6*	X
RXCJ0821.8+0112	0.08	0.74	$(2.67 \pm 1.64) \times 10^{-6}$	0	$(7.97 \pm 4.52) \times 10^{-2}$	0	6	X
RXCJ0958.3-1103	0.17	1.06	$(1.67 \pm 3.68) \times 10^{-8}$	0	$(2.97 \pm 0.32) \times 10^{-3}$	0	1,6*	X
RXCJ1044.5-0704	0.13	0.83	2.14×10^{-9}	1	$(3.73 \pm 0.20) \times 10^{-3}$	0	6	X
RXCJ1141.4-1216	0.12	0.82	$(1.23 \pm 1.44) \times 10^{-8}$	0	$(2.82 \pm 0.41) \times 10^{-3}$	0	6	X
RXCJ1236.7-3354	0.08	0.75	4.07×10^{-8}	1	$(3.12 \pm 0.42) \times 10^{-3}$	0	6	X
RXCJ1302.8-0230	0.08	0.79	$(1.33 \pm 0.42) \times 10^{-7}$	0	$(2.21 \pm 0.07) \times 10^{-2}$	0	6	X
A1689	0.18	1.40	$(3.38 \pm 2.29) \times 10^{-9}$	0	$(2.03 \pm 0.19) \times 10^{-3}$	0	1,3,6*	X
RXCJ1516.3+0005	0.12	0.98	$(1.30 \pm 1.42) \times 10^{-8}$	0	$(9.00 \pm 0.42) \times 10^{-3}$	0	6	X
RXCJ1516.5-0056	0.12	0.86	$(9.77 \pm 1.89) \times 10^{-7}$	0	$(1.62 \pm 0.10) \times 10^{-2}$	0	6	X
RXCJ2014.8-2430	0.15	1.00	$(1.72 \pm 0.64) \times 10^{-8}$	0	$(6.46 \pm 0.22) \times 10^{-3}$	0	6	X
RXCJ2023.0-2056	0.06	0.76	$(7.82 \pm 6.79) \times 10^{-8}$	0	$(2.14 \pm 0.14) \times 10^{-2}$	0	6	X
RXCJ2048.1-1750	0.15	0.99	$(3.83 \pm 0.79) \times 10^{-7}$	0	$(1.58 \pm 0.07) \times 10^{-2}$	0	6	X
RXCJ2129.8-5048	0.08	0.91	$(1.10 \pm 0.69) \times 10^{-7}$	0	$(5.18 \pm 0.10) \times 10^{-2}$	0	6	X
RXCJ2149.1-3041	0.12	0.82	$(1.33 \pm 0.31) \times 10^{-7}$	0	$(4.55 \pm 0.55) \times 10^{-3}$	0	6	X
RXCJ2217.7-3543	0.15	1.01	$(7.94 \pm 2.61) \times 10^{-8}$	0	$(4.36 \pm 0.34) \times 10^{-3}$	0	6	X
RXCJ2218.6-3853	0.14	1.13	$(8.61 \pm 2.23) \times 10^{-8}$	0	$(1.72 \pm 0.06) \times 10^{-2}$	0	1,6*	X
RXCJ2234.5-3744	0.15	1.32	$(4.06 \pm 3.77) \times 10^{-9}$	0	$(2.10 \pm 0.04) \times 10^{-2}$	0	1,6*	X
RXCJ2319.6-7313	0.10	0.66	2.29×10^{-8}	1	$(1.91 \pm 0.11) \times 10^{-2}$	0	6	X
RXCJ2157.4-0747	0.06	0.72	$(9.67 \pm 2.36) \times 10^{-6}$	0	$(2.15 \pm 0.88) \times 10^{-1}$	0	6	X
High-z 400SD sample								
1212+2733	0.35	1.08	$(3.59 \pm 0.94) \times 10^{-6}$	0	$(9.49 \pm 1.79) \times 10^{-3}$	0	7	C
0350-3801	0.36	0.61	$(1.08 \pm 1.51) \times 10^{-6}$	0	$(5.23 \pm 3.13) \times 10^{-3}$	0	7	C
0318-0302	0.37	0.81	4.84×10^{-7}	1	$(4.10 \pm 0.41) \times 10^{-2}$	0	7	C
0159+0030	0.39	0.82	7.45×10^{-7}	1	$(4.35 \pm 2.34) \times 10^{-3}$	0	7	C
0958+4702	0.39	0.74	9.22×10^{-7}	1	$(8.90 \pm 4.59) \times 10^{-3}$	0	7	C
1003+3253	0.42	0.93	$(2.36 \pm 1.56) \times 10^{-6}$	0	$(2.67 \pm 0.58) \times 10^{-2}$	0	7	C
0141-3034	0.44	0.54	2.97×10^{-6}	1	$(2.18 \pm 5.28) \times 10^{-3}$	0	7	C
1701+6414	0.45	0.80	1.63×10^{-7}	1	$(1.35 \pm 0.27) \times 10^{-2}$	0	7	C
1641+4001	0.46	0.68	$(6.65 \pm 10.2) \times 10^{-7}$	0	$(4.65 \pm 4.25) \times 10^{-3}$	0	7	C
1222+2709	0.47	0.73	1.14×10^{-6}	1	2.51×10^{-3}	1	7	C
0355-3741	0.47	0.82	$(1.37 \pm 1.33) \times 10^{-6}$	0	$(5.27 \pm 4.15) \times 10^{-3}$	0	7	C
0030+2618	0.50	0.66	1.10×10^{-6}	1	$(4.25 \pm 5.31) \times 10^{-3}$	0	7	C
1002+6858	0.50	0.75	$(5.40 \pm 10.4) \times 10^{-7}$	0	$(2.63 \pm 0.47) \times 10^{-2}$	0	7	C
1524+0957	0.52	0.76	3.11×10^{-7}	1	$(1.46 \pm 0.25) \times 10^{-2}$	0	7	C
1120+2326	0.56	0.67	5.98×10^{-7}	1	$(3.10 \pm 0.48) \times 10^{-2}$	0	7	C
1120+4318	0.60	0.79	$(1.10 \pm 0.71) \times 10^{-6}$	0	$(2.63 \pm 2.70) \times 10^{-3}$	0	7	C
1202+5751	0.68	0.68	2.08×10^{-6}	1	$(4.36 \pm 0.65) \times 10^{-2}$	0	7	C
0405-4100	0.69	0.66	$(6.20 \pm 9.07) \times 10^{-7}$	0	$(3.06 \pm 2.46) \times 10^{-3}$	0	7	C
1221+4918	0.70	0.88	$(1.55 \pm 3.50) \times 10^{-7}$	0	$(1.23 \pm 0.29) \times 10^{-2}$	0	7	C
0230+1836	0.80	0.75	1.05×10^{-6}	1	$(1.92 \pm 0.50) \times 10^{-2}$	0	7	C
0809+2811	0.40	0.81	1.03×10^{-6}	1	$(1.19 \pm 0.46) \times 10^{-2}$	0	7	C
0333-2456	0.48	0.66	$(1.61 \pm 2.30) \times 10^{-6}$	0	4.27×10^{-3}	1	7	C
1334+5031	0.62	0.72	3.31×10^{-6}	1	$(3.28 \pm 4.75) \times 10^{-3}$	0	7	C
0542-4100	0.64	0.81	$(5.48 \pm 9.29) \times 10^{-7}$	0	$(5.04 \pm 0.59) \times 10^{-2}$	0	7	C

Table 5.5: continued.

Cluster	Redshift	r_{500}	$P3/P0$	UL	w	UL	Reference	Image
0152-1358	0.83	0.72	$(5.76 \pm 0.95) \times 10^{-5}$	0	$(6.64 \pm 0.57) \times 10^{-2}$	0	7	C
0302-0423	0.35	0.90	7.48×10^{-8}	1	$(1.56 \pm 0.87) \times 10^{-3}$	0	7	C
1312+3900	0.40	0.75	2.27×10^{-6}	1	$(3.42 \pm 0.85) \times 10^{-2}$	0	7	C
1416+4446	0.40	0.70	3.54×10^{-7}	1	$(1.32 \pm 0.28) \times 10^{-2}$	0	7	C
0328-2140	0.59	0.81	2.25×10^{-7}	1	$(5.99 \pm 1.97) \times 10^{-3}$	0	7	C
0522-3624	0.47	0.70	$(1.34 \pm 1.46) \times 10^{-6}$	0	$(3.16 \pm 4.01) \times 10^{-3}$	0	7	C
0853+5759	0.48	0.69	9.04×10^{-7}	1	$(5.24 \pm 0.96) \times 10^{-2}$	0	7	C
0926+1242	0.49	0.82	$(3.12 \pm 5.24) \times 10^{-7}$	0	2.40×10^{-3}	1	7	C
0956+4107	0.59	0.74	$(1.26 \pm 1.01) \times 10^{-6}$	0	$(7.14 \pm 0.57) \times 10^{-2}$	0	7	C
1226+3332	0.89	1.05	1.93×10^{-7}	1	$(1.11 \pm 0.17) \times 10^{-2}$	0	7	C
1354-0221	0.55	0.70	2.26×10^{-6}	1	$(1.42 \pm 0.55) \times 10^{-2}$	0	7	C
1357+6232	0.53	0.79	5.91×10^{-7}	1	$(1.25 \pm 0.29) \times 10^{-2}$	0	7	C
High-z SPT sample								
SPT-CLJ0000-5748	0.74	1.00	3.55×10^{-7}	1	$(8.34 \pm 3.25) \times 10^{-3}$	0	8	C
SPT-CLJ0509-5342	0.46	1.04	4.27×10^{-7}	1	$(3.13 \pm 1.33) \times 10^{-3}$	0	8	C
SPT-CLJ0516-5430	0.29	1.12	$(7.91 \pm 3.33) \times 10^{-7}$	0	$(2.88 \pm 0.22) \times 10^{-2}$	0	1*,2,8	X
SPT-CLJ0528-5300	0.76	0.74	$(2.92 \pm 2.37) \times 10^{-6}$	0	$(7.35 \pm 3.69) \times 10^{-3}$	0	8	C
SPT-CLJ0533-5005	0.88	0.59	$(4.36 \pm 12.70) \times 10^{-6}$	0	$(1.42 \pm 0.93) \times 10^{-2}$	0	8	C
SPT-CLJ0546-5345	1.07	0.76	7.08×10^{-7}	1	$(6.75 \pm 2.25) \times 10^{-3}$	0	8	C
SPT-CLJ0551-5709	0.42	0.79	1.17×10^{-6}	1	$(2.75 \pm 0.60) \times 10^{-2}$	0	8	C
SPT-CLJ0559-5249	0.61	1.01	$(1.06 \pm 1.05) \times 10^{-6}$	0	$(2.93 \pm 0.41) \times 10^{-2}$	0	8	X
SPT-CLJ2331-5051	0.57	0.89	$(2.47 \pm 3.26) \times 10^{-7}$	0	$(6.18 \pm 2.10) \times 10^{-3}$	0	8	C
SPT-CLJ2337-5942	0.78	0.99	1.55×10^{-7}	1	$(4.32 \pm 4.34) \times 10^{-3}$	0	8	C
SPT-CLJ2341-5119	1.00	0.82	3.89×10^{-7}	1	$(5.78 \pm 1.87) \times 10^{-3}$	0	8	C
SPT-CLJ2342-5411	1.08	0.60	8.71×10^{-7}	1	2.45×10^{-3}	1	8	C
SPT-CLJ2332-5358	0.32	1.17	$(6.23 \pm 16.90) \times 10^{-7}$	0	$(4.38 \pm 3.42) \times 10^{-3}$	0	8	X
SPT-CLJ2355-5056	0.35	0.97	$(2.20 \pm 4.02) \times 10^{-7}$	0	$(6.42 \pm 2.11) \times 10^{-3}$	0	8	C
SPT-CLJ2359-5009	0.76	0.83	1.32×10^{-6}	1	$(1.44 \pm 0.58) \times 10^{-2}$	0	8	C

Chapter 6

Morphological analysis of galaxy clusters using the asymmetry parameter

A. Weißmann, H. Böhringer, G. Chon

in preparation, to be submitted to A&A

Abstract
A reliable quantification of the dynamical state of galaxy clusters is based on well-studied morphology estimators. This is especially important when using large datasets which vary in terms of data quality. Opening the window to higher redshifts enables the study of the evolution of the galaxy cluster population through e.g. the fraction of disturbed clusters. However, it also triggers multiple issues such as the difference in data quality for low- and high-z observations. To assess how influential these problems are on the quantification of the clusters' dynamical state using the asymmetry parameter A, we performed a detailed study of this substructure measure. Owing to its definition as a per-pixel statistic, A is sensitive to the pixel resolution and most importantly Poisson noise, hence the data quality. Using simulated galaxy cluster X-ray images, we quantified this influence and propose to minimize this effect through smoothing. In addition, we define a morphological A boundary to divide a cluster sample into relaxed and disturbed objects. Based on the findings of the parameter study, we applied the asymmetry parameter to 129 galaxy clusters with $0.05 < z < 1.08$ observed with *XMM-Newton* and *Chandra* and measured the disturbed cluster fraction for different redshifts. After taking into account the difference in the photon statistics of low- and high-z observations, we found a mild increase of the disturbed cluster fraction with redshift and a shallow positive slope for the $A-$ redshift relation. Our findings agree well with previous studies using two other substructure measures ($P3/P0$ and w), but have a higher significance.

6.1 Introduction

It has been long known that not all galaxy clusters are in dynamical equilibrium, but that some exhibit substructure which indicates that merging and accretion activities have not yet ceased in these objects (e.g. Geller & Beers 1982; West & Bothun 1990). Substructures can be detected especially well in X-rays because X-ray studies are less susceptible to contamination from fore- and background objects than for example optical studies. With the advance of X-ray imaging observatories such as *ROSAT*, *XMM-Newton* and *Chandra* and large observing programs, it was finally confirmed that a large number of galaxy clusters show substructures, which are observed as multiple surface brightness peaks or a generally disturbed morphology (for a review see e.g. Buote 2002). Since then a variety of methods to quantify the morphology and thus the dynamical state of clusters have been proposed, including among others visual classification (e.g. Jones & Forman 1992), ellipticity measurements (e.g. McMillan et al. 1989; Hashimoto et al. 2007a), the examination of residuals after subtracting a β model from the X-ray image (e.g. Davis & Mushotzky 1993; Neumann & Böhringer 1997), wavelet decomposition (e.g. Slezak et al. 1994; Arnaud et al. 2000), power ratios (e.g. Buote & Tsai 1995, 1996; Jeltema et al. 2005; Böhringer et al. 2010; Weißmann et al. 2013b) and the center shift parameter (e.g. Mohr et al. 1993; O'Hara et al. 2006; Weißmann et al. 2013b).

Quantifying the dynamical state of clusters and classifying them as relaxed or disturbed objects is interesting for studying astrophysical processes within the cluster potential but is also very important for cosmological applications. The evolution of the cluster mass function traces the process of structure formation and the underlying cosmological model. Cluster masses are often derived from X-ray observations assuming spherical shape and hydrostatic equilibrium (HE) of the ICM. The accuracy of these assumptions and the extent of non-thermal pressure support due to e.g. turbulent gas motions is still debated. Several studies reported that mass estimates based on HE are $\sim 5-20\%$ lower than mass estimates from weak lensing data (e.g. Kay et al. 2004; Rasia et al. 2006; Nagai et al. 2007; Arnaud et al. 2007; Mahdavi et al. 2008; Piffaretti & Valdarnini 2008; Lau et al. 2009; Meneghetti et al. 2010; Zhang et al. 2010; Mahdavi et al. 2013). The HE mass bias is larger for disturbed objects, but also relaxed clusters show residual bulk motions due to past merging activities and the incomplete thermalization of the ICM (e.g. Evrard 1990; Nagai et al. 2007; Rasia et al. 2012).

Regarding cluster physics, the effect of substructure on cluster properties such as temperature or luminosity has been studied to quantify how merging events contribute to the scatter in scaling relations (e.g. Rowley et al. 2004; Ventimiglia et al. 2008; Pratt et al. 2009), which are calibrated preferentially using relaxed clusters. For disturbed objects, a connection between the presence of a radio halo and signs of recent merging activity was found (e.g. Buote 2001; Venturi et al. 2008; Cassano et al. 2010). Large samples of merging clusters thus provide means for studying the formation process of radio halos and will help in distinguishing between the two most discussed scenarios, the turbulent re-acceleration model where relativistic electrons in the ICM are re-accelerated by the merger-driven MHD turbulence (e.g. Brunetti et al. 2001; Petrosian 2001) and the secondary models, in which relativistic electrons are secondary products of the collisions between intergalactic cosmic rays and thermal protons in the ICM (Dennison 1980; Pfrommer & Enßlin 2004).

These and other studies of astrophysical processes in galaxy clusters require the accurate

knowledge of the cluster morphology. It is therefore important to establish reliable morphology estimators to quantify the kind and amount of substructure in galaxy cluster X-ray observations.

Recently, studies of cluster morphologies have been extended to redshift ~ 1, showing a larger fraction of disturbed objects at $z > 0.5$ than at low redshift (e.g. Jeltema et al. 2005; Andersson et al. 2009; Mann & Ebeling 2012; Weißmann et al. 2013a). In contrary to observations of nearby clusters, high-redshift observations suffer from Poisson noise due to their low photon statistics. Exploring a large redshift range therefore requires well-studied morphology estimators, especially regarding their performance when using observations with low data quality. Weißmann et al. (2013b) published such a study on the two popular parameters power ratio $P3/P0$ and w and found a clear dependence on the performance of $P3/P0$ on the data quality due to the increasing influence of noise when going to lower photon statistics.

In this work, we focus on the asymmetry parameter A. We present a detailed study of A, testing its performance for simulated observations with varying data quality. We introduce the simulations which were used for the study in Sect. 6.2 and give the definition of the asymmetry parameter A in Sect. 6.3. In addition, we give a morphological boundary to distinguish between relaxed and disturbed objects and discuss the influence of pixel resolution. In Sect. 6.4 we raise the question whether and how A can be safely applied to high- and low-z (or low- and high-count) observations. We thus study how to minimize the effect of Poisson noise by smoothing the image. Based on the findings of the parameter study, we computed A for 129 galaxy clusters which are introduced in Sect. 6.5. Sect. 6.6 contains the study of A as a function of redshift in order to answer the question whether there is an evolution in the disturbed cluster fraction. We compare A to other well-defined morphology estimators in Sect. 6.7 and show its statistical strength. We discuss our findings in Sect. 6.8 and conclude with Sect. 6.9. Throughout the paper, a standard ΛCDM cosmology with the following parameters was assumed: $H_0 = 70$ km s^{-1} Mpc^{-1}, $\Omega_\Lambda = 0.7$, $\Omega_\mathrm{M} = 0.3$.

6.2 Simulations

For the systematic study of the asymmetry parameter A, we use 121 simulated X-ray images of galaxy clusters. This set of simulations was already discussed in Weißmann et al. (2013b) and Böhringer et al. (2010), where it was used for a study of two other morphology estimators. It includes 117 simulated galaxy clusters from Borgani et al. (2004) and 4 from Dolag et al. (2009) to cover the desired mass range ($0.8 \times 10^{14} - 2.2 \times 10^{15} h^{-1}\ M_\odot$). The clusters were extracted from the simulation, which was performed with the TreePM/SPH code GADGET-2 (Springel 2005), at $z = 0$. Ameglio et al. (2007) created 256×256 pixel wide X-ray images without observational artifacts in the $0.5 - 2$ keV range with a pixel resolution of $\sim 0.031\ r_{500}$. The simulated X-ray images do not include any observational artifacts (noise, bad pixels etc.) or background. All structures in the images are infalling groups or clusters. We use the simulated cluster images exclusively to study the noise and error properties of the asymmetry parameter. We do not require these images to represent the true morphology distribution of galaxy clusters.

6.3 Asymmetry parameter

The asymmetry parameter gives the normalized absolute residual flux when subtracting a rotated image from the original one. While originally used in the study of galaxy morphologies (Conselice 1997; Conselice et al. 2000), it has recently been applied to galaxy clusters (Okabe et al. 2010; Rasia et al. 2013). Following the definition of Conselice et al. (2000) and Okabe et al. (2010), the A parameter is computed as a sum over all pixels i within r_{500} around the centroid of the surface brightness distribution as

$$A = \frac{\sum_i \mid I_i - R_i \mid}{\sum_i I_i}, \tag{6.1}$$

where I and R give the flux of the original and rotated image. The original image I is point-source corrected and background subtracted. The rotated image R is created by rotating I by 180° around the centroid of the surface brightness distribution. We take the error on A as $(\sigma^2_{\mathrm{POSITION}} + \sigma^2_{\mathrm{POISSON}})^{1/2}$, which includes the error on the position of the centroid ($\sigma_{\mathrm{POSITION}}$) and the error component due to Poisson noise in the image ($\sigma_{\mathrm{POISSON}}$). The uncertainty in the determination of the centroid position is estimated by taking into account the position resolution of $\sim 4''$ (~ 1 pixel) for *XMM-Newton*. We let the centroid fall into each neighboring pixel of its original position, calculate A for all these cases and take $\sigma_{\mathrm{POSITION}}$ as the standard deviation of this distribution. The Poisson component $\sigma_{\mathrm{POISSON}}$ is obtained from poissonized realizations of the cluster image. We apply the *zhtools*[1] task *poisson* on the background-included cluster image to add Poisson noise, but subtract the background image before calculating A. $\sigma_{\mathrm{POISSON}}$ is then defined as the standard deviation of the A distribution of the 100 poissonized images.

The A parameter is based on the assumption that dynamically disturbed objects deviate further from symmetry than rather relaxed ones. A large value of A indicates asymmetry and a disturbed morphology. Okabe et al. (2010) first applied this parameter to X-ray observations of galaxy clusters. In combination with the fluctuation parameter F, which gives the normalized absolute residual flux after subtracting a smoothed image, A performs well in finding relaxed objects. Using 20 simulated *Chandra*-like, 100ks exposure X-ray observations of galaxy clusters, Rasia et al. (2013) studied several morphology estimators, including A. They tested the efficiency of A in distinguishing between relaxed and disturbed objects in comparison to other widely used morphology estimators like power ratio $P3/P0$ or center shift w. They find A to be a very good indicator of morphology, especially in combination with $P3/P0$ or w. In the course of our argumentation, we will sometimes refer to this work since it comprises the motivation of our more detailed study of the asymmetry parameter.

6.3.1 Morphological boundary

To define a morphological boundary for A, we visually classified all simulated galaxy clusters as relaxed or disturbed, depending on whether they show some sign of substructure within r_{500} or not. Disturbed objects show a general disturbed appearance, asymmetry or a second component of about equal size, while relaxed cluster have an overall regular shape. We show the

[1] http://hea-www.harvard.edu/RD/zhtools/

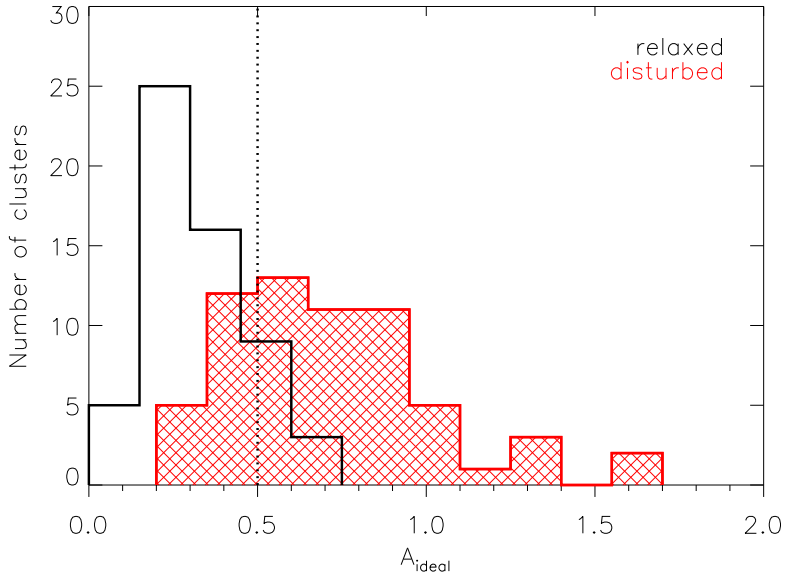

Figure 6.1: Distribution of the asymmetry parameter A for simulated ideal cluster images after classifying them visually as relaxed and disturbed objects. Relaxed clusters (black outlined histogram) are preferentially found below the morphological boundary of $A = 0.5$ (dotted line), while disturbed clusters (red filled histogram) have on average higher A values.

A distribution of simulated cluster images without noise – ideal hereafter – in Fig. 6.1. Relaxed objects are preferentially found below $A = 0.5$, while disturbed objects yield on average higher asymmetry values. The small number of misclassifications is caused by the definition of the asymmetry parameter. Depending on the geometry and position of the substructure, subtracting a 180° rotated image from the original one may yield only a small number of residual counts and thus $A < 0.5$ although the cluster shows signs of disturbance. Some relaxed objects, on the other hand, give $A > 0.5$. These clusters are classified as relaxed due to their overall appearance, but show slight disturbances in their X-ray images and thus yield $A > 0.5$.

Rasia et al. (2013) found that $A = 1.15$ works well in distinguishing between relaxed and disturbed objects, especially in combination with other morphology estimators. The difference in their value of the morphological boundary to ours is mainly because of the difference in the data quality (see Sect. 6.4) and the pixel size (see Sect. 6.3.2). While we are using simulated ideal images with 0.031 r_{500} resolution, Rasia et al. (2013) use *Chandra*-like $2'' \times 2''$ binned observations including noise. The influence of Poisson noise on the determination of A will be discussed in detail in the next section, but we want to emphasize here that noise in general leads to an overestimation of A. Using the same data quality and pixel size as in Rasia et al. (2013), our boundary of $A = 0.5$ shifts to $A = 1.1$ and is consistent with their definition. This boundary should thus be modified depending on the data quality (see Sect. 6.4) and whether the original or smoothed image (see Sect. 6.4.1) is used.

6.3.2 Dependence on the pixel size

Owing to the definition of A as a per-pixel-statistic, we tested its dependence on the pixel size before discussing its Poisson noise properties. The simulated cluster images have an

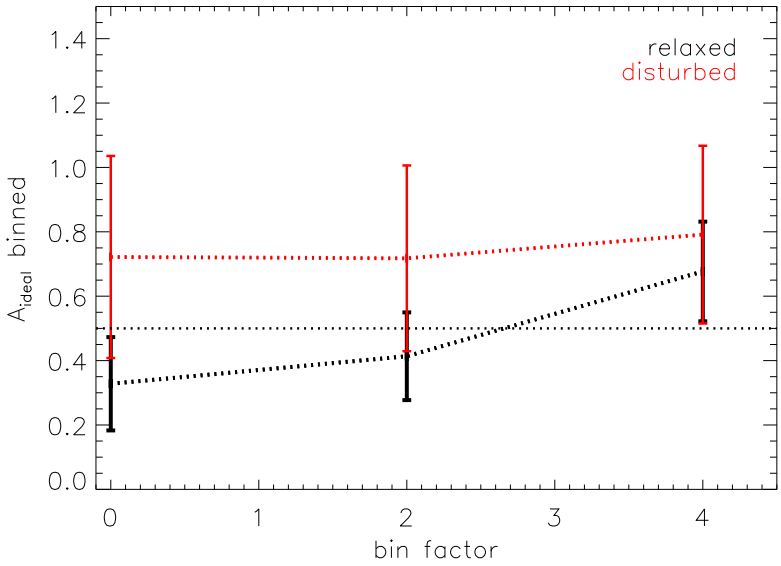

Figure 6.2: Dependence of A on the bin factor for ideal simulated cluster images with a pixel resolution of 0.031 r_{500}. The mean A parameters of relaxed (black) and disturbed (red) clusters including the σ for their distribution is shown. The classification is defined in Sect. 6.3.1. The dotted horizontal line indicates the morphological boundary $A = 0.5$.

initial pixel size of 0.031 r_{500} and we binned them by a factor of 2 and 4 using the *ftools* task *fimgbin* to mimic the effect of lower resolution. To explore the effect of binning for relaxed and disturbed objects we used the same visual classification as for the definition of the morphological boundary and show the mean A parameter for both dynamical states in Fig. 6.2. Lowering the resolution by a factor of 2 or 4 from 0.031 r_{500} leads to an increase of the obtained A value and makes it harder to distinguish between an average relaxed and disturbed cluster. For relaxed objects, binning and thus merging of surrounding pixels into one leads to the creation of artificial structure. Disturbed clusters show the same trend but less pronounced.

XMM-Newton observations are typically binned to 4″, but *Chandra* images have better resolution with a pixel size of 2″ or less. We tested the effect of binning for smaller initial pixel sizes by binning 2″ *Chandra* images by a factor of 2, 4 and 8. We did not find a significant difference in A when going from 2″ to 4″, which shows that binning has only a mild effect on small scales. For larger binning factors we saw the same behavior as with the simulated images, namely an increase for larger pixel sizes.

We conclude that there is a dependence of A on the pixel size and that it is important to use images with the same pixel resolution when computing A. The effect is very mild for images with pixel sizes $\leq$ 4″ for a certain redshift range and increases for larger bins. We based this work including the discussion of the noise properties and the bias correction method on simulated images with a pixel resolution of 0.031 r_{500}. For images with significantly lower pixel resolution ($>$ 0.1 r_{500}) our conclusions hold, but the morphological boundary and the smoothing kernel to minimize the effect of Poisson noise should be adjusted.

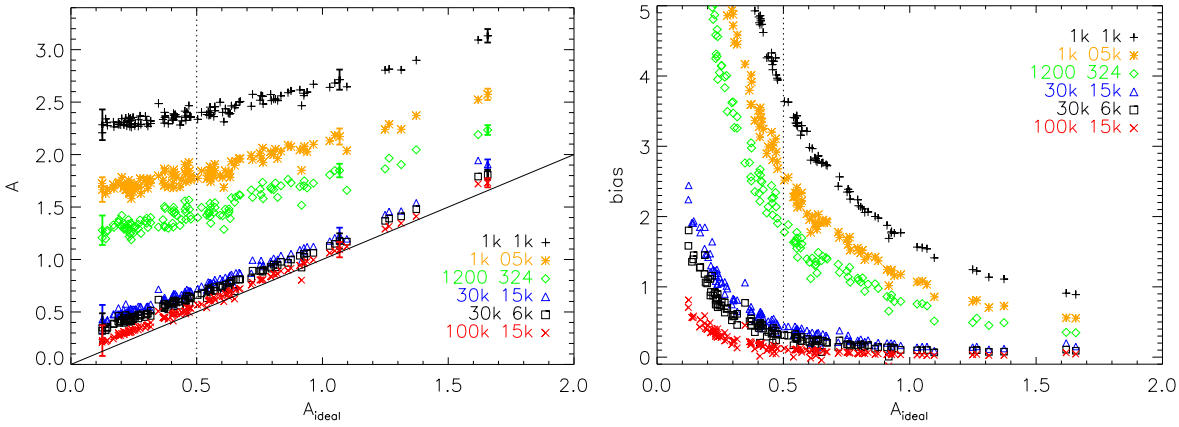

Figure 6.3: Dependence of A on the photon statistics. **Left**: The A parameter of the ideal image A_{ideal} is given in comparison to the mean A of 100 simulated observations for different net and background counts combinations. These are indicated by the left (net counts) and right (background counts) number in the legend. The solid line marks the 1-1 relation. Typical errors for small, intermediate and large A values, calculated as described in Sect. 6.3, are shown. **Right:** Bias due to Poisson noise for the same net and background counts as in the left panel. The bias is defined as $(A - A_{\mathrm{ideal}})/A_{\mathrm{ideal}}$ and thus given as a fraction of A_{ideal}.

6.4 Study of shot noise bias

The good performance of A as an morphology estimator has been shown for data sets with long exposure time and high photon statistics for both galaxies and galaxy clusters. The asymmetry parameter gives the residual flux per pixel, integrated over a certain region like r_{500} and is expected to be increasingly sensitive to noise for decreasing photon statistics. Conselice et al. (2000) investigated this effect for images of galaxies and found that A begins to be dominated by noise for a signal-to-noise below 100 after correcting the noise by estimating it in a blank region of the image. However, galaxy observations have much better photon statistics and it is therefore necessary to perform a detailed study of the statistical properties of A for typical galaxy cluster observations.

To quantify the performance of A and the influence of noise, we used the set of 121 simulated X-ray images of galaxy clusters described in Sect. 6.2. The images in the 0.5 – 2 keV range represent a wide range of morphologies and have a pixel resolution of $\sim 0.031\ r_{500}$. Different observational depths were simulated by creating poissonized images with different net photon counts. In detail, we first normalized the ideal simulated image to obtain the desired net photon count number within r_{500}. Second, we applied the *zhtools* task *poisson* to the normalized image, creating 100 poissonized images per normalized cluster image. Since the background introduces additional Poisson noise, we added a poissonized flat background to the poissonized cluster images. This gives us several sets of 100 *simulated observations* per cluster with a certain number of net and background photon counts.

We want to start our argument that A is increasingly sensitive to Poisson noise for decreasing net photon counts and an increasing background level with Fig. 6.3. For six different observational depths, we computed A_{ideal}, the A parameter of the ideal image, the mean A of

100 simulated observations per cluster and its bias due to Poisson noise. The bias is defined as the difference between A and $A_{\rm ideal}$, normalized by $A_{\rm ideal}$. Fig. 6.3 shows the direct comparison between $A_{\rm ideal}$ and A in the left panel, the bias as a function of $A_{\rm ideal}$ is given in the right one. Two of the six combinations of net and background counts shown in this figure represent the mean photon statistics of the low-z (100 000 net, 15 000 background counts) and high-z 400SD (1 200 net, 324 background counts) sample. 1 000 and 30 000 net counts are typical values of high-z and short exposure low-z observations, respectively. Two different background levels were added to illustrate the effect of the background when computing A. When dealing with observations with $>$ 30 000 net counts, the background has only a mild effect. For 30 000 net counts, an increase of the background from 6 000 to 15 0000 counts within r_{500} leads to a small increase of the bias. In the low net counts regime, A is much more sensitive to noise and the additional background. Comparing the case of 1 000 net, 500 background counts to 1200 net, 324 background counts shows that a small change in net counts or in the ratio of net-to-background counts leads to a large increase of the bias and very different results for low photon statistics. This fact becomes very important for the discussion in Sect. 6.6, where we are dealing with a spread in the data quality of high-z observations and need to apply an additional correction for low-count images.

6.4.1 Noise correction

Quantifying the bias in the A signal due to Poisson noise is essential to make A a reliable morphology estimator. The low scatter in the $A_{\rm ideal} - A$ relation shown in Fig. 6.3 encourages to estimate and correct the bias by using a fit to the $A_{\rm ideal} - A$ relation. Comparing the different net and background counts configurations in Fig. 6.3 shows that a small change in the photon statistics – especially for low-count observations – can lead to a large increase of the bias. It is thus necessary to compute the $A_{\rm ideal} - A$ relation for the specific net and background counts configuration of each observation to infer the true A value from the fit. For large data sets with a wide range of photon statistics, this method is computationally expensive, but it is reasonable to apply it to small cluster samples.

A slightly modified approach can be used if a number of observations have the same net and background counts configuration. This is shown in Sect. 6.6, where we degrade all low-z observations to the mean photon statistics of the high-z 400SD sample and use this net and background counts configuration as reference point for the correction of the high-z observations. Instead of inferring $A_{\rm ideal}$ directly from the obtained A values, one can locate the cluster in the respective $A_{\rm ideal} - A$ relation, compare it to the position in the reference $A_{\rm ideal} - A$ relation and correct the difference. This procedure allows a very rough correction of the different noise levels to match the photon statistics of the reference configuration.

Conselice et al. (2000) propose a method to correct uncorrelated noise in galaxy images by computing the asymmetry parameter for the source and a blank background region. We tested this approach for galaxy cluster images, but due to the low photon statistics and signal-to-noise it did not perform as well as for galaxy images.

The most straightforward approach to reduce Poisson noise is smoothing. Differently to binning, which creates artificial structures, smoothing can smear out features of the substructure depending on the smoothing kernel and the morphology. We quantified this effect by smoothing the simulated ideal cluster images with different smoothing kernels, starting with

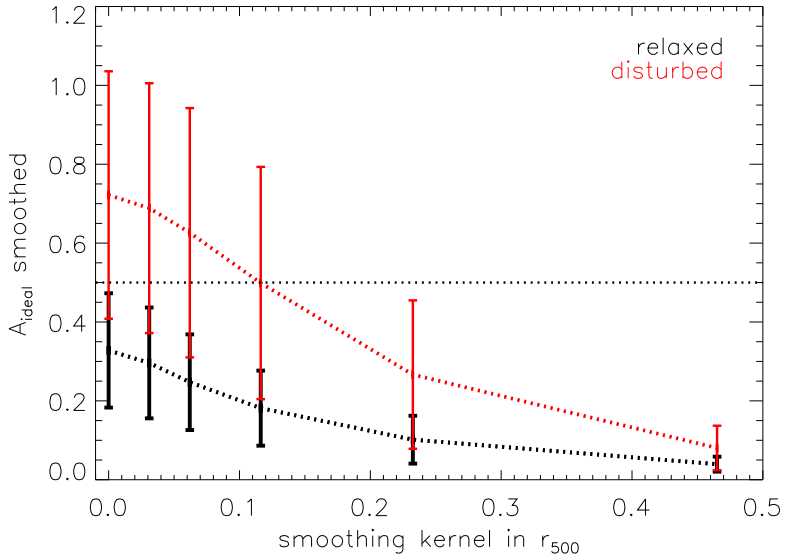

Figure 6.4: A as a function of the smoothing kernel in units of r_{500} for ideal cluster images. The mean A parameters of relaxed (black) and disturbed (red) clusters as defined in Sect. 6.3.1 is shown, including the σ of the distribution. The dotted horizontal line indicates the morphological boundary $A = 0.5$.

0.03 r_{500}. The *ftools*[2] task *fgauss* was used to convolve the image with an elliptical Gaussian function, whose σ is the smoothing kernel. In Fig. 6.4 we show the mean A value after smoothing the ideal image as a function of the smoothing kernel in units of r_{500} for relaxed and disturbed objects. Smoothing with a kernel smaller than 0.15 r_{500} yields slightly lower A values, but a larger kernel smears out almost all features in the disturbed clusters and makes it very hard to distinguish between the two cases. A smoothing kernel smaller than 0.15 r_{500} seemed reasonable.

Based on this finding, we applied several smoothing kernels $< 0.15\ r_{500}$ on the simulated observations to test which one performs best for different net and background counts combinations. For observations with good photon statistics and a low noise level, minimal smoothing is preferred since large smoothing kernels smear out a lot of substructure. In the case of low-count images, however, a larger smoothing kernel is required to correct for Poisson noise. Considering a wide range of photon statistics, the best compromise is a smoothing kernel of 0.05 r_{500}. Fig. 6.5 shows the performance of A after smoothing with this kernel size for the two mean net and background counts combinations of the high-z 400SD (1200 net, 324 background counts) and the low-z (100 000 net, 15 000 background counts) sample. In addition, we adjusted the morphological boundary of $A_{\rm ideal} = 0.5$ to $A = 0.6$ for the low- and $A = 0.4$ for the high-quality case. In the low-count case (left panels), smoothing enables a sufficient correction of noise for objects with $A_{\rm ideal} > 0.5$, while it slightly smears out structure in the high-count case (right panels). The residuals for structured objects with $A_{\rm ideal} > 0.5$ are acceptably small in both cases.

We conclude that smoothing with a kernel of 0.05 r_{500} significantly lowers the bias due

[2] `http://heasarc.gsfc.nasa.gov/ftools/`

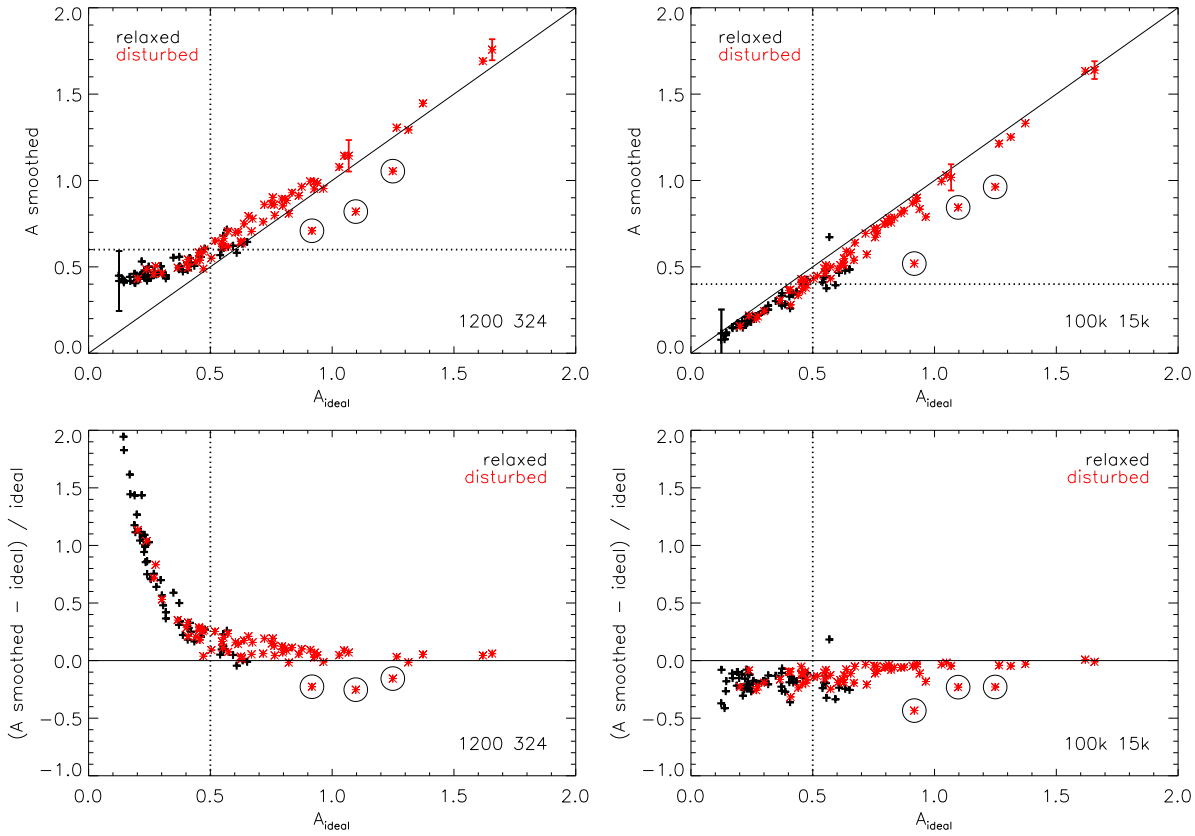

Figure 6.5: Performance of the A parameter after smoothing with a kernel of 0.05 r_{500} for the mean photon statistics of the high-z 400SD (left) and low-z (right) sample. The color-coded morphologies are defined in Sect. 6.3.1. Typical errors are shown for the same clusters as in Fig. 6.3. The circles highlight the three clusters with a small merging component close to r_{500}. Smoothing smears out this small structure and leads to an underestimation of A. **Top panels:** Direct comparison of A_{ideal} to the mean A parameter of 100 smoothed simulated observations. **Bottom panels:** Residuals after smoothing.

to Poisson noise and makes images with low and high photon statistics roughly comparable. It does not enable a full correction of the effect of Poisson noise, but merely reduces it sufficiently to obtain reasonable results. Low-count observations of clusters with $A_{\mathrm{ideal}} < 0.5$ still show large residuals, but remain below the morphological boundary. While relaxed objects stay below and disturbed ones above this boundary, mildly disturbed objects with $A_{\mathrm{ideal}} \sim 0.5$ might be misclassified in some cases. Due to the opposite sign of the residuals for low- and high-count images and the very small range of A from 0 to 2, smoothing only allows a very rough comparison of clusters with a large difference in the data quality. This issue will be discussed in more detail in Sect. 6.6, where we want to study the A-redshift relation and a comparison of low- and high-count images becomes necessary.

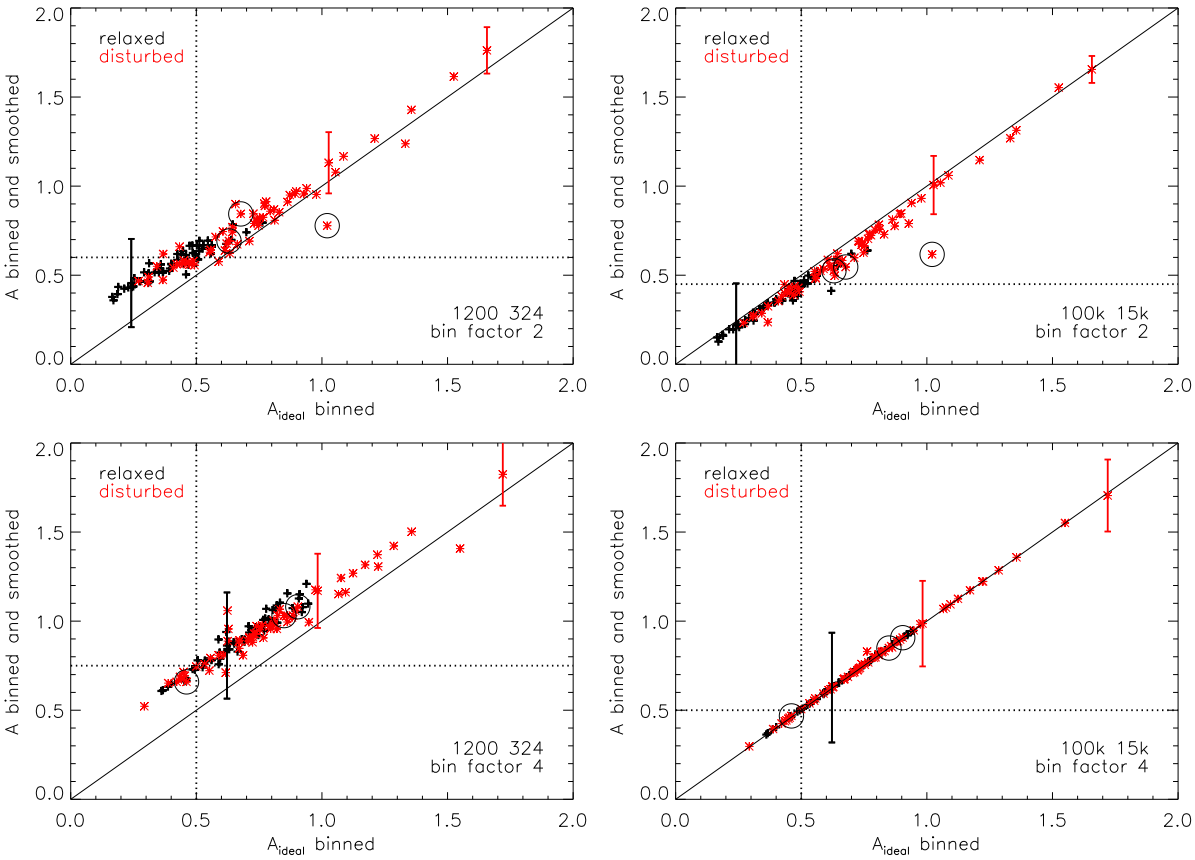

Figure 6.6: Same as Fig. 6.5 but for binned images. We compare the results to the A value of the ideal images binned with a factor of 2 (top panels) and 4 (bottom panels) instead of $A_{\rm ideal}$ and adjusted the morphological boundaries. The not-binned pixel resolution is 0.031 r_{500}. Due to the binning, the underestimation of A for the three special clusters (highlighted by circles) decreases.

6.4.2 Influence of binning

As the last point of our parameter study we want to discuss whether smoothing with a kernel of 0.05 r_{500} significantly reduces the bias due to Poisson noise also for images with lower pixel resolution. As discussed in Sect. 6.3.2, lower pixel resolution leads to an overestimation of A which is independent of the influence of Poisson noise. To quantify the effect of Poisson noise for binned images, we repeated the exercise of Sect. 6.4 and show the results in Fig. 6.6. After binning the ideal simulated images by a factor of 2 or 4 (for details on the binning procedure see Sect. 6.3.2), we created poissonized realizations with the desired net and background counts number. We found that the noise properties of poissonized binned images are consistent with the results found in Sect. 6.4. It is therefore reasonable to try to minimize the effect of Poisson noise through smoothing, which cannot reduce the effect of binning, however. We therefore do not compare the obtained A values to $A_{\rm ideal}$ but to the A value of the ideal images with the same pixel resolution. We showed that for reasonable pixel sizes ($\leq$ 0.1 r_{500}) the effect of binning is mild and therefore do not expect significantly different results for a bin

factor of 2.

Fig. 6.6 illustrates the strength of smoothing to overcome the problem of Poisson noise for low pixel resolution. Analogously to Sect. 6.4.1, we smoothed the poissonized binned images with a smoothing kernel of 0.05 r_{500}. For a bin factor of 2, hence a pixel resolution of 0.062 r_{500}, smoothing can reduce the bias due to noise significantly. In fact, the results are consistent with the not-binned case (compare top panels of Figs. 6.5 and 6.6) except for the larger error for the binned images. Larger pixel size does not effect the Poisson component of the error, but leads to a larger error on the position of the centroid. This component increases with decreasing pixel resolution because of the definition of A as a per-pixel statistic.

When using a bin factor of 4, we find larger A values than in the not-binned case (compare top panels of Fig. 6.5 and bottom panels of 6.6). This leads to an almost perfect match for the high-count images, since the overestimation due to binning and the underestimation due to the slightly too large smoothing kernel are comparable. For low-count observations the overestimation because of the binning and the slightly too small smoothing kernel add up. In this case we propose to increase the smoothing kernel and adjust the morphological boundaries to obtain comparable results.

6.5 Observations and data reduction

The complete dataset of 129 galaxy clusters used in this work for studying the behavior of A when applying it to *XMM-Newton* and *Chandra* observations and for investigating a possible evolution of A with redshift comprises three samples: 1) the low-z sample discussed in detail in Weißmann et al. (2013b), 2) the high-z subset of the 400d^2 survey (Vikhlinin et al. 2009a) and 3) the high-z subset of the SPT sample (Andersson et al. 2011). A detailed description of the three samples is given in Weißmann et al. (2013a), who determined the substructure parameters $P3/P0$ and w for all 129 clusters to study the evolution of the substructure frequency. Weißmann et al. (2013b) provide an X-ray image gallery for the low-z sample, the website of the 400d^2 survey for the high-z 400SD objects and Andersson et al. (2011) for the high-z SPT clusters.

6.5.1 Cluster samples

The low-redshift (low-z) sample comprises 78 archival *XMM-Newton* observations of galaxy clusters in the redshift range $0.05 < z < 0.31$. This sample has no unique selection function, but consists of clusters drawn from several well-studied samples: REXCESS (Böhringer et al. 2007), LoCuSS (Smith et al., Zhang et al. 2008), the Snowden Catalog (Snowden et al. 2008), the REFLEX-DXL sample (Zhang et al. 2006) and clusters from Buote & Tsai (1996). We required the clusters to be nearby ($z < 0.31$), to have known temperature measurements in the literature to compute r_{500} using the formula of Arnaud et al. (2005), to be publicly available in the *XMM-Newton* archive[3] (in 2009) and to have r_{500} fitting on the detector. The majority of the clusters are part of the representative samples REXCESS and LoCuSS and it is thus valid to assume that the complete low-z sample has a roughly representative character.

For $z > 0.3$ we use the X-ray-selected high-z subset of the 400d^2 survey and the SZ-

[3] http://xmm.esac.esa.int/xsa/

selected high-z subset of the SPT sample. Concerning the 400d^2 sample the question was raised whether the detection algorithm leads to a lack of concentrated objects (e.g. Santos et al. 2010) and thus a too high number of disturbed clusters compared to other X-ray-selected high-z samples such as the *ROSAT* Deep Cluster Survey (RDCS, Rosati et al. 1998). We therefore analyze each of the two high-z samples individually to account for this effect.

The high-z 400d^2 (short: 400SD) sample consists of 36 objects with $0.35 < z < 0.89$ and forms a complete, at $z > 0.5$ quasi-mass-limited, subsample of the 400d^2 survey (Burenin et al. 2007; Vikhlinin et al. 2009a). Pointed observation of all 36 galaxy clusters are publicly available in the *Chandra* archive[4].

The high-z SPT sample comprises 15 SZ-selected galaxy clusters which were chosen for X-ray follow-up from the significance-limited catalog of the 178 deg^2 survey of the South Pole Telescope. They cover a redshift range of $0.29 < z < 1.08$ and were observed mainly with *Chandra*. For three objects *XMM-Newton* data was used because either no *Chandra* data was available or due to better photon statistics in the *XMM-Newton* images (for details see Weißmann et al. 2013a, Table 5).

The complete sample thus includes 81 *XMM-Newton* and 48 *Chandra* observations.

6.5.2 Data reduction

The *XMM-Newton* observations of the 78 low-z and 3 high-z SPT clusters were analyzed with the *XMM-Newton* SAS[5] v.9.0.0 (low-z and one SPT cluster) and v.12.0.1 (2 SPT clusters). X-ray images binned by $4'' \times 4''$ in the standard $0.5 - 2$ keV range, which covers most of the cluster signal, were created following the data reduction recipe of Böhringer et al. (2007). To increase the sensitivity of the point source detection, we applied the SAS task *ewavelet* on the combined image of the three *XMM-Newton* detectors. We removed the point sources from each detector image individually and filled the gaps using the CIAO[6] task *dmfilth*. The background was estimated by a vignetted model fit to a source-excised, hard-band-scaled blank sky field.

For the data reduction of the *Chandra* observations of the 400SD and SPT clusters, we followed the standard reduction pipeline using the CIAO software package v4.4. and CALDB v4.4.7 (see Weißmann et al. (2013a) for details). We applied the standard corrections such as the detection of afterglows, the latest charge transfer inefficiency (CTI) correction or the removal of flared periods. Images with pixel resolution of $2'' \times 2''$ in the $0.5 - 2$ keV range and 1 keV monochromatic exposure maps were obtained. As in the case of *XMM-Newton* observations, we detected and removed point sources, refilling the gaps with *dmfilth*. Blank-sky event files were reprojected, scaled to the exposure time of the flare-cleaned observation and restricted to the $0.5 - 2$ keV range to generate background images.

Based on the findings discussed in Sect. 6.3.2 that A is sensitive to the pixel size, it is desirable to use images with the same binning in fractions of r_{500}. The r_{500} size of an average low-z object is roughly $450''$. This translates into a pixel resolution of $\sim 0.01\ r_{500}$ for $4'' \times 4''$ images. The angular size of the objects decreases at higher redshift and to obtain the same resolution, a smaller pixel size ($< 2''$) is required. When using smoothed images, the influence

[4] `http://cxc.cfa.harvard.edu/cda/`

[5] Science Analysis Software: `http://xmm.esa.int/sas/`

[6] *Chandra* Interactive Analysis of Observations software package: `http://cxc.harvard.edu/ciao/`

Table 6.1: Overview of the data quality of the samples. Mean net photon counts and mean S/B calculated within r_{500} of the reduced and point source corrected X-ray image. S/B gives the ratio of net photon counts (signal) to background photon counts. This table was taken from Weißmann et al. (2013a).

	Low-z	400SD	SPT
Number of clusters	78	36	15
Redshift range	0.05-0.31	0.35-0.89	0.29-1.08
Mean net photon counts	96997	1203	1735
Mean S/B	6.6	3.7	3.2

of the pixel resolution is limited by the size of the smoothing kernel. In our analysis, the smoothing kernel is 0.05 r_{500} and thus the difference in the binning has only a minor effect. In addition, since our sample spans a wide redshift range and the options of bin sizes are limited (multiples of 2″ for *Chandra* and 4″ for *XMM-Newton* observations), it is valid to compare smoothed $4'' \times 4''$ *XMM-Newton* to smoothed $2'' \times 2''$ *Chandra* images.

However, we apply a correction to 13 high-z objects using the $A_{\rm ideal} - A$ relations obtained from the simulations (see Sects. 6.4.1 and 6.6). Since the high-z samples have $\langle r_{500} \rangle \sim 130''$, the same pixel resolution of 0.031 r_{500} as the simulations is obtained for 4″ pixels. To be fully consistent with the simulations, we bin the $2'' \times 2''$ *Chandra* images by a factor of two to obtain $4'' \times 4''$ images. The analysis shown in Sect. 6.6 was done twice, for $2'' \times 2''$ and $4'' \times 4''$ *Chandra* images. Since the binning has only a very mild effect on these scales, as was shown in see Sect. 6.3.2, we found the results to be well within 1-σ and only report them for the latter case.

For all clusters, we obtained the A parameter and its error in the same way as for the simulations, applying the recipe given in Sect. 6.3 on images which were smoothed with a 0.05 r_{500} wide kernel.

6.5.3 Data quality

The low- and high-z samples differ severely in terms of data quality, as was discussed in detail in Sect. 4 of our previous work Weißmann et al. (2013a). The majority of low-z clusters have observations with very high photon statistics, with a sample mean (median) of 100 000 (66 000) net and 15 000 (10 000) background counts within r_{500} (see Table 6.1). Much lower values are found for the high-z samples with on average < 2000 net counts and a mean net-to-background counts ratio ∼ 3.5.

The discrepancy in data quality translates into very different noise levels and does not allow a consistent comparison of A (Fig. 6.3). Applying smoothing with a kernel of 0.05 r_{500} significantly lowers the bias due to Poisson noise and makes the average 400SD observation roughly comparable to the average low-z one (Fig. 6.5). The situation can be improved by degrading the high-quality low-z observations to the mean photon statistics of the high-z sample. This ensures a consistent noise level in the low-z observations and a more reliable comparison to the high-z observations.

The low-z observations were degraded to 1200 net and 324 background photon counts,

the mean photon statistics of the 400SD sample (see Table 6.1). The method of degrading is described in detail in Weißmann et al. (2013a). Before mentioning the main points, we want to point out that, unless explicitly stated otherwise, the term cluster image describes the point-source-corrected but not background-subtracted observation. After extracting the net and background counts within r_{500} of the cluster and background image, a rescaled background is added to the cluster image to decrease the initially much higher net-(signal-)to-background counts ratio (S/B) to the desired S/B of 3.7. Next, this image is normalized to 1524 total counts within r_{500}, out of which 1 200 are net and 324 background counts. The background image is normalized to 324 counts within r_{500} to match the new low-count image. The result is a degraded cluster image with the same photon statistics as the average high-z observation. As in the case of the simulated observations, we create 100 poissonized degraded cluster images by applying the *zhtools* task *poisson* to the degraded cluster image. After the degrading, the images are smoothed with a kernel of 0.05 r_{500}. When quoting parameters for the (smoothed) degraded cluster images, we use the mean parameters of these 100 (smoothed) poissonized degraded cluster images.

6.6 Evolution of the substructure frequency

Using A as an indicator of the cluster morphology, we investigated the possible evolution of the substructure frequency. To ensure a reliable comparison of clusters with $z = 0.05 - 1.08$, we take into account the sensitivity of A to noise and the pixel resolution. To mimic the same average noise level in the low- and high-z observations, we use poissonized degraded images of the low-z clusters. Since these are derived from real observations, they have a higher noise level than expected from simulations with the same photon statistics. However, smoothing minimizes this effect and it is thus justified to compare A derived from smoothed poissonized degraded low-z images to the average smoothed high-z image.

While the low-z observations are now consistent in terms of data quality, the high-z observations cover a range of net and background counts combinations around the mean value of 1 200 net, 324 background counts. We checked the data quality of each high-z image by creating simulated poissonized observations with the same photon statistics and smoothed them with a kernel of 0.05 r_{500}. 13 observations (10 400SD, 3 SPT) are not consistent with the mean high-z photon statistics and yield too high A values. In these cases, we apply the correction method described in Sect. 6.4.1 using the $A_{\rm ideal} - A$ relation with 1 200 net, 324 background counts as reference point. Since this correction is only a rough estimate of the true A value, we always quote two results. In case i) we omit these clusters, while we use the corrected values in case ii).

The final $A-z$ relation is shown in Fig. 6.7 for case i) on the left and for case ii) on the right side. We form two samples to study the $A-z$ relation: sample I consists of the low-z and high-z 400SD clusters; sample II comprises the low-z and high-z SPT clusters. These two samples are used to study possible selection effects in the high-z samples. We fit the data with the linear relation $A = a \times z/0.55 + b$ using the BCES (Y|X) fitting method (Akritas & Bershady 1996) which minimizes the residuals in Y. The fitting parameters of case i) and ii) are very similar and are given in Table 6.2. In both cases and for both samples, we find a significant mild increase of A with redshift. Sample I gives a steeper and more significant slope with

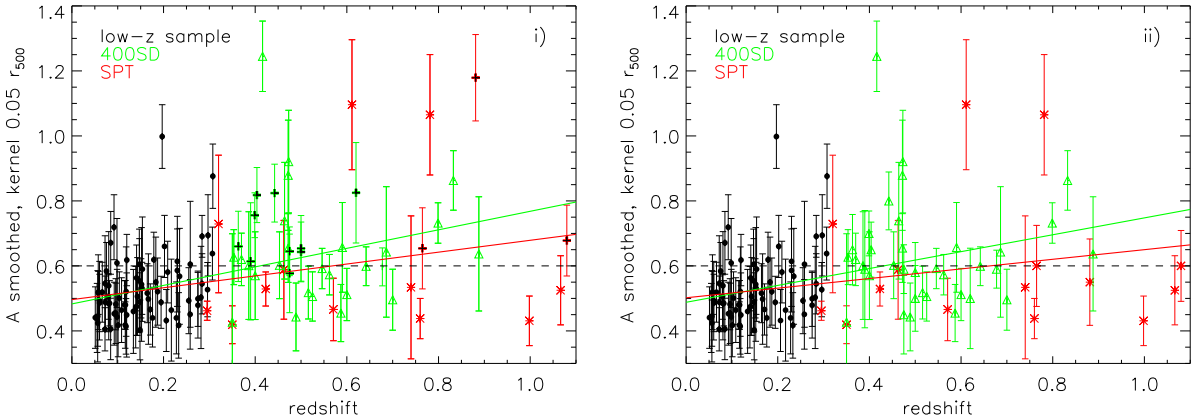

Figure 6.7: $A - z$ relation using smoothed poissonized degraded low-z and smoothed high-z observations. Black circles give the low-z, green triangles the high-z 400SD and red asterisks the high-z SPT clusters. The morphological boundary was adjusted to the mean high-z data quality and shown as a dotted line at $A = 0.6$. **Left:** case i). High-z clusters with insufficient data quality are shown as plus signs (10 400SD objects: green and black, 3 SPT clusters: red and black) in the figure, but omitted for the fits. **Right:** case ii). A values of clusters which are omitted in case i) are corrected to mimic the mean high-z data quality. This correction is a rough estimate using the $A_{\mathrm{ideal}} - A$ relation of simulated observations.

Table 6.2: Fitting parameters of the linear relations $A = a \times z/0.55 + b$ presented in Fig. 6.7.

i)	a	b
Sample I	0.16 ± 0.05	0.48 ± 0.02
Sample II	0.10 ± 0.07	0.50 ± 0.02
ii)	a	b
Sample I	0.14 ± 0.03	0.49 ± 0.01
Sample II	0.08 ± 0.05	0.50 ± 0.02

$a = 0.16 \pm 0.05$ than sample II with $a = 0.10 \pm 0.07$. This reflects the difference in the A-distribution of the two high-z samples. Adjusting the morphological boundary to $A = 0.6$ to match the data quality shown in Fig. 6.7 (see Sect. 6.3.1), we find a larger fraction of disturbed clusters in the 400SD than in the SPT sample. Including the corrected A parameters of clusters with too low photon statistics yields 50% (33%) disturbed and 50% (67%) relaxed objects for the 400SD (SPT) sample. Comparing these values to the 18% disturbed low-z clusters confirms the positive slope of the $A - z$ relation.

6.7 Combination with other morphology estimators

Quantifying the dynamical state of galaxy clusters can be done using a variety of morphology estimators. Among the most popular ones are power ratios and center shift. Power ratios (Buote & Tsai 1995, 1996) are based on the multipole expansion of the gravitational potential. Especially $P3/P0$, the normalized hexapole, has proved to be a reliable morphology estimator

Table 6.3: Fraction of clusters classified as relaxed ($A < 0.6$) and disturbed ($A > 0.6$) using the updated morphological boundary. The last column gives the fraction of clusters which do not have sufficient data quality for a direct comparison. In case ii) these clusters have corrected A values using the $A_{\mathrm{ideal}} - A$ relation of simulated observations.

i)	$A < 0.6$	$A > 0.6$	omitted
Low-z	82%	18%	0
400SD	31%	39%	30%
SPT	60%	20%	20%
ii)	$A < 0.6$	$A > 0.6$	omitted
Low-z	82%	18%	–
400SD	50%	50%	–
SPT	67%	33%	–

(e.g. Buote & Tsai 1995; Jeltema et al. 2005; Böhringer et al. 2010; Weißmann et al. 2013b). Center shift w (Mohr et al. 1993) gives the displacement of the centroid when calculating it in a number of regions with increasing area. As in the case of $P3/P0$, a large value of w indicates a disturbed cluster. Weißmann et al. (2013b) performed a detailed analysis of $P3/P0$ and w and investigated their noise properties and their dependence on the data quality. The center shift parameter w can be estimated well for low data quality and is a reliable morphology estimator when comparing low-z and high-z data (Weißmann et al. 2013a). The reliability of the $P3/P0$ determination begins to suffer severely below 1 000 net counts, especially for high backgrounds (net-to-background counts ratio < 2). They give a method to estimate and correct the bias due to noise for $P3/P0$ and w by adding Poisson noise to the observations. For low data quality, however, the bias is overestimated and sometimes a negative value is obtained after correction. In such a case, no information can be deduced from this cluster and the 1-σ Poisson error is used as an upper limit.

Rasia et al. (2013) compared the performance of $P3/P0$, w and A individually and in combination with each other in distinguishing between relaxed and disturbed objects. All three parameters work well in separating relaxed and disturbed clusters. Best results are obtained when combining them, as is shown by the significant correlation between these estimators with a Spearman's rank correlation coefficient $\rho = 0.72$ for $\log(P3/P0) - A$ and $\rho = 0.66$ for $\log(w) - A$.

We want to take this test one step further by introducing four different morphologies and test the position of the low-z clusters in the $\log(P3/P0) - A$ and $\log(w) - A$ plane. The visual classification of the low-z clusters into regular, intermediate, complex and double is taken from Weißmann et al. (2013b), who provide a detailed gallery of the low-z cluster sample. The definitions are as follows: Regular – regular clusters without structure. Intermediate – overall regular clusters which show some kind of locally restricted structure or slight asymmetry. Complex – clusters without two distinct maxima but global complex structure. Double – clusters with two distinct maxima.

Fig. 6.8 shows the relation between $P3/P0$, w and A for the low-z sample. $P3/P0$ and w

Table 6.4: Spearman ρ and Kendall τ rank correlation coefficients including the significance of its deviation from zero (*prob.*) for the relations between A, $P3/P0$ and w, calculated for the low-z sample.

	ρ	*prob.*	τ	*prob.*
$\log(P3/P0) - A$	0.53	7×10^{-6}	0.38	1×10^{-5}
$\log(w) - A$	0.66	9×10^{-11}	0.48	0
$\log(P3/P0) - \log(w)$	0.48	7×10^{-5}	0.35	4×10^{-5}

values are taken from Weißmann et al. (2013a), who calculated them from the original image in the r_{500} aperture and applied bias- and background correction. Upper limits are used for non-significant detections and marked in the figures. In addition, we use the morphological boundaries of $P3/P0 = 10^{-7}$ and $w = 0.01$ presented in their work. A was obtained from images smoothed with a kernel of 0.05 r_{500}. Owing to the slight underestimation of A when applying smoothing to high-quality images, which is shown in Fig. 6.5 (right), we adjusted the morphological boundary to $A = 0.4$ which corresponds to $A_{\mathrm{ideal}} = 0.5$ for the average low-z image with 100 000 net, 15 000 background counts.

Combining A with $P3/P0$ strengthens its reliability to find disturbed objects. 6 out of 7 double and 6 out of 10 complex clusters are found in the $A > 0.4$ and $P3/P0 > 10^{-7}$ region. On the other hand, the majority of intermediate and regular clusters is located in the $A < 0.4$ and $P3/P0 < 10^{-7}$ quadrant. For high-quality data, Weißmann et al. (2013b) gave two morphological $P3/P0$ boundaries to distinguish between relaxed ($P3/P0 < 10^{-8}$), mildly disturbed ($10^{-8} < P3/P0 < 5 \times 10^{-7}$) and disturbed clusters ($P3/P0 > 5 \times 10^{-7}$). Using these boundaries, we find only double and complex objects at $A > 0.4$ and $P3/P0 > 5 \times 10^{-7}$ and except for one intermediate cluster only regular objects in the $A < 0.4$ and $P3/P0 < 10^{-8}$ part of the $P3/P0 - A$ plane.

Similarly good results are obtained when combining A and w. Again, 6 out of 7 double and 5 out of 10 complex clusters are found at $A > 0.4$ and $w > 0.01$, while the majority of regular clusters is located in the $A < 0.4$ and $w < 0.01$ part of the figure. Both combinations work well in detecting regular and very disturbed (complex, double) objects, but the $\log(w) - A$ relation has less scatter. We find a Spearman's rank correlation coefficient $\rho = 0.66$ and a Kendall's rank correlation coefficient $\tau = 0.48$ for the $\log(w) - A$ relation, compared to $\rho = 0.53$ and $\tau = 0.38$ for $\log(P3/P0) - A$ (Table 6.4). Taking into account the fact that w is less sensitive to noise, using the $\log(w) - A$ plane might give more reliable results when analyzing large datasets with a wide range of data quality.

6.8 Discussion

The dynamical state of galaxy clusters has been investigated in recent years using a variety of morphology estimators. The increasing availability of high-z cluster observations enables the systematic study of cluster morphologies also at high redshift. However, the caveat is the low data quality and the high noise level which complicate the assessment of the dynamical state. It is therefore important to combine well-defined samples and well-understood morphology estimators to allow representative conclusions regarding the evolution of the disturbed

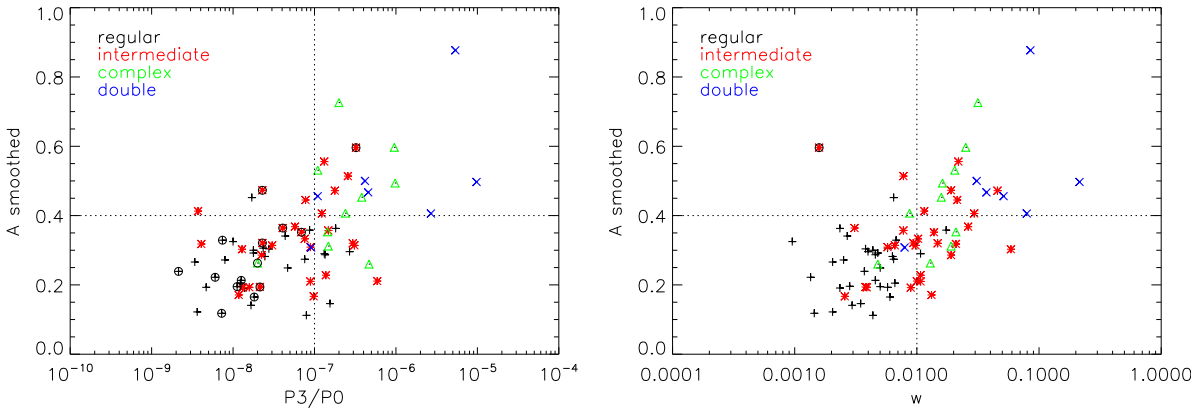

Figure 6.8: Comparison of well-known morphology estimators (left: $P3/P0$, right: w) and A for the low-z sample. $P3/P0$ and w values are taken from Weißmann et al. (2013a), calculated in the r_{500} aperture and bias- and background-corrected. A is determined after smoothing the image with an 0.05 r_{500} wide kernel. The dotted lines indicate the boundaries to divide the sample into relaxed and disturbed objects: $P3/P0 = 10^{-7}$ and $w = 0.01$ as defined in Weißmann et al. (2013b) and the updated A boundary at 0.4. The morphological classification, taken from Weißmann et al. (2013b), is color-coded: regular (black crosses), intermediate (red asterisks), complex (green triangles) and double (blue X). For non-significant detections of $P3/P0$ and w, upper limits are shown and indicated by black circles.

cluster fraction.

The asymmetry parameter in combination with the samples used in this study fulfills these requirements. The sensitivity of A to Poisson noise and the data quality in general has been tested in detail and smoothing was found to minimize these effects sufficiently. Adjusting the smoothing kernel depending on the photon statistics of the observations yields the best results. In this work we use a smoothing kernel of 0.05 r_{500} as a compromise for low and high-quality data. It gives sufficiently good results for all observations, but it could be larger/smaller for observations with lower/better data quality.

Although smoothing decreases the bias due to Poisson noise significantly, the best results are obtained when comparing observations of equal data quality. Degrading the high-quality low-z observations to the mean high-z data quality and correcting A of the high-z clusters with data quality below the high-z average yields the most meaningful results. Although sample I and sample II differ in the significance of their slopes, a mild increase of A with redshift is shown with both samples. Taking into account a possible bias in the 400d^2 detection algorithm (e.g. Santos et al. 2010) resulting in a lack of concentrated and relaxed clusters compared with other high-z samples, the slope of sample I can be taken as an upper limit for the $A-z$ evolution. In addition, we can exclude the case of no evolution with 1.4σ (SPT) to 3.2σ (400SD).

Using different morphology estimators, several authors found a more or less pronounced increase of the disturbed cluster fraction with redshift (e.g. Jeltema et al. 2005; Hashimoto et al. 2007a; Maughan et al. 2008; Andersson et al. 2009; Mann & Ebeling 2012; Weißmann et al. 2013a). Most recently, Weißmann et al. (2013a) investigated the $P3/P0 - z$ and $w - z$ relation using the same dataset as this work. They found a positive, but not significant, slope

for both parameters indicating a mild evolution of the substructure frequency. Within the significance limits, however, their result was also consistent with no evolution. The main disadvantage of determining $P3/P0$ for high-z clusters and thus low-quality data is the overestimation of Poisson noise for not very structured objects. The bias-corrected values for such objects are often negative or have large errors. In such cases only upper limits can be derived, which were not taken into account when fitting the $P3/P0 - z$ relation. w, on the other hand, is less sensitive to noise and can be considered as more reliable. In Sect. 6.3.1 we found a tight correlation with a large scatter between A, $P3/P0$ and w. The shallow slope of the $A - z$ relation agrees well with the findings reported by Weißmann et al. (2013a), but gives a more significant result. Combining the results from these three well-tested parameters and especially based on the significant result of the $A - z$ relation, we see evidence for a very mild positive evolution of the substructure frequency with redshift.

6.9 Conclusions

We performed a detailed study to quantify the effect of Poisson noise and pixel resolution on the asymmetry parameter A. Since it was originally defined for galaxy classification, where the data quality is much better than in X-ray observations, it was essential to explore its properties in detail before applying it to a large set of galaxy cluster images. In addition, we set the morphological boundary to $A = 0.5$ to divide a sample into relaxed and disturbed objects. This boundary needs to be slightly adjusted depending on the data quality and whether the image is smoothed or not. The study of the A parameter was done using a set of 121 simulated X-ray observations of galaxy clusters with an initial pixel resolution of $0.031\ r_{500}$. Binning and thus a lower pixel resolution leads to an overestimation of the true A value. This effect is mild for pixel sizes $< 8''$ but increases for larger bin sizes.

The sensitivity to the data quality was explored by creating mock observations with varying net and background count numbers within r_{500} and by adding Poisson noise. We found a clear dependence of A on the data quality, where A is severely overestimated for increasing Poisson noise. This problem can be minimized by smoothing the cluster image prior to the calculation of A. We tested a variety of smoothing kernel sizes and found a kernel of $0.05\ r_{500}$ to work well for low- and high-quality observations. Although smoothing can decrease the overestimation of A significantly, it cannot completely diminish the effect of noise. The remaining bias, however, is small and almost negligible for images with $> 1\,000$ net counts and not too high background.

Based on these findings, we could safely apply the A parameter to a set of 129 *XMM-Newton* and *Chandra* observations of galaxy clusters with $0.05 < z < 1.08$. We compared the performance of A as substructure parameter to the previously studied and well-known morphology estimators $P3/P0$ and w. We found a significant correlation of A with both parameters, but with large scatter. Very disturbed and very relaxed clusters are identified by all three estimators. For a more precise identification of mildly disturbed clusters, however, it seems favorable to use A in combination with $P3/P0$ and w.

We explored the evolution of the disturbed cluster fraction using A as substructure parameter. Since it is essential to compare images with the same pixel resolution and data quality, we rebinned the *Chandra* images and degraded the high-quality low-z observations to the

mean data quality of the high-z images. We reduce the effect of Poisson noise by smoothing the cluster images with a smoothing kernel of 0.05 r_{500}. For very low-quality high-z observations, we applied an additional correction by hand. We find that the fraction of disturbed clusters increases from 18% for the low-z sample to 50% (33%) for the 400SD (SPT) high-z sample. In addition, we performed a fit in the $A-$ redshift plane and found significant slopes of 0.14 ± 0.03 (0.08 ± 0.05) for the 400D (SPT) high-z sample. Taking into account that the high-z subset of the 400SD survey might contain an unrepresentative high number of disturbed objects, this result should be taken as upper limits for $A - z$ relation.

We conclude that the asymmetry parameter performs well in quantifying the dynamical state of galaxy clusters provided that the issues of pixel resolution and data quality are taken into account. In agreement with previous studies of the evolution of the substructure frequency, we find a mild increase of the disturbed cluster fraction with higher redshift. However, in contrary to results presented in Weißmann et al. (2013a), the results presented here are significant with $1.4 - 3.2\sigma$. We can therefore not only exclude a negative evolution but confirm a mild positive slope of the $A - z$ relation.

Acknowledgements
This work is based on observations obtained with *XMM-Newton* and *Chandra*. *XMM-Newton* is an ESA science mission with instruments and contributions directly funded by ESA Member States and NASA. The *XMM-Newton* project is supported by the Bundesministerium für Wirtschaft und Technologie/Deutsches Zentrum für Luft- und Raumfahrt (BMWI/DLR, FKZ 50 OX 0001), the Max-Planck Society and the Heidenhain-Stiftung. A part of the scientific results reported in this article are based on data obtained from the *Chandra* Data Archive. AW acknowledges the support from and participation in the International Max-Planck Research School on Astrophysics at the Ludwig-Maximilians University. GC acknowledges the support from Deutsches Zentrum für Luft- und Raumfahrt (DLR) with the program ID 50 R 1004. HB and GC acknowledge support from the DfG Transregio Program TR33 and the Munich Excellence Cluster "Structure and Evolution of the Universe".

Chapter 7

Conclusions

Studies of the X-ray morphology of galaxy clusters aim at quantifying their dynamical state. This information is crucial since many global cluster properties are derived assuming clusters to be relaxed objects. Deviations from this assumption lead to biases when studying astrophysical processes acting within the cluster and when using galaxy clusters as cosmological tracers.

A reliable determination of the dynamical state of galaxy clusters is only possible with well-studied and well-calibrated morphology estimators such as the ones presented in this work. This is especially important for low-quality X-ray images which are usually obtained for high-redshift clusters or in X-ray surveys. It is therefore essential for cluster studies in general and especially for investigations of the redshift evolution of cluster properties to conduct detailed performance tests of these parameters to locate and quantify weaknesses of the estimators and biases due to photon noise, which increases with decreasing data quality.

The main conclusions of this thesis and its contribution to morphological studies are summarized by providing answers to the questions raised in the beginning of this work.

- How reliable is the determination of the X-ray morphology and the dynamical state of galaxy clusters using common substructure measures such as power ratios, center shift or the asymmetry parameter, especially for varying data quality?

All three morphology estimators suffer from photon noise, but to a different degree (see Chapter 4 and 6). The center shift parameter w is most robust to Poisson noise and can be determined with small errors even for very shallow observations ($< 1\,000$ net photon counts) and reasonable background levels. This parameter is sensitive to asymmetries and can distinguish well between regular and irregular morphologies, but it is not suitable to characterize specific morphological types.

The third order power ratio $P3/P0$ is very sensitive to Poisson noise, which is difficult to quantify for this parameter. Obtaining a significant signal for low-quality data ($\lesssim 1\,000$ net photon counts and net-to-background counts ratio $\lesssim 3$) is only possible for very structured clusters, i.e. merging systems with two clear components. Such observations of mildly disturbed morphologies return spuriously high $P3/P0$ values and partly insignificant $P3/P0$ signals, where the error exceeds the obtained $P3/P0$ value. In case of a significant signal, the Poisson noise bias can be estimated and corrected. For high-quality observations ($< 30\,000$

net photon counts), $P3/P0$ is well-suited to distinguish between relaxed, mildly disturbed and merging systems.

The asymmetry parameter A is most severely affected by Poisson noise since it measures the residual flux of each pixel after subtracting a rotated image. It is thus very sensitive to the data quality and in addition also to the pixel size. Using this parameter to analyze X-ray images of a sample of clusters with varying net and background photon counts (photon statistics) and maybe also obtained from different instruments, requires additional steps to align the data quality of the images before performing the analysis. This issue is discussed for the first time for galaxy clusters in Chapter 6. Resolving it makes A a powerful tool to characterize the cluster morphology, especially in combination with $P3/P0$ and w.

- Can the bias in the X-ray images due to shot noise be estimated and corrected sufficiently to ensure a fair comparison of low- and high-quality data?

As is shown in detail in Chapters 4–6, all three parameters can be employed to analyze X-ray images of clusters with different redshift, but in the case of $P3/P0$ and A special care has to be taken. Since w is robust against Poisson noise, the bias correction for most cases is very small and often not necessary. When applying $P3/P0$ and A to X-ray images, correcting the bias is recommended for all observations. The Poisson bias is in general a function of the data quality but in the case of $P3/P0$ it also depends on the amount of structure, since merging systems can be detected even in shallow observations. This encouraged a non-parametric method to estimate the bias for $P3/P0$, which is presented in Chapter 4 (published as Weißmann et al. 2013b). It is based on the assumption that adding additional Poisson noise to the X-ray image can mimic the effect of the photon noise introduced during the observation. This method works well for $P3/P0$ (and also for w) for average low-redshift observations with good photon statistics, but tends to overestimate the bias for low data quality, yielding negative $P3/P0$ signals for not very structured objects after the bias correction. This issue is especially critical when comparing clusters spanning a wide range in redshift and thus data quality. One way to resolve this problem is presented in Chapter 5 (published as Weißmann et al. 2013a) by degrading high-quality observations to match the low-quality X-ray images before applying the bias correction. For low data quality, the overestimation of A is severe, but can be overcome by smoothing the X-ray image before the analysis. Since A is also sensitive to the pixel size, the most appropriate smoothing kernel depends on the data quality. Chapter 6 provides an example for the low- and high-redshift samples used in the framework of this thesis and shows that the bias can be reduced sufficiently. However, best results are obtained when using X-ray images with similar data quality – as in the case of $P3/P0$.

- What is the best definition of a morphological boundary to divide a sample into relaxed and disturbed objects?

The morphological boundaries presented in this work are based on the visual classification of the morphology of simulated galaxy cluster X-ray images and were tested for varying data quality. The *simple morphological boundary* at $P3/P0 = 10^{-7}$ and the *w boundary* at $w = 0.01$ roughly divide a sample into relaxed and disturbed objects. A more detailed analysis can be done using the *morphological P3/P0 boundaries* at $P3/P0 = 10^{-8}$ and $P3/P0 = 5 \times 10^{-7}$,

which allows the distinction between relaxed, mildly disturbed and disturbed objects. However, this refined classification scheme requires sufficient data quality (see Chapter 4). For the asymmetry parameter A, the best distinction between relaxed and disturbed clusters was found for $A = 0.5$. Previously to this work, the morphological boundary for A was derived only empirically from observations. It deviates significantly from the one based on simulations due to the sensitivity of A to the data quality and pixel size. Chapter 6 thus provides the first observation-independent definition of this boundary and discusses possible adjustments for different pixel sizes and data quality.

- Can the predicted increase of the fraction of disturbed galaxy clusters with redshift be confirmed by observations and quantified using the above mentioned substructure parameters?

Based on the detailed performance tests described above (and in detail in Chapter 4 and 6), a fair comparison of the dynamical state of low- and high-redshift galaxy clusters is ensured by matching the data quality of all observations. Doing so yields a very mild positive, but not significant, increase of the disturbed cluster fraction at higher redshift when employing $P3/P0$ and w. This result is significantly different to previous studies which reported a much steeper evolution (e.g. Jeltema et al. 2005). Although they corrected for Poisson noise, they did not take into account the effect of decreasing photon statistics for high-redshift observations and thus obtained a too steep slope in the $P3/P0 - z$ relation. The asymmetry parameter A returns the same result, namely a very mild positive evolution, but with higher significance. This work therefore concludes that there is a clear trend that the fraction of disturbed galaxy clusters increases with higher redshift, as is shown by all three morphology estimators. Owing to the low data quality of the X-ray images and the resulting uncertainties in the quantification of the clusters' dynamical state, however, the significance of this result is low.

Summarizing the above mentioned points, this thesis contributed to morphological studies of galaxy clusters by providing detailed performance tests of common morphology estimators, which ensure a reliable quantification of the dynamical state of galaxy clusters also at high redshift and for shallow observations. This will be especially important for future X-ray surveys such as *eROSITA*, which is expected to detect $\sim 10^5$ galaxy clusters, but partly only with short exposure times. Simulations predict that ~ 2900 $z < 0.3$ and ~ 350 $z > 0.3$ objects will have $> 1\,000$ net photon counts and are thus well-suited for morphological analyses.

On these large samples, the morphological information can be used for studying astrophysical processes and the influence of substructure on cluster properties. In addition, cosmological applications benefit from the knowledge of the clusters' dynamical state since it helps improving the accuracy of the mass estimates. Taking these investigations to higher redshift requires the morphological analysis of large cluster samples with a wide redshift range. The number of high-redshift observations of galaxy clusters increased significantly in the recent years, but is still small compared to low-redshift objects. Based on the results presented in this thesis, future morphological studies employing larger samples such as the one provided by *eROSITA* will be able to provide better constraints on e.g. the merger rates at higher redshift and the evolution of the disturbed cluster fraction in general, or the redshift dependence

of X-ray scaling relations including the impact of substructure on their scatter. Such a huge uniformly selected sample in combination with well-calibrated morphology estimators will thus help to deepen our understanding of the formation and evolution of galaxy clusters.

Appendix A

Chandra data reduction pipeline

A general overview of X-ray data reduction for galaxy clusters using the example of *XMM-Newton* data is given in Sect. 3.3. For the analysis of *Chandra* observations discussed in Chapter 5 and 6, I compiled a reduction pipeline using the standard CIAO tools as described in the CIAO Analysis Guides[1]. This section describes the pipeline, individual CIAO tasks and *Chandra*-specific issues. A flowchart of the main tasks used in the reduction of *Chandra* observations for galaxy clusters is given in Fig. A.1. All details mentioned are based on the CIAO software v4.4 and calibration database v4.4.7.

Data retrieval and observation details
Public *Chandra* Data is available at the *Chandra* Data Archive[2] and can be found and downloaded using the tool *chaser*[3]. After selecting an observation which is characterized by an observation identification number (ObsID), chaser offers the download of several directories and files such as the observation index file which contains a summary of the data products[4] associated with the ObsID, the primary and the secondary directory. The primary directory contains data products which were already processed by the Standard Data Processing (SDP) with the − at the time of the processing − most recent calibration files. This includes the so-called level=2 event file which was obtained from the level=1 event file after filtering on the good time intervals (GTI). The level=2 event file is suitable for data analysis, however, software and calibration change over time and updates might be available. The CIAO Team therefore recommends to reprocess the level=1 files (for details see below).

To perform an accurate data reduction and to evaluate whether reprocessing is needed, it is necessary to know details of the observation such as the observation mode or the version of the calibration files used for standard processing. These details can be extracted from the header of the level=1 event file using a command like *dmkeypar evt1.fits DATE-OBS echo+* to read out the date of the observation. Other interesting header keywords are CALDB and ASCDSVER which give the version of the calibration database and CIAO version used during SDP or DETNAM which returns the chips used for the observation. The level=1 event file

[1] `http://cxc.cfa.harvard.edu/ciao/guides`
[2] `http://asc.harvard.edu/cda`
[3] `http://cda.harvard.edu/chaser`
[4] For a detailed description of all data files see `http://cxc.harvard.edu/ciao/data_products_guide`

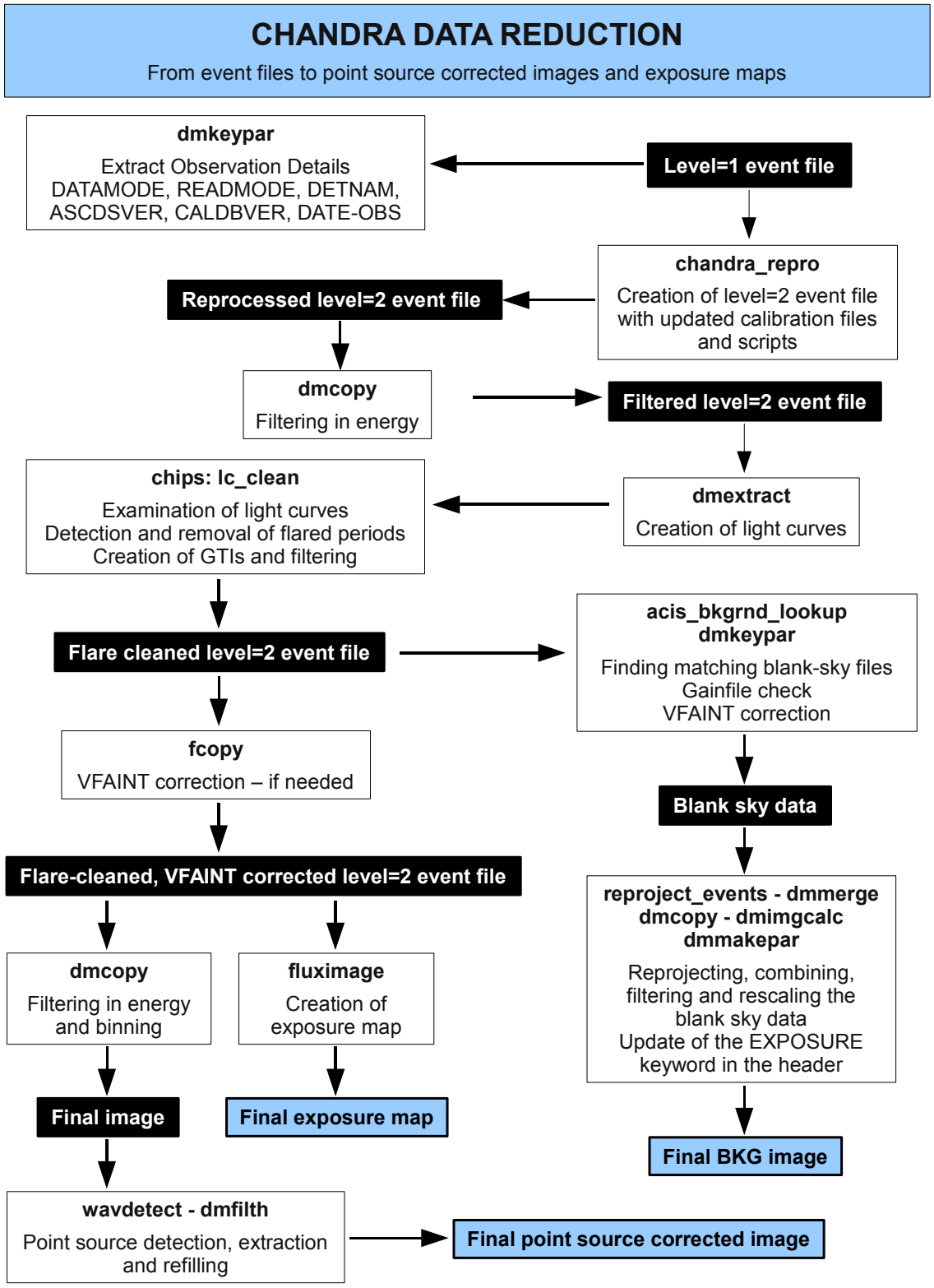

Figure A.1: *Chandra* data reduction pipeline flowchart.

is a list of all events which were recorded during the observation including those which are flagged as "bad" and will be removed during the data reduction process.

Reprocessing with *chandra_repro*

The CIAO software and the calibration files are continuously updated. The *Chandra* Science Team therefore recommends to check the CIAO and CALDB version used in the SDP and to recalibrate the event data. This ensures the use of the most recent software and calibration updates. For this purpose, they provide *chandra_repro*, an automated reprocessing script which is applied to the secondary data products such as the level=1 event file or the bad pixel file. *chandra_repro* runs a number of tasks and creates new primary products, most importantly a new level=2 event file and a new bad pixel file.

Reprocessing starts with *acis_clear_status_bits* which resets the ACIS status bits to remove effects from previous processing. Then the data (primarily the chip S4) is cleared from streak events using *destreak. acis_find_afterglow* and *acis_build_badpix* detect and flag cosmic ray afterglows, hot pixels and pixels adjacent to them and generate a new, updated bad pixel file. Afterglows are residual charges from interactions of cosmic rays with CCD pixels and might result in spurious detections of point sources. *acis_process_events* creates the new level=1 event file including the latest calibration information such as the most recent temperature-dependent charge transfer inefficiency (CTI) correction, time-dependent gain adjustment, gain map, the newly created bad pixel file, PHA randomization and sub-pixel adjustment. For observations taken in DATAMODE VFAINT (READMODE TIMED), the grade analysis[5] is done using a 5×5 pixel event island compared to 3×3 for the FAINT mode. This enables the use of the outer 16 pixels to detect bad events and can reduce the particle background significantly[6]. The last steps are filtering the newly calibrated level=1 event file for ACIS grades $(0, 2, 3, 4, 6)$ and a clean status column (status=0) using *dmcopy* and on good time intervals (GTI). This concludes the reprocessing and a new level=2 event file is created.

Flare cleaning

The reprocessed level=2 event file is then subject to flare cleaning following the COOKBOOK of Markevitch[7], who recommends to use exactly the same criteria for flare-cleaning on the science and background data (e.g. additonal cleaning for VFAINT). Since all *Chandra* observations used for this work are obtained with the front-illuminated ACIS-I chips, the discussion of the ACIS-S treatment is omitted.

The level=2 event file is filtered on the $0.3 - 12$ keV energy range using *dmcopy*. Cluster and point source emission are detected and masked out before extracting light curves for the combined array and each chip individually using the task *dmextract* and visualizing it with ChIPS[8]. This enables consistency checks between the individual chips and the full array. *lc_clean* removes flared periods and creates GTIs. For observations with only moderate flaring events, *lc_clean* runs automatically and without any problems. For strongly flared periods,

[5]Grades are integer numbers which are assigned to each event based on the values of the surrounding pixel island. For details on grades see `http://cxc.harvard.edu/proposer/POG/html/ACIS.html#sec:GRADES`

[6]For details on the VFAINT correction see `http://cxc.harvard.edu/cal/Acis/Cal_prods/vfbkgrnd/`

[7]`http://cxc.harvard.edu/contrib/maxim/acisbg`

[8]The *Chandra* Imaging and Plotting System: `http://cxc.cfa.harvard.edu/chips/`

manual adjustments are needed. The level=2 event file is filtered on the GTIs and an additional background correction is applied for VFAINT observations.

Problems with flare cleaning

- For strong flares the mean counts obtained by *lc_clean*, which is used for sigma-clipping the light curve, may not fit the light curve. In such cases it is recommended to obtain the mean by hand and to manually include it in the command when running *lc_clean*. In case this does not work sufficiently, one can adjust the mean by hand or manually cut out the flared period before creating the light curve. Running *lc_clean* again will tell whether this was sufficient or if another iteration is needed.
- If the cluster covers almost a full chip, the fluctuations can be very large and thus a lot of time bins are detected as flared periods. In such cases chip-by-chip cleaning is not recommended, but the full array should be used.
- "StandardError: Unable to calculate an initial mean level via sigma clipping." This error message shows that *lc_clean* is not able to calculate an initial mean level. After taking a closer look at the light curves of all chips before and after source removal, flared periods need to be cut out by hand and *lc_clean* has to be rerun.

Background

As in the case of *XMM-Newton*, blank sky field data is used to estimate the background contribution. As part of the CIAO CALDB package, Markevitch provides flare-cleaned blank sky images for the ACIS-I and S chips, which differ e.g. in the time bins for the flare detection. They were created following his COOKBOOK and flare-cleaned as the science data described above. *acis_bkgrnd_lookup* finds blank sky files from the CALDB for each detector which match the observation (VFAINT, GAINFILE etc). If needed, VFAINT correction is applied to the blank sky data. In specific cases, *acis_bkgrnd_lookup* returns a blank sky file whose gainfile is different to the one of the observation. In such cases, the background files needs to be reprocessed with *acis_process_events*, specifying the gainfile of the observation. The blank sky data are then reprojected onto the sky using *reproject_events* to match the sky position of the observation. The background files of each chip are merged into one background event file with *dmmerge* and events in the $0.5-2$ keV range are extracted using *dmcopy*. After creating an 2×2 arcsec image, it is normalized to the exposure time of the observation, calculating the scale factor with *dmimgcalc*. Last, *dmmakepar* is used to update the header keyword EXPOSURE.

Creation of science products

Using *dmcopy*, events in the $0.5-2$ keV range are extracted from the flare-cleaned event file and binned by a factor of 4 (bin sky=4) to obtain 2×2 arcsec images. For the creation of exposure maps *fluximage* is applied which allows two options to create an exposure map. If a standard *Chandra* band is selected (e.g. broad $0.5-7$ keV), the exposure map for the standard centerband energy (2.3 keV for broad) is returned. For this work the $0.5-2$ keV *XMM-Newton* standard band is used and monochromatic 1 keV exposure maps are created. It is also possible to generate spectrally weighted instrument maps, which are used to create exposure maps and which take the energy dependence of the effective area into account. However, in order to

obtain spectral weights, a spectral fit is needed.

Comment on *fluximage*
One disadvantage of *fluximage* is the fact that it automatically crops the exposure map to the smallest possible size. Since the output size cannot be specified, the image and the background file need to be cropped to ensure a fair analysis. *get_sky_limits* returns the exact pixel size of the exposure map. Creating a region file which fits the exposure map exactly and applying it to the image and background file solves this issue.

Point source removal
At last, point sources (including all sources which do not belong to the galaxy cluster) need to be detected and removed from the image. A rough detection of point sources was already done with *wavdectect* before the flare cleaning. However, at this point one should examine each source in detail to make sure whether it is part of the galaxy cluster or a fore-/background source. *wavdectect* is rerun on the final flare-cleaned image and returns a list of point sources. After a visual inspection of the sources and manual adjustments of the cut-out regions around the point sources, *dmfilth* cuts out the specified regions and refills them by sampling the new pixel value from the distribution of pixel values in the background region annuli (inner radius: radius of the source region; outer radius: $2 \times$ radius of the source region).

To obtain background-subtracted images, the background image is subtracted from the flare-cleaned, point-source corrected image.

Multiple observations
Multiple pointings of the same cluster can be combined to enhance the quality of the data. However, before blindly merging several observations, one should examine whether a combination will indeed improve the quality or just increase the noise. This can be especially critical when merging a long and a short exposure. The CIAO software offers the possibility to merge observational data on both the event file and the image level. Both methods are outlined below, including possible problems and work-arounds. As in the case of a single pointing, the aim is to create a point-source corrected image, an exposure map and a background image.

Merging multiple observations on the event file level seems to be a very clean way. After excluding flared periods from the event list and background cleaning for VFAINT observations, two (or more) event files can be combined with *merge_all*, which returns a merged event file and an exposure map. Comparing the exposure map produced by *merge_all* to the merged exposure map created by *reproject_image* on the image level revealed inconsistencies. Communications with the CXC Help desk confirmed that *merge_all* works well when observations, which should be merged, were taken closely together with the same SIM offsets and without a change of the CCD characteristics. But it cannot take all ancillary files into account and can only use the bad pixel file of one pointing. This is reasonable for split observations, which were taken consecutively, but in this work multiple pointings, which were obtained in different observation cycles and years, are used.

For this work it is thus recommended to merge pointings on the image level. Each observation is reduced following the recipe outlined above including flare cleaning and the creation of an exposure map, image and background image. These data products are then merged us-

ing *reproject_image*, taking e.g. img1.fits as matchfile to specify the orientation of the final product. The position and pixel size of img1.fits remain the same while img2.fits is rotated and rebinned to match img1.fits. In addition, the pixel values of img2.fits change from integer (as img1.fits) to real. For counts images (cluster and background image) the option *method=sum* is used, which adds the pixel information of the two images. Exposure maps are combined using *method=average* with the same matchfile as for the counts images (e.g. img1.fits). For exposure maps which have the same pixel size as the matchfile, the options *method=sum* and *method=average* give the same result, since the exposure maps are added but not rebinned. In all other cases, however, *method=average* ensures that the exposure information is correct after rebinning.

Bibliography

Abell, G. O. 1958, ApJS, 3, 211

Akritas, M. G. & Bershady, M. A. 1996, ApJ, 470, 706

Allen, S. W., Rapetti, D. A., Schmidt, R. W., et al. 2008, MNRAS, 383, 879

Allen, S. W., Schmidt, R. W., Ebeling, H., Fabian, A. C., & van Speybroeck, L. 2004, MNRAS, 353, 457

Ameglio, S., Borgani, S., Pierpaoli, E., & Dolag, K. 2007, MNRAS, 382, 397

Ameglio, S., Borgani, S., Pierpaoli, E., et al. 2009, MNRAS, 394, 479

Andersson, K., Benson, B. A., Ade, P. A. R., et al. 2011, ApJ, 738, 48

Andersson, K., Peterson, J. R., Madejski, G., & Goobar, A. 2009, ApJ, 696, 1029

Andrade-Santos, F., Lima Neto, G. B., & Laganá, T. F. 2012, ApJ, 746, 139

Arnaud, M., Maurogordato, S., Slezak, E., & Rho, J. 2000, A&A, 355, 461

Arnaud, M., Pointecouteau, E., & Pratt, G. W. 2005, A&A, 441, 893

Arnaud, M., Pointecouteau, E., & Pratt, G. W. 2007, A&A, 474, L37

Arnaud, M., Pratt, G. W., Piffaretti, R., et al. 2010, A&A, 517, A92

Ascasibar, Y. & Markevitch, M. 2006, ApJ, 650, 102

Bartelmann, M. 2010, Classical and Quantum Gravity, 27, 233001

Bauer, F. E., Fabian, A. C., Sanders, J. S., Allen, S. W., & Johnstone, R. M. 2005, MNRAS, 359, 1481

Beers, T. C., Flynn, K., & Gebhardt, K. 1990, AJ, 100, 32

Benson, B. A., de Haan, T., Dudley, J. P., et al. 2013, ApJ, 763, 147

Best, P. N., Kaiser, C. R., Heckman, T. M., & Kauffmann, G. 2006, MNRAS, 368, L67

Birzan, L., Rafferty, D. A., McNamara, B. R., Wise, M. W., & Nulsen, P. E. J. 2004, ApJ, 607, 800

Biviano, A. 2000, in Constructing the Universe with Clusters of Galaxies

Biviano, A. & Girardi, M. 2003, ApJ, 585, 205

Biviano, A., Murante, G., Borgani, S., et al. 2006, A&A, 456, 23

Böhringer, H., Dolag, K., & Chon, G. 2012, A&A, 539, A120

Böhringer, H. & Hensler, G. 1989, A&A, 215, 147

Böhringer, H., Nulsen, P. E. J., Braun, R., & Fabian, A. C. 1995, MNRAS, 274, L67

Böhringer, H., Pratt, G. W., Arnaud, M., et al. 2010, A&A, 514, A32

Böhringer, H., Schücker, P., Pratt, G. W., et al. 2007, A&A, 469, 363

Böhringer, H., Voges, W., Fabian, A. C., Edge, A. C., & Neumann, D. M. 1993, MNRAS, 264, L25

Böhringer, H. & Werner, N. 2010, A&A Rev., 18, 127

Borgani, S. 2008, in Lecture Notes in Physics, Berlin Springer Verlag, Vol. 740, A Pan-Chromatic View of Clusters of Galaxies and the Large-Scale Structure, ed. M. Plionis, O. López-Cruz, & D. Hughes, 287

Borgani, S. & Kravtsov, A. V. 2011, Adv. Sci. Lett.

Borgani, S., Murante, G., Springel, V., et al. 2004, MNRAS, 348, 1078

Bothun, G. D., Geller, M. J., Beers, T. C., & Huchra, J. P. 1983, ApJ, 268, 47

Briel, U. G., Henry, J. P., & Böhringer, H. 1992, A&A, 259, L31

Briel, U. G., Henry, J. P., Schwarz, R. A., et al. 1991, A&A, 246, L10

Broadhurst, T., Takada, M., Umetsu, K., et al. 2005, ApJ, 619, L143

Brunetti, G., Setti, G., Feretti, L., & Giovannini, G. 2001, MNRAS, 320, 365

Buote, D. A. 2001, ApJ, 553, L15

Buote, D. A. 2002, in Astrophysics and Space Science Library, Vol. 272, Merging Processes in Galaxy Clusters, ed. L. Feretti, I. M. Gioia, & G. Giovannini, 79–107

Buote, D. A. & Tsai, J. C. 1995, ApJ, 452, 522

Buote, D. A. & Tsai, J. C. 1996, ApJ, 458, 27

Burenin, R. A., Vikhlinin, A., Hornstrup, A., et al. 2007, ApJS, 172, 561

Burns, J. O. 1990, AJ, 99, 14

Burns, J. O., Hallman, E. J., Gantner, B., Motl, P. M., & Norman, M. L. 2008, ApJ, 675, 1125

Byram, E. T., Chubb, T. A., & Friedman, H. 1966, AJ, 71, 379

Carlberg, R. G., Yee, H. K. C., Ellingson, E., et al. 1997, ApJ, 485, L13

Cassano, R., Ettori, S., Giacintucci, S., et al. 2010, ApJ, 721, L82

Cavagnolo, K. W., Donahue, M., Voit, G. M., & Sun, M. 2008, ApJ, 683, L107

Cavagnolo, K. W., McNamara, B. R., Wise, M. W., et al. 2011, ApJ, 732, 71

Cavaliere, A. & Fusco-Femiano, R. 1976, A&A, 49, 137

Cavaliere, A. & Fusco-Femiano, R. 1978, A&A, 70, 677

Chon, G., Böhringer, H., & Smith, G. P. 2012, A&A, 548, A59

Churazov, E., Brüggen, M., Kaiser, C. R., Böhringer, H., & Forman, W. 2001, ApJ, 554, 261

Churazov, E., Forman, W., Jones, C., & Böhringer, H. 2003, ApJ, 590, 225

Clarke, T. E., Blanton, E. L., & Sarazin, C. L. 2004, ApJ, 616, 178

Clowe, D., Bradač, M., Gonzalez, A. H., et al. 2006, ApJ, 648, L109

Cohn, J. D. & White, M. 2005, Astroparticle Physics, 24, 316

Conselice, C. J. 1997, PASP, 109, 1251

Conselice, C. J., Bershady, M. A., & Jangren, A. 2000, ApJ, 529, 886

Croston, J. H., Arnaud, M., Pointecouteau, E., & Pratt, G. W. 2006, A&A, 459, 1007

Croston, J. H., Pratt, G. W., Böhringer, H., et al. 2008, A&A, 487, 431

da Silva, A. C., Kay, S. T., Liddle, A. R., & Thomas, P. A. 2004, MNRAS, 348, 1401

Davis, D. S. 1993, in BAAS, Vol. 25, American Astronomical Society Meeting Abstracts, #125.03

Davis, D. S. & Mushotzky, R. F. 1993, AJ, 105, 409

Dennison, B. 1980, ApJ, 239, L93

Dolag, K., Borgani, S., Murante, G., & Springel, V. 2009, MNRAS, 399, 497

Doria, A., Gitti, M., Ettori, S., et al. 2012, ApJ, 753, 47

Dunn, R. J. H. & Fabian, A. C. 2006, MNRAS, 373, 959

Eckert, D., Molendi, S., & Paltani, S. 2011, A&A, 526, A79

Eisenstein, D. J. & Hu, W. 1999, ApJ, 511, 5

Eke, V. R., Navarro, J. F., & Frenk, C. S. 1998, ApJ, 503, 569

ESA: XMM-Newton SOC. 2012, XMM-Newton Users Handbook, Issue 2.10

Escalera, E. & Mazure, A. 1992, ApJ, 388, 23

Ettori, S. 2000a, MNRAS, 318, 1041

Ettori, S. 2000b, MNRAS, 311, 313

Ettori, S., Gastaldello, F., Gitti, M., et al. 2013, A&A, 555, A93

Evrard, A. E. 1990, ApJ, 363, 349

Fabian, A. C. 1994, ARA&A, 32, 277

Fabian, A. C. 2012, ARA&A, 50, 455

Fabian, A. C., Crawford, C. S., Edge, A. C., & Mushotzky, R. F. 1994, MNRAS, 267, 779

Fabian, A. C. & Nulsen, P. E. J. 1977, MNRAS, 180, 479

Fabian, A. C., Sanders, J. S., Allen, S. W., et al. 2011, MNRAS, 418, 2154

Fabian, A. C., Sanders, J. S., Allen, S. W., et al. 2003, MNRAS, 344, L43

Fabian, A. C., Sanders, J. S., Ettori, S., et al. 2000, MNRAS, 318, L65

Feigelson, E. D. & Nelson, P. I. 1985, ApJ, 293, 192

Felten, J. E., Gould, R. J., Stein, W. A., & Woolf, N. J. 1966, ApJ, 146, 955

Feretti, L., Giovannini, G., Govoni, F., & Murgia, M. 2012, A&A Rev., 20, 54

Finoguenov, A., Böhringer, H., & Zhang, Y.-Y. 2005, A&A, 442, 827

Finoguenov, A., Reiprich, T. H., & Böhringer, H. 2001, A&A, 368, 749

Finoguenov, A., Sarazin, C. L., Nakazawa, K., Wik, D. R., & Clarke, T. E. 2010, ApJ, 715, 1143

Flin, P. & Krywult, J. 2006, A&A, 450, 9

Forman, W., Jones, C., Churazov, E., et al. 2007, ApJ, 665, 1057

Geller, M. J. & Beers, T. C. 1982, PASP, 94, 421

Ghizzardi, S., Rossetti, M., & Molendi, S. 2010, A&A, 516, A32

Giacintucci, S., Venturi, T., Macario, G., et al. 2008, A&A, 486, 347

Giodini, S., Lovisari, L., Pointecouteau, E., et al. 2013, Space Sci. Rev., 177, 247

Girardi, M. & Biviano, A. 2002, in Astrophysics and Space Science Library, Vol. 272, Merging Processes in Galaxy Clusters, ed. L. Feretti, I. M. Gioia, & G. Giovannini, 39–77

Gitti, M., Brighenti, F., & McNamara, B. R. 2012, Advances in Astronomy, 2012

Gitti, M., Feretti, L., & Schindler, S. 2006, A&A, 448, 853

Gitti, M., Nulsen, P. E. J., David, L. P., McNamara, B. R., & Wise, M. W. 2011, ApJ, 732, 13

Governato, F., Babul, A., Quinn, T., et al. 1999, MNRAS, 307, 949

Gross, M. A. K., Somerville, R. S., Primack, J. R., Holtzman, J., & Klypin, A. 1998, MNRAS, 301, 81

Hallman, E. J. & Jeltema, T. E. 2011, MNRAS, 418, 2467

Hart, B. C. 2008, PhD thesis, University of California, Irvine, arXiv:0801.4093

Hashimoto, Y., Böhringer, H., Henry, J. P., Hasinger, G., & Szokoly, G. 2007a, A&A, 467, 485

Hashimoto, Y., Henry, J. P., Böhringer, H., & Hasinger, G. 2007b, A&A, 468, 25

Hasselfield, M., Hilton, M., Marriage, T. A., et al. 2013, J. Cosmology Astropart. Phys., 7, 8

Henning, J. W., Gantner, B., Burns, J. O., & Hallman, E. J. 2009, ApJ, 697, 1597

Ho, S., Bahcall, N., & Bode, P. 2006, ApJ, 647, 8

Hoekstra, H., Bartelmann, M., Dahle, H., et al. 2013, Space Sci. Rev., 177, 75

Horner, D. J. 2001, PhD thesis, University of Maryland College Park

Hudson, D. S., Mittal, R., Reiprich, T. H., et al. 2010, A&A, 513, A37

Ikebe, Y., Ezawa, H., Fukazawa, Y., et al. 1996, Nature, 379, 427

Isobe, T., Feigelson, E. D., & Nelson, P. I. 1986, ApJ, 306, 490

Jeltema, T. E., Canizares, C. R., Bautz, M. W., & Buote, D. A. 2005, ApJ, 624, 606

Jeltema, T. E., Hallman, E. J., Burns, J. O., & Motl, P. M. 2008, ApJ, 681, 167

Jenkins, A., Frenk, C. S., White, S. D. M., et al. 2001, MNRAS, 321, 372

Jones, C. & Forman, W. 1984, ApJ, 276, 38

Jones, C. & Forman, W. 1991, in BAAS, Vol. 23, Bulletin of the American Astronomical Society, 1338

Jones, C. & Forman, W. 1992, in NATO ASIC Proc. 366: Clusters and Superclusters of Galaxies, ed. A. C. Fabian, 49

Jones, C. & Forman, W. 1999, ApJ, 511, 65

Jones, C., Mandel, E., Schwarz, J., et al. 1979, ApJ, 234, L21

Jones, L. R., Scharf, C., Ebeling, H., et al. 1998, ApJ, 495, 100

Kaiser, N. 1986, MNRAS, 222, 323

Kay, S. T., da Silva, A. C., Aghanim, N., et al. 2007, MNRAS, 377, 317

Kay, S. T., Thomas, P. A., Jenkins, A., & Pearce, F. R. 2004, MNRAS, 355, 1091

Kelly, B. C. 2007, ApJ, 665, 1489

King, I. 1962, AJ, 67, 471

Kneib, J.-P., Ellis, R. S., Smail, I., Couch, W. J., & Sharples, R. M. 1996, ApJ, 471, 643

Kolokotronis, V., Basilakos, S., Plionis, M., & Georgantopoulos, I. 2001, MNRAS, 320, 49

Komatsu, E., Smith, K. M., Dunkley, J., et al. 2011, ApJS, 192, 18

Kravtsov, A. V. & Borgani, S. 2012, ARA&A, 50, 353

Kravtsov, A. V., Vikhlinin, A., & Nagai, D. 2006, ApJ, 650, 128

Lau, E. T., Kravtsov, A. V., & Nagai, D. 2009, ApJ, 705, 1129

Lea, S. M., Silk, J., Kellogg, E., & Murray, S. 1973, ApJ, 184, L105

Liang, H., Hunstead, R. W., Birkinshaw, M., & Andreani, P. 2000, ApJ, 544, 686

Limber, D. N. 1959, ApJ, 130, 414

Mahdavi, A., Hoekstra, H., Babul, A., et al. 2013, ApJ, 767, 116

Mahdavi, A., Hoekstra, H., Babul, A., & Henry, J. P. 2008, MNRAS, 384, 1567

Mann, A. W. & Ebeling, H. 2012, MNRAS, 420, 2120

Mantz, A., Allen, S. W., Rapetti, D., & Ebeling, H. 2010, MNRAS, 406, 1759

Markevitch, M. 1998, ApJ, 504, 27

Markevitch, M. 2006, in ESA Special Publication, Vol. 604, The X-ray Universe 2005, ed. A. Wilson, 723

Markevitch, M. 2010, arXiv:1010.3660

Markevitch, M., Gonzalez, A. H., David, L., et al. 2002, ApJ, 567, L27

Markevitch, M. & Vikhlinin, A. 2007, Physics Reports, 443, 1

Markevitch, M., Vikhlinin, A., & Mazzotta, P. 2001, ApJ, 562, L153

Maughan, B. J., Giles, P. A., Randall, S. W., Jones, C., & Forman, W. R. 2012, MNRAS, 421, 1583

Maughan, B. J., Jones, C., Forman, W., & Van Speybroeck, L. 2008, ApJS, 174, 117

Maurogordato, S., Sauvageot, J. L., Bourdin, H., et al. 2011, A&A, 525, A79

Mazzotta, P., Bourdin, H., Giacintucci, S., Markevitch, M., & Venturi, T. 2011, Mem. Soc. Astron. Italiana, 82, 495

Mazzotta, P. & Giacintucci, S. 2008, ApJ, 675, L9

Mazzotta, P., Markevitch, M., Vikhlinin, A., et al. 2001, ApJ, 555, 205

McDonald, M., Bayliss, M., Benson, B. A., et al. 2012, Nature, 488, 349

McMillan, S. L. W., Kowalski, M. P., & Ulmer, M. P. 1989, ApJS, 70, 723

McNamara, B. R., Kazemzadeh, F., Rafferty, D. A., et al. 2009, ApJ, 698, 594

McNamara, B. R. & Nulsen, P. E. J. 2012, New Journal of Physics, 14, 055023

McNamara, B. R., Nulsen, P. E. J., Wise, M. W., et al. 2005, Nature, 433, 45

McNamara, B. R. & O'Connell, R. W. 1989, AJ, 98, 2018

Melott, A. L., Chambers, S. W., & Miller, C. J. 2001, ApJ, 559, L75

Meneghetti, M., Rasia, E., Merten, J., et al. 2010, A&A, 514, A93

Million, E. T., Werner, N., Simionescu, A., et al. 2010, MNRAS, 407, 2046

Mitchell, R. J., Culhane, J. L., Davison, P. J. N., & Ives, J. C. 1976, MNRAS, 175, 29P

Mitchell, R. J., Dickens, R. J., Burnell, S. J. B., & Culhane, J. L. 1979, MNRAS, 189, 329

Mitchell, R. J., Ives, J. C., & Culhane, J. L. 1977, MNRAS, 181, 25P

Mittal, R., Hicks, A., Reiprich, T. H., & Jaritz, V. 2011, A&A, 532, A133

Mittal, R., Hudson, D. S., Reiprich, T. H., & Clarke, T. 2009, A&A, 501, 835

Mohr, J. J., Evrard, A. E., Fabricant, D. G., & Geller, M. J. 1995, ApJ, 447, 8

Mohr, J. J., Fabricant, D. G., & Geller, M. J. 1993, ApJ, 413, 492

Motl, P. M., Hallman, E. J., Burns, J. O., & Norman, M. L. 2005, ApJ, 623, L63

Nagai, D., Vikhlinin, A., & Kravtsov, A. V. 2007, ApJ, 655, 98

Nelson, K., Rudd, D. H., Shaw, L., & Nagai, D. 2012, ApJ, 751, 121

Neumann, D. M. & Böhringer, H. 1997, MNRAS, 289, 123

Nulsen, P. E. J., Li, Z., Forman, W. R., et al. 2013, arXiv:1307.8072

Nulsen, P. E. J., McNamara, B. R., Wise, M. W., & David, L. P. 2005, ApJ, 628, 629

O'Hara, T. B., Mohr, J. J., Bialek, J. J., & Evrard, A. E. 2006, ApJ, 639, 64

Okabe, N., Zhang, Y.-Y., Finoguenov, A., et al. 2010, ApJ, 721, 875

Pandge, M. B., Vagshette, N. D., Sonkamble, S. S., & Patil, M. K. 2013, Ap&SS, 345, 183

Paterno-Mahler, R., Blanton, E. L., Randall, S. W., & Clarke, T. E. 2013, ApJ, 773, 114

Peacock, J. A. 2003, arXiv:0309240

Pen, U.-L. 1997, New A, 2, 309

Peterson, J. R., Kahn, S. M., Paerels, F. B. S., et al. 2003, ApJ, 590, 207

Peterson, J. R., Paerels, F. B. S., Kaastra, J. S., et al. 2001, A&A, 365, L104

Petrosian, V. 2001, ApJ, 557, 560

Pfrommer, C. & Enßlin, T. A. 2004, Journal of Korean Astronomical Society, 37, 455

Piffaretti, R. & Valdarnini, R. 2008, A&A, 491, 71

Pinkney, J., Roettiger, K., Burns, J., & Bird, C. 1996, ApJS, 104, 1

Planck Collaboration, Ade, P. A. R., Aghanim, N., et al. 2013a, arXiv:1303.5076

Planck Collaboration, Ade, P. A. R., Aghanim, N., et al. 2013b, arXiv:1303.5080

Plionis, M. 2002, ApJ, 572, L67

Poole, G. B., Babul, A., McCarthy, I. G., et al. 2007, MNRAS, 380, 437

Poole, G. B., Babul, A., McCarthy, I. G., Sanderson, A. J. R., & Fardal, M. A. 2008, MNRAS, 391, 1163

Poole, G. B., Fardal, M. A., Babul, A., et al. 2006, MNRAS, 373, 881

Pratt, G. W., Croston, J. H., Arnaud, M., & Böhringer, H. 2009, A&A, 498, 361

Press, W. H. & Schechter, P. 1974, ApJ, 187, 425

Rafferty, D. A., McNamara, B. R., Nulsen, P. E. J., & Wise, M. W. 2006, ApJ, 652, 216

Rahman, N., Krywult, J., Motl, P. M., Flin, P., & Shandarin, S. F. 2006, MNRAS, 367, 838

Rasia, E., Ettori, S., Moscardini, L., et al. 2006, MNRAS, 369, 2013

Rasia, E., Mazzotta, P., Evrard, A., et al. 2011, ApJ, 729, 45

Rasia, E., Meneghetti, M., & Ettori, S. 2013, Astron. Rev., 8, 40

Rasia, E., Meneghetti, M., Martino, R., et al. 2012, New Journal of Physics, 14, 055018

Reichert, A., Böhringer, H., Fassbender, R., & Mühlegger, M. 2011, A&A, 535, A4

Reiprich, T. H., Basu, K., Ettori, S., et al. 2013, Space Sci. Rev., 177, 195

Reiprich, T. H. & Böhringer, H. 2002, ApJ, 567, 716

Roediger, E., Brüggen, M., Simionescu, A., et al. 2011, MNRAS, 413, 2057

Roediger, E., Kraft, R. P., Forman, W. R., Nulsen, P. E. J., & Churazov, E. 2013, ApJ, 764, 60

Roediger, E., Lovisari, L., Dupke, R., et al. 2012, MNRAS, 420, 3632

Rosati, P., della Ceca, R., Norman, C., & Giacconi, R. 1998, ApJ, 492, L21

Rossetti, M., Eckert, D., Cavalleri, B. M., et al. 2011, A&A, 532, A123

Rossetti, M., Eckert, D., De Grandi, S., et al. 2013, A&A, 556, A44

Rowley, D. R., Thomas, P. A., & Kay, S. T. 2004, MNRAS, 352, 508

Russell, H. R., McNamara, B. R., Sanders, J. S., et al. 2012, MNRAS, 423, 236

Russell, H. R., Sanders, J. S., Fabian, A. C., et al. 2010, MNRAS, 406, 1721

Sanders, J. S., Fabian, A. C., Allen, S. W., et al. 2008, MNRAS, 385, 1186

Sanders, J. S., Fabian, A. C., & Taylor, G. B. 2005, MNRAS, 356, 1022

Sanderson, A. J. R., Edge, A. C., & Smith, G. P. 2009, MNRAS, 398, 1698

Sanderson, A. J. R., Ponman, T. J., Finoguenov, A., Lloyd-Davies, E. J., & Markevitch, M. 2003, MNRAS, 340, 989

Santos, J. S., Tozzi, P., Rosati, P., & Böhringer, H. 2010, A&A, 521, A64

Sasaki, S. 1996, PASJ, 48, L119

Schindler, S., Castillo-Morales, A., De Filippis, E., Schwope, A., & Wambsganss, J. 2001, A&A, 376, L27

Schindler, S. & Diaferio, A. 2008, Space Sci. Rev., 134, 363

Schuecker, P., Böhringer, H., Collins, C. A., & Guzzo, L. 2003, A&A, 398, 867

Schuecker, P., Böhringer, H., Reiprich, T. H., & Feretti, L. 2001, A&A, 378, 408

Sheth, R. K. & Tormen, G. 1999, MNRAS, 308, 119

Silk, J. 1976, ApJ, 208, 646

Simionescu, A., Werner, N., Urban, O., et al. 2012, ApJ, 757, 182

Slezak, E., Durret, F., & Gerbal, D. 1994, ApJ, 108, 1996

Snowden, S. L., Mushotzky, R. F., Kuntz, K. D., & Davis, D. S. 2008, A&A, 478, 615

Springel, V. 2005, MNRAS, 364, 1105

Springel, V. 2010, ARA&A, 48, 391

Springel, V., White, S. D. M., Jenkins, A., et al. 2005, Nature, 435, 629

Sugiyama, N. 1995, ApJS, 100, 281

Sunyaev, R. A. & Zeldovich, Y. B. 1970, Ap&SS, 7, 3

Sunyaev, R. A. & Zeldovich, Y. B. 1972, Comments on Astrophysics and Space Physics, 4, 173

Suwa, T., Habe, A., Yoshikawa, K., & Okamoto, T. 2003, ApJ, 588, 7

Tinker, J., Kravtsov, A. V., Klypin, A., et al. 2008, ApJ, 688, 709

Vanderlinde, K., Crawford, T. M., de Haan, T., et al. 2010, ApJ, 722, 1180

Ventimiglia, D. A., Voit, G. M., Donahue, M., & Ameglio, S. 2008, ApJ, 685, 118

Venturi, T., Giacintucci, S., Dallacasa, D., et al. 2008, A&A, 484, 327

Vikhlinin, A., Burenin, R. A., Ebeling, H., et al. 2009a, ApJ, 692, 1033

Vikhlinin, A., Forman, W., & Jones, C. 1999, ApJ, 525, 47

Vikhlinin, A., Kravtsov, A., Forman, W., et al. 2006, ApJ, 640, 691

Vikhlinin, A., Kravtsov, A. V., Burenin, R. A., et al. 2009b, ApJ, 692, 1060

Voit, G. M. 2005, Reviews of Modern Physics, 77, 207

Weinberg, S. 2008, Cosmology (Oxford University Press)

Weißmann, A., Böhringer, H., & Chon, G. 2013a, A&A, 555, A147

Weißmann, A., Böhringer, H., Šuhada, R., & Ameglio, S. 2013b, A&A, 549, A19

Werner, N., Durret, F., Ohashi, T., Schindler, S., & Wiersma, R. P. C. 2008, Space Sci. Rev., 134, 337

West, M. J. & Bothun, G. D. 1990, ApJ, 350, 36

West, M. J., Oemler, J. A., & Dekel, A. 1988, ApJ, 327, 1

White, M., Hernquist, L., & Springel, V. 2002, ApJ, 579, 16

White, S. D. M., Navarro, J. F., Evrard, A. E., & Frenk, C. S. 1993, Nature, 366, 429

Yang, H.-Y. K., Ricker, P. M., & Sutter, P. M. 2009, ApJ, 699, 315

Zhang, Y.-Y., Böhringer, H., Finoguenov, A., et al. 2006, A&A, 456, 55

Zhang, Y.-Y., Finoguenov, A., Böhringer, H., et al. 2008, A&A, 482, 451

Zhang, Y.-Y., Okabe, N., Finoguenov, A., et al. 2010, ApJ, 711, 1033

ZuHone, J. A., Markevitch, M., Brunetti, G., & Giacintucci, S. 2013, ApJ, 762, 78

ZuHone, J. A., Markevitch, M., & Johnson, R. E. 2010, ApJ, 717, 908

Zwicky, F. 1937, ApJ, 86, 217

Acknowledgements

Doing a PhD is not just about answering astrophysical questions and publishing results, but about enjoying the thrill and freedom of doing research, growing up and dealing with real-life issues. Therefore, I would like to thank everyone who made this thesis possible by being part of my life in these last three years and for encouraging me along the way.

Most of all, I would like to thank my supervisor, Prof. Hans Böhringer, for giving me the opportunity to do my PhD in the cluster group and to work on such an interesting project.

Special thanks go to the Weißmann family for encouraging me and supporting me in every possible way. Thank you, Martin, for always being there for me and for providing advice and a shoulder to cry on whenever it was needed. Thank you for sharing the good and the bad times of the last three years with me.

I am very grateful to Robo, who guided me in the first part of my PhD and became a good friend.

Thank you, Heike, for the lively and interesting discussions we had, for supporting me, for putting up with me during stressful periods and for showing me that there is more to life than work.

I would like to thank Ghazaleh and Mohammad, who provided me with tea and very interesting tasting Iranian sweets and who shared my joys and fears during this PhD.

Also, I am grateful to Lisa, Gregor and Julia for making me laugh and for discussions about any topic one can imagine.

Last, but not least, the IAYC family in general, but especially the leader team, has to be mentioned, who share my passion for stuff, devices, cookies, astronomy and the starry sky in general.

Thank you to all of you and many more who are not mentioned on this page!